

**GRAPHENE-BASED ELECTROCHEMICAL APTASENSOR
FOR THE DETECTION OF SALMONELLA TYPHIMURIUM**

SHALINI A/P MUNIANDY

INSTITUTE FOR ADVANCED STUDIES

UNIVERSITY OF MALAYA

KUALA LUMPUR

2020

**GRAPHENE-BASED ELECTROCHEMICAL APTASENSOR FOR
THE DETECTION OF SALMONELLA TYPHIMURIUM**

SHALINI A/P MUNIANDY

**THESIS SUBMITTED IN FULFILMENT OF THE
REQUIREMENTS FOR THE DEGREE OF DOCTOR OF
PHILOSOPHY**

**INSTITUTE FOR ADVANCED STUDIES
UNIVERSITY OF MALAYA
KUALA LUMPUR**

2020

UNIVERSITI MALAYA

ORIGINAL LITERARY WORK DECLARATION

Name of Candidate: **SHALINI A/P MUNIANDY**

Registration/Matric No: **HVA 170001**

Name of Degree: **DOCTOR OF PHILOSOPHY (Ph.D)**

Title of Project Paper/Research Report/Dissertation/Thesis ("this Work"): **Graphene-Based Electrochemical Aptasensor For the Detection of *Salmonella* Typhimurium**

Field of Study: **Chemistry (Chemical Chemistry)**

I do solemnly and sincerely declare that:

- (1) I am the sole author/writer of this Work;
- (2) This Work is original;
- (3) Any use of any work in which copyright exists was done by way of fair dealing and for permitted purposes and any excerpt or extract from, or reference to or reproduction of any copyright work has been disclosed expressly and sufficiently and the title of the Work and its authorship have been acknowledged in this Work;
- (4) I do not have any actual knowledge nor do I ought reasonably to know that the making of this work constitutes an infringement of any copyright work;
- (5) I hereby assign all and every rights in the copyright to this Work to the University of Malaya ("UM"), who henceforth shall be owner of the copyright in this Work and that any reproduction or use in any form or by any means whatsoever is prohibited without the written consent of UM having been first had and obtained;
- (6) I am fully aware that if in the course of making this Work I have infringed any copyright whether intentionally or otherwise, I may be subject to legal action or any other action as may be determined by UM.

Candidate's Signature:

Date:

Subscribed and solemnly declared before,

Witness's Signature:

Date:

Name:

Designation:

ABSTRACT

Recent foodborne outbreaks in multiple locations necessitate the continuous development of highly sensitive and specific biosensors that offer rapid and sensitive detection of foodborne pathogens. The emergence of electrochemical aptasensor which is a compact analytical device with a combination of an aptamer as the biorecognition element integrated on the transducer surface created a breakthrough in the detection of foodborne bacterial pathogens. Graphene has emerged as a promising nanomaterial for reliable detection of pathogenic bacteria due to its exceptional properties such as high electrical conductivity, large surface to volume ratio, high mechanical strength and its unique interactions with DNA bases of the aptamer. However, the large surface area and strong interfacial interaction caused by van der Waals force of graphene result in severe aggregation in the composite matrix. These reduce the analytical performance, overall conductivity and electron transfer rate in aqueous conditions. The challenges identified in the process of fabrication of graphene-based aptasensor can be addressed through surface modification of graphene with electrochemically active material. As such, the present thesis sought to synthesize the novel reduced graphene oxide (rGO)-organic dye/metal oxide/polymer nanocomposite materials which were then coated on glassy carbon electrode (GCE) for the rapid, sensitive and selective detection of test organism, *Salmonella enterica* serovar Typhimurium. The strategy of using these nanocomposite materials is driven by the synergistic effect between the rGO and nanoparticles which essentially boosts the overall electrochemical activity and sensing performance of the sensors. The rGO and rGO-nanocomposites were synthesized using novel and one-pot simple chemical reduction method by using a minimal amount of reducing agent (hydrazine) which could minimize the defects created on graphene sheet and reduces the overall production cost. The electrochemical properties of the graphene-nanocomposites modified electrode were studied using electrochemical characterization techniques.

Moreover, the interaction of the label-free single-stranded aptamer *S. Typhimurium* was monitored by differential pulse voltammetry analysis and this aptasensor showed high sensitivity and selectivity for whole-cell bacteria detection. Under optimum conditions, this aptasensor exhibited a linear range of detection from 10^8 to 10^1 cfu mL⁻¹ with good linearity and a detection limit of 10^1 cfu mL⁻¹. Furthermore, the developed aptasensor was evaluated with other strains of *Salmonella* and non-*Salmonella* bacteria. The results obtained showed good specificity and selectivity, respectively. The fabricated rGO-nanocomposite aptasensor was also exposed to artificially *S. Typhimurium* spiked chicken food samples. The results demonstrated that rGO-nanocomposite aptasensor possess a high potential to be adapted for the effective and rapid detection of a specific whole-cell foodborne pathogen by an electrochemical approach. Furthermore, the mechanism involving the interaction of the biorecognition element and bacterial target on the rGO-nanocomposite was also studied to understand the underlying detection strategy which will serve as guidance for the design, optimization and operation of graphene-based biosensors for future applications.

Keywords: Aptasensor, foodborne pathogen, reduced graphene oxide, rGO-nanocomposite, *S. Typhimurium*

ABSTRAK

Berekoran dengan kejadian kes-kes wabak bawaan makanan yang menular di pelbagai lokasi baru-baru ini menyebabkan penyeldikkan berterusan untuk pembangunan alat pengesan patogen bawaan makanan yang sangat sensitif dan spesifik. Kemunculan aptasensor elektrokimia yang merupakan peranti analitik padat dengan kombinasi aptamer sebagai elemen biorekognisi yang terintegrasi pada permukaan transducer mejadi penciptaan yang penting dalam proses pengesanan patogen bakteria. Grafिन pula telah muncul sebagai salah satu bahan nano yang penting untuk mengesan bakteria patogen kerana sifat-sifatnya yang luar biasa seperti kekonduksian elektrik yang tinggi, permukaan besar kepada nisbah isipadu, kekuatan mekanikal yang tinggi, dan interaksi uniknya dengan pangkalan asid nukleik yang terdapat pada aptamer. Walau bagaimanapun, permukaan yang luas dan interaksi pada ruang hubung kait yang kuat pada grafिन yang disebabkan oleh daya van der Waals menyebabkan agregasi teruk dalam matriks komposit. Ini mengurangkan prestasi analisis, konduktiviti keseluruhan dan kadar pemindahan elektron. Cabaran yang dikenal pasti dalam proses fabrikasi aptasensor berasaskan grafिन dapat ditangani melalui pengubahsuaian permukaanya dengan bahan aktif elektrokimia. Oleh itu, dalam tesis ini kami berusaha untuk mensintesis grafिन oksida terturun (rGO) dengan bahan organik, bahan oksida atau polimer nano nanokomposit yang kemudiannya dilapisi pada elektrod karbon (GCE) untuk pengesan organisma, *Salmonella enterica* serovar Typhimurium dalam masa yang singkat, sensitif, dan selektif. Strategi menggunakan bahan-bahan nanokomposit ini didorong oleh kesan sinergi antara rGO dan nanopartikel yang pada dasarnya meningkatkan aktiviti elektrokimia secara keseluruhan dan prestasi mengesan oleh sensor. rGO dan rGO-nanokomposit telah disintesis dengan menggunakan kaedah penurunan kimia yang mudah dan murah dalam satu pot dengan menggunakan ejen pengurangan (hidrazin) dalam jumlah kecil supaya ia dapat meminimumkan kerosakkan permukaan grafिन.

Sifat-sifat elektrokimia daripada elektrod grafin yang diubahsuai dengan nanopartikel telah dikaji dengan menggunakan teknik pencirian elektrokimia. Lebih-lebih lagi, interaksi oleh aptamer dengan *S. Typhimurium* juga telah dipantau dengan kaedah voltammetri denyut pembeza dan aptasensor ini menunjukkan sensitiviti dan selektiviti yang tinggi untuk pengesanan bakteria. Pada keadaan yang optimum, aptasensor ini mempamerkan keluk kalibrasi adalah linear untuk kepekatan bakteria yang berlainan iaitu dari 10^8 hingga 10^1 cfu mL⁻¹ dengan had pengesanan 10^1 cfu mL⁻¹. Selain itu, aptasensor yang dibangunkan juga telah diselidik dengan spesies and jenis *Salmonella* yang lain. Keputusan hasil daripada penyelidikan tersebut menunjukkan kekhususan dan selektiviti yang baik. Aptasensor rGO-nanokomposit juga telah didedahkan kepada sampel makanan ayam yang mengandungi *S. Typhimurium*. Hasilnya menunjukkan bahawa aptasensor rGO-nanokomposit mempunyai potensi tinggi untuk disesuaikan untuk pengesanan bakteria yang unggul dan cepat dengan teknik pendekatan elektrokimia. Selain itu, mekanisme yang melibatkan interaksi elemen biorekognisi dan sasaran bakteria pada permukaan rGO-nanokomposit juga dikaji untuk memahami strategi pengesanan yang akan menjadi panduan bagi reka bentuk, pengoptimuman dan operasi biosensor berasaskan grafin untuk aplikasi masa hadapan.

Kata kunci: Aptasensor, patogen bawaan makanan, grafin oksida terturun, rGO-nanokomposit, *S. Typhimurium*

ACKNOWLEDGEMENTS

The completion of this work has been made possible by the support of many, and I am truly thankful to the following people who have played a significant role along this doctoral journey.

Foremost, I would like to take this chance to thank Universiti of Malaya for giving me the opportunity to perform this research project. I would also like to express my sincere gratitude to my supervisors, Prof. Thong Kwai Lin, Dr. Leo Bey Fen, and Dr. Lai Chin Wei for their continuous support, patience, motivation, enthusiasm and immense knowledge throughout the entire year of research which have been so invaluable. Their guidance helped me all the time in this project and in writing of this thesis.

Besides that, my sincere thanks goes to my seniors and fellow labmates Dr. Teh Swe Jyan, Dr. Jimmy Nelson, Ignatius Julian Dinshaw, Anis Nadyra, Dolqun, and Thiruchelvi for their guidance, insightful comments, cooperation and moral support given to me to complete this research work. To the dedicated staff at the Nanotechnology and Catalysis Research Centre (NANOCAT): thank you for your service and technical support, and for always delivering with a cheerful heart.

This project is funded in part by the Ministry of Higher Education (MOHE) Transdisciplinary Research Grant Scheme [TR002B-2014B, TR002C-2014B] and University of Malaya Flagship grant [FL001A-14AET].

Finally, I would like to thank my family members especially my late father, Mr Muniandy for helping and giving me moral support in striving towards this achievement.

TABLE OF CONTENTS

ABSTRACT	iii
ABSTRAK	v
ACKNOWLEDGEMENTS	vii
TABLE OF CONTENTS	viii
LIST OF FIGURES	xiv
LIST OF TABLES	xxi
LIST OF APPENDICES	xxiv
CHAPTER 1	1
INTRODUCTION	1
1.1 Introduction	1
1.2 Problem statement	4
1.3 Objectives of the study	5
1.4 Scope of the study	6
CHAPTER 2	8
LITERATURE REVIEW	8
2.1 Foodborne pathogens	8
2.1.1 Foodborne illness	8
2.1.2 <i>Salmonella</i> serovars and salmonellosis	11
2.2 Existing method for the detection of foodborne pathogen	12

2.3 Biosensor for foodborne pathogen detection.....	18
2.3.1 Definition of biosensor	18
2.3.2 Electrochemical biosensors as a promising analytical tool for bacterial detection.....	20
2.3.3 Electrochemical aptasensor for bacterial detection	25
2.4 Carbon nanomaterials in biosensor	28
2.4.1 Graphene nanomaterial as a suitable transducer in biosensor	29
2.5 Integration of graphene-based nanocomposites and aptamers in biosensors for foodborne bacteria detection	40
2.5.1 Interaction of aptamer with targeted bacterial cell.	40
2.5.2 Graphene-based nanocomposite electrochemical aptasensor for foodborne pathogen detection.	42
2.5 Summary	44
CHAPTER 3	47
EXPERIMENTAL PROCEDURES	47
3.1 Reagents and chemicals.....	47
3.1.1 Aptamer preparation and bacterial culturing	48
3.2 Sample preparation.....	48
3.2.1 Preparation of Graphene Oxide (GO).....	48
3.2.2 Preparation of rGO and rGO-nanocomposites.....	49
3.3 Characterization techniques.....	52
3.3.1 Fourier transform infrared (FTIR) spectroscopy	52

3.3.2 X-ray diffraction (XRD)	52
3.3.3 Raman and Photoluminescence (PL) spectroscopy	53
3.3.4 Electron microscopy	53
3.4 Electrochemical cell set-up.....	53
3.5 Fabrication of the electrodes	55
3.5.1 Preparation of rGO modified electrodes.....	55
3.5.2 Preparation of rGO-based nanocomposite modified electrodes	55
3.6 Electrochemical sensing techniques	56
3.6.1 Cyclic Voltammetry (CV) and Electrochemical Impedance Spectroscopy (EIS)	56
3.6.2 Differential Pulse Voltammetry (DPV)	57
3.7 The analytical performance of the rGO/GCE and rGO-nanocomposites/GCE electrodes.....	58
3.7.1 Electrochemical detection of Ascorbic Acid (AA).....	59
3.7.2 Electrochemical detection of the bacteria	59
3.8 Statistical analysis	62
3.9 Reproducibility and shelf-life studies.....	62
3.10 Validation of the experimental results with PCR reaction.	63
CHAPTER 4	64
CONDUCTIVITY MEASUREMENT OF REDUCED GRAPHENE OXIDE MODIFIED ELECTRODE FOR ELECTROCHEMICAL DETECTION OF ASCORBIC ACID: A PRELIMINARY STUDY	64

4.1 Overview	64
4.2 Structural characterization of rGO nanomaterial.	69
4.3 Morphological characterization of rGO nanomaterial	73
4.4 Electrochemical characterization of rGO modified GCE electrode	75
4.5 Electrochemical detection of AA	77
4.5.1 Electrocatalytic oxidation of AA	77
4.5.2 Optimization studies	79
4.2.3 Reproducibility and shelf life of the modified electrode.	80
4.6 Summary	81
CHAPTER 5	82
REDUCED GRAPHENE OXIDE-NANOCOMPOSITE MODIFIED ELECTRODE FOR ELECTROCHEMICAL DETECTION OF THE FOODBORNE PATHOGEN	82
5.1 Reduced Graphene Oxide-Azophloxine nanocomposite electrochemical aptasensor for <i>Salmonella enterica</i> detection.....	82
5.1.1 Overview.....	82
5.1.2 Structural and morphological characterization of rGO-AP nanocomposite... 84	
5.1.3 Electrochemical characterization of rGO-AP modified GCE electrode	90
5.1.4 Electrochemical detection of <i>Salmonella</i> using rGO-AP nanocomposite modified electrode	92
5.2 Reduced Graphene Oxide-Titanium dioxide nanocomposite electrochemical aptasensor for <i>Salmonella enterica</i> detection.....	104
5.2.1 Overview.....	104

5.2.2 Structural and morphological characterization of rGO-TiO ₂ nanocomposite.	106
5.2.3 Electrochemical characterization of rGO-TiO ₂ modified GCE electrode	111
5.2.4 Electrochemical detection of <i>Salmonella</i> using rGO-TiO ₂ nanocomposite-modified electrode	113
5.3 Reduced Graphene Oxide-Nafion (rGO-Nf) nanocomposite electrochemical aptasensor for <i>Salmonella enterica</i> detection.....	123
5.3.1 Overview.....	123
5.3.2 Structural and morphological characterization of rGO-Nf nanocomposite..	126
5.3.3 Electrochemical characterization of rGO-Nf/GCE.....	130
5.4 Validation of experimental results with PCR method.....	140
5.5 Summary	142
CHAPTER 6	143
THE MECHANISM OF APTAMER-BACTERIAL INTERACTION ON THE SURFACE OF RGO-NANOCOMPOSITE	143
6.1 Overview	143
6.2 Chemical characterization of aptamer-bacteria interaction on graphene-nanocomposite.....	147
6.2.1 Raman spectroscopy	147
6.2.2 Photoluminescence spectroscopy	148
6.2.3 FTIR spectroscopy	155
6.3 Summary	157

CHAPTER 7	159
CONCLUSION	159
7.1 Conclusion and future perspectives.....	159
REFERENCES	162
LIST OF PUBLICATIONS	194
APPENDIX	195

Universiti Malaya

LIST OF FIGURES

Figure 1.1. Flowchart of the research studies.....	7
Figure 2.1. The relative contribution of YLL and YLD to the total burden of disease caused by foodborne hazards in 2010.....	9
Figure 2.2. Scanning electron microscopy images of <i>Salmonella</i> Typhimurium bacteria grown on human gallstones.....	11
Figure 2.3. The overall working principle of biosensors.....	19
Figure 2.4. Examples of different types of bioreceptors used in electrochemical biosensing.....	20
Figure 2.5. Three-electrode system of the electrochemical cell and a simple redox process. O=oxidized species, R=reduced species, -e=electrons, kO and kR represents the oxidation and reduction reaction rate constant, respectively.....	21
Figure 2.6. Schematic presentation of a typical aptamer selection process for whole bacterial cells.....	26
Figure 2.7. Schematic diagram of crucial steps in aptasensing.....	27
Figure 2.8. The different dimension of carbon nanomaterials which consist of (A) 0D fullerenes, (B) 1D CNT, (C) 2D graphene and (D) 3D graphite.....	30
Figure 2.9. Schematic diagram of carbon atom hybridization in graphene.....	31
Figure 2.10. Schematic representation of the methods used for the synthesis of graphene.....	33

Figure 2.11. Graphene-based nanocomposites can be functionalized with DNA's, avidin-biotin, aptamers, peptides, bacteria, cell, protein and small molecules through chemical conjugation or physical adsorption for biosensing applications.....	40
Figure 2.12. Schematic view of the aptamer molecular recognition principle.....	41
Figure 3.1. Schematic representation for the synthesis of GO using simplified Hummers' method.....	49
Figure 3.2. The overall process of the rGO preparation from Graphite.....	50
Figure 3.3. Schematic representation of the electrochemical cell setup.....	54
Figure 3.4. The Randles equivalent circuit model (left) and Nyquist plot of EIS (right).....	57
Figure 3.5. The voltammogram obtained through DPV measurement.....	58
Figure 3.6. Schematic diagram of the approach for the fabrication of rGO-AP and electrochemical detection of bacteria.....	60
Figure 3.7. Schematic diagram of the approach for the fabrication of rGO-TiO ₂ and electrochemical detection of bacteria.....	60
Figure 3.8. Schematic diagram of the approach for the fabrication of rGO-Nf and electrochemical detection of bacteria.....	61
Figure 4.1. The overall schematic of rGO chemical reduction process.....	65
Figure 4.2. The electrochemical detection of the AA.....	68

Figure 4.3. (A). FTIR spectra obtained for the GO, rGO@6h, rGO@12h and rGO@24h nanomaterial. (B) Raman spectra obtained for the GO, rGO@6h, rGO@12h and rGO@24h nanomaterial. (C) The XRD patterns of GO and rGO.....72

Figure 4.4. (A) SEM image obtained for the GO, rGO@6h, rGO@12h and rGO@24h nanomaterial. (B) TEM image obtained for the GO, rGO@6h, rGO@12h and rGO@24h nanomaterial.....74

Figure 4.5. (A) Nyquist plots for bare GCE, rGO/GCE, rGO@6h, rGO@12h and rGO@24h nanomaterial at different reduction time (Inset shows the electrical equivalent circuit that fit the Nyquist plot of GC/rGO-Nf (16 h)), respectively. (B) Bode plots obtained for different modified electrodes.....77

Figure 4.6. Schematic representation of detection of AA on the surface of rGO@12h/GCE electrode.....78

Figure 5.1. The chemical structure of Azophloxine dye.....83

Figure 5.2 (A). The FTIR spectra of AP, rGO, rGO-AP@0.002M, rGO-AP@0.005M and rGO-AP@0.01M. (B) Raman spectra of AP, rGO, rGO-AP@0.002M, rGO-AP@0.005M and rGO-AP@0.01M. (C) The XRD spectra of rGO and rGO-AP.....87

Figure 5.3 (A). The SEM of (a) rGO, (b) rGO-AP@0.002M, (c) rGO-AP@0.005M and (d) rGO-AP@0.01M. (B) The TEM of (a) rGO, (b) rGO-AP@0.002M, (c) rGO-AP@0.005M and (d) rGO-AP@0.01M. The inset in (b) shows the rGO-AP@0.005M in high magnification with 10.09 nm thickness.....89

Figure 5.4. (A) CV and (B) Nyquist plots for bare GCE, rGO/GCE, rGO-AP@0.2M/GCE, rGO-AP@0.4M/GCE and rGO-AP@0.6M/GCE electrodes.....92

Figure 5.5 (A) CV of bare GCE, rGO/GCE, rGO-AP@0.005M/GCE and ssDNA/rGO-AP@0.005M/GCE electrodes in 10X PBS (pH 7.0) at the scan rate of 100 mV s ⁻¹ . (B) DPV signal of bare GCE, rGO-AP@0.005M/GCE, STM/ssDNA/rGO-AP@0.005M/GCE and ssDNA/rGO-AP@0.005M/GCE electrodes in Tris-HCl buffer, pH 7.4.....	95
Figure 5.6. (A) DPV of ssDNA/rGO-AP@0.005M/GCE, (b) 10 ⁸ cfu mL ⁻¹ , (c) 10 ⁶ cfu mL ⁻¹ (d) 10 ⁴ cfu mL ⁻¹ , (e) 10 ² cfu mL ⁻¹ , (f) 10 ¹ cfu mL ⁻¹ and (g) rGO-AP@0.005M/GCE in Tris-HCl buffer, pH 7.4. (B) A linear relationship between the current density and cell concentration (logarithm). (C) DPV of <i>S. Typhimurium</i> , <i>E. coli</i> , <i>V. cholerae</i> , <i>K. pneumoniae</i> and <i>Sh. dysenteriae</i> in Tris-HCl buffer, pH 7.4.....	99
Figure 5.7. DPV of spiked chicken food samples with different concentrations of bacteria recorded in Tris-HCl buffer, pH 7.4.....	101
Figure 5.8. (A) CV curves of five different rGO-AP@0.005M/GCE modified electrodes and (B) histogram of shelf life of rGO-AP@0.005M/GCE electrode up to 28 days recorded in 10X PBS at a scan rate of 100 mV/s.....	103
Figure 5.9 (A) The FTIR spectra of rGO, TiO ₂ , rGO-TiO ₂ @0.2M, rGO-TiO ₂ @0.4M and rGO-TiO ₂ @0.6M. (B) The Raman spectra of rGO, TiO ₂ , rGO-TiO ₂ @0.2M, rGO-TiO ₂ @0.4M and rGO-TiO ₂ @0.6M. (C) The XRD spectra of rGO and rGO-TiO ₂	109
Figure 5.10 (A). SEM images of rGO, rGO-TiO ₂ @0.2M, rGO-TiO ₂ @0.4M and rGO-TiO ₂ @0.6M. (B) TEM image of rGO, rGO-TiO ₂ @0.2M, rGO-TiO ₂ @0.4M and rGO-TiO ₂ @0.6M.....	111

Figure 5.11 (A) The DPV plot of blank GCE, rGO/GCE, rGO-TiO ₂ @0.2M/GCE, rGO-TiO ₂ @0.4M/GCE and rGO-TiO ₂ @0.6M/GCE in Zobell's solution at scan rate 100 mV/s.....	112
Figure 5.12. The Nyquist plot of (a) bare GCE, (b) rGO/GCE, (c) STM/ssDNA/rGO-TiO ₂ @0.4M/GCE, (d) ssDNA/rGO-TiO ₂ @0.4M/GCE and (e) rGO-TiO ₂ @0.4M/GCE electrodes in Zobell's solution.....	115
Figure 5.13. Electrochemical detection of bacterial cells using the fabricated electrodes. (A) DPV of (a) rGO-TiO ₂ @0.4M/GCE, (b) ssDNA/rGO-TiO ₂ @0.4M/GCE, (c) 10 ⁸ cfu mL ⁻¹ , (d) 10 ⁶ cfu mL ⁻¹ (e) 10 ⁴ cfu mL ⁻¹ , (f) 10 ² cfu mL ⁻¹ and (g) 10 ¹ cfu mL ⁻¹ in Zobell solution (pH 7.0). (B) Linear relationship between the current density and cell concentration (logarithm). (C). Graph of peak currents obtained for (a) <i>S. Typhimurium</i> , (b) <i>E. coli</i> , (c) <i>V. cholerae</i> , (d) <i>K. pneumoniae</i> , (e) <i>Sh. Dysenteriae</i> and (f) <i>Staph. aureus</i> in Zobell's solution (pH 7.0). Data are expressed as mean ± standard deviation (n = 3).....	118
Figure 5.14. DPV signal obtained for food samples tested with the fabricated electrodes. (a) FS 1, (b) FS 2, (c) FS 3, (d) FS 4, (e) FS 5, (f) FS 6 and (g) FS 7.....	120
Figure 5.15. (A) Histogram of shelf life of rGO-TiO ₂ @0.4M/GCE electrode up to 28 days recorded in Zobell's solution at a scan rate of 100 mV/s and (B) CV curves of five different rGO-TiO ₂ @0.4M/GCE modified electrodes.....	122
Figure 5.16. The Structure of Nafion.....	23
Figure 5.17. (A) FTIR spectra of rGO, rGO-Nf@0.002M, rGO-Nf@0.005M and rGO-Nf@0.01M. (B) Raman spectra of rGO, rGO-Nf@0.002M, rGO-Nf@0.005M and rGO-Nf@0.01M. (C) The XRD spectra of rGO and rGO-Nf.....	128

Figure 5.18 (A). SEM of (a) rGO, (b) rGO-Nf@0.002M, (c) rGO-Nf@0.005M and (d) rGO-Nf@0.01M. (B). TEM of (a) rGO, (b) rGO-Nf@0.002M, (c) rGO-Nf@0.005M and (d) rGO-Nf@0.01M.....	130
Figure 5.19. The Nyquist plots for bare GCE, rGO-Nf@0.002M, rGO-Nf@0.005M and rGO-Nf@0.01M.....	132
Figure 5.20. The Nyquist plot of bare GCE, rGO-Nf@0.005M/GCE, STM/ssDNA/rGO-Nf@0.005M/GCE and ssDNA/rGO-Nf@0.005M/GCE electrodes in Tris-HCl buffer, pH 7.4.....	134
Figure 5.21 (A) DPV of ssDNA/rGO-Nf@0.005M/GCE, (b) 10^8 cfu mL ⁻¹ , (c) 10^6 cfu mL ⁻¹ (d) 10^4 cfu mL ⁻¹ , (e) 10^2 cfu mL ⁻¹ , (f) 10^1 cfu mL ⁻¹ and (g) rGO-Nf@0.005M/GCE in Tris-HCl buffer, pH 7.4. (B) A linear relationship between the current density and cell concentration (logarithm). (C). DPV of <i>S. Typhimurium</i> , <i>E. coli</i> , <i>V. cholerae</i> , <i>K. pneumoniae</i> and <i>Sh. dysenteriae</i> in Tris-HCl buffer, pH 7.4.....	137
Figure 5.22 DPV of spiked chicken food samples with different concentrations of bacteria recorded in Tris-HCl buffer, pH 7.4.....	138
Figure 5.23. (A) CV curves of five different rGO-Nf@0.005M/GCE modified electrodes and (B) histogram of shelf life of rGO-Nf@0.005M/GCE electrode up to 28 days recorded in 10X PBS at a scan rate of 100 mV s ⁻¹	139
Figure 5.24. (A) The sensitivity of detection by PCR for <i>S. Typhimurium</i> . Gel electrophoresis patterns of PCR products obtained at different concentration of DNA: Lane 1, 10^8 cfu mL ⁻¹ ; Lane 2, 10^6 cfu mL ⁻¹ ; Lane 3, 10^4 cfu mL ⁻¹ ; Lane 4, 10^2 cfu mL ⁻¹ ; Lane 5, 10^1 cfu mL ⁻¹ ; Lane 6, negative control; and Lane 7, 100 bp ladder. (B) The specificity test for different types of <i>Salmonella</i> bacteria: Lane 1, 100 bp ladder; Lane	

2, *S. Typhimurium*; Lane 3, *S. Enteritidis*; Lane 4, *S. Paratyphi A*; Lane 5, *S. Typhi*; Lane 6, *S. Albany*; Lane 7, *S. Corvallis*; Lane 8, *S. Pullorum*; and Lane 9, negative control. (C) The selectivity test for non-*Salmonella* bacteria: Lane 1, *V. cholerae*; Lane 2, *Sh. dysenteriae*; Lane 3, *E. coli*; Lane 4, *K. pneumoniae*; and Lane 5, *Staph. aureus* with 100 bp ladder.....141

Figure 6.1. The Brillouin zone of graphene.....144

Figure 6.2. The electronic band structure of graphene. Red lines indicate σ bands and the blue line indicates π bands..... 144

Figure 6.3. The Fermi level in graphene for (a) absence of doping, (b) p-doped and (c) n-doped.....146

Figure 6.4. The Raman spectra of rGO-nanocomposites in the presence of aptamer and bacteria.....148

Figure 6.5. The photoluminescence spectra of rGO-nanocomposites in the presence of aptamer and bacteria.....155

Figure 6.6. The FTIR spectra of rGO-nanocomposites in the presence of aptamer and bacteria.....156

LIST OF TABLES

Table 2.1: Summary of conventional and modern analytical methods used for bacterial detection.....	17
Table 2.2: Overview of the evaluation and properties of graphene-based aptasensors for foodborne pathogen detection.....	46
Table 3.1: List of reagents and chemicals.....	47
Table 5.1. The comparison of biosensor developed in this study with other detection methods.....	100
Table 5.2. Detection response (Mean \pm S.D) (n=3) obtained with bacterial suspensions and spiked food sample.....	102
Table 5.3. Comparison of various bacterial detection techniques with the current study.....	119
Table 5.4. The comparison between measured concentration and enumeration of <i>S. Typhimurium</i> from the food samples. Data are expressed as mean \pm standard deviation.....	121
Table 6.1: Summary of the changes in the bandgap in rGO-nanocomposites.....	149

LIST OF SYMBOLS AND ABBREVIATIONS

AA	:	Ascorbic acid
AP	:	Azophloxine
CV	:	Cyclic voltammetry
PCR	:	Polymerase Chain Reaction
DNA	:	Deoxyribonucleic acid
DPV	:	Differential pulse voltammetry
EIS	:	Electrochemical impedance spectroscopy
RNA	:	Ribonucleic acid
FESEM	:	Field emission scanning electron microscopy
GCE	:	Glassy carbon electrode
GO	:	Graphene oxide
H ₂ O ₂	:	Hydrogen peroxide
H ₂ SO ₄	:	Sulphuric acid
H ₃ PO ₄	:	Phosphoric acid
HCl	:	Hydrochloric acid
N ₂ H ₄	:	Hydrazine
TEM	:	Transmission electron microscopy
KMnO ₄	:	Potassium permanganate
FTIR	:	Fourier transform infrared spectroscopy
TiO ₂	:	Titanium dioxide
WHO	:	World Health Organization

WE	:	Working electrode
PL	:	Photoluminescence
rGO	:	Reduce graphene oxide
XRD	:	X-ray diffraction
Nf	:	Nafion
Rct	:	Charge transfer resistance
ELISA	:	Enzyme-linked immunosorbent assays
LFI	:	Lateral flow immunoassay
Zw	:	Warburg impedance
Rs	:	Resistance of the electrolyte solution
Cdl	:	Capacitor

Universiti Malaysia

LIST OF APPENDICES

Appendix A1. CV curve of for bare GCE, rGO/GCE, rGO@6h, rGO@12h and rGO@24h nanomaterial at different reduction time.....	195
Appendix A2. CV plot obtained for bare GCE, rGO/GCE, rGO@6h, rGO@12h and rGO@24h modified electrodes in presence of 0.1 M PBS (pH 6.5) solution containing 100 μ M AA at a scan rate of 100 mV/s.....	195
Appendix A3. (A) CV curves obtained for the rGO@12h/GCE modified electrode in the 0.1 M PBS (pH 6.5) and different concentration of AA (10 to 100 μ M) at a scan rate of 100 mV/s. (B) linear relationship between current density and the concentration of AA.....	196
Appendix A4. (A) CV curves obtained for the rGO@12h/GCE modified electrode in the Zobell's solution at a scan rate of 10-100 mV/s. (B) the corresponding plot of anodic and cathodic peak currents versus scan rate.....	197
Appendix A5.(A) CV plot of rGO@12h/GCE modified electrode with different loading amount of sample and (B) Line plot of peak current response versus rGO@12h/GCE loading obtained in 0.1 M PBS (pH 6.5) at a scan rate of 100 mV/s.....	198
Appendix A6. (A) CV curves of five different rGO@12h/GCE modified electrodes and (B) Shelf life of rGO@12h/GCE modified electrodes measured for 21 days with 0.1 M PBS (pH 6.5) at a scan rate of 100 mV/s.....	199

Appendix B1. Effects of (A) rGO-AP@ 0.005M concentration (mg mL^{-1}), (B) Aptamer concentration ($\mu\text{mol L}^{-1}$), (C) Bacteria incubation time (min) on the peak current measured with CV at a scan rate of 100 mV s^{-1} . (D) CV curves obtained for the rGO-AP@ 0.005M modified electrode in the Zobell's solution at a scan rate of 10-100 mV/s and (E) The linear relationship of maximum peak currents obtained at various scan rates.....202

Appendix C1. The CV plot of blank GCE, rGO/GCE, rGO-TiO₂@0.2M/GCE, rGO-TiO₂@0.4M/GCE and rGO-TiO₂@0.6M/GCE in Zobell's solution at scan rate 100 mV/s.....203

Appendix C2. Effects of rGO-TiO₂ concentration, aptamer concentration and various scan rate on the sensing performance of the fabricated electrodes. The effect of (A) rGO-TiO₂ concentrations (mg mL^{-1}) and (B) aptamer concentrations ($\mu\text{mol L}^{-1}$) on peak currents measured with CV at a scan rate of 100 mVs^{-1} . The effect of (C) various scan rates (mVs^{-1}) on peak currents measured using CV at scan rate of (a) 10, (b) 20, (c) 40, (d) 60, (e) 80 and (f)100. (D) The linear relationship of maximum peak currents obtained at various scan rates.....205

Appendix C3. CV of (a) rGO-TiO₂@0.4M/GCE, (b) ssDNA/rGO-TiO₂@0.4M/GCE, (c) rGO/GCE and (d) bare GCE in Zobell solution (pH 7.0) at the scan rate of 100 mVs^{-1}205

Appendix D1. The CV for bare GCE, rGO-Nf@0.002M, rGO-Nf@0.005M and rGO-Nf@0.01M.....206

Appendix D2. Effects of rGO-Nf concentration, aptamer concentration and various scan rate on the sensing performance of the fabricated electrodes. The effect of (A)

rGO-Nf@0.005M concentrations (mg mL^{-1}) and (B) aptamer concentrations ($\mu\text{mol L}^{-1}$) on peak currents measured with CV at a scan rate of 100 mVs^{-1} . The effect of (C) various scan rates (mVs^{-1}) on peak currents measured using CV at scan rate of (a) 10, (b) 20, (c) 40, (d) 60, (e) 80 and (f)100. (D) The linear relationship of maximum peak currents obtained at various scan rates.....208

Appendix D3: The CV of GCE, rGO/GCE, rGO-Nf@0.005M/GCE and ssDNA/rGO-Nf@0.005M/GCE electrodes in 10X PBS at the scan rate of 100 mV s^{-1}208

Universiti Malaysia

CHAPTER 1

INTRODUCTION

1.1 Introduction

Foodborne illness remains a major concern worldwide due to its negative impact on public health and the world's economy in terms of medical expenses and loss of productivity. The World Health Organization (WHO) reported 1.7 billion global episodes of the diarrheal disease annually which associated with 1.87 million deaths predominately in Africa and Southeast Asia (Troeger et al., 2018). The most prevalent gastroenteritis-causing bacteria in Asian countries (e.g. Japan, Korea, Singapore and Thailand) is nontyphoidal *Salmonella enterica* (Sinwat et al., 2016). In Malaysia, the major *Salmonella* serovars responsible for the foodborne outbreaks are *Salmonella enterica* serovar Enteritidis and ser. Typhimurium (Ngoi, Teh, Chai, & Thong, 2015; Thung et al., 2016) mostly due to poor hygiene in food handling and sanitation practices (Salleh, Lani, Abdullah, Chitek, & Hassan, 2017). Hence, the development of rapid, cost-effective and sensitive detection techniques for the presence of foodborne pathogens is crucial to ensure safe food supply and to reduce the outbreaks of foodborne disease especially, those caused by *Salmonella enterica* (Law, Ab Mutalib, Chan, & Lee, 2015).

The existing traditional culture methods of detecting foodborne pathogens require days (48 h to 72 h) to confirm the presence of target pathogens due to the need for pre-enrichment of the food matrix and extensive culture plating procedures (López-Campos, Martínez-Suárez, Aguado-Urda, & López-Alonso, 2012). Thus, molecular-based methods such as Polymerase Chain Reaction (PCR) and real-time PCR were employed to complement the traditional time-consuming culture methods (Priyanka, Patil, & Dwarakanath, 2016). PCR is an effective tool for the detection of *Salmonella* which involves rapid exponential amplification of a DNA fragment or sequence of interest

(Heymans et al., 2018). However, the PCR approach is a qualitative analysis leading to insufficient cell number quantitation and false-positive results due to nonspecific amplification of DNA (Kralik & Ricchi, 2017). To rectify these issues, real-time PCR was applied to quantify DNA in real-time but it is laborious and requires costly reagents coupled with PCR-inhibitory effects in complex food matrixes (Lopes, Albuquerque, & Maciel, 2018). The existing methods used for the detection and identification of foodborne pathogens are costly and time-consuming since they involve a multi-step process (DNA extraction is often needed) and require specialized equipment along with trained users (Law, Ab Mutalib, Chan, & Lee, 2015).

Electrochemical aptasensors are analytical devices that consist of aptamer immobilized on a working electrode targeting an analyte of interest and a transduction element for converting the recognition process into an amperometric, potentiometric or impedimetric signal. The intrinsic specificity and high affinity accompanied by high stability of RNA/DNA single-stranded aptamers are novel detection probe in electronic biosensing platforms (Abbaspour, Norouz-Sarvestani, Noori, & Soltani, 2015). The electrochemical approach coupled with aptamer is also able to detect whole-cell bacteria because the outer membrane of bacteria itself is composed of conductive layers of macromolecules with electrochemical active groups that can react with the free ions in the electrolyte (Becerro, Paredes, & Arana, 2015). Advances in the electrochemical aptasensor help to overcome drawbacks of traditional culture and molecular methods by providing rapid, sensitive, specific, cost-effective and direct detection of whole-cell bacteria in food matrixes.

Recently, graphene and its derivatives-based nanocomposites have been popularly adapted for the development of highly sensitive electrochemical aptasensors. They offer diverse advantages in electrochemical sensing of foodborne pathogens especially by

providing high performance in terms of field-effect mobility and sensitivity (Angione et al., 2011). Excellent physico-chemical properties of graphene and its derivatives such as high conductivity ($\sim 1,000 \text{ S cm}^{-1}$) (Chen et al., 2016), large specific surface area ($400\text{-}700 \text{ m}^2 \text{ g}^{-1}$) (Raza, 2012), biocompatibility (Huang et al., 2019), great mechanical strength ($\sim 130 \text{ G Pa}$) (Xia et al., 2015) and the presence of versatile functional groups such as -OH , -COOH and -CHO which aids the interaction with biomolecules make it a suitable material for the development of electrochemical biosensors (Krishnan, Singh, Singh, Meyyappan, & Nalwa, 2019). Moreover, graphene is also composed of hexagonally arrayed sp^2 -bonded carbon atoms which facilitate its surface modifications through non-covalent interaction such as π - π stacking or hydrogen bonding between graphene derivatives and biomolecules for electroanalytical sensing applications (Adhikari, Govindhan, & Chen, 2015).

The main challenge in fabrication of graphene-based biosensors is the aggregation of the graphene layer caused by the strong van der Waals interaction decreases its surface area, conductivity (slow electron transfer) and hinders the overall electrochemical activity (Ke & Wang, 2016). Besides, the electrocatalytic activity of pure graphene is low and immobilization of biomolecules can be difficult due to the presence limited number of oxygen-bearing groups in chemically reduced graphene (Mazánek et al., 2019; Yin, Kim, Choi, & Lee, 2013). Thus, most researchers used chemical modification strategy to functionalize or conjugate graphene with active materials such as, metal/metal oxide, organic materials (e.g. amino acids, surfactants, organic dyes) and polymer (chitosan, polyaniline, polypyrrole, Nafion) to enhance their electrochemical properties, electrical conductivity, surface area and sensitivity that lead too high signal-to-noise ratio (Chang & Baek, 2016; Khan et al., 2015; Liu et al., 2018).

The synergistic effect between graphene and nanocomposites helps to completely exfoliate graphene sheets and increases its dispersibility in solution state which increases its surface area accompanied with good biocompatibility to aid the immobilization of bioreceptor on its surface. Moreover, the nanocomposites on graphene's surface enhance a smoother and rapid electron flow which can increase its overall conductivity. This research was focused on the fabrication of simple and cost-effective different combinations of graphene-based nanocomposites as an effective sensing platform for achieving sensitive, selective, rapid and low-cost aptasensor for electrochemical detection of foodborne pathogens.

1.2 Problem statement

Despite good progress in developing a graphene-based electrochemical biosensor for the detection of foodborne pathogens, it holds several challenges in the fabrication process for an electrochemical biosensor such as:

- Poor electrocatalytic properties and slow heterogeneous electron transfer on the surface of pure graphene led to the low sensitivity and high detection limit.
- Aggregation of pure graphene in water decreases the active surface area which limits the immobilization of aptamer and hinders the regeneration of redox species.
- The presence of lesser oxygen-bearing groups on the surface of graphene making the immobilization process more challenging.
- The use of enzymes and antibodies are costly and their vulnerabilities towards pH, temperature, humidity and toxic chemicals prompted the instability of the electrode.

- The slow response times during the analysis has lowered the sensitivity of the electrode and further limits its application in the real-time monitoring of biological processes.

Therefore, the fundamental research in finding the suitable material for modifying the graphene material, immobilization of suitable bioreceptors for whole-cell bacteria detection and identifying suitable analytical technique needs to be proposed by considering the simple preparation method, low cost of production, high conductivity, good biocompatibility, large active surface area, excellent selectivity and specificity.

1.3 Objectives of the study

The primary focus of the research is to explore the potential of novel graphene derivative, rGO nanocomposites based on the organic dye and metal oxides for the development of a highly sensitive and selective electrochemical aptasensor for the whole-cell bacterial detection. The specific objectives of this study are:

- 1) To develop an easy and cost-effective method in synthesizing rGO and rGO-nanocomposites to be used for biosensor applications.
- 2) To study the electrochemical properties of rGO and rGO-nanocomposites as an active material platform for biosensors.
- 3) To investigate and optimize the electrochemical detection of the whole-cell *Salmonella* bacteria using the rGO-nanocomposite electrodes.
- 4) To investigate the interaction of aptamer with bacterial cells on the surface of rGO-nanocomposites.

1.4 Scope of the study

The combination of graphene-based nanocomposite and aptamer biorecognition element with the electrochemical analytical tool for the detection of whole-cell bacteria which eliminates the need for DNA extraction was not common due to the expensive cost of production and difficult probe immobilization process. This problem provides a motivation to explore for potential solutions of bacterial detection in biosensors field of study. Moreover, the application of graphene with organic dye, metal oxide and polymer nanocomposites in the field of bacterial detection using electrochemical aptasensor is novel.

The selection of organic dye, metal oxide nanoparticle and polymer to be combined with graphene is driven by its excellent physical and chemical properties, which is capable to enhance the electroactive surface area and improving the electrocatalytic features of the electrode. The synergistic effect between these nanocomposite helps to improve its dispersibility in aqueous solution and enhances overall sensitivity and selectivity of the sensor.

Several factors have been considered in realizing the objectives of this study including, the use of the simple technique to synthesize the nanocomposites materials, minimum use of raw material, effective sensing technique and validation of the proposed sensor electrode in term of its capability of the detection in real food samples, reproducibility and stability.

The rGO and rGO-nanocomposites were synthesized using a simple chemical reduction method by using a minimal amount of reducing agent (hydrazine). The chemical and physical properties of the materials were analyzed using Fourier transform infrared spectroscopy (FTIR), X-ray diffraction (XRD), Raman spectroscopy, photoluminescence (PL) spectroscopy, Field emission scanning electron microscopy

(FESEM) and Transmission Electron Microscopy (TEM). The electrochemical properties of the graphene-nanocomposites modified electrode were studied using electrochemical characterization techniques i.e. cyclic voltammetry (CV) and electrochemical impedance spectroscopy (EIS). Moreover, the electrochemical detection of the whole-cell *Salmonella* and non-*Salmonella* bacteria were also studied using Differential Pulse Voltammetry (DPV).

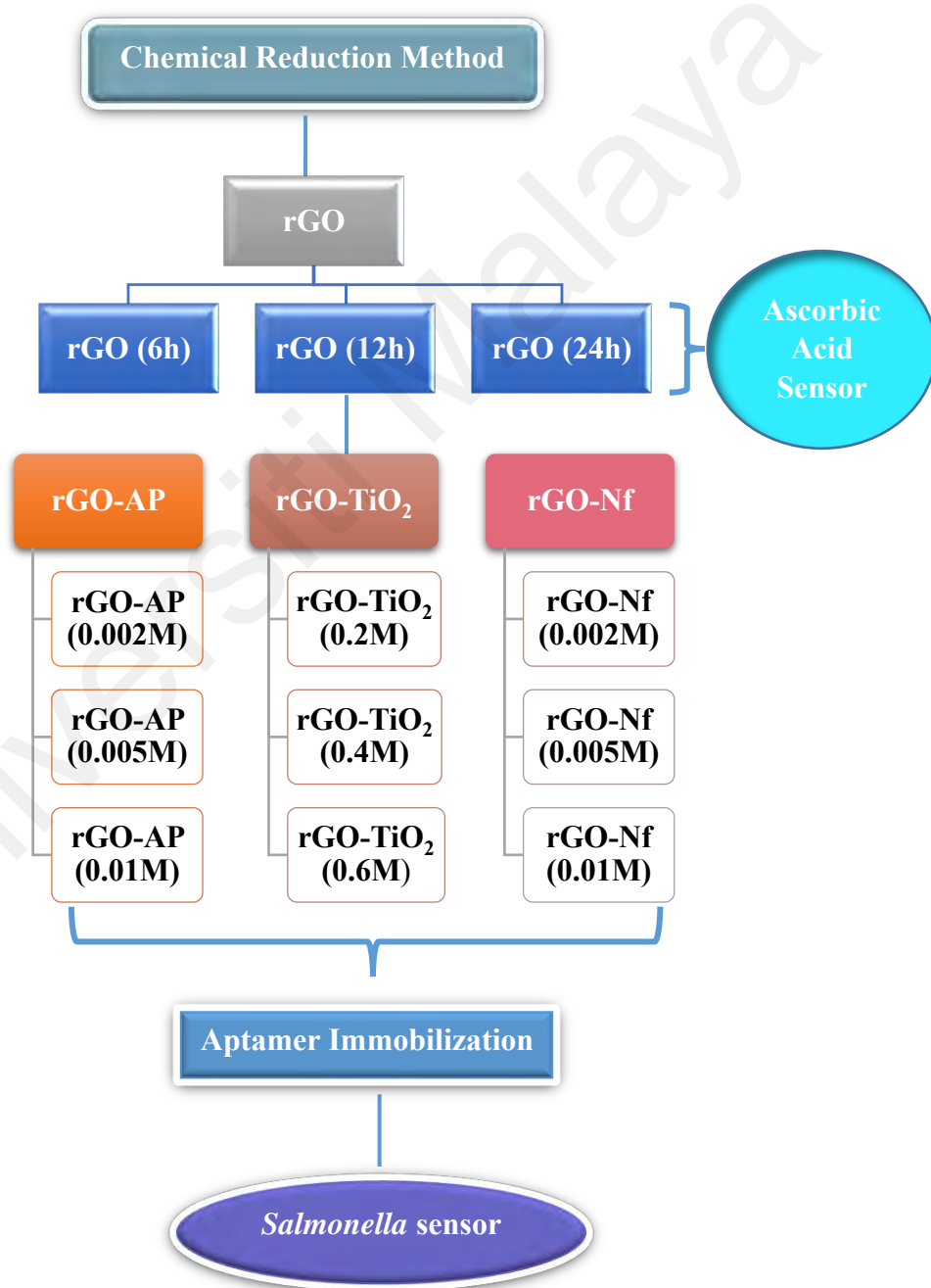


Figure 1.1. Flowchart of the research studies.

CHAPTER 2

LITERATURE REVIEW

2.1 Foodborne pathogens

More than 250 different types of bacterial foodborne illness and 90% of foodborne disease outbreaks worldwide (Kibret & Abera, 2012). Microbial pathogens such as *Escherichia coli* (especially O157:H7 strain), *Salmonella enterica* (non-typhoidal serotypes), *Campylobacter jejuni*, *Listeria monocytogenes*, *Bacillus cereus* and *Shigella spp.*, *Vibrio cholerae*, *Salmonella Typhi* and *Salmonella Paratyphi* are the most pronounced foodborne pathogens with known high case-fatality ratios which have led to 33 million Disability Adjusted Life Years (DALYs) including approximately 230,000 deaths of worldwide human population (Havelaar et al., 2015). Approximately, 54% of the total burden was attributed to diarrheal disease agents, particularly to non-typhoidal *S. enterica* which was responsible for 4.0 million DALYs. Six diarrheal disease agents such as norovirus, *Campylobacter spp.*, pathogenic *Escherichia coli*, *V. cholerae* and *Shigella spp.*) caused a foodborne burden of 1–3 million DALYs individually.

2.1.1 Foodborne illness

World health organization (WHO) defined foodborne disease is an infectious illness caused by the ingestion of adulterated foods or water. There are two main types of foodborne illness namely intoxication and infection which initiate diseases caused by the consumption of bacterial toxins and direct consumption of viable pathogens present in food products (Bintsis, 2017). Food poisoning resulted from the ingestion of contaminated food and drinks will be manifested in the form of severe gastrointestinal disease in humans. Foodborne diseases remain as one of the important global issues of great magnitude in terms of human life treat and economic burden. Foodborne diseases

are also the major cause of morbidity and mortality of the human population in both developed and developing nations (Scharff, 2012). Thus, WHO proposed Foodborne Illness Disability Adjusted Life Years (DALYs) calculations to assess the safety of food systems by quantifying the harmful health outcomes which include foodborne illnesses, foodborne disease burden and cases reported as food poisoning (Organization, 2015). DALYs are calculated by adding the number of years lived with a disability (YLD) with the number of years of lost life (YLL) due to a given foodborne illness.

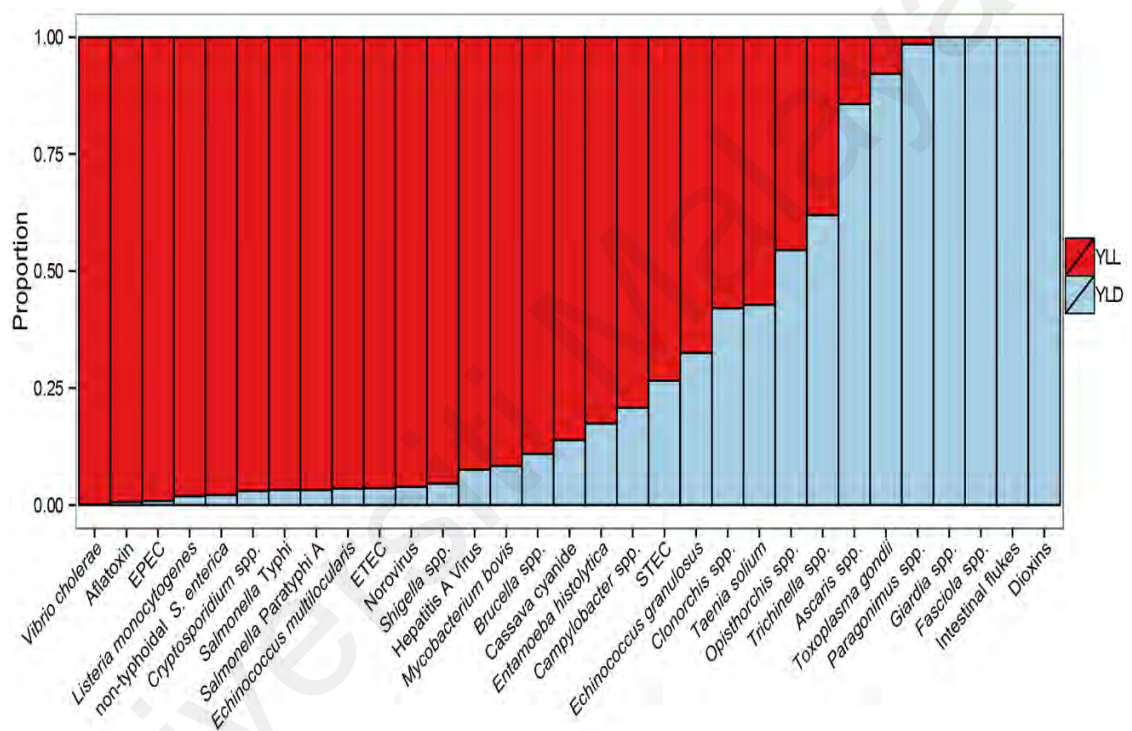


Figure 2.1. The relative contribution of YLL and YLD to the total burden of disease caused by foodborne hazards in 2010 adapted from (Havelaar et al., 2015).

In 2010, WHO reported the global estimates and regional comparison on the impact of foodborne diseases on the human population. The relative contribution of mortality (measured as YLL) and morbidity (measured as YLD) to the total burden of disease varied widely between hazards as shown in **Figure 2.1**. According to the statistical analysis, the highest foodborne illness burden was borne by Africa with 2500 DALYs per 200000 of population and most importantly, in Southeast Asia about 1400

DALYs per 200000 of the population were recorded (Havelaar et al., 2015). In Malaysia, the incidence and mortality rates due to food poisoning were reported as 47.34 and 0.01, respectively per 100,000 populations (R. New, 2017). Although the recorded mortality rate is low, the number of food poisoning cases especially among school-aged children rose to an alarming level (R. New, 2017).

Besides fatality, foodborne diseases also cause a high economic burden across countries (Hoffmann & Scallan, 2017). The economics loses can be categorized into direct cost and indirect cost. Direct cost includes medical expenditures associated with disease diagnosis, treatment and management whereas, indirect cost included loss of productivity due to illness or death (McLinden, Sargeant, Thomas, Papadopoulos, & Fazil, 2014) or the economic impact due to decreased income from the tourism and export business (Lee, 2017). In United States, Australia and New Zealand foodborne illness costs US\$10-83 billion, US\$1.3 billion and US\$86 million, respectively per year as compared to Europe which is about US\$173 million (Lake, Cressey, Campbell, & Oakley, 2010; McLinden et al., 2014; McPherson, Kirk, Raupach, Combs, & Butler, 2011; Nyachuba, 2010). In Asian countries such as India and Indonesia, the economic losses associated with foodborne illness achieved US\$28 billion and US\$78 million, respectively (Kristkova, 2017; Rahayu et al., 2016).

This problem remains a major threat to the socioeconomic status of all nations due to prevailing poor knowledge of sanitation, improper food handling approaches, improper agricultural practices, lower safety standards and weak enforcement of food safety laws (Kibret & Abera, 2012). To prevent ongoing transmissions of diseases and loss of human life, the reliable and rapid detection of foodborne pathogens is required because diagnosing and treating foodborne diseases have been life-and-death situations in healthcare settings (Zhao, Lin, Wang, & Oh, 2014).

2.1.2 *Salmonella* serovars and salmonellosis

Salmonella (Figure 2.2) is a flagellated enteric rod-shaped, facultative anaerobe and Gram-negative bacteria that classified under the family of *Enterobacteriaceae*. *Salmonella* is the most predominant cause of foodborne gastroenteritis worldwide (Humphries & Linscott, 2015). It can be commonly isolated from poultry, eggs, beef, milk products, fruits, vegetables and seafood (Carrasco, Morales-Rueda, & García-Gimeno, 2012). *Salmonella* serovars are classified into the host-restricted (*Salmonella* Typhi, *Salmonella* Paratyphi A, B, C and *Salmonella* Pullorum), host-adapted (*Salmonella* Choleraesuis and *Salmonella* Typhisuis) and broad-host-range (*Salmonella* Typhimurium and *Salmonella* Enteritidis) serovars (Jajere, 2019). The two most important serotypes of *Salmonella* that cause foodborne illness especially gastroenteritis disease in humans are *S.* Typhimurium and *S.* Enteritidis (Eng et al., 2015). *Salmonella* serovars capable of adapting to extreme environmental conditions (Finn, Condell, McClure, Amézquita, & Fanning, 2013). For example, *Salmonella* can grow at a temperature between 5-47 °C with an optimum temperature of 35-37 °C. They are sensitive to heat and can be killed at a temperature of 70 °C or higher. *Salmonella* grows in a pH range of 4.5 to 9.5 with an optimum between pH 6.5 and 7.5.

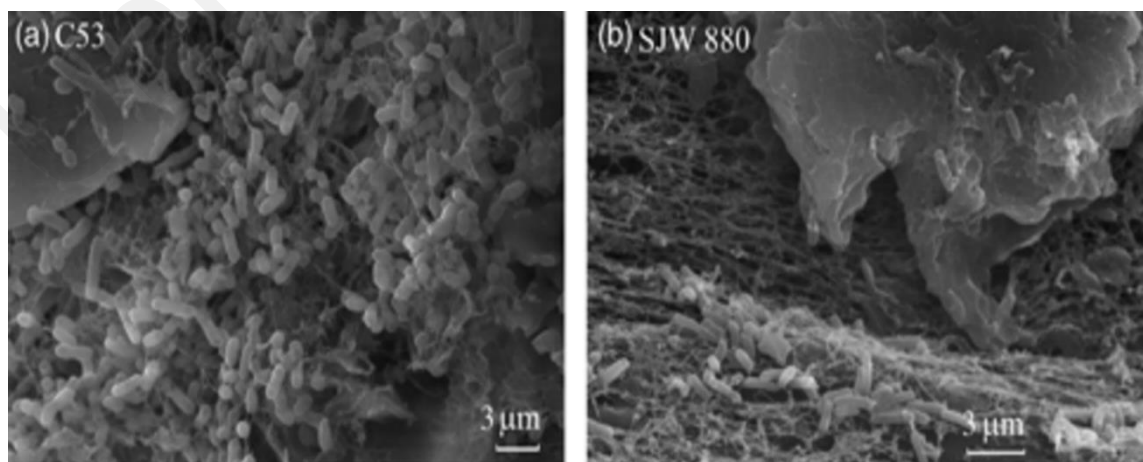


Figure 2.2. Scanning electron microscopy images of *S.* Typhimurium bacteria grown on human gallstones (Galkina et al., 2011)

Salmonellosis resulting from a foodborne infection/intoxication is a significant health problem in humans. The annual global burden of non-typhoid *Salmonella*-mediated gastroenteritis has been estimated as high as 93.8 million cases with 155,000 deaths (Majowicz et al., 2010). This pathogen is transmitted to its host through a fecal-oral route facilitated by unhygienic and poor sanitation conditions. *Salmonella* evades and exploits the host immune systems to promote its colonization and replication in the inflamed gut mucosa that leads to gastrointestinal diseases (Winter et al., 2010). Salmonellosis is a primary cause of mortality in human especially in under-developed countries (Marzel et al., 2016). However, in developed countries, the occurrence of Salmonellosis is less fatal, but it causes significant economic burden due to healthcare and social-related cost (Tennant, MacLennan, Simon, Martin, & Khan, 2016). Among the other diarrheal disease agents, non-typhoidal *S. enterica* serovars which consist of 2600 serovars is the leading cause of foodborne disease in countries such as Africa, South-East and Eastern Mediterranean (R. New, 2017). It accounts for 4.07 million DALYs per 100,000 of the worldwide population which is about 12% burden of foodborne disease (Havelaar et al., 2015). *Salmonella* Enteritidis was the most common serotype in Asia, Latin America and Europe, accounting for 38%, 31% and 87% of the clinical isolates, respectively (Eng et al., 2015). In Africa, *S. Enteritidis* and *S. Typhimurium* were the two most common serotypes reported, occurring in 26% and 25% of the isolates, respectively.

2.2 Existing method for the detection of foodborne pathogen

There are several conventional strategies for bacterial isolation and detection in food samples. The main process in microbial testing of food samples involves (1) homogenization of the contaminated food sample in a buffer, (2) pre-enrichment in appropriate media, (3) selective enrichment in selective media to revive sub-lethally injured bacterial cells to a detectable level and (4) isolation of bacterial colonies using selective agars (Rohde, Hammerl, Appel, Dieckmann, & Al Dahouk, 2015). The

presumed positive colonies of microbes further confirmed or identified through biochemical and serological tests.

Over the years, microbiologists and researchers have devised many molecular methods for microbial identification and characterization. Immunological and nucleic acid-based methods are some of the examples of the advances in bacterial detection tools used in the early 90s (Mandal, Biswas, Choi, & Pal, 2011). These techniques help to complement the culture methods which pose a limited impact on outbreak control and decision-making efforts as they are not able to provide rapid results within 24h.

Immunological or antibody-based assays detect foodborne pathogens through specific interactions between the target antigen and diagnostic antibody without the need for culturing steps. There are two commonly used immunoassays for foodborne pathogen detections which are enzyme-linked immunosorbent assays (ELISAs) and lateral flow immunoassays (LFIs). Both ELISAs and LFIs are operated by colorimetric detection of bacteria involving enzyme-mediated interactions with the target pathogens that create color changes proportional to the concentration of the pathogens present. ELISA is a biochemical technique that involves the immobilization of a capture antibody on a solid matrix that is responsible to capture antigens from an enriched culture. ELISA is the most widely used antibody assay to detect and quantify foodborne pathogens. When a test sample is introduced onto the surface of the ELISA plate, the target antigen will bind to the immobilized enzyme to form the antigen-antibody complex. The observed color change indicates the presence of antigens which implies positive detection of the targeted pathogen. The detection limit of this method varies from 10^4 - 10^5 cfu mL⁻¹ depending on the antibody and the affinity to its epitopes (López-Campos, Martínez-Suárez, Aguado-Urda, & López-Alonso, 2012). This method is not cost-effective as it requires specialized equipment and trained personnel, thus more cost-effective and simple methods such as

LFI are developed for more rapid on-site detection of foodborne pathogens (Zhao et al., 2014). LFI utilizes a simple dipstick coated with colored particle labeled antibodies or antigens. Once the filtrate of food homogenate is introduced into the system, it travels *via* capillary action and mixes with the conjugate resulting in visualization of colors approximately between two to 10 min after the introduction of the sample. The most challenging issue in the analysis of food samples through immunoassays is a separation of the target organism from the food matrix debris (Kim, Taitt, Ligler, & Anderson, 2010). Moreover, all immunological assays still suffer from lack of specificity due to the presence of common ubiquitous epitopes present in the bacterial species, despite the emergence of many monoclonal, polyclonal and recombinant antibodies to overcome these limitations (Sousa & Pereira, 2013).

Nucleic acid-based techniques, most notably PCR-based detection is highly specific in pathogen detection (Law, Ab Mutalib, Chan, & Lee, 2014). The invention of PCR in 1985 by Kary B. Mullis has revolutionized the implementation of molecular methods in foodborne pathogen detection. The general principle of PCR is a process of *in-vitro* enzymatic synthesis and amplification of DNA sequences with thermo-resistant DNA polymerases. The invention of the automated duplication of a target DNA sequence in a short amount of time made PCR as a widely used method in the field of microbiology. There are many variations of PCR but only multiplex and real-time PCR (quantitative-PCR) have been adopted in food safety monitoring with an improved detection limit of $10^2 - 10^4$ cfu mL⁻¹ (Wang & Salazar, 2016). Multiplex PCR is capable of amplifying more than one target genes of the same or different pathogens simultaneously whereas, real-time PCR enables concurrent detection and quantification of the target sequence in real-time with the aid of fluorescence technology. Although these methods are far more advantageous in terms of cost and time than a simple PCR method, it still requires some improvements to enable the detection of pathogens present in food samples due to the

presence of food-inhibitors that affect the PCR reaction by degrading the target nucleic acid or inhibiting the polymerase enzymes activity (Schrader, Schielke, Ellerbroek, & Johne, 2012). However, the problem involving the removal of inhibitory substances from food matrixes is often rectified by coupling PCR-based techniques with IMS. In IMS, super-paramagnetic beads coated with specific ligand complementary to the target microbes were utilized to capture viable bacterial targets up to 10^1 cfu mL⁻¹ within 2.5 h from the heterogeneous suspension and concentrate bacterial cells from complex food matrices (Laube, Cortes, Llagostera, Alegret, & Pividori, 2014). IMS coupled with PCR capable to speed up the detection process and gives a useful sample for PCR with little or no non-specific DNA and interfering factors.

Loop-mediated isothermal amplification (LAMP) is another novel nucleic acid amplification method that provides a rapid, sensitive and specific detection of foodborne pathogens. LAMP involves auto-cycling strand displacement DNA synthesis that is carried out under isothermal conditions. This method utilizes two inner primers and two outer primers to amplify six specific regions of target DNA which will result in the final product of cauliflower-like DNA structures. LAMP capable to produce a huge number of amplified products within 60 min assay time which is usually 10^3 -fold or higher as compared to simple PCR and these amplified amplicons can be detected by agarose gel electrophoresis or SYBR Green I dye (Zhao et al., 2014). The development of real-time LAMP also favors the real-time monitoring of turbidity or fluorescence of the reaction mixture which eliminates the need for staining and gel electrophoresis. The summary of all the methods used for bacterial detection is discussed in **Table 2.1**.

For the aforementioned modern techniques, low sensitivity (without pre-enrichment) is the major limitation as the techniques may not be sensitive enough to detect pathogenic microorganisms in food samples without further processing steps.

Typically, the concentration of foodborne pathogens in food samples is less than 10^2 cfu mL⁻¹ (López-Campos et al., 2012). Consequently, these methods are unfavorable for direct detection of the pathogen in food matrixes and also require time-consuming pre-enrichments of microbial cultures prior to analysis in order to achieve lower detection limit or high sensitivity.

Universiti Malaya

Table 2.1: Summary of conventional and modern analytical methods used for bacterial detection.

Method	Foodborne pathogen	LOD	Assay time	Ref
ELISA	<i>E. coli</i> O157:H7	6.8 X 10 ² to 6.8 X 10 ³ cfu mL ⁻¹	3h	(Shen et al., 2014)
	<i>Vibrio parahaemolyticus</i>	10 ³ cfu mL ⁻¹	16h*	(Kumar et al., 2011)
LFI	<i>Vibrio cholera</i>	5.0 X 10 ⁵ to 10 ⁶ cfu mL ⁻¹	15 min	(Chaivisuthangkura, Pengsuk, Longyant, & Sithigorngul, 2013)
		10 ² to 10 ¹ cfu mL ⁻¹	12h *	
	<i>Staphylococcus aureus</i>	3.0 X 10 ⁰ cfu mL ⁻¹	2 h	(Chen, 2014)
Multiplex-PCR	<i>Salmonella spp.</i> , <i>Salmonella</i> Enteritidis	10 ³ cfu/mL	24 h	(Pinto et al., 2011)
	<i>Salmonella spp</i>	1.0 X 10 ² cfu/reaction	Not stated	(Xu et al., 2019)
	<i>Listeria monocytogenes</i> , <i>Cronobacter sakazakii</i> , <i>Staphylococcus aureus</i> and <i>Salmonella spp</i>	10 ² cfu mL ⁻¹	<7 h	(Qin et al., 2020)
Real-time PCR	<i>L. monocytogenes</i> and <i>E. coli</i> O157:H7	1.0 X 10 ¹ cfu g ⁻¹	4h*	(Kawasaki et al., 2010)
	<i>Salmonella typhi</i>	10 ⁻⁶ cfu mL ⁻¹	24 h*	(Nurjayadi et al., 2019)
LAMP	<i>Salmonella spp.</i> and <i>Shigella spp.</i>	1.0 X 10 ⁰ cfu mL ⁻¹	<20 h	(Shao, Zhu, Jin, & Chen, 2011)
	<i>Vibrio vulnificus</i>	2.5 X 10 ³ cfu mL ⁻¹	8 h	(Han, Wang, & Ge, 2011)
	<i>V. parahaemolyticus</i>	1.0 X 10 ¹ cfu/reaction	16 h	(Wang, Shi, Su, Ye, & Zhong, 2013)
	<i>Salmonella spp</i>	6.7 X 10 ⁰ cfu mL ⁻¹	45 min	(Mei et al., 2019)

* With pre-enrichment

2.3 Biosensor for foodborne pathogen detection

There is a consensus for the application of sanitation measures in the food supply chain to curb the presence of non-typhoidal serovars and a multitude of medical tools and approaches have been developed for a point of care. However, the existing methods of detection are slow, costly, laborious and require sophisticated instruments operating in centralized laboratories. Thus, the food analysis should be done rapidly on-site with high sensitivity and without the need for laboratory equipment for sample processing. The continuous occurrence of foodborne outbreaks has created a demand for the development of easy to use, cost-effective, highly selective and sensitive electronic devices that enable direct detection and rapid analysis of microbial manifestation in food products (Billington, Hudson, & D'Sa, 2014). Biosensor-based technologies have met those requirements and created a breakthrough in the detection of foodborne pathogens (Turner, 2013).

2.3.1 Definition of biosensor

A biosensor is a self-contained integrated device that provides analytical information (quantitative or semi-quantitative) based on the interaction between target analytes with bioreceptors immobilized on an electrochemical transducer. The electrical signal produced during the analyte-bioreceptor interaction is proportional to its concentration. The mechanisms of bacterial detection using biosensors involve a chemical or physical translation and transduction of biological information into a digital signal. This biological information is the result of the interactions between recognition elements (antibodies, enzymes, nucleic acids, bacteria and viruses) with biological targets. Typically, recognition elements will be immobilized onto a transducer surface *via* adsorption, entrapment, cross-linking, encapsulation or covalent binding (Luz, Iost, & Crespilho, 2013). Depending on the principle of signal transduction, various types of

transducers such as mass-based, optical and electrochemical sensors are used to change the biological event into a measurable signal (Bhalla, Jolly, Formisano, & Estrela, 2016). The general working principle of a biosensor is summarized in **Figure 2.3**.

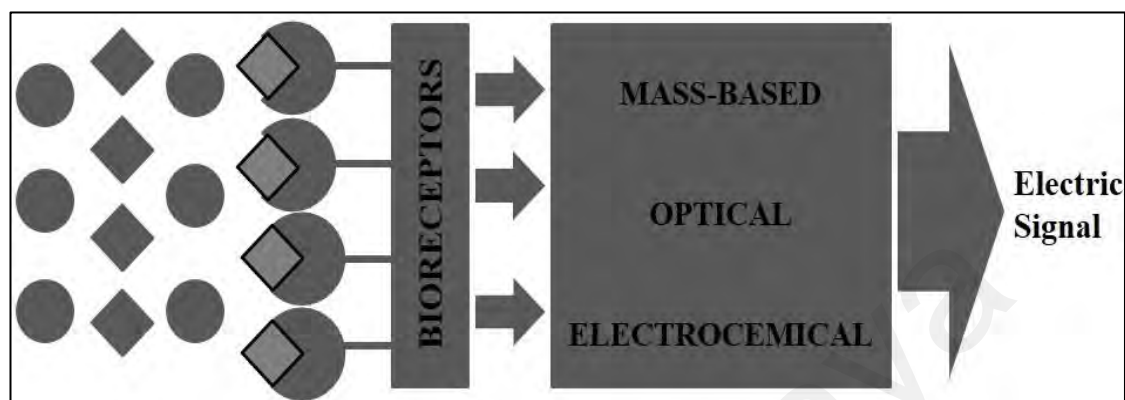


Figure 2.3. The overall working principle of biosensors

Biosensors also can be categorized into direct (label-free) and indirect (labeled) detection systems. In a direct detection system, physical changes induced by the interaction of target analyte are measured directly in real-time and no label is required whereas, in indirect detection systems, the product of biochemical reactions is detected via a label by the sensor. Specificity is a key element in the process of designing a biosensor. The bioreceptor serves as a binding site for the target analyte to produce a change in signal and the selection of the bioreceptor largely contributes to the specificity of a biosensor. Enzymes, antibodies and nucleic acids are the most commonly used bioreceptors in biosensor applications (**Figure 2.4**).

Among many transducer types, electrochemical biosensors are very promising due to their low cost, rapid response, high sensitivity, ease of use, high signal-to-noise ratio, flexibility in employing recognition elements, low interference with food matrices and instrumental simplicity (Ronkainen, Halsall, & Heineman, 2010; Tothill, 2011) Technological advancements have allowed for the miniaturization of electrochemical biosensors and offered an excellent tool for identifying and quantifying foodborne

pathogens present in various food matrices with a low detection limit in the range of 10^1 cfu mL⁻¹ (Abdalthai et al., 2015).

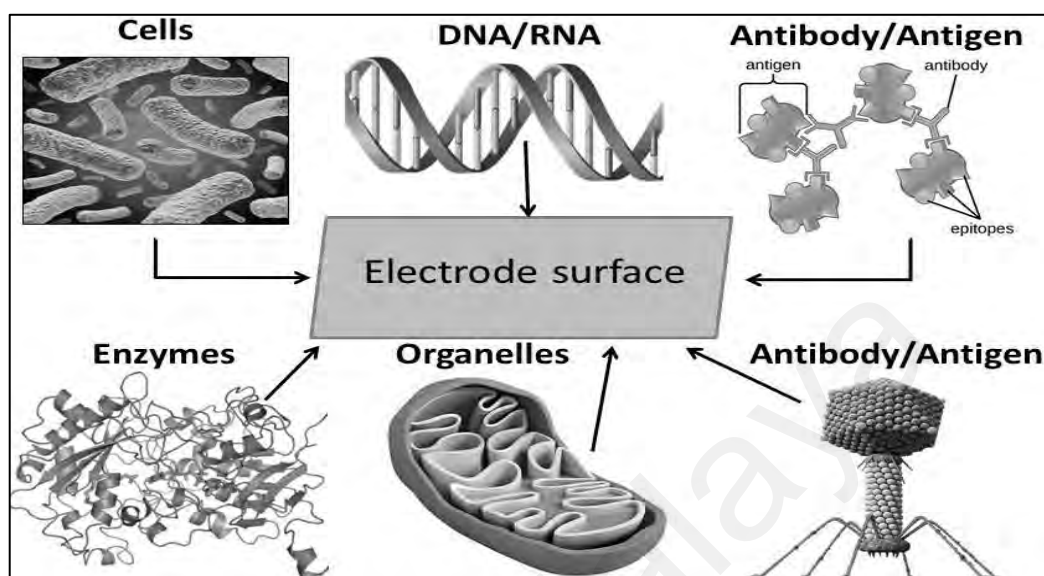


Figure 2.4. Examples of different types of bioreceptors used in electrochemical sensors

2.3.2 Electrochemical biosensors as a promising analytical tool for bacterial detection

In a typical biosensing process, biological interactions are transduced as a mechanical, electrical, or optical signal. Specifically, electrochemical biosensors offer numerous advantages in the medical and biotechnology fields by offering direct transformation of a biological recognition to a readable electrical signal (Grieshaber, MacKenzie, Voeroes, & Reimhult, 2008). This electrochemical approach has a potential to be applied in biosensor for whole-cell bacteria detection because the outer membrane of bacteria itself is composed of conductive layers of macromolecules with electrochemical active groups that can react with the free ions in the electrolyte (Becerro et al., 2015). An electrochemical cell consists of three electrodes: the working (WE), the reference (RE) and the counter (CE) electrodes arranged in an electrolyte (ionic solution) as shown in **Figure 2.5**. In the presence of the targeted analyte, the redox reaction will be

blocked at the working electrode and the potential that drives the reaction is measured between the WE and RE. To complete the circuit, the CE performs the second electrode reaction proportional to the rate of reaction at the working electrode. This makes the quantification of targets at the WE possible.

An electrochemical biosensor is one of the popular approaches that has been adapted for the detection of foodborne pathogens. Electrochemical biosensors have some advantages over other analytical systems such as the ability to work with turbid samples, low fabrication cost, instrumental sensitivity and offer easy miniaturization. Electrochemical biosensors are categorized according to the parameters measured by the device, namely amperometric (current), potentiometric (potential or charge accumulation), impedimetric (impedance) and conductometric (conductivity).

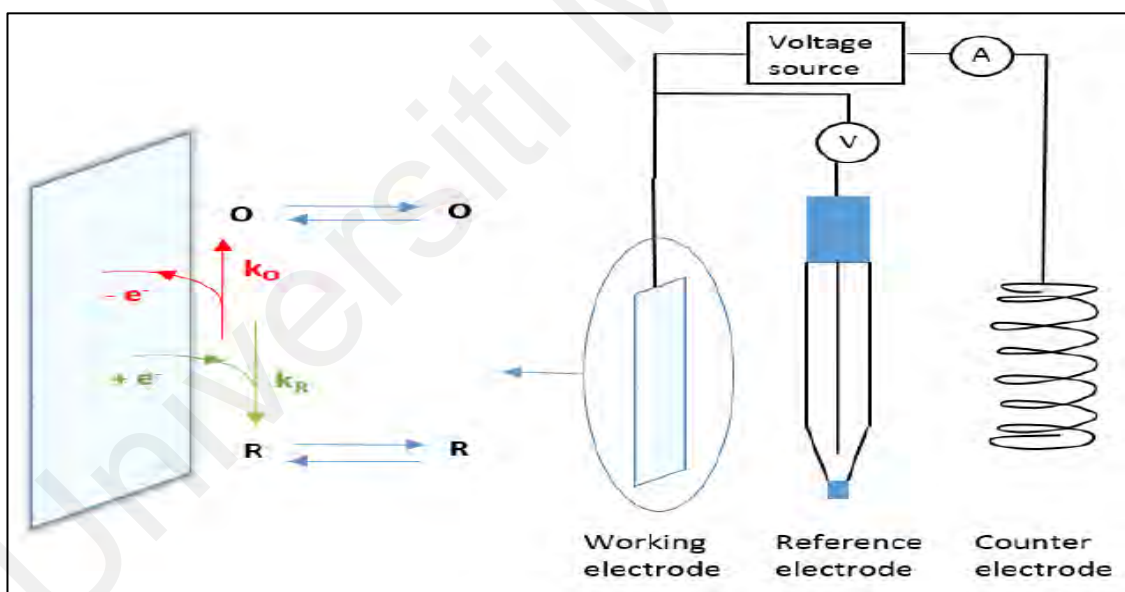


Figure 2.5. Three-electrode system of the electrochemical cell and a simple redox process. O=oxidized species, R=reduced species, $-e^-$ =electrons, k_O and k_R represents the oxidation and reduction reaction rate constant, respectively (Mahe, 2015).

2.3.2.1 Potentiometric biosensors

Potentiometric biosensors measure the changes in pH or ion concentration that occur during the interaction of an analyte with the working electrode (an ion-selective electrode or ISE). One of the advantages of potentiometric sensors is that redox probes are not required to measure the interaction between the target analyte and biorecognition elements. Moreover, this system is capable to perform the continuous measurement and possess a wider detection range of ions ranging from 10^{-6} to 10^{-1} mol L⁻¹ (Hernandez & Ozalp, 2012). The apparatus is inexpensive, portable, and it is well suited for in situ measurements. However, the lack of overall sensitivity and interference from the sample matrix are the main disadvantage of this system.

2.3.2.2 Amperometric biosensors

Amperometric is a well-exploited electrochemical method for foodborne pathogen detection due to its superior sensitivity compared to potentiometric analysis (Alahi & Mukhopadhyay, 2017). The biological recognition element applied in amperometric food analysis varies from enzymes, antigen/antibody, bacteriophages, cellular structures/cells, to nucleic acids/DNA and biomimetic bases (Cinti, Volpe, Piermarini, Delibato, & Palleschi, 2017). An amperometric biosensor consists of three electrodes namely working electrode, reference electrode (which controls the potential of working electrode) and an auxiliary electrode which helps to measure the current flow. The working principle of this system mainly involves the measurement of variations in current because of biochemical oxidation and reduction of electroactive species. Usually, a constant potential that facilitates the electron transfer reaction is applied to the system and the current is recorded. The observed current is a direct indicator of the rate of electron transfer and hence also reflects the amount of target analyte present in the sample. The electrons may be transferred either from the analyte to the working electrode or from

the electrode to the analyte depending on whether the working electrode is functioning as an anode or cathode, respectively (Bănică, 2012). Moreover, the rate of electron flow (current) is greatly influenced by the concentration of target analyte diffusing to the surface of the working electrode. Many researchers have reported amperometric detection for various foodborne pathogens such as *E. coli* O157:H7 (Singh, Poshtiban, & Evoy, 2013), *Salmonella* (Liu, Chai, & Yao, 2013), *L. monocytogenes* (Cheng et al., 2014) and *C. jejuni* (Yang, Kirsch, & Simonian, 2013).

2.3.2.3 Impedimetric and conductometric biosensors

Impedimetric and conductometric biosensors are the most powerful electrochemical analytical systems for the detection of foodborne pathogens. The impedimetric detection system measures the conductance, capacitance and impedance of the analyte-containing medium as well as changes in the electron transfer properties on the electrode surface. It uses a technique called electrochemical impedance spectroscopy (EIS), which involves an alternating current (AC) applied across the electrodes. This causes electron buildup and discharge processes to occur at the electrode surface and in the electrolyte. By changing the frequency of the sinusoidal current, the electron-transfer and capacitance properties of the electrodes interacting with the analyte can be studied. During a bio-recognition event, conductance and capacitance increases while impedance decreases across a working electrode surface (Ramli et al., 2017). The changes in conductance and impedance are dependent on the analyte concentration. Moreover, the changes in voltage allow the evolution of interfacial capacitance, conductance and resistance. Both impedimetric and conductometric techniques are important for a rapid and automated detection system which leads to the miniaturization of the device. These techniques are mostly applicable for measuring the biorecognition involving DNA/nucleic acid hybridization, antibody-antigen reactions and enzyme reactions (Bahadır & Sezgintürk, 2014). The measurement of changes in the electrical properties

of bacterial cells also makes the whole-cell as an attractive analyte for detection (Ahmed, Rushworth, Hirst, & Millner, 2014). Several analytical devices are developed based on conductance and impedance technology for food-borne pathogens detection, however, impedimetric measurement is widely studied for culture-independent bacterial detection due to its high sensitivity regardless of the sample matrix, label-free, cost-effective and high-throughput device (Joung et al., 2013). The applications of conductometric biosensors are limited in food analysis due to poor sensitivity caused by the variable ionic background of the food matrix and require high ionic strength media for better detection (Thévenot, Toth, Durst, & Wilson, 2001). Moreover, the selectivity of conductometric biosensors is relatively poor because all charge carriers could result in the change of conductivity (Grieshaber et al., 2008).

In recent years, the integration of impedance and biological recognition technology has gained increasing attention in the field of foodborne pathogen detection. The changes in impedance are a consequence of the interaction of the analyte with the bioreceptors. This interaction will cause a change in capacitance and electron transfer resistance on the surface of the working electrode and the impedance increases as the amount of analyte binding to the bioreceptor increases (Bahadır & Sezgentürk, 2014). Impedimetric sensors usually use antibodies as bioreceptors however, whole-bacterial cells can also be used for direct detection of food samples (Bahadir & Sezgenturk, 2016). EIS is the mostly used impedimetric biosensors technique because it can monitor the physico-chemical changes resulting from the interaction of the analyte with the bioreceptor immobilized on the transducer. These include the information on charge transfer from the solution to the electrode surface, the resistance of the solution, diffusion rate of species to and from the bulk solution and also its formation of double-layer capacitance (Lvovich, 2015). The overall sensitivity of the impedimetric biosensor can

be improved using interdigitated array microelectrode which allows the miniaturization of the impedimetric biosensors into a chip form.

2.3.3 Electrochemical aptasensor for bacterial detection

Aptasensor is a class of electrochemical biosensor which utilizes DNA or RNA aptamer as a biological recognition element. Aptamers are an artificial nucleic acids DNA or RNA generated from combinatorial libraries of oligonucleotides that undergo a selection methodology to bind with high affinity and specificity to analytes of interest. This selection methodology is termed as SELEX (systematic evolution of ligands by exponential enrichment). SELEX methods have the advantage of selecting multiple aptamers that could potentially bind to different targets on a single cell in their native conformation as illustrated in **Figure 2.6**. Among SELEX technologies, whole-cell SELEX is a method developed and modified for creating aptamers that bind to live bacteria (Medley, Bamrungsap, Tan, & Smith, 2011). Typical whole-cell SELEX process involves: (1) screening of random nucleic acid bound to target bacteria, (2) repeated separation and exponential amplification of the oligonucleotide and (3) cloning and sequencing of the specific binding molecules ultimately identified (Moon, Kim, Park, Lim, & Mo, 2015). Aptamers selected through whole-cell SELEX bind to the surface molecule of live bacteria more effectively with little cross-reactivity to non-target bacteria (Dwivedi, Smiley, & Jaykus, 2013).

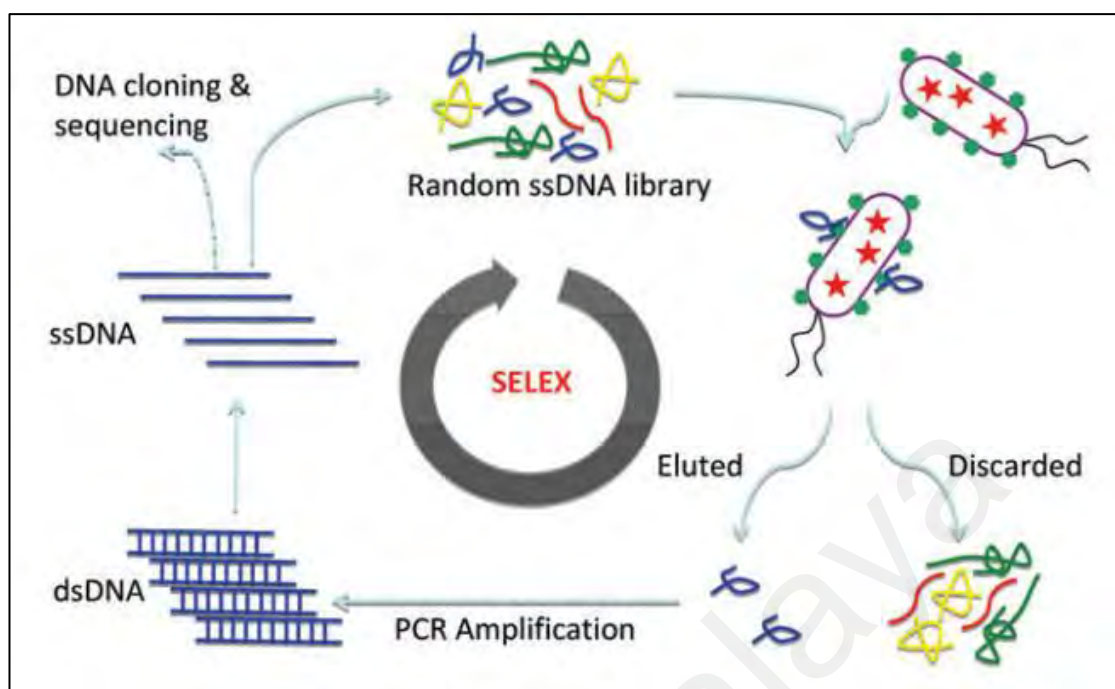


Figure 2.6. Schematic presentation of a typical aptamer selection process for whole bacterial cells (Huang Po-Jung, Liu, & Liu, 2013).

The intrinsic specificity and high affinity accompanied by high stability of RNA/DNA single-stranded aptamers rendered them particularly interesting candidates for novel detection probe in the diagnosis of pathogens using electronic biosensing platforms (Abbaspour, Norouz-Sarvestani, Noori, & Soltani, 2015). The interaction of the aptamer and its targets is based on their definite three-dimensional conformation (Chang et al., 2013; Zhang et al., 2015), thus aptamers have higher specificity enabling the discrimination of homologous targets with few DNA bases or amino acid mismatches (Davydova et al., 2016; Ye et al., 2012). Unlike antibodies, aptamers are produced through chemical synthesis with extreme accuracy and reproducibility which increases the stability of aptamer in extreme conditions (e.g. high temperatures, various pH). Chemically synthesized aptamers also has the ability to recover its native active conformation after thermal denaturation as compared to other existing biological

recognition elements which has limited shelf life and suffer from irreversible denaturation (Meirinho, Dias, Peres, & Rodrigues, 2015).

The biosensing event in aptasensor consists of three important steps as shown in **Figure 2.7**. In some special cases, additional steps are needed to amplify and quantify the signal produced from the bio-recognition event.

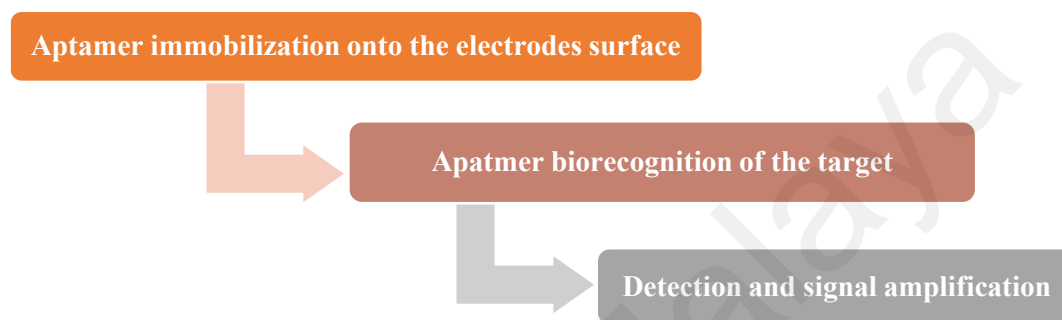


Figure 2.7. Schematic diagram of crucial steps in aptasensing

2.3.3.1 Immobilization of aptamer on electrodes surface

An essential step in aptasensing is the aptamer immobilization onto an electrode surface. There are many available strategies for a high orientation and stable immobilization of aptamers without losing their biophysical characteristics and minimizes non-specific binding events (Radi, 2011). Aptamers can be physically adsorbed on the surface, covalently attached to functional groups or immobilized by streptavidin-biotin interaction (Rhouati, Catanante, Nunes, Hayat, & Marty, 2016).

Physical adsorption involves ionic interactions between the negatively charged aptamers and positively charged nanomaterials covering electrodes surface without the need for any aptamer modifications (Hughes & Walsh, 2017). This method is simple, rapid and cost-effective because it does not require any reagents or special nucleic acid modifications to aid the adsorption. However, the aptamer orientation on the electrode's

surface is random and weak causing easy desorption of aptamer during the exposure to buffers or reagents when performing the detection assays (Nimse, Song, Sonawane, Sayyed, & Kim, 2014). Aptamer also can be strongly immobilized onto the electrode's surface using chemical binding called covalent modification. Covalent attachment involves interaction between functional groups found on the surface of the electrode and chemical groups (e.g. –thiol, –amine) at the ends of chemically modified aptamers (Roushani & Shahdost-Fard, 2016). This type of interaction offers good stability and high binding strength thus improves the overall biorecognition efficiency. The time-consuming and costly aptamer modification process are the notable drawbacks of this technique. In the immobilization by streptavidin-biotin interactions, streptavidin is first linked to the solid surface then the biotinylated aptamers form a complex of streptavidin-biotin. Streptavidin is a tetrameric protein that has four identical binding sites for biotin that has a very high affinity to the streptavidin binding sites (Nimse et al., 2014).

2.4 Carbon nanomaterials in biosensor

A great effort has been channeled into the development of highly sensitive and selective biosensors worldwide over the past decade. Advancements in the field of nanotechnology have made a profound influence on biosensor development and application due to its fascinating properties such as high surface area, mechanical properties and high thermal and electric conductivity (Abu-Salah, Alrokyan, Khan, & Ansari, 2010). At the nanoscale, unique physico-chemical changes occur to nanomaterials due to surface effect and quantum effect (Zhu, 2017). As the surface to volume ratio increases, the interface of recognition element increases and results in the overall improvement of biosensor's sensitivity. Most importantly, the quantum confinement phenomenon in nanomaterials leads to the rise in the bandgap energy with decreasing size. This causes the electrical and optical properties of nanomaterials to become size and shape-dependent and this size-tunable property is a crucial point for biosensing devices

(Poulsen & Hansen, 2017). Owing to their intriguing high electrical conductivity, chemical stability, biocompatibility and promising mechanical strength accompanied by the capacity to hybridize into sp, sp² and sp³ configurations with narrow gaps between 2s and 2p electron shells, carbon-based nanomaterial leads to the sensitive detection of biological compounds (Chatterjee & Chen, 2012; Revin & John, 2012) .

Most carbon nanomaterials, especially the planar and tubular geometries of graphene and CNTs, respectively possess a comparable Debye length, λ_D to the dimensions of these nanostructures. Debye length, λ_D can be defined as a measure of electric field penetration into the bulk electrolyte. This will result in the change of electrical properties of the nanomaterial upon the binding of the analytes and also induces physio-chemical changes in the transduction material (Ramnani, Saucedo, & Mulchandani, 2016). Moreover, these changes will permit the label-free detection of analytes with higher sensitivities and lower detection limits (Reiner-Rozman, Larisika, Nowak, & Knoll, 2015). These superior properties of graphene and CNT allow a wide range of applications in microelectronics through its incorporation in biosensor device fabrication processes. Moreover, the usage of graphene/CNTs in the biosensing field has been greatly extended by modifying the physico-chemical properties through surface modification.

2.4.1 Graphene nanomaterial as a suitable transducer in biosensor

To date, the use of graphene nanomaterials in the development of biosensors has received great attention. Graphene is a 2D planar sheet that exists in a honeycomb lattice structure with zero-bandgap semiconductor and serves as a basic building block for graphite and graphitic materials of all dimensions (Shao et al., 2010). Graphene can be stacked together to form 3D graphite, rolled-up to 1D CNTs or wrapped into 0D fullerenes as shown in **Figure 2.8**. The fullerene carbon allotropes are a fundamental building block

of the crystalline phase with sixty carbon atoms completely bonded in an icosahedral symmetry that forms a spherical structure. In a 1D structure, carbon atoms are arranged in tubular-like structures as CNTs whereas, in 2D structure, carbon atoms form a monolayer packed into honeycomb lattice called graphene (Zhang, Rajaraman, Liu, & Ramakrishna, 2014). Graphite which exists in 3D is another form of the carbon atom that arranged like stacks of graphene layers coupled by van der Waals forces of attraction (Georgakilas, Perman, Tucek, & Zboril, 2015).

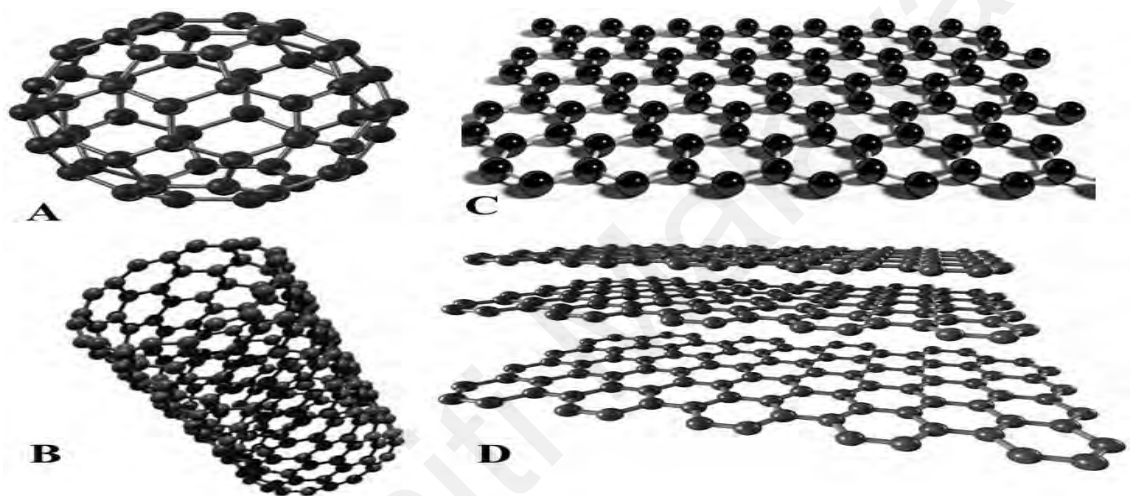


Figure 2.8. The different dimension of carbon nanomaterials which consist of (A) 0D fullerenes, (B) 1D CNT, (C) 2D graphene and (D) 3D graphite.

The carbon atoms in graphene are sp^2 hybridized which consist of one s -orbital and two p -orbitals that hybridize together to form a honeycomb lattice structure (Zhang, Rajaraman, et al., 2014). Hence, the p_z (π -orbitals) regulates the conductivity or charge mobility of graphene through the formation of delocalized π systems. In detail, the s , p_x and p_y orbitals of carbon form a σ -bond between neighboring carbon atoms leaving the p_z orbital unhybridized as shown in **Figure 2.9**. This p_z orbital on each carbon atom overlaps with neighboring carbon atoms to form a π -bond (valence energy band), causing the delocalization of excess π -orbitals to form a conduction energy band (Allen, Tung, & Kaner, 2010). This atomic structure of graphene largely contributes to its exceptional

mechanical strength (130 GPa), excellent electrical conductivity (6000 S cm^{-1}) due to the fast electron transportation (Sang, Shin, Kim, & Yu, 2019).

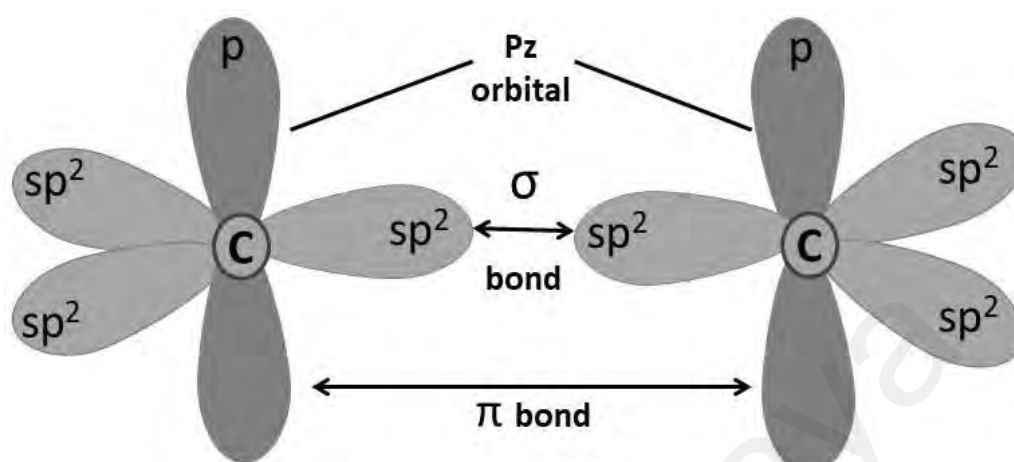


Figure 2.9. Schematic diagram of carbon atom hybridization in graphene

Besides, graphene also possesses several extraordinary properties including large surface area ($2630 \text{ m}^2 \text{ g}^{-1}$), superior thermal conductivity ($\sim 3000 \text{ W/mK}$) and most importantly good biocompatibility (Gurunathan & Kim, 2016). Thus, graphene materials have great potential for the development of highly sensitive and selective biosensors (Qing et al., 2014). Besides the physico-chemical properties, biocompatibility is another important selection criterion. The high surface area of graphene enables the smooth interaction with biological molecules such as enzymes, nucleic acid, aptamer, protein, antibody, virus and bacterial cell (Li et al., 2016; Notley, Crawford, & Ivanova, 2013). The honeycomb lattice structures also favor non-covalent forces, such as hydrogen bonding, π - π stacking, electrostatic forces, van der Waals forces and hydrophobic interactions with biomolecules (Li et al., 2016; Yang, Asiri, Tang, Du, & Lin, 2013).

Graphene can be exfoliated and oxidized to form graphene oxide (GO) to produce stable dispersion in water due to the presence of the hydroxyl, carboxyl and epoxide functional groups (Chang, Zhou, Christensen, Heideman, & Chen, 2014). After reduction, GO is transformed into reduced graphene oxide (rGO) with some residual oxygen and

structural defects yielding high thermal conductivity (Pumera, 2011). The enriched oxygen functional groups of GO endow it with the ability to immobilize the biomolecules through covalent binding which is greatly influenced by the C/O ratio. Generally, high C/O ratios promote stronger binding to biomolecules than low C/O ratio (Hong, An, Compton, & Nguyen, 2012). Besides the interaction with biomolecules, these functional groups also facilitate the production of graphene-based composites.

Graphene has been successfully used as a transducer material in impedimetric, amperometric and conductometric sensors for the detection of pathogenic bacteria. Graphene has many interesting properties that make it a valuable material in biosensing. For instance, the fluorescence quenching properties of GO was used in a PDMS/paper/glass hybrid microfluidic biochip for the simultaneous detection of *Staph. aureus* and *S. enterica* (Zuo, Li, Dominguez, & Ye, 2013). Graphene has also been found to be an excellent host for ssDNA, aptamers and antibodies owing to the surface functional groups being able to participate in the covalent immobilization of the biorecognition elements. The electroconductive properties of graphene are affected by factors such as a number of layers, the substrate, adsorbed impurities, flatness, defects, size of the sheet, edge types and functionalization (Yang, Ratinac, et al., 2010). The tunable properties of graphene are widely exploited to cater to the specifications of each designed sensor.

2.4.1.1 Synthesis of graphene and graphene-based nanocomposites

There are many physical and chemical methods adapted to produce graphene, graphene-derivatives and graphene-based nanocomposites. There are two types of strategies for the preparation of graphene namely top-down and bottom-up methods (**Figure 2.10**) (Tour, 2014). The top-down method involves breaking down large piece graphene sheets or graphite into smaller pieces whereas, bottom-up methods build

graphene layer by using small molecules as starting materials. Mechanical cleavage technique (Yi & Shen, 2015) and acidic oxidation of graphite and followed up by reduction process (Huang, Lim, Chia, Yarmo, & Muhamad, 2011; Pei & Cheng, 2012) are the strategies involved in top-down approaches. Graphene also can be fabricated using chemical vapor deposition (Mattevi, Kim, & Chhowalla, 2011), arc discharge and epitaxial growth on silicon carbide (SiC) wafer (Kusunoki, Norimatsu, Bao, Morita, & Starke, 2015) in bottom-up techniques.

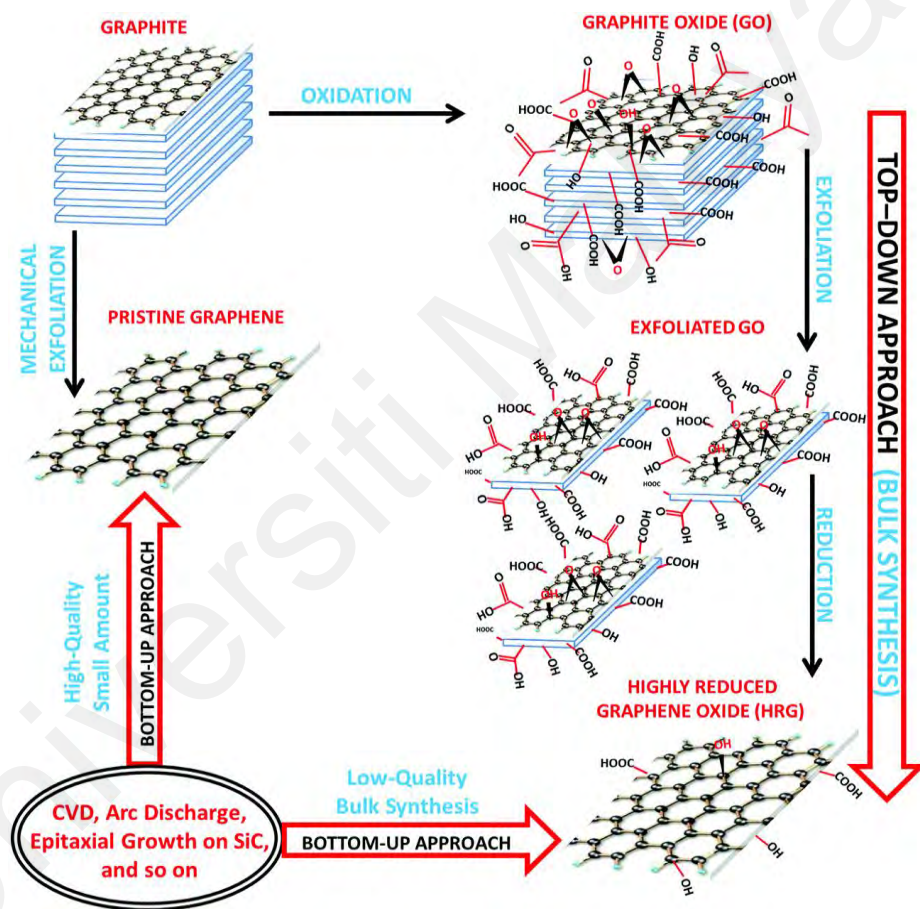


Figure 2.10. Schematic representation of the methods used for the synthesis of graphene (Khan et al., 2015).

Researchers utilize mechanical exfoliation of layered compounds to produce graphene layer samples. In 2004, Geim's group (Novoselov et al., 2004) reported the exfoliation of graphene monolayers onto 300 nm silicon dioxide substrate using graphite as the starting material. This method uses cellophane tape to successively remove layers

from graphite flakes. A thin and transparent graphene layer can be obtained, and its quality can be preserved because this method introduces minimal defects to the sheets (Van Noorden, 2012). However, the major drawback mechanical exfoliation method is the inconsistency in the number of graphene layers produced and the production on a large scale is difficult using this approach. Moreover, graphene can be synthesized using chemical synthesis. In this method, intercalating agents were introduced between basal planes of graphite layers. Firstly, the simplified Hummer's method should be employed to the graphite to weaken the van der Waals forces of graphite. By introducing oxygen functional groups, graphite can be completely exfoliated into graphene oxide (GO) in aqueous media (Huang, Lim, et al., 2011). However, the oxygen-bearing groups of GO act as an insulator which disrupts the π -conjugation leading to a decrease in electron mobility and overall conductivity. Thus, the graphitic π -network of GO can be restored by using several reducing agents which include sodium borohydride, NaBH_4 and hydrazine hydrate (Xu, Yuan, & Wang, 2014). These agents are capable to remove most of the oxygen-containing groups of GO and produce reduced graphene oxide (rGO) with partially recovered graphene-conjugated structure. The whole idea is to intercalate the water molecules between the graphite sheets to increase the interlayer distance of graphite sheets that weakens the van der Waals interaction between the graphite sheets. Electrostatic repulsion of the graphite layer will result in the exfoliation of GO caused by the low van der Waals interaction which might produce a monolayer, bilayer or few-layer graphene layer. The brown color of GO will turn to black and precipitate easily during the reaction that can be explained by the less hydrophilicity resulted from the loss of the oxygen functional group. The usage of chemical agents can be extremely toxic and hazardous to humans but chemicals especially hydrazine can be used in a very small quantity for mass production of rGO (Surajit et al., 2012). In addition, there are many environmentally friendly methods available which uses green and natural reducing agents

such as amino acids, garlic (Ikhsan et al., 2015), vitamin C (Fernández-Merino et al., 2010) and glucose (Zhu, Guo, Fang, & Dong, 2010).

Epitaxial growth refers to the growth of a crystalline layer on a crystalline substrate, silicon carbide (SiC) (Wang et al., 2016). Graphene can be synthesized by heating SiC at high temperatures ($> 1,000$ °C) in a vacuum or in an argon atmosphere condition (Curtin et al., 2011). Heating in an extreme temperatures and low pressure causes the decomposition and migration of silicon atoms leaving rearranged carbon atoms which forms few layers of graphene (Wang et al., 2016). Furthermore, graphene grown on SiC substrate, a wide bandgap semiconductor is suitable for many optoelectronic applications (Kusunoki et al., 2015). This method favors large scale production of graphene but a high production cost and difficulties in controlling the thickness of epitaxial graphene which is very crucial for electronic performance are the major drawbacks (Norimatsu & Kusunoki, 2014). Finally, chemical vapor deposition (CVD) has been widely used to produce monolayer or few-layer graphene. CVD growth techniques are widely employed to grow graphene due to their high compatibility with the current complementary metal-oxide semiconductor (CMOS) technology. There are various types of CVD processes: thermal (T-CVD), plasma enhanced (PECVD), catalytic (Cat-CVD) and etc. (Losurdo, Giangregorio, Capezzuto, & Bruno, 2011; Othman et al., 2015; Stojanović, Woehrl, & Buck, 2012). The types of CVD process to be employed depends on the production cost, graphene quality, thickness and the structure needed. Transition metals such as nickel (Ni), copper (Cu), ruthenium (Ru) and gold (Au) have been used as metal substrate but Cu is the most commonly studied metal (Mattevi et al., 2011). In general, the formation of graphene by CVD technique was carried out by introducing carbon sources such as methane (CH_4) diluted with hydrogen (H_2) to be dissociated at a high temperature of 900-1,000 °C or by plasma means (Mattevi et al.,

2011). The carbon sources will then decompose to produce active carbon species to be deposited as a graphene layer.

All types of production methods produce graphene with surface defects and oxygen-bearing groups but these defects favor further surface modification with chemical or biomolecules (Pumera, 2011). The chemical modification of graphene is important to prevent aggregation in water and after pre-functionalization, its surface can be easily modified.

2.4.1.2 Graphene-based nanocomposite for enhanced sensing properties

rGO contains oxygen-containing functional groups and a certain number of defects. This defect allows rapid electron transfer as compared to pristine graphene (Gupta & Irihame, 2015). Thus, rGO is the most suitable material to be exploited for the fabrication of electrochemical sensors. The presence of oxygen-bearing groups on rGO also facilitates the adsorption and pre-concentration of redox species or targeted analytes and effectively catalyze redox reaction during the electrochemical process (Gupta & Irihame, 2015). On the other hand, agglomeration of rGO in most solvents limits its usage in electrochemical sensing applications (Pandikumar, Thien, et al., 2014). The agglomeration happens due to the reformation of π - π stacking interactions and strong van der Waals forces of attraction when dispersed in any solvents (Ambrosi et al., 2016). The aggregation of graphene makes the graphene-based working electrode fabrication process difficult because a homogeneously dispersed thin film of graphene is often needed for an improved electron transfer (Suvarnaphaet & Pechprasarn, 2017). Most importantly, the agglomeration of graphene reduces the overall active surface area available for the interaction with bio-recognition elements (Tien, Huang, Yang, Wang, & Ma, 2011). Therefore, many types of research have been extensively developed for the synthesis of graphene-based nanocomposites for better sensing properties (Jin, Nackashi, Lu, Kittrell,

& Tour, 2010; Ramos Ferrer, Mace, Thomas, & Jeon, 2017). Graphene-based nanocomposites significantly improve graphene's catalytic properties, biocompatibility, electrical and electrochemical properties (Artiles, Rout, & Fisher, 2011; Bich Ha & Van Hieu, 2016; Dhand, Rhee, Ju Kim, & Ho Jung, 2013). To date, many graphene-based nanocomposites coupled with nanomaterials such as metal/metal oxides, polymers and organic dyes have been successfully synthesized (Bai, Chen, & Shiu, 2013; Lu et al., 2010; Shan et al., 2010). The presence of reactive oxygen groups of rGO facilitates the functionalization of graphene with nanocomposite and functional molecules (McCallion, Burthem, Rees-Unwin, Golovanov, & Pluen, 2016; Yang, Asiri, et al., 2013). Chemical reduction methods were often employed for the preparation of nanocomposites because of its capability to produce a high yield of product and facile decoration of nanostructure materials on the graphene surface (Yin, Shah, Chhowalla, & Lee, 2015). The integration of nanocomposites with graphene usually happens through chemical bonding between the functional group of composite's molecules and carbon-based structure or by forming electrostatic interactions, π - π or/and van der Waals forces of attractions (Bhattacharya, 2016; Georgakilas et al., 2012).

A variety of inorganic nanoparticles and metal/metal oxides have been utilized for the synthesis of graphene nanoparticles nanocomposite. These include metals such as, Au (Thavanathan, Huang, & Thong, 2014), Ag (Tien et al., 2011), Pt (Kurt, Durmus, & Durmus, 2016), Pd (Kurt et al., 2016), Fe (Zhang, Sun, et al., 2016), Sn (Hidong, Otgonbayar, Altaibaatar, & Jae, 2016), Cu (Sevim et al., 2016) and Co (Hatamie et al., 2016), as well as metal oxides such as Fe₂O₃ (Radhakrishnan, Krishnamoorthy, Sekar, Wilson, & Kim, 2014), TiO₂ (Morales-Torres, Pastrana-Martínez, Figueiredo, Faria, & Silva, 2012), ZnO (Marlinda et al., 2012), Cu₂O (Zhang, Hu, Guan, & Luo, 2016), NiO (Jiang et al., 2013), SnO₂ (Nurzulaikha et al., 2015), Co₃O₄ (Shahid et al., 2015), MnO₂ (Yu, Hu, et al., 2011) and Al₂O₃ (Zheng et al., 2014). The incorporation of inorganic

nanoparticles enhances the electronic conduction of graphene due to the synergistic effect between graphene and inorganic nanoparticles which elevates its overall biocompatibility, electrical and electronic properties (Khan et al., 2015). Besides that, metal/metal oxides also act as a stabilizer to prevent the aggregation of graphene sheets.

The combination of polymers with graphene for the preparation of electrochemical sensors opens up exciting areas of research due to their mechanical stability, biocompatibility, improved redox behavior and excellent selectivity with enhanced sensitivity (Salavagione, Diez-Pascual, Lazaro, Vera, & Gomez-Fatou, 2014). The graphene-polymer nanocomposites have been popularly produced using “grafting to” or “grafting from” routes which involve the synthesis of a polymer with the aid of reactive groups or radical precursor that is attached to the surface of graphene and growing polymers on graphene’s surface *via in-situ* polymerizations of monomers, respectively. Besides, graphene-polymer composites also can be produced *via* covalent or non-covalent functionalization (Layek & Nandi, 2013). Covalent functionalization involves the interaction between oxygen-containing groups of graphene and the functional groups of the polymers such as $-NH_2$ and $-OH$. For instance, GO-polyvinyl alcohol composite was prepared using esterification reaction between $-COOH$ groups of GO and the $-OH$ groups in polyvinyl alcohol (Layek & Nandi, 2013). Hence, the non-covalent functionalization of graphene-polymers utilizes π - π stacking or electrostatic interaction (Bai et al., 2013). Polyethylene glycol, polyvinyl alcohol, polyvinyl pyrrolidone, polyaniline and chitosan are the most commonly used polymers to be grafted on graphene (Teodorescu & Bercea, 2015; Vikas, 2014; Yang, Tu, Li, Shang, & Tao, 2010).

The utilization of graphene-based organic dye nanocomposite serves as a novel approach in the fabrication of electrochemical sensors (Bai et al., 2013). The usage of organic dyes offers a label-free detection of biological targets (Guo, Guo, & Dong, 2013).

The organic dyes usually consist of a planar aromatic structure that can interact non-covalently with the graphene sheet through π - π stacking. The synergistic non-covalent charge transfer and π - π stacking forces of attraction between graphene and electroactive dyes improve the overall electrochemical properties and solubility of graphene in the water besides preserving its intrinsic properties (Guo, Guo, et al., 2013). For instance, Zhu et al. (Zhu, Luo, & Wang, 2012) developed a thionine-graphene nanocomposite modified gold electrode for electrochemical detection of DNA. Moreover, Guo et al. also reported the graphene nanosheets functionalized with two individual different aromatic organic dyes, Orange II and Azophloxine for electrochemical detection of protein and viral DNA, respectively (Guo, Guo, et al., 2013; Guo, Han, Guo, & Dong, 2013).

The key importance of production graphene-based nanocomposites is to prevent its aggregation in solvents that helps to increase the overall surface area of the nanocomposite for the adsorption of a wider range of bio-recognition elements (Perreault, Fonseca de Faria, & Elimelech, 2015). The reaction between graphene and nanocomposites converts the carbon atoms from sp^2 to sp^3 hybridization and introduces a vast number of functional groups on the surface of graphene such as, -OH, -COOH, -NO₂, -C \equiv C and etc. feasible for further linkage or modification with biomolecules (Bekyarova et al., 2009) as shown in **Figure 2.11**.

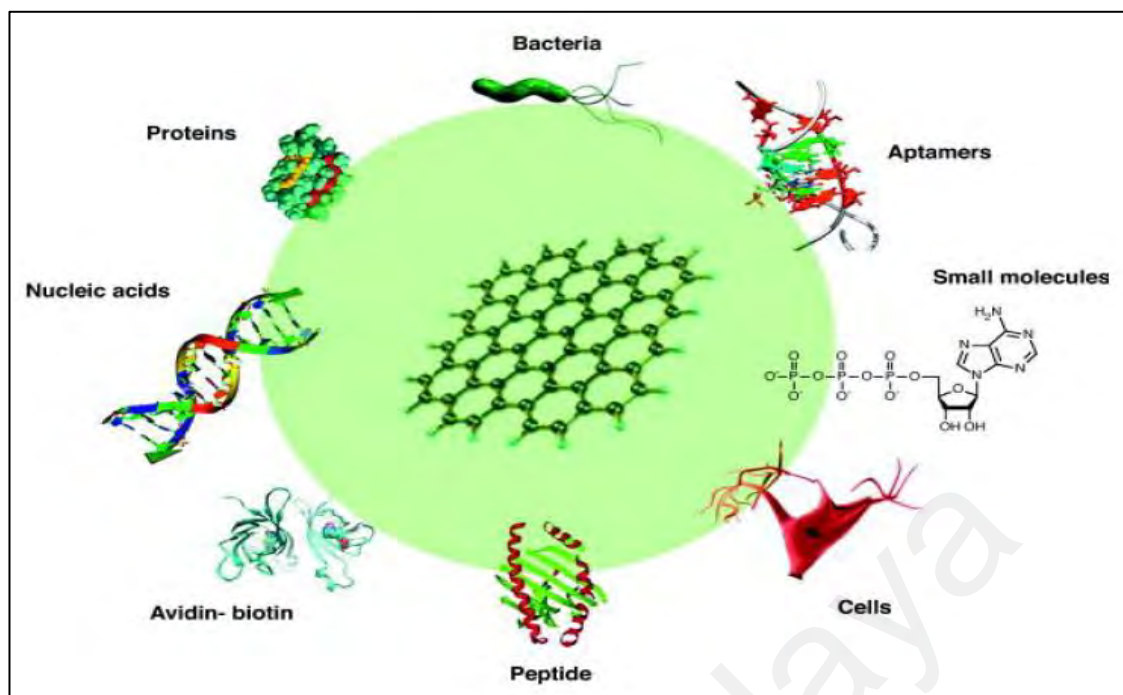


Figure 2.11. Graphene-based nanocomposites can be functionalized with DNA's, avidin-biotin, aptamers, peptides, bacteria, cell, protein and small molecules through chemical conjugation or physical adsorption for biosensing applications (Wang, Li, Wang, Li, & Lin, 2011).

2.5 Integration of graphene-based nanocomposites and aptamers in biosensors for foodborne bacteria detection

2.5.1 Interaction of aptamer with targeted bacterial cell.

There are many reports on the interaction of aptamer with bacterial DNA for an effective electrochemical detection (Akbari, Buntat, Afroozeh, Zeinalinezhad, & Nikoukar, 2015; Akhavan, Ghaderi, & Rahighi, 2012; Ma et al., 2014). However, the extraction of bacterial DNA can be time-consuming and hinders the rapid, direct and on-site detection of pathogens present in food matrixes (Ahmed et al., 2014; Fang, Wu, Lu, & Zeng, 2014; Yun & K., 2016). Thus, significant research efforts are now focused to tailor the aptamers that can directly bind to whole-cell bacteria (Urmann, Arshavsky-Graham, Walter, Scheper, & Segal, 2016; Zelada-Guillen, Sebastian-Avila, Blondeau,

Riu, & Rius, 2012). The surface antigens found on the cell envelopes of whole bacteria such as proteins, glycoproteins, lipopolysaccharides and peptidoglycan can act as targets for biorecognition (Ahmed et al., 2014). Thus, aptamers can be tailored to specifically bind on surface antigens. Aptamers that recognize bacterial cells have been used in biosensors devices allowing specific and rapid detection. In the presence of the bacterial cell, aptamer binds to its surface antigen through non-covalent interactions and undergo three-dimensional (3D) conformational changes (Sun et al., 2014). The presence of stem-loops in the predicted secondary structures aptamers plays a vital role in the interaction of aptamers with their ligands in the bacterial cell wall (Marton, Cleto, Krieger, & Cardoso, 2016). The encapsulation of the targeted bacterial cells with an aptamer (aptamer-target complex) happens through stacking, shape complementarity, electrostatic interactions and hydrogen bonding as shown in **Figure 2.12**. Aptamers also bind to their target analytes by two different recognition events; (a) binding to their ligands and (b) binding to their Watson-Crick complementary strand (Abe & Ikebukuro, 2011; Zavyalova & Kopylov, 2018). The utilization of SELEX system enables the selection of aptamer that binds bacteria with high specificity and affinity (in the nanomolar or picomolar ranges) (Dong, Xu, Yong, Chu, & Wang, 2014).

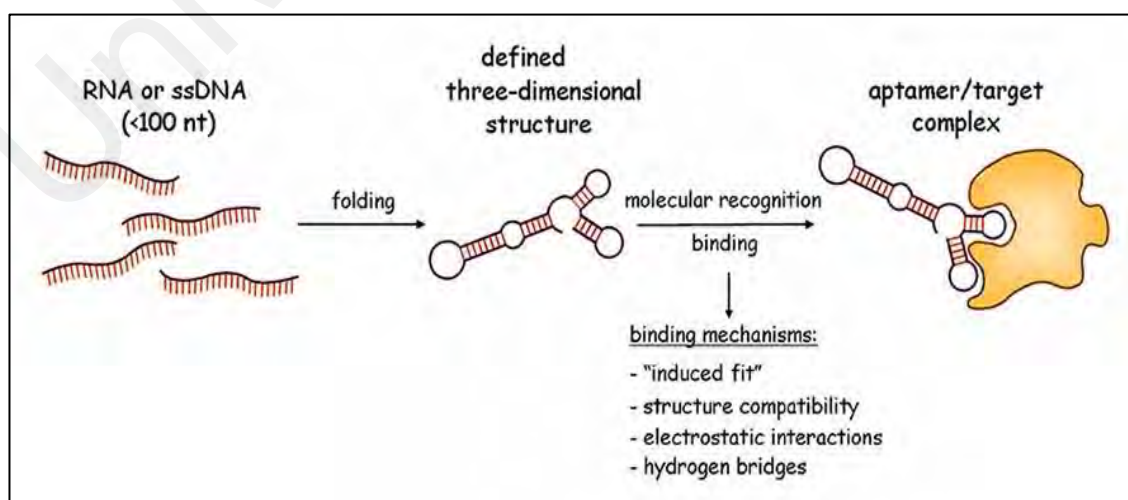


Figure 2.12. Schematic view of the aptamer molecular recognition principle (Reinemann & Strehlitz, 2014)

However, there are only a few reports on the aptamers developed against whole-cell targets. For instance, Marton et al. have isolated four different types of aptamers that specifically bind to *E. coli* cells (ATCC generic strain 25922) through the SELEX process (Marton et al., 2016). For the detection of *Salmonella*, Joshi et al. (Joshi et al., 2009) have reported DNA aptamers for outer membrane protein (OmpC) of *S. Typhimurium*. This study was also verified by Zifruddin and Thong (2018). This finding enables the detection of foodborne pathogens directly from complex food and environmental samples

2.5.2 Graphene-based nanocomposite electrochemical aptasensor for foodborne pathogen detection.

In recent years, graphene-based nanocomposite has been widely applied in impedimetric biosensors as a transducer material. Impedimetric and conductometric biosensors measure the conductivity of the solution/medium or analyses the electron transfer at the electrode-electrolyte interface which can be expressed as an impedimetric response. Graphene-based nanocomposite has been found to provide added values such as (1) efficient electron-transfer properties, (2) alternative flexible solid substrate, (3) reinforced mechanical strength, (4) functionalized surface for easy immobilization of biorecognition element and (5) increases the binding affinity between metal nanoparticles and solid substrate.

A *Salmonella* aptasensor was prepared on a glassy carbon electrode modified with GO and gold nanoparticles by non-covalent immobilization of thiolated ssDNA specific to *Salmonella* outer membrane proteins (Ma et al., 2014). The ssDNA sequence used in the reported study was previously reported (Joshi et al., 2009). The sensor quantified *Salmonella* based on the resistance between the electrode and electrolyte. The impedance increases with increasing bacterial concentration as more bacterial cells bind to the electrode surface. This detection system was reported to produce a detection limit of 3.0

$\times 10^0$ cfu mL⁻¹ and the low detection limit was attributed to the binding specificity of the aptamer and the electron-transfer ability of the GO and gold nanoparticle composite. In another study, a gold nanoparticle and reduced graphene oxide (Au-NP/rGO) nanocomposite was utilized as an electroconductive immobilization matrix for the immobilization of thiolated aptamers specific to *Staph. aureus* (Jia et al., 2014). The Au-NP/rGO/glassy carbon sensor was utilized to quantify *Staph. aureus* in the concentration range from 10^0 to 10^6 cfu mL⁻¹ and gave a detection limit of 10^1 cfu mL⁻¹. The authors attributed the increase in sensitivity and stability of the Au-NP/rGO/glassy carbon biosensor to the binding affinity between GCE and rGO, in comparison to direct deposition of Au-NP on bare glassy carbon electrode. Hybrid carbon nanomaterials have also been considered as an alternative sensing platform. The hybridization of carbon nanomaterials, for instance, CNTs and graphene may enhance the detection performance by combining the desirable qualities of both materials. For instance, an amino-modified aptamer specific to *Salmonella* was attached to a reduced GO and MWCNT nanocomposite using EDC-NHS chemistry (Jia et al., 2016). This *Salmonella* aptasensor demonstrated a detection limit of 2.5×10^1 cfu mL⁻¹. The authors attributed the wrapping of MWCNTs with reduced GO improved the electrochemical performance of the composite due to synergistic effects between MWCNT and reduced GO. The potential application of graphene-based biosensors for bacterial detection was discussed in **Table 2.2**.

Cyclic voltammetry (CV) and differential pulse voltammetry (DPV) are common analytical techniques used to measure the changes in current or potential, although square wave voltammetry has also been considered for the evaluation due to its sensitivity. Amperometric detection has been used in the detection of DNA (genosensors) as well as for whole-cell bacteria. Many researchers have developed electrochemical label-free aptasensors for instance, the detection of *S. Typhimurium* was carried out with an

aptasensor prepared using reduced GO-chitosan (rGO-CHI) composite as the conductive substrate (Dinshaw et al., 2017). The aptamer was functionalized with a thiol group and immobilized on rGO-CHI using glutaraldehyde as the crosslinker. This aptasensor demonstrated a detection limit of 10^1 cfu mL⁻¹ in raw chicken samples spiked with *S. Typhimurium*. In the selectivity test, the aptasensor was found to specifically detect *S. Typhimurium* and did not give any response to non-*Salmonella* bacteria (*Staph. aureus*, *Klebsiella pneumoniae* and *E. coli*).

2.5 Summary

In this chapter, the synthesis, fabrication and recent studies of graphene and graphene-based nanomaterials with possible applications in foodborne pathogen detections were reported. The utilization of different biorecognition elements such as antibody, DNA, and enzymes with their advantages and disadvantages were also discussed. Overall, the type of sensor selected will depend on the type of application.

The development of graphene based electrochemical biosensors is vital for rapid and sensitive detections for foodborne pathogens in food safety field. Despite the excellent sensitivity and specificity of the traditional methods of detecting bioagents involves tedious process and multi-step procedures that limits their execution at point - of-care. Moreover, the detection of low concentration targets in complex biological media can be challenging. Graphene is a most commonly exploited 2D materials with outstanding physio-chemical properties such as large surface area, zero-bandgap semiconductor, high tensile strength, biocompatible, and ultra-high charge mobility. The synthesis method of graphene and graphene-based nanomaterials is important in the electrochemistry of the biosensing applications. A well-maintained graphene property throughout the synthesis and fabrication process preserves its electronic properties, biocompatibility and increases the active sites for biomolecule immobilization and

recognition. The integration of graphene in electronic biosensors giving an ultra-high sensitivity and rapid detection of foodborne pathogens which is very promising. Besides detection limit, the economical and facile approach for sensor design and fabrication is another important element in the field of biosensing.

Although graphene is an excellent material in the field of biosensing for foodborne pathogen detection, better understanding of the physics and chemistry at the surface of graphene is crucial to ensure proper orientation of biorecognition elements which gives highly sensitive detection. In addition, cost-effective and reproducible production and miniaturization of compact electrochemical biosensors is an emergent need for a reliable diagnostic purpose. Cost-effective biosensors increase their availability in rural areas for emergency uses and miniaturization of the sensing device allow rapid and on-site detection of foodborne pathogens. These factors limit the translation of biosensors into industrial production and commercialization. Methods for producing reproducible sensor batches and scaling-up to mass production, as well as integration of biosensors into automated and miniaturized systems are yet to be developed. However, the toxicity and biocompatibility need to be evaluated for a guaranteed performance and safety of the sensors.

Table 2.2: Overview of the evaluation and properties of graphene-based aptasensors for foodborne pathogen detection

Analyte	Sensor type	Biorecognition element	Immobilization technique	Transducer material	Detection mode	Detection limit	Ref.
<i>Staph. aureus</i>	Aptasensor	<i>Staph. aureus</i> binding aptamer	Non-covalent binding	rGO-gold nanoparticles	Impedimetry	1.0 X 10 ¹ cfu mL ⁻¹	(Jia et al., 2014)
<i>Salmonella</i>	Aptasensor	Thiolated ssDNA specific to <i>Salmonella</i>	Non-covalent binding	GO-gold nanoparticles	Impedimetry	3.0 X 10 ⁰ cfu mL ⁻¹	(Ma et al., 2014)
<i>Salmonella</i> ATCC 50761	Aptasensor	Amino-modified aptamer specific to <i>Salmonella</i>	EDC-NHS	rGO-MWCNT nanocomposite	Impedimetry	2.5 X 10 ¹ cfu mL ⁻¹	(Jia et al., 2016)
<i>Staphylococcus aureus</i>	Aptasensor	<i>Staph. aureus</i> binding aptamer	Non-covalent binding	rGO	Potentiometry	1.0 X 10 ⁰ cfu mL ⁻¹	(Hernández et al., 2014)
<i>Salmonella</i> Typhimurium	Aptasensor	Thiol-modified <i>Salmonella</i> aptamer	Non-covalent binding	rGO-chitosan nanocomposite	Amperometry	1.0 X 10 ¹ cfu mL ⁻¹	(Dinshaw et al., 2017)
<i>Salmonella</i> Typhimurium	Aptasensor	Aptamer-gold nanoparticles	Covalent	rGO- UiO-67 metal	Amperometry	5.0 X 10 ⁰ cfu mL ⁻¹	(Dai et al., 2019)
<i>Salmonella</i> Typhimurium	Aptasensor	<i>Salmonella</i> aptamer	Non-covalent binding	rGO-carbon nanotube	Amperometry	1.0 X 10 ¹ cfu mL ⁻¹	(Appaturi et al., 2020)
<i>Cronobacter sakazakii</i>	Aptasensor	<i>C. sakazakii</i> aptamer	Non-covalent binding	rGO	Amperometry	7.0 X 10 ⁰ cfu mL ⁻¹	(Peng et al., 2019)
<i>Salmonella</i> spp	Aptasensor	<i>invA</i> specific aptamer	Covalent	rGO-polypyrrole	Amperometry	8.0 X 10 ⁰ cfu mL ⁻¹	(Ye et al., 2019)

CHAPTER 3

EXPERIMENTAL PROCEDURES

3.1 Reagents and chemicals

The reagents and chemicals used in this work are summarized in **Table 3.1**. The chemicals and reagents were used with the mentioned purity (%) and sources.

Table 3.1: List of reagents and chemicals

Chemicals	Formula	Purity (%)	Brand
Graphite flakes	-	90	Ashbury Inc
Sulfuric acid	H ₂ SO ₄	95~97	Merck
Phosphoric acid	H ₃ PO ₄	85	Merck
Hydrazine hydrate	N ₂ H ₄	80	Sigma-Aldrich
Hydrochloric acid	HCl	37	Merck
Ammonia solution	NH ₃	25	Merck
Hydrogen peroxide	H ₂ O ₂	30	SYSTEM
Potassium permanganate	KMnO ₄	-	R&M Chemicals
L (+)-Ascorbic acid	C ₆ H ₈ O ₆	99	Sigma-Aldrich
Azophloxine (AP)	C ₁₈ H ₁₃ N ₃ Na ₂ O ₈ S ₂	-	Sigma-Aldrich
Titanium (IV) isopropoxide (TTIP)	Ti [OCH(CH ₃) ₂] ₄	97	Sigma-Aldrich
Potassium chloride	KCl	99	Sigma-Aldrich
10X Phosphate buffer solution (PBS)	-	-	Biowest
Tris-Hydrochloride (Tris-HCl)	NH ₂ C(CH ₂ OH) ₃ . HCl	-	Sigma-Aldrich
Sodium chloride	NaCl	99.5	Sigma-Aldrich
Magnesium chloride	MgCl ₂	98	Sigma-Aldrich
Potassium Ferricyanide	K ₃ Fe (CN) ₆	97	Sigma-Aldrich
Triethanolamine (TEA)	(HOCH ₂ CH ₂) ₃ N	99	Sigma-Aldrich
Nafion	C ₉ HF ₁₇ O ₅ S	-	Ion-Power Inc.
Luria-Bertani (LB) Agar	-	-	Thermo-Fisher
Brilliance <i>Salmonella</i> Agar™	-	-	Thermo-Fisher

3.1.1 Aptamer preparation and bacterial culturing

DNA aptamer sequences were purchased from First Base (Malaysia) adapted from Joshi *et al.* (5'-TATGGCGGCGTCACCCGACGGGGACTTGACATTATGACAG-3') (Joshi *et al.*, 2009). This DNA oligomers were dissolved in 37 μ L of deionized distilled water to obtain the stock concentration of 100 μ M. The bacterial cultures used in this study were obtained from the culture collection of the Biomedical Science Laboratory, University of Malaya, Malaysia. *S. Typhimurium*, *Escherichia coli*, *Shigella dysenteriae*, *V. cholerae*, *Staphylococcus aureus* and *K. pneumoniae* are the bacterial cultures used. The cultures were kept viable in LB agar plants and slants. All the bacterial cultures were checked for purity according to standard microbiological procedures before use.

3.2 Sample preparation

3.2.1 Preparation of Graphene Oxide (GO)

In the present study, GO was prepared from graphite powder using the modified Hummer's method (Hummers & Offeman, 1958) as illustrated in **Figure 3.1**. Briefly, 150 mL of an acid mixture consisting of 115.5 mL of H₂SO₄ and 35.5 mL of H₃PO₄ was prepared. Then, 5 mg of graphite powder was added into the mixture with continuous stirring in an ice bath for 1 h. Next, 30 mg of KMnO₄ was added gradually and the mixture solution was left to oxidize whilst being continuously stirred for 3 days to obtain a yellowish-brown paste. This paste was then diluted with 250 mL of distilled water containing 10 mL of H₂O₂ followed by centrifugation. The pH of the solution was optimized by continuous washing and centrifuging the paste with 1 M HCl for three times and water for six times to obtain GO dispersion in light brown color. The solution was centrifuged at 12,000 rpm for 10 min to obtained GO with neutral pH.



Figure 3.1. Schematic representation for the synthesis of GO using simplified Hummers' method.

3.2.2 Preparation of rGO and rGO-nanocomposites

The rGO and rGO-nanocomposites were synthesized using a chemical reduction method using hydrazine hydrate (N_2H_4) as a reducing agent. Minimal volume of N_2H_4 was used to mass-produce the materials to cope with the toxicity problem caused by this reducing agent. The whole process of rGO preparation was schematically depicted in **Figure 3.2.**

3.2.2.1 Synthesis of rGO

The rGO was prepared as follows. Briefly, 12.5 mg of GO was dispersed in 10 mL of distilled water (1.25 mg mL^{-1}) and sonicated for 1 h. Then, 100 μL of NH_3 solution was added to the GO solution and stirred for 10 min to adjust the pH. After that, 10 μL was added to the reaction mixture and shake vigorously. Finally, the GO mixture was refluxed at 80 $^\circ\text{C}$. Three samples were prepared with different reduction durations (6, 12 and 24 h) and labeled as rGO (6 h), rGO (12 h) and rGO (24 h). The final product was

obtained through filtration with a nylon membrane (0.22 μm). The rGO powder obtained by filtration can be readily dispersed in ethanol by ultra-sonication to obtain a series of concentrations ranging from 1 mg mL^{-1} to 8 mg mL^{-1} .

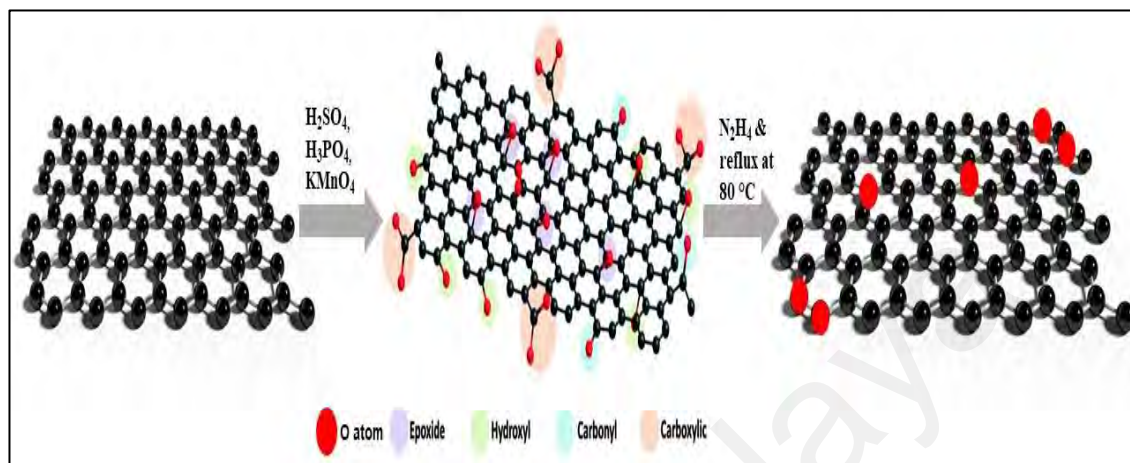


Figure 3.2. The overall process of the rGO preparation from Graphite.

3.2.2.2 Synthesis of rGO-AP nanocomposite

The protocol for the rGO-AP synthesis was adapted from Guo *et al.* (Guo, Guo, et al., 2013). Firstly, 10 mg of AP powder was dissolved in 10 mL of homogenous stable GO dispersion (1.25 mg mL^{-1}) in water. This suspension was stirred for 30 min at room temperature. Then, 100 μL of ammonia solution was added to the mixture for pH adjustment. The reduction of GO was aided by the addition of 10 μL of hydrazine solution into the mixture. After vigorous shaking for several min, the mixture was refluxed for 12 h at $80\text{ }^\circ\text{C}$ followed by filtration of the product with a nylon membrane (0.22 μm). The preparation procedure was repeated to obtain different content of AP dye in the composite material to understand the effect of AP dye concentration on its electrochemical property. The final products (nanocomposites) were labeled as rGO-AP@0.002M, rGO-AP@0.005M and rGO-AP@0.01M. The rGO-AP nanocomposite obtained by filtration can be readily dispersed in water by ultra-sonication to obtain a series of concentrations ranging from 1 mg mL^{-1} to 8 mg mL^{-1} .

3.2.2.3 Synthesis of rGO-Titanium dioxide (TiO₂) nanocomposite

rGO-TiO₂ was synthesized using a similar chemical reduction method. Firstly, 750 μL of TTIP was added into 375 μL of TEA to produce Titanium (IV) ionic (Ti₄⁺) solution. To form rGO-TiO₂, 12.5 mg of GO was dispersed in 10 mL of distilled water (1.25 mg mL⁻¹) for 1 h using an ultrasound bath sonicator. After that, 1 mL of Ti₄⁺ solution was added to the nanocomposite, and the resultant mixture was stirred for 1 h at room temperature. Then, 100 μL of ammonia solution was added to the mixture for pH adjustment followed by the addition of 10 μL of hydrazine solution to aid the reduction of GO functionalized with TiO₂. After vigorous shaking for several min, the mixture was refluxed for 12 h at 80 °C. The product was then filtered using a nylon membrane (0.22 μm) to obtain rGO-TiO₂ nanocomposite. The preparation procedure was repeated to obtain a different concentration of TiO₂ in the composite material to understand the effect of TiO₂ concentration on its electrochemical property. The final product obtained was labeled as rGO-TiO₂@0.2M, rGO-TiO₂@0.4M and rGO-TiO₂@0.6M. The product obtained was then dispersed in water by ultra-sonication to obtain a series of concentrations ranging from 1 mg mL⁻¹ to 9 mg mL⁻¹.

3.2.2.4 Synthesis of rGO-Nafion (Nf) nanocomposite

Firstly, to synthesize rGO-Nf, 10 mg of Nafion powder was added to the 10 mL of homogenous stable GO dispersion (1.25 mg mL⁻¹) in water and stirred for 30 min at room temperature. Then, 100 μL of ammonia solution was added to the mixture for pH adjustment. The reduction of GO was aided by the addition of 10 μL of hydrazine solution into the mixture. After vigorous shaking for several min, the mixture was refluxed for 12 h at 80 °C followed by filtration of the product with a nylon membrane (0.22 μm). The preparation procedure was repeated to obtain a different concentration of Nf in the composite material to understand the effect of Nf concentration on its electrochemical

property. The final products (nanocomposites) were labeled as rGO-Nf@0.002M, rGO-Nf@0.005M and rGO-Nf@0.01M. The rGO-Nf nanocomposite obtained by filtration can be readily dispersed in water by ultra-sonication to obtain a series of concentration ranging from 1 mg mL⁻¹ to 8 mg mL⁻¹.

3.3 Characterization techniques

The rGO and rGO nanocomposites samples synthesized were characterized using different methods to study and understand the physico-chemical and their applications.

3.3.1 Fourier transform infrared (FTIR) spectroscopy

FTIR spectroscopy is a useful analytical technique to identify the types of bonding present within the sample. FTIR spectroscopy involves the transmission of infrared (IR) radiation through the sample, whereby frequencies that are resonant to the chemical bond within the sample will be absorbed. Therefore, the FTIR spectrum represents the molecular transmission of the sample. In this study, FTIR spectroscopy (Bruker IFS 66V/S, USA) was used to determine the successful functionalization of the formations of rGO and its nanocomposites. The sample was mixed with using potassium bromide (KBr) pellets at a weight ratio of sample: KBr = 1:10. All the samples were run in the spectral region range of 400-4000 cm⁻¹.

3.3.2 X-ray diffraction (XRD)

The crystallographic information of the sample in this work was determined using XRD testing, Siemens D5000 with monochromatic Cu K α radiation ($\lambda = 1.5406 \text{ \AA}$) at a scan rate of 0.02° s⁻¹ operated at 40 kV and 40 mA scanning from 5°-80°. PAN analytical X'pert Highscore software was used to analyze the atomic structure.

3.3.3 Raman and Photoluminescence (PL) spectroscopy

Raman spectroscopy is a powerful technique for the characterization of carbon-based materials. Photons from the laser light will hit the sample surface and undergo absorption, reflection, or scattering and provides us information including rotational, vibrational and frequency transitions of the samples. In this study, Raman spectra were obtained using a Renishaw inVia Raman microscope, UK with a laser emitting at 514 nm. The measurement was carried out in a scan region ranging from 100-3000 cm^{-1} . The samples with concentration 1 mg/mL were drop cast on a cleaned glass slide and dried in an oven overnight before Raman characterization. A similar procedure was repeated for the PL analysis except the lens was changed to 325 nm. The bandgap energy of the materials was calculated using Planck's Equation:

$$E \text{ (eV)} = h \times C \div \lambda$$

where, E= energy, λ = wavelength, h = Plank's constant (6.63×10^{-34} J·s), C = speed of light 3.0×10^8 m/s.

3.3.4 Electron microscopy

Surface structure and morphology of as-prepared samples were characterized using a scanning electron microscope (SEM, FEI, Quanta FEG 650) at a working distance around 5 mm and a transmission electron microscope (TEM, Carl Zeiss, LEO LIBRA 120). The powder samples were placed on a carbon tape attached to the stub, which was used as the substrates for FESEM characterization. For TEM, the samples were drop-casted on a copper grid and dried in an oven overnight before the characterization.

3.4 Electrochemical cell set-up

The electrochemical measurements were carried out at room temperature by using a PGSTAT302N electrochemical workstation supplied by Metrohm AG, Switzerland and

controlled by Nova Autolab software. A conventional three-electrode electrochemical cell was used, consisting of a platinum wire as counter electrode, silver/silver chloride (Ag/AgCl) as a reference electrode and glassy carbon electrode (GCE, dia. 3mm) as a working electrode (WE). The platinum working electrode is responsible to apply current to the electrolyte solution to balance the charge added or removed at the working electrode whereas, Ag/AgCl was used to measure the potential of the working electrode. All electrochemical studies were carried out by flowing N₂ gas atmosphere. PBS 10X (137 mM of Sodium chloride, 2.7 mM of potassium chloride and 10 mM of phosphate buffer, pH 7.4 at 25 °C), tris-hydrochloric acid buffer (20 mM L⁻¹ of Tris-HCl, 0.1 mol L⁻¹ of sodium chloride and 5 mM L⁻¹ of magnesium chloride, pH 7.4 at 25 °C) or Zobel's solution [3mM Potassium Ferricyanide, K₃Fe(CN)₆ and 0.1 M Potassium Chloride, KCl] were used as an electrolyte depending on the different analytical techniques involved. A schematic diagram showing the electrochemical cell setup was presented in **Figure 3.3**.

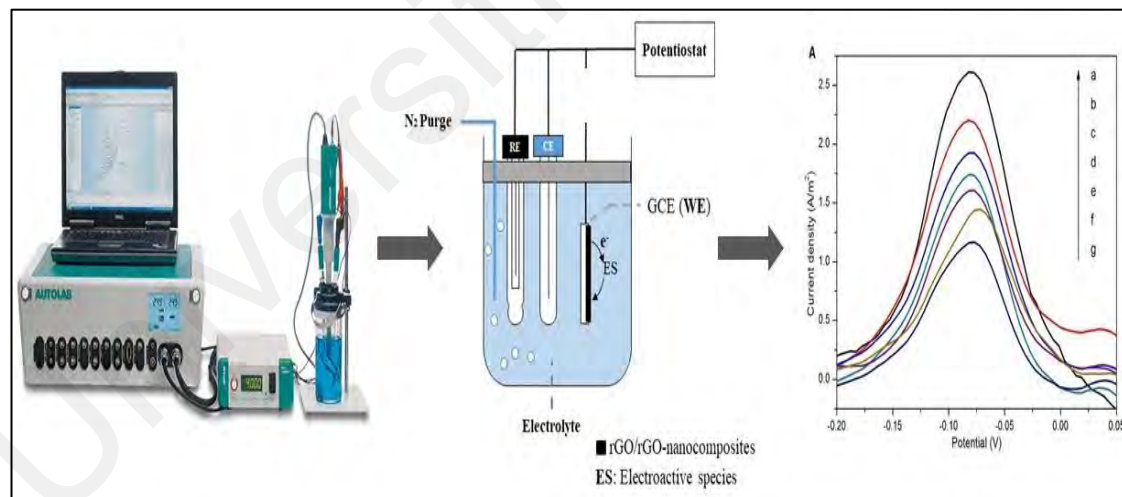


Figure 3.3. Schematic representation of the electrochemical cell setup.

From the calibration plot of the current response versus the concentration of a targeted analyte, the values for a limit of detection (LOD) and Limit of Quantification (LOQ) were calculated. LOD can be described as the lowest concentration of an analyte is a sample that can be detected and LOQ is the lowest concentration of an analyte in a

sample that can be determined with acceptable precision and accuracy under the stated conditions of the test. The LOD and LOQ were estimated based on Equations (1) and (2) as follows:

$$(1) \textit{Limit of Detection (LOD)} = \frac{F\sigma}{m}$$

$$(2) \textit{Limit of Quantification (LOQ)} = \frac{F\sigma}{m}$$

where F is the signal-to-noise ratio 3 and 10 for LOD and LOQ, respectively, σ is the residual standard deviation and m is the slope of the regression line.

3.5 Fabrication of the electrodes

The rGO and rGO-based nanocomposite materials were fabricated on the surface of the GCE (WE) to study their electrochemical properties using the electrochemical analytical method.

3.5.1 Preparation of rGO modified electrodes.

Prior to each experiment, the GCE was carefully polished with 0.05 μm alumina powder, followed by rinsing thoroughly with distilled water and the electrode was sonicated in acetone/ethanol (1:1, v/v) mixture for 3 min and rinsed again with distilled water. The electrodes were dried at room temperature. After the cleaning process, 10 μL of rGO solution ranging from different concentrations (1 to 10 mg mL^{-1}) were dropped cast onto the surface of GCE electrodes and air-dried to form rGO/GCE.

3.5.2 Preparation of rGO-based nanocomposite modified electrodes

The GCE was carefully polished with 0.05 μm alumina powder, followed by rinsing thoroughly with distilled water and the electrode was sonicated in acetone/ethanol (1:1, v/v) mixture for 3 min and rinsed again with distilled water. The electrodes were dried at room temperature. After the cleaning process, 10 μL of rGO-nanocomposites

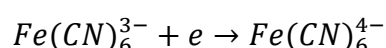
(AP, TiO₂, Fe₃O₄) solution ranging from different concentrations (1 to 10 mg mL⁻¹) were dropped cast onto the surface of GCE electrodes and air-dried to form rGO-nanocomposite/GCE.

3.6 Electrochemical sensing techniques

There are many sensing techniques that can be employed in an electrochemical sensor to detect targeted analyte even at low concentration. In this study, voltammetric and impedimetric techniques involving cyclic voltammetry (CV), differential pulse voltammetry (DPV) and electrochemical impedance spectroscopy (EIS) techniques. A suitable type of analytical technique was chosen based on its sensitivity for the detection of analytes at the surface of WE.

3.6.1 Cyclic Voltammetry (CV) and Electrochemical Impedance Spectroscopy (EIS)

CV and EIS were used to understand the electrochemical behavior of the rGO and rGO-nanocomposite modified electrodes. CV was applied to study a reversible redox couple reaction which involves potential sweep at the WE immersed in an electrolyte solution that results in measurable currents. During the potential sweeps, a forward and reverse scan at a fixed potential will measure the oxidation and reduction current peaks. The overall conductivity of the WE can be accessed through the CV. In this study, the CV was conducted in Zobel's solution at a scan rate of 100 mV.s⁻¹ and the potential scan was cycled at different ranges depending on the type of fabricated electrodes. The half-reaction of Zobel's solution takes place at WE as follow:



A series of scan rates were used to measure redox peaks to ensure surface-confined redox reaction at the WE. Surface-confined reactions are considered as a charge

transfer reaction in which both the reactant and the product are strongly adsorbed on the electrode surface.

EIS is used to monitor the impedance change at the electrode-solution interface due to a change in electrical properties at the electrode surface. In this study, EIS measurements were performed within the frequency range of $0.1\text{--}10^3$ Hz with a single sine wave type at room temperature. The resistance of the electrolyte solution (R_s), Warburg impedance (Z_w) and charge transfer resistance (R_{ct}) of the electrical circuit were modeled using the Nova software. The EIS measurement was also done using Zobel's solution. The Randles equivalent circuit model employed as illustrated below (Figure 3.4):

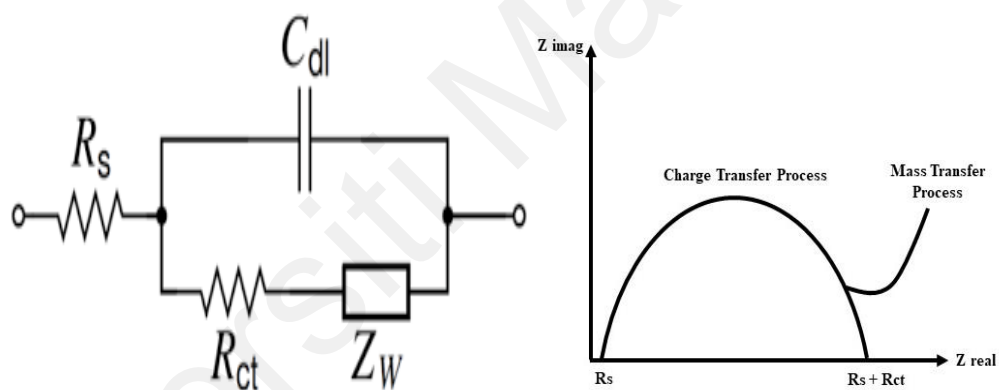


Figure 3.4. The Randles equivalent circuit model (left) and Nyquist plot of EIS (right).

where R_s is the resistance of the solution, R_{ct} is the electron transfer resistance and a Warburg element (Z_w) was connected to a capacitor (C_{dl}) in a parallel circuit. The expression for Z_w is composed of a real and an imaginary part measured at different frequencies which can be reflected using the Nyquist plot.

3.6.2 Differential Pulse Voltammetry (DPV)

DPV is one of the pulse voltammetry techniques that are highly sensitive to detect analytes at very low concentrations. DPV is also more sensitive towards oxidation or reduction currents (faradaic currents) since it permits discriminating charging

(capacitance) current. In this technique, the end of the current of the pulse (I_1) and just before pulse application (I_2) is measured, using pulses superimposed on a slowly changing base potential at changing amplitude (10 to 100mV). The difference between the two currents ($\Delta I = I_2 - I_1$) is plotted against base potential and leads to a voltammogram with a peak-shaped waveform as shown in **Figure 3.5**.

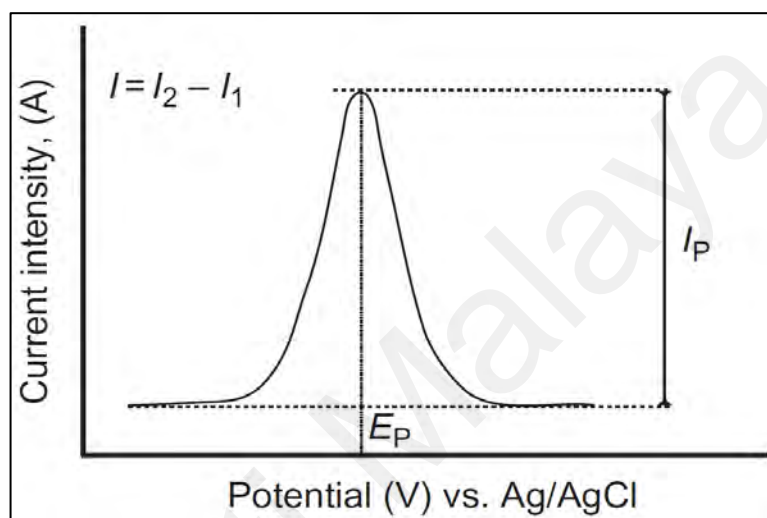


Figure 3.5. The voltammogram obtained through DPV measurement

The E_p is referring to the target analyte's peak position. The height of the peak (I_p , faradaic response current peak) is directly proportional to the concentration of the analyte. The sensitivity and lowest detection limit can be achieved by optimizing several parameters including the modulation amplitude, step potential and step width. In this study, the following parameters were applied for the DPV measurements, pulse amplitude: 0.025 V, pulse width: 0.05 s and pulse period: 0.05 s.

3.7 The analytical performance of the rGO/GCE and rGO-nanocomposites/GCE electrodes

The relationship between the different types of materials and sensor performance was investigated. The electrochemical determination of targeted analytes was studied

using the amperometric technique. The parameters that affect the sensing performance of the electrodes were optimized to exhibit a good sensitivity and become highly stable and reproducible for the repetitive experiments. The schematic diagram of the fabrication and electrochemical detection of rGO-nanocomposites electrodes as illustrated in **Figure 3.6** to **Figure 3.8**.

3.7.1 Electrochemical detection of Ascorbic Acid (AA)

The electrochemical properties of the rGO/GCE modified electrodes were characterized by using CV and electrochemical impedance spectroscopy (EIS). CV curves were recorded for the different modified electrodes in the presence of AA to determine the best sensor electrode for the electrochemical detection of AA. The CV characteristics of bare GCE, GO/GCE and three different rGO/GCE modified electrodes were recorded in a 0.1 M PBS (pH 6.5) solution containing 100 μM AA at a scan rate of 100 mV/s. The most conductive rGO/GCE electrodes were chosen to study the sensitivity test using DPV in 10X PBS (pH 7.0). The electrode was tested against different types of AA concentrations ranging from (10 μM to 100 μM). In this study, possible interferences from some co-existing compounds such as lactose, fructose, sucrose and hydrogen peroxide were chosen to evaluate.

3.7.2 Electrochemical detection of the bacteria

The GCE was cleaned with 0.05 μm alumina powder and sonicated with acetone and water prior to use. Then, 10 μL of different concentration of the rGO-nanocomposites solution was dropped onto the surface of GCE and allowed to dry in room temperature to form rGO-nanocomposite/GCE. To develop an optimized sensing platform, 1-10 μL of aptamer (ssDNA) concentrations ranging from 1 to 20 $\mu\text{mol L}^{-1}$ was loaded on the rGO-nanocomposite/GCE platform to study the optimal volume and concentration of aptamer.

The electrodes were then air-dried to obtain ssDNA/rGO-nanocomposite/GCE. This sensing platform was stored at 4 °C until use.

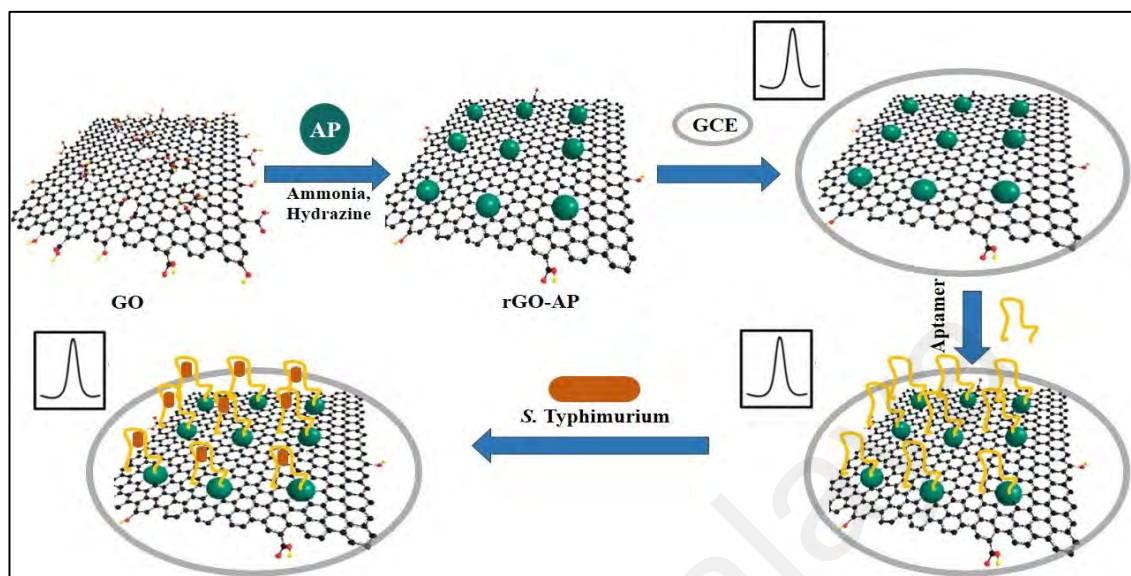


Figure 3.6. Schematic diagram of the approach for the fabrication of rGO-AP and electrochemical detection of bacteria.

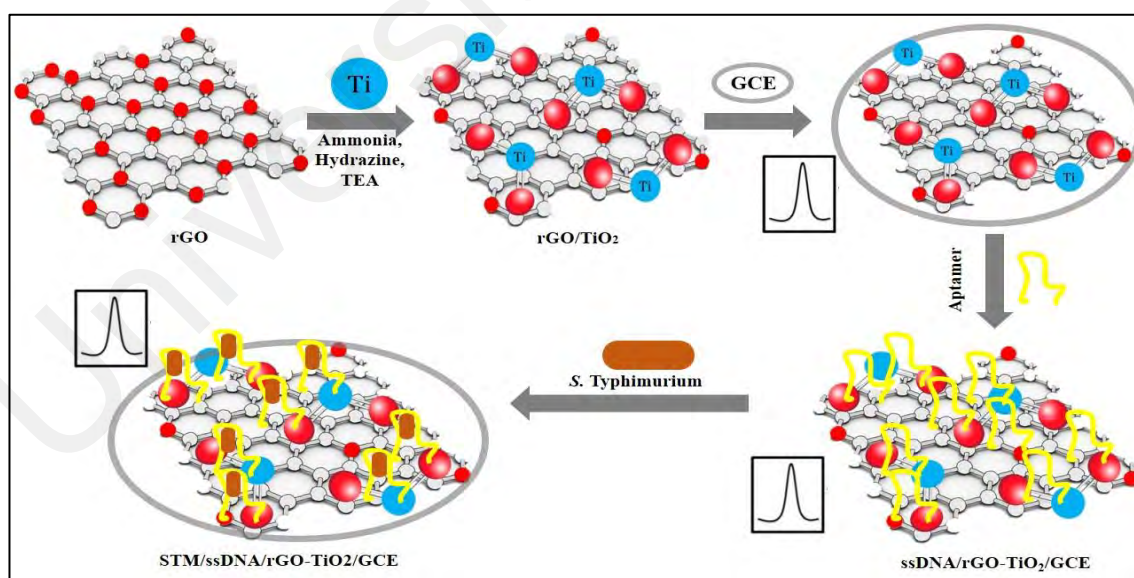


Figure 3.7. Schematic diagram of the approach for the fabrication of rGO-TiO₂ and electrochemical detection of bacteria

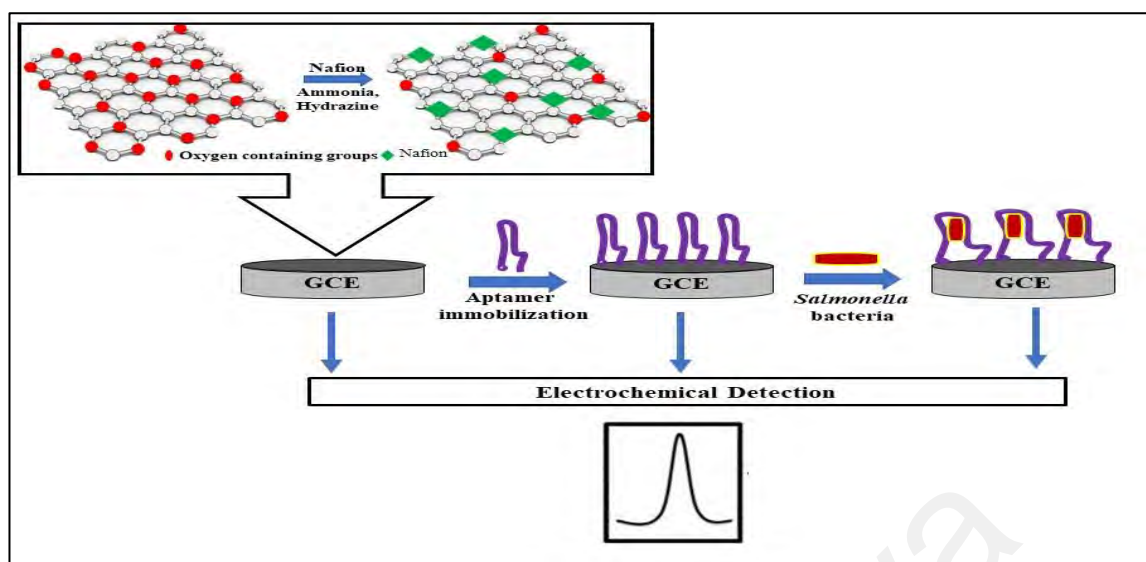


Figure 3.8. Schematic diagram of the approach for the fabrication of rGO-Nf and electrochemical detection of bacteria

3.7.2.1 Sensitivity and selectivity test

To study the sensitivity and detection limit of the sensing platform, DPV study was conducted in Zobell's or Tris-HCL solutions depending on the sensing platform involved, with controlled instrumental parameters (pulse amplitude: 0.025 V, pulse width: 0.05 s and pulse period: 0.05 s). The ssDNA/ rGO-nanocomposites/GCE electrodes were incubated for 5 min with serially diluted *S. Typhimurium* (STM) suspensions of different concentrations ranging from 10^8 – 10^1 cfu mL⁻¹ for varying duration (1 min to 20 min). The selectivity of aptamer was also studied with different types of non-*Salmonella* bacteria at a concentration of 10^2 cfu mL⁻¹ namely *V. cholerae*, *Sh. dysenteriae*, *E. coli*, *K. pneumoniae* and *Staph. aureus*. The DPV was collected for all types of bacteria.

3.7.2.2 Real food sample analysis

For the evaluation with food sample, raw chicken meat was artificially spiked with *S. Typhimurium* cultures ($\sim 10^7$ – 10^8 cfu mL⁻¹) and then homogenized in Buffer Peptone

Water (BPW) (1:10, w/v) followed by incubation for 4 h at room temperature. Then, an aliquot of the homogenate was serially diluted in Tris-HCl buffer to obtain a bacterial suspension range of 10^4 – 10^1 cfu mL⁻¹ and confirmed by viable plate count. The developed sensing bio-electrodes were incubated in the diluted bacterial suspension for 5 min followed by electrochemical detection. Food homogenates from non-spiked chicken meat were used as negative controls. All the tests were repeated three times to ensure the reproducibility of the results. The results obtained from sensitivity test were validated by PCR using oligonucleotides primers targeting the outer membrane protein C (ompC) of *Salmonella* as previously described by Alvarez et al. (Alvarez et al., 2004). The PCR reagents (25 μ L) consisted of 1 \times green GoTaq Flexi Buffer, 1.5 mmol L⁻¹ magnesium chloride (MgCl₂), 280 μ mol L⁻¹ deoxynucleotide triphosphate (dNTP) mix, 0.4 μ mol L⁻¹ of each primer pair, 1 U *Taq* DNA polymerase (Promega, Madison, USA) and approximately 100 ng of bacterial genomic DNA. The PCR assay was carried out in a thermal cycler using the following conditions: initial denaturation at 95 °C for 2 min; followed by 35 cycles of 95°C for 1 min, 55 °C for 1 min and 72 °C for 2 min; with a final extension step of 72 °C for 5 min and then held at 4 °C.

3.8 Statistical analysis

Analysis of variance (ANOVA) was used for all statistical analyses. Means, error bars and standard deviations were calculated based on triplicate tests. Differences between variables were tested for significance using a one-way analysis of variance (ANOVA) and significantly different means ($p < 0.05$) are separated using Tukey's Honestly Significant Differences (HSD) test.

3.9 Reproducibility and shelf-life studies

The reproducibility of the rGO/GCE and rGO-nanocomposite/GCE modified electrode was evaluated by recording the CV curves at a series of freshly prepared five

electrodes in an electrolyte. DI water was used to rinse the electrode surface after each measurement. The shelf-life of the developed sensor was investigated by CV for a period of 8 weeks. The electrodes were stored at 4 °C in a refrigerator when it was not in use.

3.10 Validation of the experimental results with PCR reaction.

The results obtained from the sensitivity test were validated by PCR using oligonucleotides primers targeting the outer membrane protein C (ompC) of *Salmonella* as previously described by Alvarez et al. (Alvarez et al., 2004). The PCR reagents (25 µL) consisted of 1× green GoTaq Flexi Buffer, 1.5 mmol L⁻¹ magnesium chloride (MgCl₂), 280 µmol L⁻¹ deoxynucleoside triphosphate (dNTP) mix, 0.4 µmol L⁻¹ of each primer pair, 1 U *Taq* DNA polymerase (Promega, Madison, USA) and approximately 100 ng of bacterial genomic DNA. The PCR assay was carried out in a thermal cycler using the following conditions: initial denaturation at 95 °C for 2 min; followed by 35 cycles of 95°C for 1 min, 55 °C for 1 min and 72 °C for 2 min; with a final extension step of 72 °C for 5 min and then held at 4 °C.

For the selectivity and specificity test, biotin-streptavidin magnetic beads coupled with aptamer were used. The assay was carried out by seeding 1 mL each serial dilution pure culture of the bacteria sample with 250 µL aliquot of the aptamer-coupled magnetic beads. The aptamer-coupled magnetic beads are pulled down using the magnetic particle concentrator for Eppendorf microtubes for 30 seconds, and the magnetic beads are washed four times with 1X PBS-5% Tween 20 (200µL) buffer. The pellet was eluted using 100µL of the nuclease-free water. The eluted pellet was subjected to a boiling method for cell lysis and DNA extraction. The PCR was carried using specific primers for each non-*Salmonella* bacteria (SArpoB for *S. aureus*, phoA for *E. coli*, ShigHI for *Shigella* spp, vatpA for *Vibrio* spp and for 16sRNA *E. coli*) and ompC primer was used for other *Salmonella* bacteria.

CHAPTER 4

CONDUCTIVITY MEASUREMENT OF REDUCED GRAPHENE OXIDE MODIFIED ELECTRODE FOR ELECTROCHEMICAL DETECTION OF ASCORBIC ACID: A PRELIMINARY STUDY

4.1 Overview

A variety of materials such as metal, semiconductor nanoparticles (Yin et al., 2011), carbon nanotubes (Bhattacharya, 2016) and organic conjugated polymer (Mulchandani & Wang, 1996) have been reported to possess potential as electrochemical sensors. However, the advantages conferred by the physical, optical and electrochemical properties of graphene have contributed to its wide applications in the fabrication of ultrasensitive and selective electrochemical biosensor devices. Fascinating properties of graphene, such as large surface area which is about 2630 m²/g (Reina et al., 2009), high conductivity (Li et al., 2009) and high electrocatalytic activity (Wang, Wan, & Zhang, 2010) makes it a suitable material for the fabrication of sensors. In terms of biocompatibility and ease of surface functionalization, GO can be more promising than rGO but the non-conductive nature of GO due to the presence of saturated sp³ bonds and the high density of electronegative oxygen atoms bonded to carbon insulates the electrical conductivity of GO (Pei & Cheng, 2012). Thus, graphene can be engineered with minimal structural defects to increase the overall conductivity by restoring the sp² carbon networks through the migration of heteroatoms, oxidation and reduction via chemical modification using low-cost fabrication techniques (Chua & Pumera, 2014). Hydrazine hydrate is the most commonly used reducing agent which aids the removal of the chemical linkages inside the interlayers of GO to produce highly hydrophobic and aggregated rGO (Suvarnaphaet & Pechprasarn, 2017). This chemical reduction method can be

advantageous due to the cost-effective and simple process for the mass production of rGO (Hirata, Gotou, Horiuchi, Fujiwara, & Ohba, 2004). Moreover, chemically derived graphene forms highly stable colloids with good mechanical strength (Lee, Kim, & Ahn, 2015; Suvarnaphaet & Pechprasarn, 2017). Graphene nanomaterials are the leading material that has been widely explored and used for the detection of biological compounds or biomolecules in the field of biosensing (Ng, Qiu, Ding, Lu, & Wu, 2017; Peng & Weng, 2017; Piccinini et al., 2017). Graphene-based materials used in biosensing for two main purposes. Firstly, it initiates the charge-biomolecule interactions at π - π domains. The electrostatic forces and charge exchange on the rGO surface leading to electrical variations. Secondly, surface defects or disorders created on the rGO surface during the chemical reduction eases the process of immobilization of biomolecules (Suvarnaphaet & Pechprasarn, 2017). The overall schematic of the chemical reduction of rGO is illustrated in **Figure 4.1**.

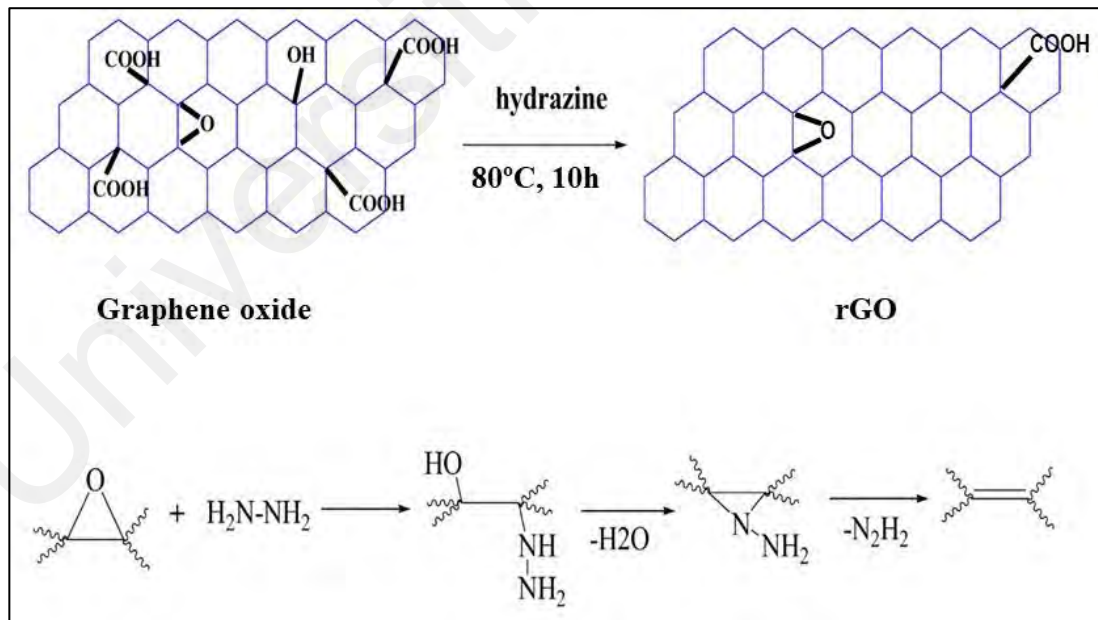


Figure 4.1. The overall schematic of rGO chemical reduction process

Recently, researchers have found that the reduction duration of GO has a certain influence on the properties of rGO, most importantly on its electrical conductivity and catalysis activity (Ramli, Hanim, Muda, Mat Isa, & Jamlos, 2015). The heating of

graphene usually causes defects on the graphene's surface which restores aromatic graphene structure and useful in modifying the graphene properties for specific applications (Pei & Cheng, 2012). A controlled number of defects introduces holes on the graphene sheet improvising their electronic properties because the vacancy defect density gives graphene a metallic property (Jafri et al., 2010). However, the surface defects created on the graphene should be within a tolerable amount. Excessive amount of structural defects will lead to a decrease in conductivity resulting from formations of scattering centers (Wu, Yang, et al., 2014). The scattering centers will prevent graphene from forming the hexagonal sp^2 carbon structure. The defect also causes a bandgap in the graphene electronic structure which limits the electron's mobility and destroys the mechanical strength of graphene (Yan et al., 2013). Besides conductivity, the prolonged reduction will result in a decrease of biocompatibility and chances of surface functionalization of rGO due to the complete removal of oxygen-containing functional groups that aid in surface modifications (Gurunathan & Kim, 2016; Monteserín, Blanco, Aranzabe, Aranzabe, & Vilas, 2017). The presence of some residual oxygen functional groups on rGO surface will help to induce the pseudocapacitive effects (electrochemical reduction and oxidation) and promote good wettability of the electrodes caused by faster electrolyte permeability (Chen, Zhang, Zhang, Yu, & Ma, 2011; Mao, Zhang, On Chan, & Wu, 2012). Moreover, these residual functional groups promote the dispersibility of hydrophobic rGO in an aqueous medium to ease the electrode fabrication process (Rajagopalan & Chung, 2014). The biocompatibility of the rGO can be also preserved by maintaining a certain degree of oxygen groups which serve as interaction sites for biomolecules immobilization (Dong & Qi, 2015). Thus, to recover the electrical conductivity of rGO, the reduction degree of GO sheets should be carefully optimized by controlling the process duration to produce good quality products. There are many studies reported the effect of reduction durations on the conductivity of graphene. For instance,

an efficient active material of rGO for the fabrication of supercapacitor electrodes is prepared by chemical reduction with hydrazine (Rajagopalan & Chung, 2014). They concluded the reduction time increased the overall performance and conductivity of rGO electrodes by accelerating the faradaic reactions and faster wetting. Similarly, Radzi Hanifah et al. (Radzi Hanifah et al., 2015) reported the effect of reduction time towards the physico-chemical properties of rGO in terms of structural, thermal and electrical conductivity using sodium oxalate as a reducing agent.

AA is a hexenoic sugar acid with two dissociable protons. It is well known for its radical scavenging capacity and powerful antioxidant property. This molecule can be electrochemically detected with a label-free rGO modified electrode with high sensitivity. The electrochemical biosensor has a series of advantages such as high sensitivity towards electroactive species, rapid, accurate response and most importantly it is portable and inexpensive compared to other existing biosensors. Chemically reduced graphene poses a larger surface area which enhances the adsorption capacity of graphene layers for the AA analyte thereby increasing the sensitivity of the graphene electrode. During the oxidation process, the π - π interaction of the graphene plane with conjugated hexenoic acid-lactone in the AA molecule plays a key role in the detection process (Dong-Fang, Chang-Sheng, Guo, Li, & Dong-Xue, 2010). As a result, an obvious oxidation peak can be observed. The electrochemical detection of AA using rGO electrodes can be highly selective even in the presence of interfering species. There are many studies have been reported for the detection of AA using rGO modified electrodes (Ghanbari & Bonyadi, 2018; Kim, Bong, et al., 2010; Sun, Lee, Yang, & Wu, 2011). The electrochemical detection of the AA at the surface of the rGO electrode is elucidated in **Figure 4.2**.

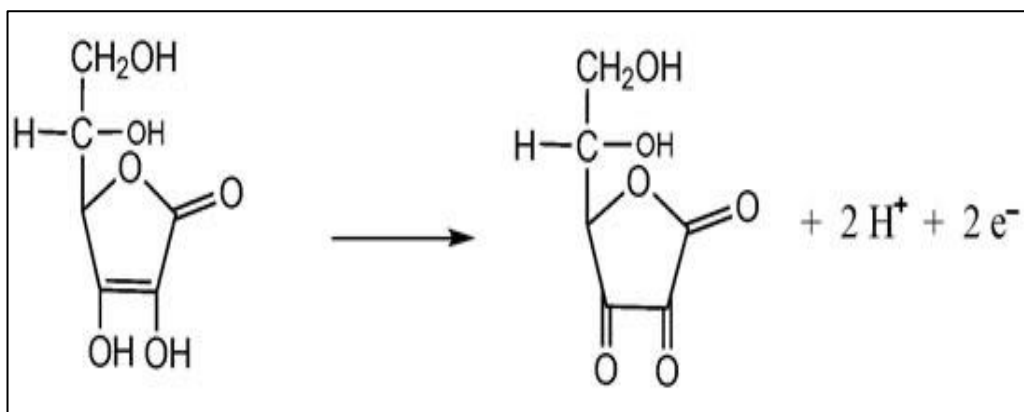


Figure 4.2. The electrochemical detection of the AA

In the present study, the conductivity of rGO synthesized at different duration of reduction time can be studied by performing the electrochemical detection of AA. A selective and sensitive electrochemical sensing platform based on a chemically reduced rGO modified electrode was fabricated for the detection of AA in the presence of other interferences. The experimental parameters such as the effect of scan rate, different reduction duration and loading amount of rGO on the electrode on electrocatalytic performance were investigated. The degree of defects on the surface of rGO solely dependent on the duration of the reduction process. This defect determines the surface area, conductivity, C/O ratio and heterogeneous electron transfer rate of rGO which affects the overall electrochemical properties. Thus, in this study, the rGO modified electrodes produced at different reduction time were employed as an active sensing material to study its conductivity, electrochemical properties, sensitivity and selectivity toward AA detection. This approach will help to identify the optimal duration of the chemical reduction process that produces the best performing and good quality rGO. Overall, an optimized rGO modified electrode could make them a suitable candidate for the detection of a wide range of biomolecules in the field of biosensing.

4.2 Structural characterization of rGO nanomaterial.

Fourier transform infrared spectroscopy (FTIR) was employed to confirm the formation of rGO at different reduction durations. **Figure 4.3** (A) shows the FTIR spectra of GO, rGO@6h, rGO@12h and rGO@24h. Theoretically, GO has several essential acute peaks that can be detected by FTIR such as C=O stretching at 1730 cm^{-1} , C–O–C stretching at 1214 cm^{-1} and C–O stretching at 1100 cm^{-1} . Similar results were obtained in this experiment thus, the presence of oxygen molecules (O) on GO was confirmed. Furthermore, a broad and intense band of a hydroxyl group (–OH) at 3300 cm^{-1} was observed from the FTIR pattern. Interestingly, a broadening of the transmittance value was also observed indicating the increased diffusion rate of oxygen molecules into the graphite flakes to form a carbonyl group, carboxylic group and an epoxy group in the GO sample.

However, after the chemical reduction, all the essential characteristic peaks of rGO samples were weakened and some hydroxyl functional groups were drastically dropped or disappeared as compared with GO sample. This phenomenon clearly illustrates that the oxygen functional groups such as C=O stretching, C–O–C stretching, C–O stretching, and hydroxyl groups were mostly removed to form rGO during the chemical reduction aided by hydrazine. In addition, the C=C conjugation at 1525 cm^{-1} was detected on rGO sample due to the sp^2 hybridization.

Meanwhile, a disappearance of the peak intensity of the –OH group in the rGO sample at 3300 cm^{-1} was also observed and it approached zero when the GO is fully reduced to rGO. The rGO@12h formed at the duration of 12 h of reduction process was selected for optimum hydroxyl groups elimination from the carbon basal plane. The structure configuration which includes disorders and defects in carbon-based materials can be studied using Raman spectroscopy. The Raman of GO and rGO samples at

different reduction time were shown in **Figure 4.3 (B)**. The Raman spectra for GO and rGO manifest the successful reduction of GO to rGO relative to the changes in intensity of two important peaks, D and G. Raman spectra for GO and rGO shows two significant in-phase vibrations at 1349 cm^{-1} (D-band) and 1593 cm^{-1} (G-band) for rGO and at 1352 cm^{-1} (D-band) and 1602 cm^{-1} (G-band) for GO. The D-band indicates the presence of a disorder or structural defects in the sp^2 -hybridized carbon system whereas, the G band obeys the first-order scattering of E_{2g} phonons due to the presence of sp^2 -hybridized carbon. The I_D/I_G ratio was used to measure structural disorder that occurs during the removal of oxygen groups attached to GO and the size of sp^2 ring clusters in a sp^3/sp^2 hybrid network of carbon atoms.

As compared to GO, the chemically reduced rGO exhibits stronger D band in the Raman spectra with higher a I_D/I_G ratio due to the structural defects created on graphene sheets. The defects were caused by the distortion of bonds and increased the formation of smaller size sp^2 graphitic domains owing to the reduction process. However, a prominent G band proves the crystallinity of the sample is preserved. The I_D/I_G ratio increased with increasing reduction time. This is due to the removal of oxygen groups which causes structural defects and a decrease in the average size of the sp^2 domains resulting from the reduction process (Mehrali *et al.*, 2014).

The surface defects created during the reduction process to produce rGO favors the charge-separation mechanism and improves the signal-to-ratio which results in enhanced transducer efficiency. However, the increased number of structural defects especially for rGO@24h decreases the conductivity of graphene sheets due to the presence of scattering centers and high bandgap in graphene electronic structure (Yan *et al.*, 2013). Thus, optimized reaction time is crucial to preserve the conductivity of rGO.

The atomic structures and interlayer spacings of the rGO were studied using X-ray diffraction (XRD). The XRD patterns of GO and rGO samples were shown in **Figure 4.3 (C)**. The XRD pattern of GO shows a sharp and intense diffraction peak at $2\theta = 10.3^\circ$ (due to 002 crystalline plane). This peak reflects the intercalation of water molecules and the formation of oxygen-containing functional groups between the layers of graphite. After the chemical reduction, the peak at 10.3° decreases and new broad peak appeared at $2\theta = 28.4^\circ$ for rGO. This is due to the removal of oxygen-containing functional groups.

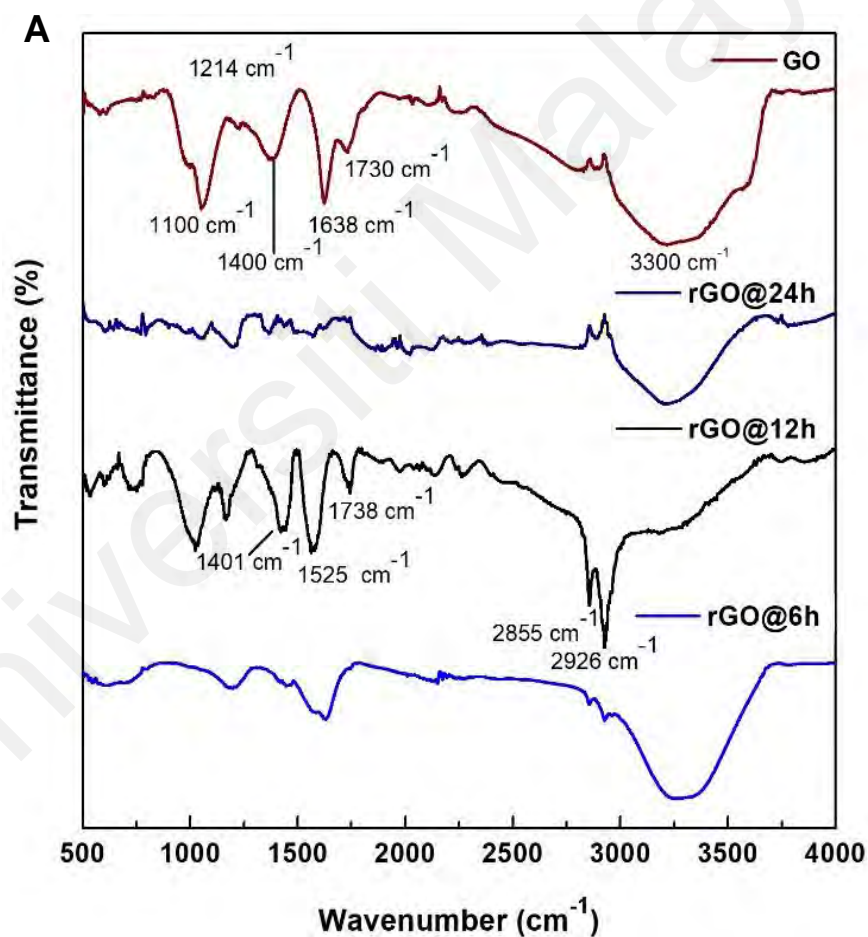


Figure 4.3, continued.

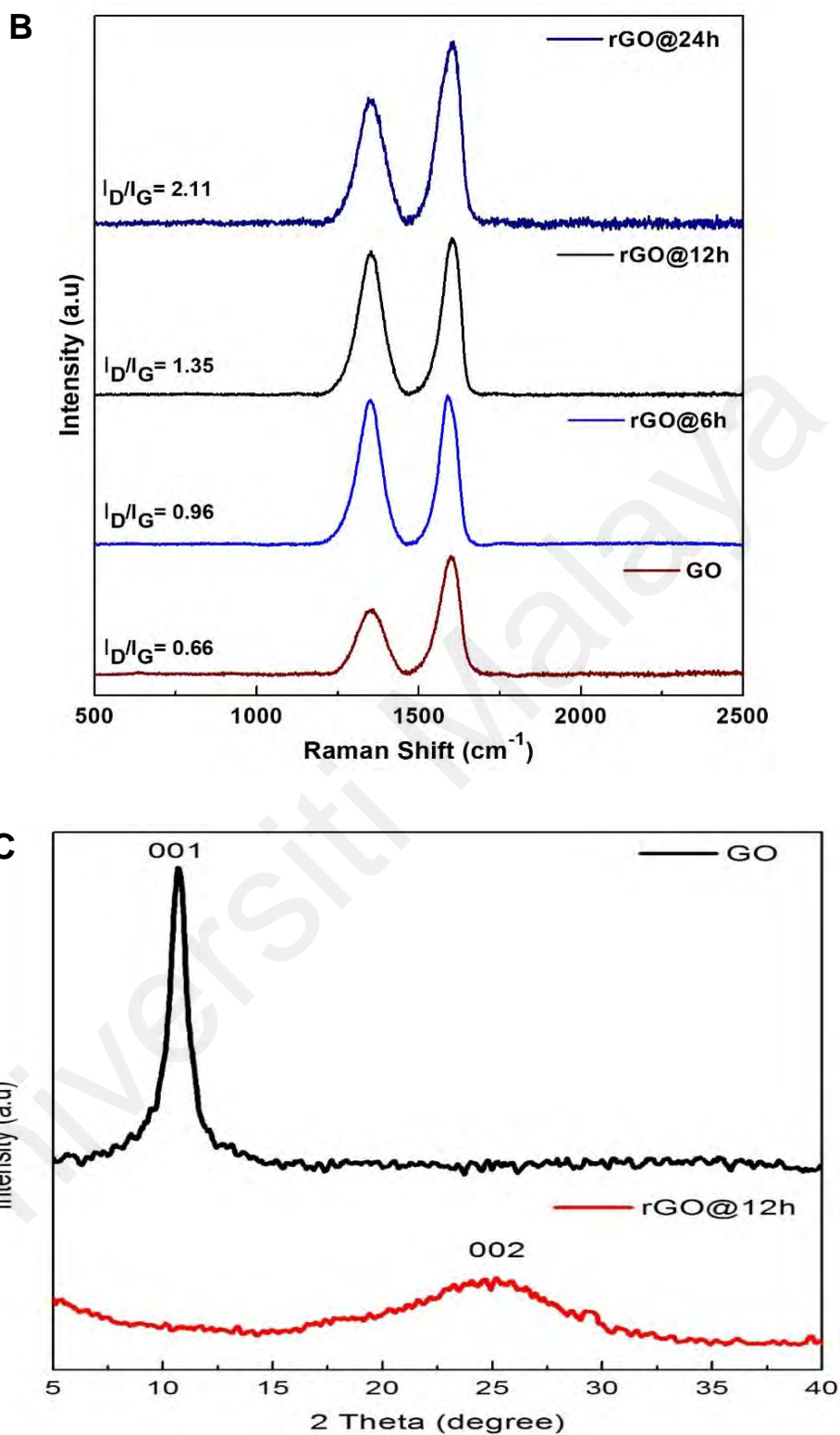


Figure 4.3. (A). FTIR spectra obtained for the GO, rGO@6h, rGO@12h and rGO@24h nanomaterial. (B) Raman spectra obtained for the GO, rGO@6h, rGO@12h and rGO@24h nanomaterial. (C) The XRD patterns of GO and rGO.

4.3 Morphological characterization of rGO nanomaterial

The morphology and structural characteristics of GO and rGO samples at different reduction times were studied using SEM and TEM. **Figure 4.4 (A)** shows the SEM images of GO and rGO samples. The GO samples contain a few layers of crumpled sheets. The GO sheets closely restacked due to the presence of oxygen-containing functional groups (-OH, -COOH and -H₂O molecules) and exhibit uniform wavy wrinkles on the surfaces. For chemical reduction of 6h, the morphology of rGO@6h still exhibits agglomerated form with a rough and cracked surface due to the insufficient reaction time to remove the oxygen functional groups that attached at the edge and basal plane of the graphene layer. However, at 12h the rGO@12 shows a wrinkled layer overlapping with each other neatly. This exfoliation of graphene layers will help the electrolyte ions to percolate between the layers hence increases the electrochemical performance (Sekharappa, Kishore, Penki, & Munichandraiah, 2014). The morphology of rGO@24 h showed a disordered, crumpled and smaller layer of graphene due to the increased reduction time.

Figure 4.4 (B) shows the TEM images of GO and rGO samples. The GO morphology exhibits a wavy wrinkle-like structure on its surface and stacked with a few layers. After the reduction of GO, rGO exhibits a typical sheet-like structure with a size of less than 10 nm. A single layer of rGO can be obtained with fewer wrinkles and folding. The carbon skeleton is well preserved even after the chemical reduction process. The distribution of rGO sheets varies with different periods of reduction time. The rGO@6h shows more stacking of graphene layers compared to rGO@12h due to insufficient reaction time. Moreover, rGO@24h exhibits more agglomeration and stacking of graphene sheets as compared to others due to the presence of a higher level of surface defects as confirmed with Raman spectra which indicated the highest I_D/I_G ratio.

Whereas, the TEM for rGO@12h sample shows a thin layer of graphene sheets with 2.24 nm of thickness suggesting the possibility for more facile movement of electrolyte ions (Muthoosamy et al., 2015).

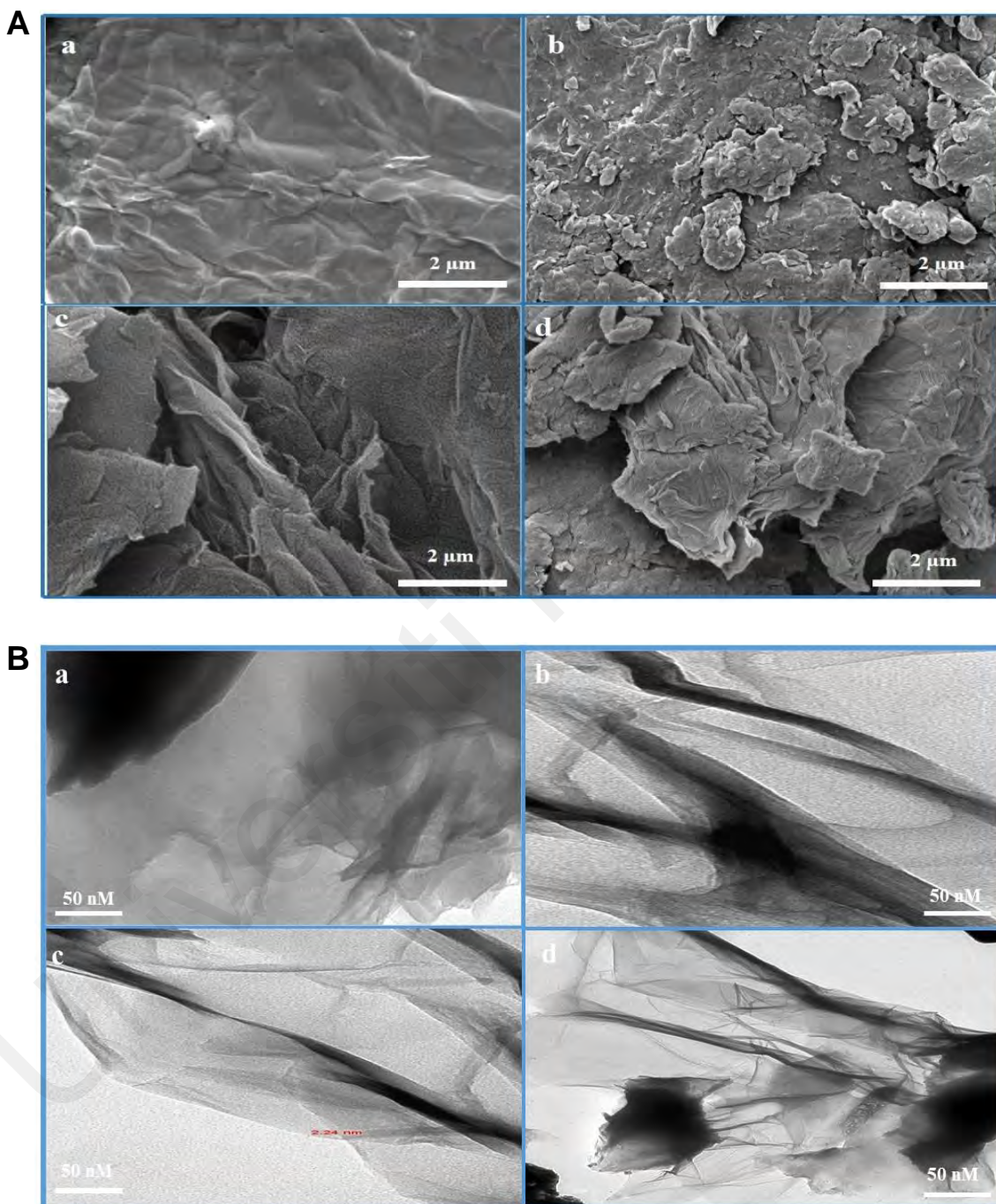


Figure 4.4. (A) SEM image obtained for the (a) GO, (b) rGO@6h, (c) rGO@12h and (d) rGO@24h nanomaterial. (B) TEM image obtained for the (a) GO, (b) rGO@6h, (c) rGO@12h with 2.24 thickness of layer and (d) rGO@24h nanomaterial.

4.4 Electrochemical characterization of rGO modified GCE electrode

The electrochemical properties of the rGO modified GCE electrodes were investigated by using CV, EIS and DPV. **Appendix A1** shows the cyclic voltammogram of rGO reduced at different reaction time in Zobell's solution at a scan rate of 100 mV/s. The CV plot for the GO, rGO@6h/GCE, rGO@12h/GCE and rGO@24h/GCE shows a quasi-reversible redox reaction with maximum peak current density at 0.3 V. The redox peak current increased in the order of rGO@6h/GCE < rGO@24h/GCE < rGO@12h/GCE and the GO/GCE exhibits the lowest conductivity due to the presence of oxygen functional groups that serves as an electrical insulator (Punckt et al., 2013). The rGO@12h/GCE achieved the smallest peak-peak separation (ΔE_p) as compared to rGO@6h and rGO@24h which is about 210 mV, 270mV and 300 mV, respectively. This peak-peak to separation indicates the quasi-reversible redox reaction. Reversibility shows the electron transfer kinetics are fast enough to balance the oxidation and reduction reactions. The highest peak current and smallest peak-peak separation were achieved by rGO@12h/GCE modified electrode which indicates enhanced electrode transfer rate and high conductivity (Lee, Choi, & Hong, 2013). The highest conductivity of the rGO@12h/GCE is due to the large surface area of the well-exfoliated graphene sheets as supported by the rGO samples characterization results (SEM and TEM).

Figure 4.5 (A) shows the Nyquist plot recorded for GO/GCE electrode and three other rGO modified electrodes. The diameter of the semicircle represents the charge transfer resistance (R_{ct}) through the graphene sheets (Jiang et al., 2014). GCE electrode exhibits the largest semicircle at the high-frequency range and followed by GO/GCE modified electrode. The diameter of semicircle changes drastically for rGO modified electrodes. The Nyquist plot for rGO@6h/GCE showed a decrease in the diameter of semicircle followed by rGO@24h/GCE as compared to bare GCE and GO/GCE. This is attributed to the enhanced electrode transfer on the surface of conductive graphene sheets

which provide better electrical contact as compared to others. The semicircle of rGO@12h/GCE was the smallest in the diameter with R_{ct} values close to zero due to its capability to accelerate the electron transfer between the redox probe and the electrode surface at a higher rate (Xi & Ming, 2012). The Randles equivalent circuit was used for fitting the impedance (inset of Figure 4.5 (B)). This circuit consists of R_s (resistance of the solution), R_{ct} (electron transfer resistance), W (Warburg element) and a CPE (constant phase element).

Figure 4.5 (B) shows the Bode plots of the phase angle versus frequency for the bare GCE, rGO@6h/GCE, rGO@24h/GCE and rGO@12h/GCE electrodes. Bare GCE electrode showed a sharp peak at the highest frequency that indicating higher R_{ct} value. However, the peak shifted to a lower frequency following the order of rGO@12h/GCE < rGO@24h/GCE < rGO@6h/GCE. This shows the lowering of the charge transfer resistance and increasing electrical conductivity. The values of the corresponding electron recombination lifetime, τ_n for rGO@6h/GCE, rGO@12h/GCE and rGO@24h/GCE were calculated as 178, 238 and 450 ms, respectively. These results demonstrate that rGO-Nf (16 h) has the longest electron recombination lifetime, which shows its application potential in electrocatalysis (Yeh et al., 2012).

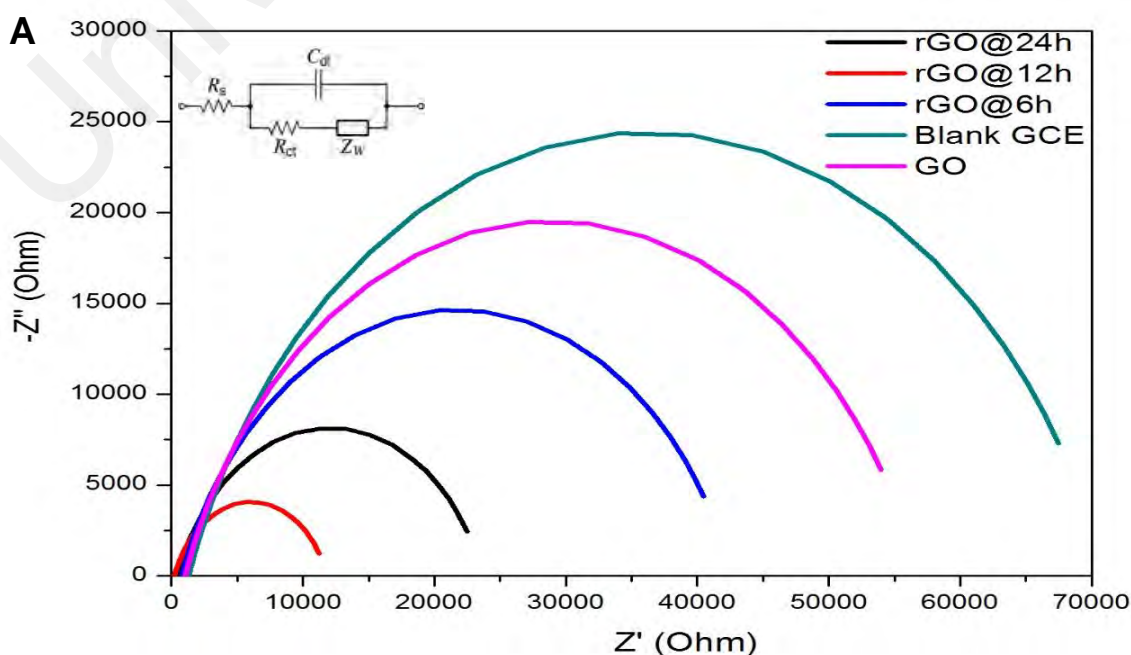


Figure 4.5, continued

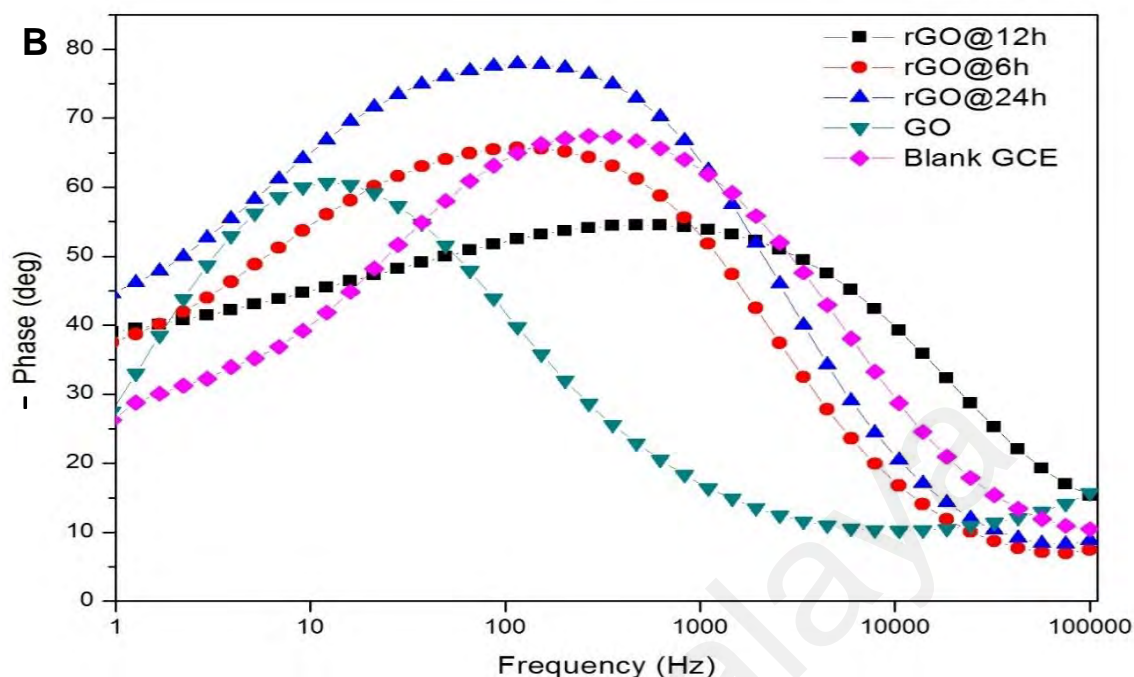


Figure 4.5. (A) Nyquist plots for bare GCE, rGO/GCE, rGO@6h, rGO@12h and rGO@24h nanomaterial at different reduction time (Inset shows the electrical equivalent circuit that fit the Nyquist plot of GC/rGO-Nf (16 h)), respectively. (B) Bode plots obtained for different modified electrodes.

4.5 Electrochemical detection of AA

4.5.1 Electrocatalytic oxidation of AA

The CV curves for rGO modified electrodes were recorded in the presence of AA to determine the best rGO (synthesized at various reaction time) nanomaterial-based sensor electrodes for the electrochemical detection of AA. The CV curves of bare GCE, GO/GCE, rGO@6h/GCE, rGO@12h/GCE and rGO@24h/GCE modified electrodes were recorded in a 0.1 M PBS (pH 6.5) solution containing 100 μ M AA at a scan rate of 100 mV/s and the results were shown in **Appendix A2**. Among all the electrodes that showing a pair of redox peaks at the potential of 0.2V, rGO@12h/GCE electrode exhibited excellent electrochemical response towards the oxidation of AA with the highest conductivity. The ΔE_p calculated for rGO@12h/GCE also showed the lowest

value which is 173 mV as compared to the other electrodes further confirms the enhanced electrocatalytic activity contributed by rapid electron transfer process on the surface of the modified electrode. Thus, the rGO@12h/GCE was chosen as the sensing electrode to further study the AA sensing.

The schematic of an electrocatalytic mechanism is shown in **Figure 4.6** to understand the electrochemical reaction process that occurs on the surface of the rGO/GCE electrode. The AA can be rapidly oxidized to DHA (dehydroascorbic acid) and it is an irreversible redox reaction due to the presence of two hydroxyl groups on its structure. Electrocatalytic oxidation only produces the anodic oxidation peak due to the donation of the electrons to the modified electrode (Huang, Chen, et al., 2011). The current response occurs due to the π - π stacking interaction between AA and graphene surface that accelerates the electron transfer on the surface of the graphene sheet (Dong-Fang et al., 2010). The rGO@12h/GCE modified electrode showed the highest current response toward the oxidation of AA as compared to the other modified electrodes due to the rapid electron transfer at the electrode/electrolyte interface. Moreover, the large surface area of rGO@12h also provides more electroactive sites for the adsorption of AA molecules. This will lead to an overall improvement of the electrical conductivity and electrochemical performance of this nanomaterial.

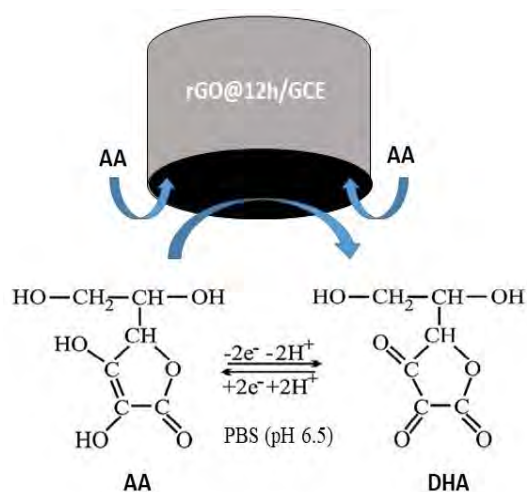


Figure 4.6. Schematic representation of detection of AA on the surface of rGO@12h/GCE electrode.

4.5.2 Optimization studies

The fabricated rGO synthesized at different reduction durations was optimized to obtain maximum sensing condition. All the results obtained from optimization studies were presented in **Appendix A**. Three important parameters have been optimized in this study. Firstly, the redox behavior of AA at different concentrations was studied using CV at a scan rate of 100 mV/s and DPV in 0.1 M PBS (pH 6.5). The electrochemical performance of rGO@12h/GCE modified electrode exposed to different concentrations of AA was investigated as shown in **Appendix A3 (A)**. In the CV plot, the peak currents were observed to increase linearly with increasing concentrations of AA from 10 to 100 μM . The linear relationship of electrochemical detection is depicted as follows (**Appendix A3 (B)**):

$$I = 0.412 (\pm 0.02) \mu\text{M} [\text{AA}] + 39.468 (\pm 0.81)$$

with the correlation coefficient of $R^2 = 0.95$, where I is the current density ($\text{A}\cdot\text{m}^{-2}$) and $\mu\text{M} [\text{AA}]$ is the logarithm of the AA concentration.

Secondly, the effect of various scan rates (10 to 100 mV/s) on the electrochemical performance of the rGO@12h/GCE modified electrode for AA detection was studied. **Appendix A4 (A)** shows the CV obtained at different scan rates. This redox process is surface-confined. The anodic peak shifted positively with good linearity between the peak current at increasing scan rate as shown in **Appendix A4 (B)**. The anodic and cathodic peak currents exhibited linear equations of $I = 0.099 (\pm 0.01) V + 0.882 (\pm 0.09)$ and $I = -0.096 (\pm 0.03) V + -1.053 (\pm 0.11)$ with correlation coefficient of $R^2 = 0.972$ and 0.984 , respectively. This proves that the direct electron transfer between the rGO@12h/GCE and AA was controlled by an adsorption process (Dessie *et al.*, 2014).

Finally, the loading amount of rGO@12h on the GCE electrode was optimized to obtain optimal sensor performance. The CV of different amount of rGO@12h loaded onto

the electrode are shown in **Appendix A5 (A)** and **(B)**. The current density was observed to increase with increasing loading amount (from 1 to 7mg/mL) of rGO@12h and achieved maximum current at 7mg/mL. The increasing amount of rGO@12h of GCE increases the overall active surface area for AA oxidation. However, the peak current reduced drastically at loading amount more than 7mg/mL. This is due to a blockage caused by a thick layer formed on the surface of the electrode that inhibits the electron from reaching the electrode and thus lowering its sensitivity. Thus, 7mg/mL of rGO@12h was used as an optimum loading amount throughout the study.

4.2.3 Reproducibility and shelf life of the modified electrode.

The reproducibility of the rGO@12h/GCE modified electrode in the Zobel's solution was evaluated by recording the CV curves of five freshly prepared electrodes (**Appendix A6 (A)**). The result revealed that the modified electrode showed good reproducibility with a relative standard deviation (RSD) of 3.92 %. The shelf life of the prepared electrode was investigated by measuring the current density up to 21 days (**Appendix A6 (B)**). The electrode exhibited approximately 95% recovery with a 10% loss of the signal on day 21. This result clearly indicates that the rGO@12h is a promising nanomaterial with good stability to use for fabrications of the electrode.

4.6 Summary

In conclusion, a stable rGO nanomaterial was formed through a simple chemical reduction of GO using a reducing agent. The TEM study showed successful production of nanosized rGO sheets with an average size of ~ 2.24 nm. The effect of the chemical reduction reaction time on the formation of rGO nanomaterials was studied and the results revealed that rGO produced at 12h (rGO@12h) of reaction time formed more uniformly with the excellent electrochemical property as compared to rGO@6h and rGO@24h that tend to agglomerate and possess low conductivity. Under optimized conditions, rGO@12h/GCE modified electrode exhibited excellent electrochemical detection of AA with a lower detection limit of about $1.64 \mu\text{M}$. This proves that the rGO@12h nanomaterial achieved an optimal degree of reduction with low surface defects which contributes to the increased electrocatalytic activity and improved the sensing performance. This result indicated that, the chemical reduction time in producing rGO is important to obtain conductive material with good electrochemical property, thus the reduction time of rGO was maintained to 12h throughout this research. Moreover, the synthesized rGO@12h nanomaterial also showed good reproducibility and high stability which possess great potential for biosensor applications.

CHAPTER 5

REDUCED GRAPHENE OXIDE-NANOCOMPOSITE MODIFIED ELECTRODE FOR ELECTROCHEMICAL DETECTION OF THE FOODBORNE PATHOGEN

5.1 Reduced Graphene Oxide-Azophloxine nanocomposite electrochemical aptasensor for *Salmonella enterica* detection.

5.1.1 Overview

A novel and simple strategy using a new conductive layer consisting of rGO-Azophloxine (AP) nanocomposite as the sensing platform for the detection of the foodborne pathogen. *S. Typhimurium* was used as the test organism in this study. The rGO concentration was fixed but the AP dye concentration that modified the graphene surface was optimized to obtain the best sensing performance.

The GO with abundant oxygen groups can be easily functionalized with AP dye to form GO-AP composite *via* simple non-covalent π - π interactions and non-covalent coupling reactions. Non-covalent functionalization is advantageous compared to covalent modifications because the functional groups will be introduced into graphene without affecting its structure and electronic network so that the novel properties of graphene are retained (Bai & Shen, 2012). The structure of the AP dye is shown in **Figure 5.1**. A single AP molecule possesses two hydrophilic sulfonates ($-\text{SO}^{3-}$) functional groups. Previous studies have shown that the dispersibility of GO in aqueous solutions increased when GO was functionalized with $-\text{SO}^{3-}$ -containing compounds e.g. sulfonic acid and 4-hydrazinobenzenesulfonic acid (Qiao, Xu, Qiu, Xiao, & Zhu, 2016; Yeo et al., 2014). Hence, the aromatic AP dye applied in this study could effectively exfoliate or solubilize GO nanosheets in water due to the presence of polar $-\text{SO}^{3-}$ functional group. With the aid

of hydrazine, the GO-AP can be reduced (12h of reduction time) to rGO nanosheets functionalized with negatively charged electroactive dye AP via π - π stacking interaction (rGO-AP). The electrostatic repulsion caused by the negative charge on the rGO-AP surface and the hydrophobic aromatic backbone of AP dye stacked on the rGO surface also function to overcome the aggregation of rGO in aqueous solutions (Guo, Han, et al., 2013; Schlierf et al., 2013). Moreover, the water-soluble rGO-AP nanocomposite formed a stable thin film on GCE by drop-casting and DNA aptamer can immobilize on the rGO-AP/GCE easily through π - π interactions between nucleotide bases of DNA and rGO-AP surface (Wang, Xu, et al., 2012) which is denoted as ssDNA/rGO-AP/GCE.

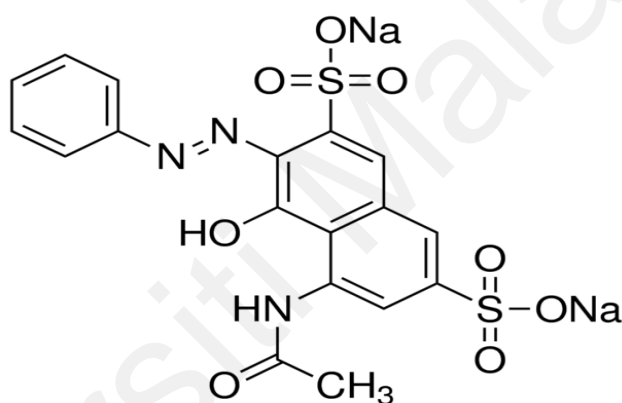


Figure 5.1. The chemical structure of Azophloxine dye

The novelty of this study is the chemical doping of rGO with electroactive AP dye enriches its free charge-carrier density, thus potentially enhancing its solubility in hydrophilic medium and electrical conductivity. It also eliminates the complex and expensive process of labeling and modification of aptamers. In addition, this electrochemical biosensor was designed by using label-free aptamers as linkers that specific to an outer membrane protein of *S. Typhimurium*. This approach is a promising, cost-effective approach and allows the rapid detection of food-borne pathogens in the food matrix. Nevertheless, there have been only a few studies on the development of rGO-

organic dye nanocomposites as biosensors and their potential as aptasensors has not been fully explored.

5.1.2 Structural and morphological characterization of rGO-AP nanocomposite.

FTIR spectra were used to identify the functional groups present in the rGO-AP film. **Figure 5.2 (A)** shows the FTIR spectra of AP, rGO, rGO-AP@0.002M, rGO-AP@0.005M and rGO-AP@0.01M. In the rGO sample, all the peaks corresponding to oxygen-containing groups were weakened and disappeared. These phenomena clearly illustrated that oxygen functional groups such as C=O stretching, C–O–C stretching, C–O stretching, and hydroxyl groups were mostly removed and became rGO during the chemical reduction process using hydrazine. In addition, the C=C conjugation at 1560 cm^{-1} was detected on the rGO sample due to the sp^2 hybridization. Meanwhile, a disappearance of the peak intensity of the O–H group in the rGO sample at 3300 cm^{-1} was observed and approached zero when the AP was fully attached to the rGO. The main reason might be attributed to the implementation of the rGO formation process for easy elimination of hydroxyl groups from the carbon basal plane and simple transformation to rGO monolayer during the attachment of the AP stage. Besides, the AP spectra also exhibited ring vibrations at 521, 600 and 694 cm^{-1} from the FTIR pattern which is in agreement with a previous report (Guo, Guo, et al., 2013). For three rGO-AP spectra, it could be noticed that all the ring vibrations of AP were visible at 533, 600 and 734 cm^{-1} . Interestingly, C-O/O-H stretching of rGO was found within the rGO-AP nanocomposite sample at 1025 and 1166 cm^{-1} followed by the bending vibration of C-H/O-H stretching at 1429 cm^{-1} . In addition, the presence of significant C=O stretching vibration (1560 cm^{-1}), C-H stretching vibration (2855 cm^{-1}) and N-H stretching vibration (3700 cm^{-1}) further to infer that the attachment of AP dyes on rGO sheet. The intensity of the AP dye characteristic peaks in the rGO-AP nanocomposite varies with the increasing concentration of the AP dye.

The Raman spectroscopy helps to characterize disorder and defects in carbon-based materials. **Figure 5.2 (B)** shows Raman scattering spectra of AP, rGO, rGO-AP@0.002M, rGO-AP@0.005M and rGO-AP@0.01M. In three nanocomposites, the broad D at G band observed at around 1350 and 1590, respectively which is the signature peaks of carbon. rGO shows two significant in-phase vibrations in 1349 (D-band) and 1593 (G-band) for rGO and. The D-band indicates the presence of a disorder or structural defects in sp^2 -hybridized carbon systems whereas, the G band obeys the first-order scattering of E_{2g} phonons due to the presence of sp^2 -hybridized carbon. The I_D/I_G ratio was used to measure structural disorder occurs during the removal of oxygen groups attached to GO and size of sp^2 ring clusters in a sp^3/sp^2 hybrid network of carbon atoms. The I_D/I_G ratio of rGO is about 0.96. The surface functionalization of rGO with AP dye causes a decrease in the I_D/I_G ratio. The presence of lower intensities D and G band after the functionalization indicates the recovery of conjugated graphitic domains of functionalized graphene surface with lesser defects and preserved the crystalline structure. Interestingly, the three rGO-AP nanocomposites spectra not only exhibits the G and D band, but also contain the bands of AP such as band N=N stretching vibrations (1406 cm^{-1}) of azo compound, C-N symmetric stretch (1111 to 1208 cm^{-1}), very strong aromatic quadrant stretch (1594 cm^{-1}), azo-benzene ring vibration (1489 cm^{-1}), phenyl-N vibration (1280 cm^{-1}), C-C stretching (1208 cm^{-1}) and a weak band of $-SO^3$ groups (1172 cm^{-1}) indicating the successful attachment of AP with rGO (Cesaratto, Centeno, Lombardi, Shibayama, & Leona, 2017; Vandenabeele, Moens, Edwards, & Dams, 2000). However, the I_D/I_G ratio of rGO-AP@ $4\mu\text{M}$, rGO-AP@ $8\mu\text{M}$ and rGO-AP@ $12\mu\text{M}$ were different and increases with increasing concentration of AP dye. This is because the surface functionalization of AP on the rGO surface leads to an increase in the surface defects on the nanocomposite materials.

The X-ray diffraction (XRD) analysis was performed to confirm the formation of the rGO-AP nanocomposite. The XRD patterns of rGO and rGO-AP were shown in **Figure 5.2 (C)**. The rGO-AP showed a broad characteristic peak at 26° which corresponds to the (002) crystalline plane (Khan et al.,2015). These results indicate the presence of rGO in the nanocomposite. Moreover, XRD also exhibited some peaks at 13° which were assigned to the crystalline scattering of the AP dye that relates to the presence of thiazole ring (Bauman, Fan, & Haase, 1989). These peaks confirm the formation of rGO-AP.

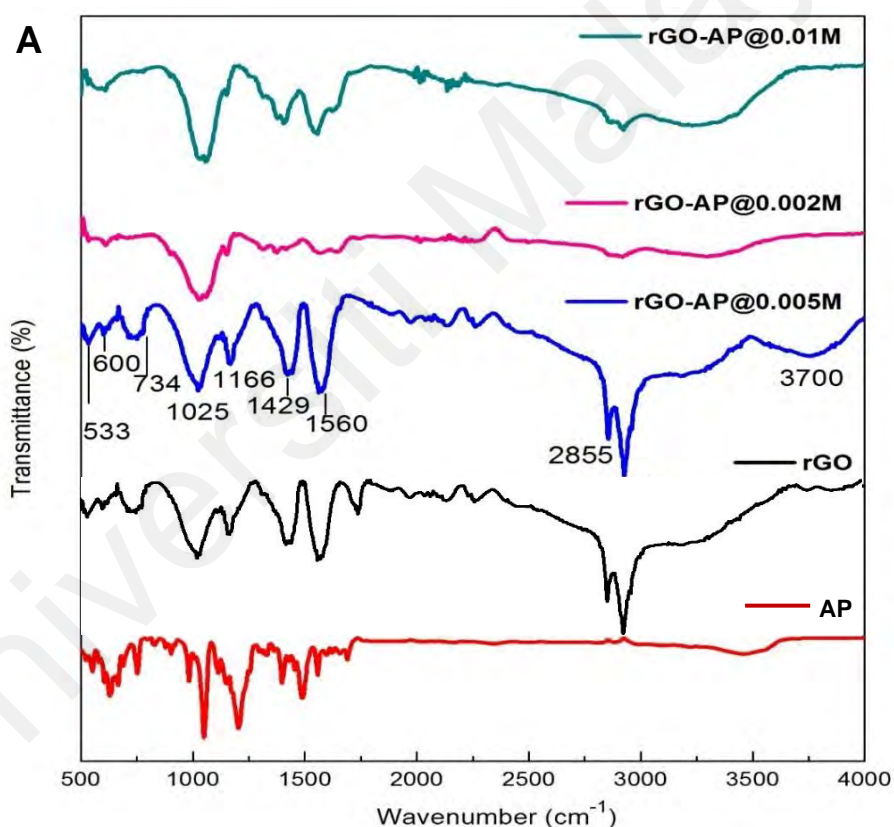


Figure 5.2, continued.

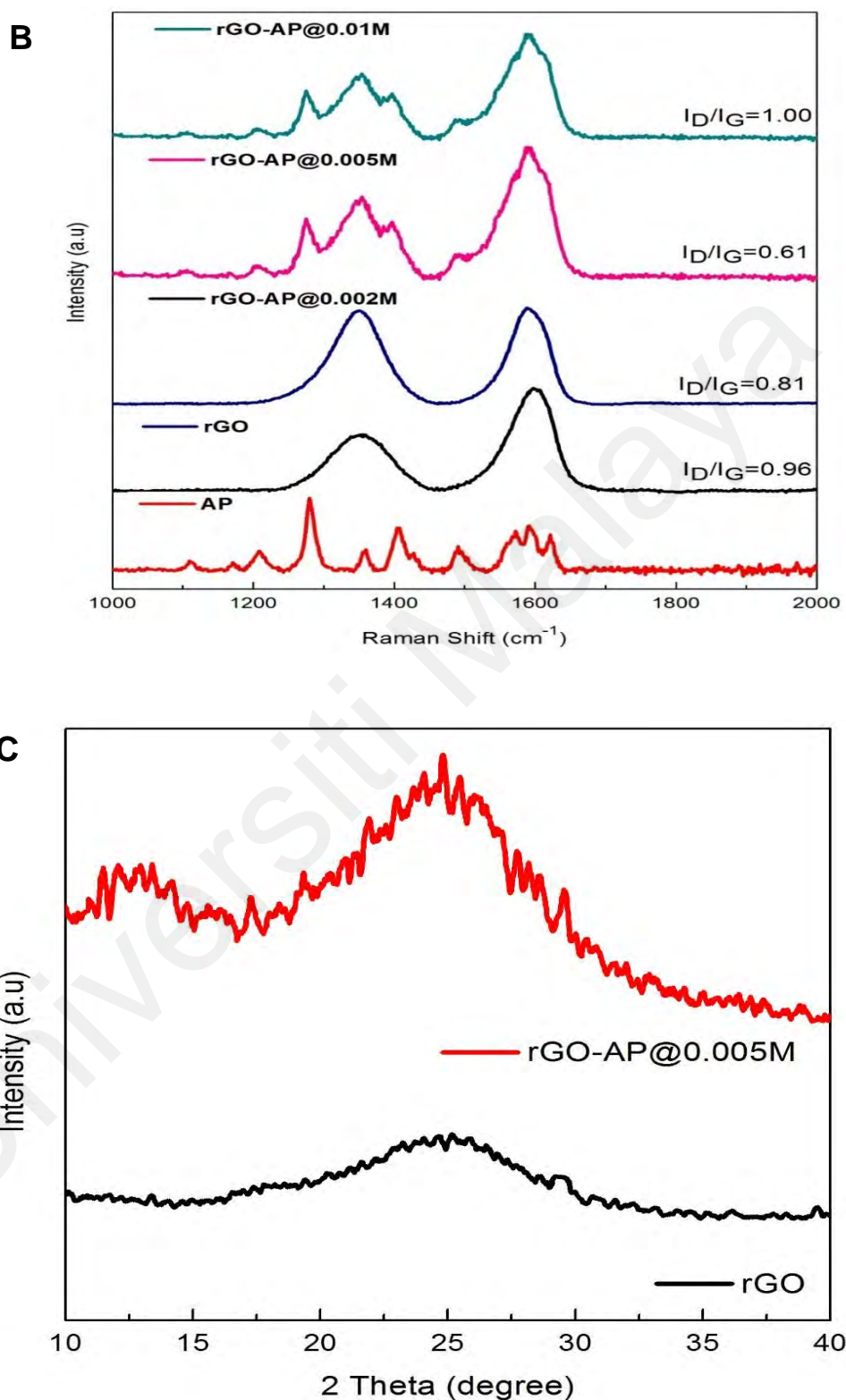


Figure 5.2 (A). The FTIR spectra of AP, rGO, rGO-AP@0.002M, rGO-AP@0.005M and rGO-AP@0.01M. **(B)** Raman spectra of AP, rGO, rGO-AP@0.002M, rGO-AP@0.005M and rGO-AP@0.01M. **(C)** The XRD spectra of rGO and rGO-AP.

The structure and morphology of the rGO-AP nanocomposite functionalized with different concentrations of AP were investigated by SEM and TEM. **Figure 5.3 (A)** shows the SEM image of (a) rGO, (b) rGO-AP@0.002M, (c) rGO-AP@0.005M and (d) rGO-AP@0.01M. The rGO appeared with less stacking and rich in the wrinkled structure of few-layer rGO nanosheets with irregular folding (Choi, Kim, Han, Kim, & Gurunathan, 2016). The well-formed AP nanoparticles covering the surface of rGO can be observed in three nanocomposites. A sheet-like morphology of rGO-AP distributed uniformly throughout the surface was observed in SEM micrographs. The synthesized rGO-AP composite showed tissue-like layers under 50 μm magnification.

Figure 5.3 (B) shows the TEM images of the rGO and three rGO-AP nanocomposites. The TEM image of (b) rGO-AP@0.002M showed no obvious difference as compared to TEM of rGO because the concentration of the AP dye loaded on the graphene surface might be too less. But, rGO-AP@0.005M and (d) rGO-AP@0.01M exhibited a uniform nanocomposite structure with some multiple folds of rGO nanosheets and the globular structure was distributed throughout the nanosheets which imply the presence of AP dye on the rGO surface. However, rGO-AP@0.01M showed densely decorated AP on the rGO surface. This could create more defects on the graphene sheet due to the creation of many nucleation sites that allow nanoparticle attachment (Torres-Mendieta et al., 2016). A higher degree of defects affects the delocalization of π -electron in graphene and hence reduces its electrical conductivity (Kumar et al., 2018). Whereas, the TEM of rGO-AP@0.005M shows a uniform distribution of AP on graphene sheets corresponding to the boxed area under higher magnification. The average thickness of the rGO-AP@0.005M sheet measured using TEM was about 10 nm. The SEM data were consistent with the TEM images and confirm the successful functionalization of AP dye molecules on the rGO surface.

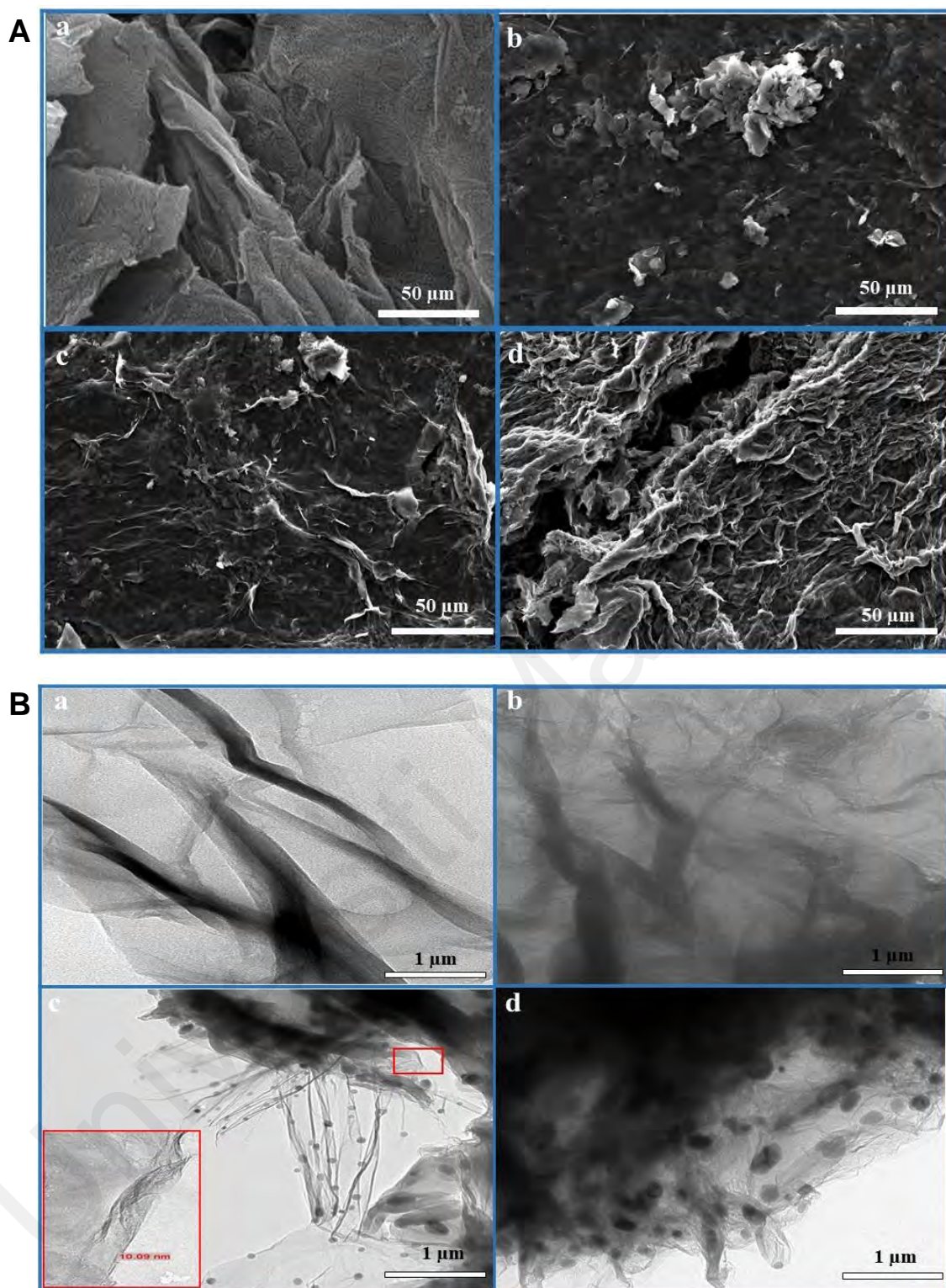


Figure 5.3 (A). The SEM of (a) rGO, (b) rGO-AP@0.002M, (c) rGO-AP@0.005M and (d) rGO-AP@0.01M. **(B)** The TEM of (a) rGO, (b) rGO-AP@0.002M, (c) rGO-AP@0.005M and (d) rGO-AP@0.01M. The inset in (b) shows the rGO-AP@0.005M in high magnification with 10.09 nm thickness.

5.1.3 Electrochemical characterization of rGO-AP modified GCE electrode

The electrochemical behavior of the rGO-AP nanocomposite modified GCE electrodes was investigated and compared. The CV and EIS analytical techniques were used to electrochemically characterize rGO-AP@0.002M/GCE, rGO-AP@0.005M/GCE and rGO-AP@0.01M/GCE electrodes. **Figure 5.4 (A)** shows the comparative CV behavior of the bare GCE, rGO/GCE and three rGO-AP nanocomposite modified electrodes in 0.1M PBS (6.5) at scan rate 100 mV/s. All the CV plots exhibited a well-defined reversible redox peak. The rGO-AP@0.002M/GCE exhibited the lowest conductivity because of insufficient concentration of AP led to low kinetics of electron transfer. Whereas, the rGO-AP@0.005M/GCE showed the highest current response due to the enhanced and rapid electron transfer at the electrode-electrolyte interface. However, at the highest concentration of AP, the current response of rGO-AP@0.01M/GCE decreases as compared to rGO-AP@0.005M/GCE. This is due to the high level of surface defects created by the AP dye's functional groups within the carbon lattice on the functionalized graphene. Optimal levels of defects on the graphene surface were proved to increase the overall conductivity of the material due to its metallic behavior around the vacancy defects (Jafri et al., 2010). However, excessive amount of defects drastically affect the overall electron transfer kinetics and reduces the electrochemical activity of graphene-based electrodes (Punckt, Pope Michael, Liu, Lin, & Aksay Ilhan, 2010).

The charge transfer resistance of the rGO-AP was also studied using EIS in Zobell's solution. **Figure 5.4 (B)** shows the Nyquist plot of Bare GCE, rGO/GCE and rGO-AP nanocomposite modified electrodes. The diameter of the semicircle reflects the charge transfer resistance (R_{ct}) value of the electrodes and the inclined straight-line attributes to the impedance created by the diffusion of the ions through the graphene sheets (Yusoff et al., 2015). The largest semicircle is shown by the bare GCE and followed by rGO/GCE. When the rGO is functionalized with AP, the R_{ct} value and

diameter of the circle decreases drastically. The decrease in R_{ct} value represents increased electron transfer kinetics and decreased charge transfer resistance. The R_{ct} value decreased in following the order of bare GCE > rGO/GCE > rGO-AP@0.002M/GCE > rGO-AP@0.01M/GCE > rGO-AP@0.005M/GCE. Among the three nanocomposites, rGO-AP@0.005M/GCE possesses the lowest R_{ct} value. The inset shows the electrochemical equivalent circuit rGO-AP@0.005M/GCE which consists of electrolyte resistance (R_s), charge transfer resistance (R_p), Warburg impedance (Z_w) and constant phase element (CPE). The CPE depicts the non-ideal capacitance of the surface layer, while Z_w accounts for the diffusion of ions from the bulk electrolyte to the electrode interface.

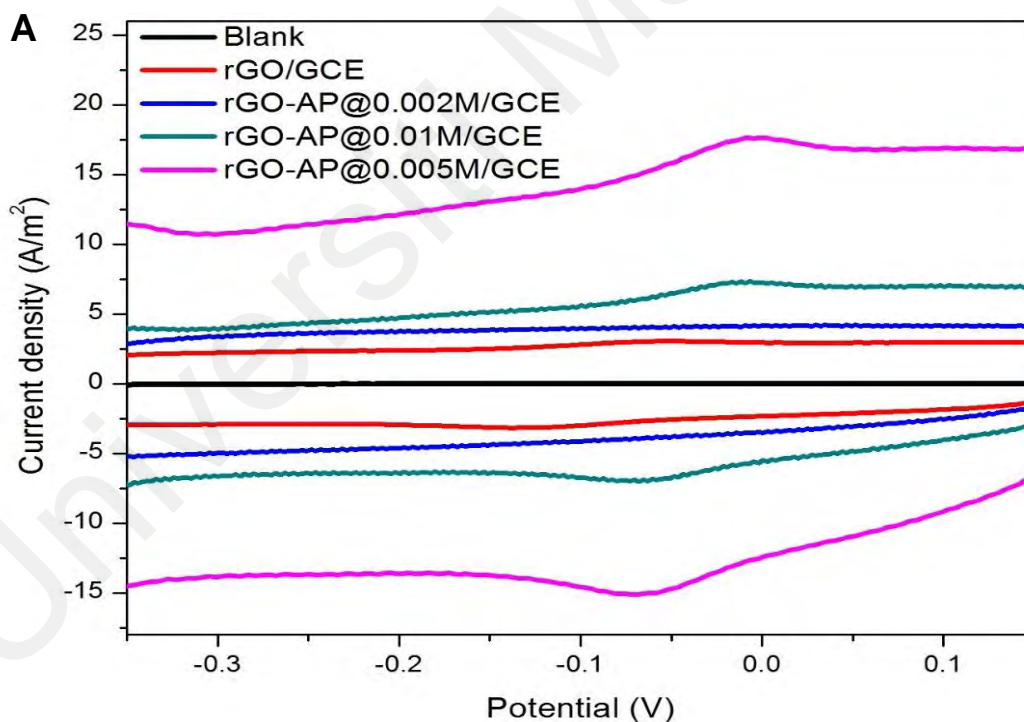


Figure 5.4, continued.

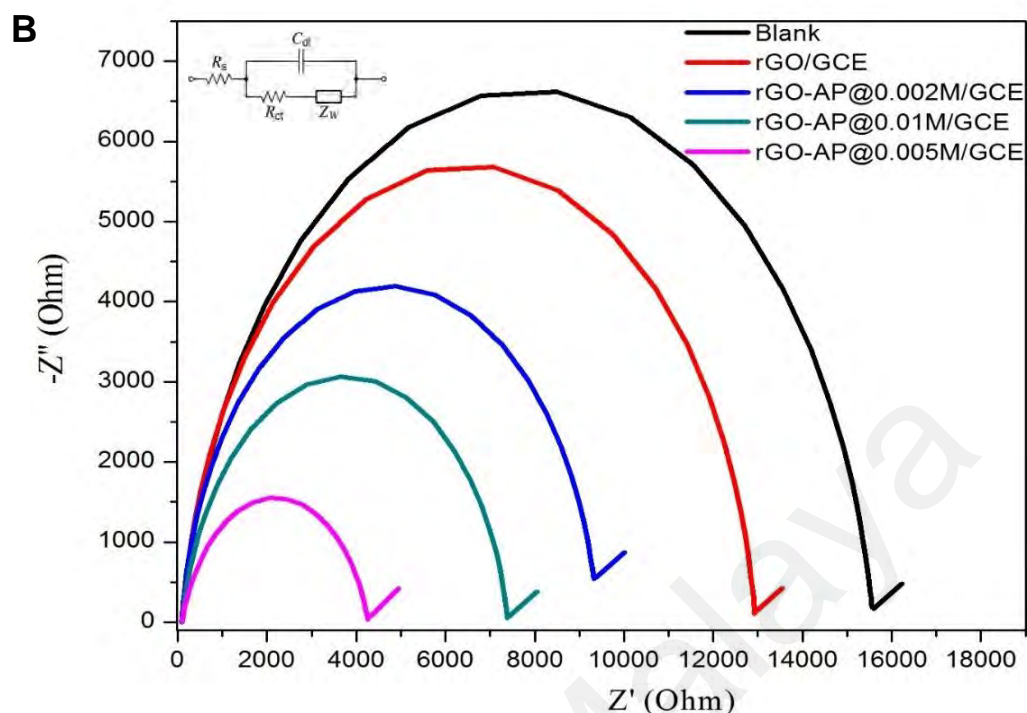


Figure 5.4. (A) CV and (B) Nyquist plots for bare GCE, rGO/GCE, rGO-AP@0.2M/GCE, rGO-AP@0.4M/GCE and rGO-AP@0.6M/GCE electrodes.

5.1.4 Electrochemical detection of *Salmonella* using rGO-AP nanocomposite modified electrode

5.1.4.1 Optimization of rGO-AP@0.005M/GCE

To obtain maximum sensing condition of rGO-AP@0.005M/GCE platform, three important parameters have been optimized in this study, namely rGO-AP@0.005M loading, the concentration of aptamer and the effect of various scan rate. The effect of the rGO-AP@0.005M amount loaded on GCE plays an important role to achieve the maximum number of electrochemical signals as shown in **Appendix B1 (A)**. The current density increased from 8 A m^{-2} to 17 A m^{-2} with the increasing rGO-AP@0.005M loading and achieved maximum peak current at 3 mg mL^{-1} . This could be due to the formation of a thicker film of rGO-AP@0.005M nanocomposite ($> 3 \text{ mg mL}^{-1}$) which blocked the

electrical conductivity (Guo, Guo, & Dong, 2013). The stock solution of the aptamer was diluted serially and then tested. The optimum current density was obtained for aptamer concentration of $5 \mu\text{mol L}^{-1}$ which is shown in **Appendix B1 (B)**. At higher concentrations of aptamer, the peak current dropped drastically due to the electrostatic repulsion created by negatively charged DNA molecules (Liu, Tuleouva, Ramanculov, & Revzin, 2010). The incubation time with the bacterial suspension was also investigated. As shown in **Appendix B1 (C)**, the electrochemical signal achieved a maximum current after 5 min incubation time with the bacterial cell suspension. The peak current decreased dramatically after 5 min of incubation which may be due to the saturation effect caused by bacterial cells blocking the current flow, leading to the decrease in electron transfer efficiency. Finally, the effect of various scan rate (10-100 mV/s) on the conductivity of the working electrode was investigated using CV. **Appendix B1 (D)** shows that the peak current increased with increasing scan rates which indicates increased electron transfer. A linear relationship ($I = 0.164V + 6.447$, $R_2=0.993$) could be depicted from the peak currents obtained at various scan rates as shown in **Appendix B1 (E)**, showing the redox process is surface-confined.

5.1.4.2 Electrochemical analysis of rGO-AP@0.005M/GCE

CV study was used to study the conductivity of rGO-AP@0.005M/GCE under optimized conditions. **Figure 5.5 (A)** shows the cyclic voltammograms of bare GCE, rGO/GCE, rGO-AP@0.005M/GCE and ssDNA/rGO-AP@0.005M/GCE electrodes in 10X PBS (pH 7.0) at the scan rate of 100 mV s^{-1} . Redox peaks were absent in bare GCE and rGO/GCE, but a pair of redox peaks were observed for rGO-AP@0.005M/GCE electrode which proved the redox reaction of AP dyes on the rGO surface. The AP dye has an innate electroactive property, thus its attachment on the rGO surface will increase the overall conductivity of the sensing platform. This AP dye also enhances a smoother

flow of electrons on the rGO surface (transducer) to the electrolyte attributing increased in peak current (Guo, Guo, et al., 2013). However, subsequently, the increase in peak current was observed for ssDNA/rGO-AP@0.005M/GCE electrode after the aptamer immobilization due to the doping effect (direct charge transfer) between the adsorbed aptamer and rGO. Moreover, the high electron transferability nature of rGO (Grumezescu, 2016) also decreases the charge transfer resistance after the DNA hybridization and increases the overall ionic conductance of the sensing platform (Johnson, Johnson, & Klein, 2008; Wang, Xu, et al., 2012).

Figure 5.5 (B) shows the DPV signals of bare GCE, rGO/GCE, rGO-AP@0.005M/GCE, ssDNA/rGO-AP@0.005M/GCE and STM/ssDNA/rGO-AP@0.005M/GCE electrodes in Tris-HCl buffer. The AP dye oxidized at -0.08 V indicating the interaction between ssDNA and bacterial cell. The oxidation peak was absent in bare GCE electrode whereas, upon the functionalization of AP dye on rGO surface (rGO-AP@0.005M/GCE), a sharp increase in peak current was observed. The oxidation peak current at -0.08 V further increased with the immobilization of aptamer on the sensing platform (ssDNA/rGO-AP@0.005M/GCE) due to the specific interaction of nucleobases of ssDNA with rGO-AP@0.005M, increasing the electron flow across the electrolyte and contributing to higher peak current. However, binding of the target bacteria with respective aptamers caused a dramatic decline in peak current of the sensing platform STM/ssDNA/rGO-AP@0.005M/GCE, indicating the hybridization event on rGO-AP@rGO-AP@0.005M/GCE sensing platform. The attachment of bacterial cells on the electrode surface will block the electron transfer process from the redox species (AP dye) resulting in the increase in resistance and subsequent decrease in current. The results obtained from the DPV analysis were consistent with the CV studies.

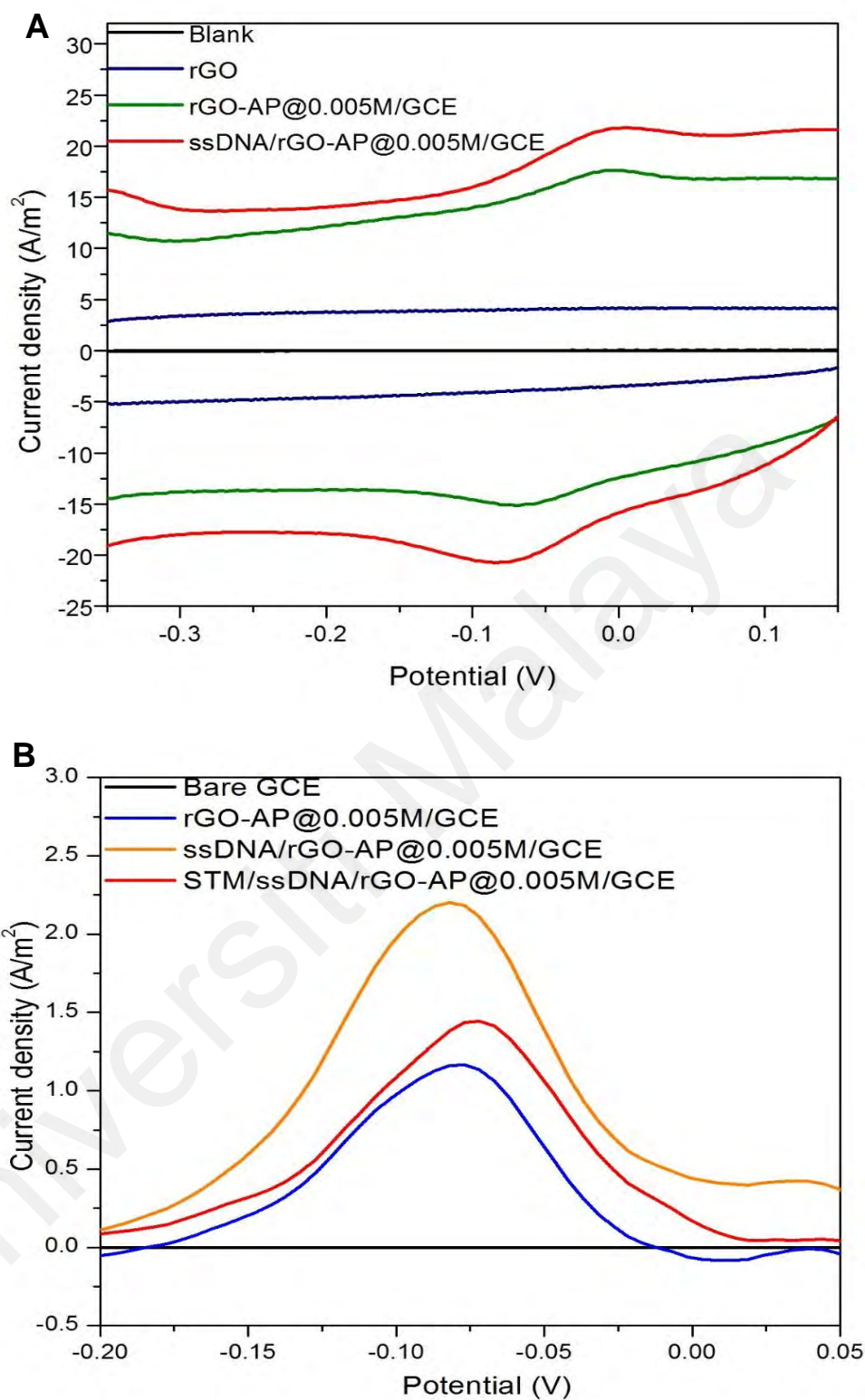


Figure 5.5 (A) CV of bare GCE, rGO/GCE, rGO-AP@0.005M/GCE and ssDNA/rGO-AP@0.005M/GCE electrodes in 10X PBS (pH 7.0) at the scan rate of 100 mV s⁻¹. (B) DPV signal of bare GCE, rGO-AP@0.005M/GCE, STM/ssDNA/rGO-AP@0.005M/GCE and ssDNA/rGO-AP@0.005M/GCE electrodes in Tris-HCl buffer, pH 7.4.

5.1.4.3 Electrochemical detection of bacterial cells using ssDNA/rGO-AP@0.005M/GCE

The sensitivity and selectivity of the fabricated electrodes were conducted using DPV detection technique in Tris-HCL buffer with controlled instrumental parameters (pulse amplitude: 0.025 V, pulse width: 0.05 s and pulse period: 0.05 s). The ssDNA/rGO-AP@0.005M/GCE electrode was incubated for 5 min in serially diluted *S. Typhimurium* (STM) suspensions ranging from 10^1 – 10^8 cfu mL⁻¹ for selectivity test and to different types of non-*Salmonella* bacteria namely *V. cholerae*, *Sh. dysenteriae*, *E. coli*, *K. pneumoniae* and *Staph. Aureus* at concentration of 10^2 cfu mL⁻¹ for selectivity test, respectively. After the incubation, the electrodes proceeded to DPV measurements.

In the sensitivity test, the changes in the DPV signal of the working electrodes in the presence and absence of bacterial cells were investigated. **Figure 5.6** (A) shows the sensitivity test of ssDNA/rGO-AP@0.005M/GCE electrode to different concentrations of bacteria cell suspensions. The DPV signal was obtained using Tris-HCl buffer. As shown in **Figure 5.6** (A), the highest oxidation peak was obtained for the ssDNA/rGO-AP@0.005M/GCE as compared to the rGO-AP@0.005M/GCE and this indicates the hybridization event of the aptamer on rGO surface. However, when the sensing platforms were incubated in Tris-HCl buffer solutions containing a different concentration of *S. Typhimurium* for 5 min, the peak current decreased dramatically. This can be due to the conformational change between the aptamer and bacterial cell causing a decrease in adsorption of aptamer on the rGO surface, resulting in changes in the charge transfer (Gedi & Kim, 2014; Liu, Morris, Macazo, Schoukroun-Barnes, & White, 2014). Moreover, the attachment of bacterial cells on the sensing electrode surface will block the electron transfer process from the redox molecule (AP) due to steric hindrance created by the bulky negatively charged bacterial cell, leading to an increase in electron transfer resistance and contributing to lower oxidation peak current (Labib et al., 2012). The

natural properties of the bacterial cell membrane which is its membrane capacitance ($0.5\text{--}1.3 \mu\text{F cm}^2$) and membrane resistance ($10^2\text{--}10^5 \Omega \text{ cm}^2$) contribute to the steric hindrance (Pethig, 1985; Wang, Ye, & Ying, 2012).

The peak current increased with the increasing complementary target concentration, exhibiting a limit of detection up to 10^1 cfu mL^{-1} . The logarithm relationship between the target bacterial concentration and oxidation peak current is plotted (**Figure 5.6 (B)**) and the linear relationship is described as:

$$I = 0.10 (\pm 0.01) \log c + 1.35 (\pm 0.15)$$

With the correlation coefficient of $R^2 = 0.98$, where I is the current density (A m^{-2}) and $\log c$ is the logarithm of the target bacterial cell concentration. The increase in peak current was proportional to the increase in target cell concentration due to the conductivity of the bacterial cell membrane and cytoplasm. The conductivity of the bacterial cell membrane is approximately 10^{-7} S m^{-1} whereas, the conductivity of the interior of a cell can be as high as 1 S m^{-1} due to the presence of charged molecules in the cytoplasm (Pethig & Markx, 1997). When the concentrations of bacterial cells increased, the number of cells packed densely on the electrode surface increased. This will lead to the formation of a conductive channel by the negatively charged bacterial cell membranes and increases the current flow (Settingington & Alocilja, 2012). Similarly, the increase in conductance of rGO was also due to the change in the electron or hole density created by the high negativity walls of the bacteria on the p-type rGO surface (Akbari, Buntat, Afroozeh, Zeinalinezhad, & Nikoukar, 2015).

The selectivity to determine aptasensor's ability in distinguishing the *S. Typhimurium* and the non-*Salmonella* bacterial cell was also studied. The selectivity test is shown in **Figure 5.6 (C)**. The DPV data showed that the aptamer was only specific for *S. Typhimurium* as compared to other foodborne bacteria namely *E. coli*, *Sh. dysenteriae*,

V. cholerae and *K. pneumoniae*. The redox peaks were visible in all bacterial cultures due to the presence of electroactive dye AP and conductivity of their cell membranes. However, all the current peaks except for *S. Typhimurium* were below the detection limit of the biosensor.

Overall, the comparison of the performances of a well-established DNA based method of detection and aptasensor is summarized in **Table 5.1**. This comparison shows that the developed rGO-AP aptasensor exhibits high sensitivity with improved detection limits and allows the rapid detection of *Salmonella*.

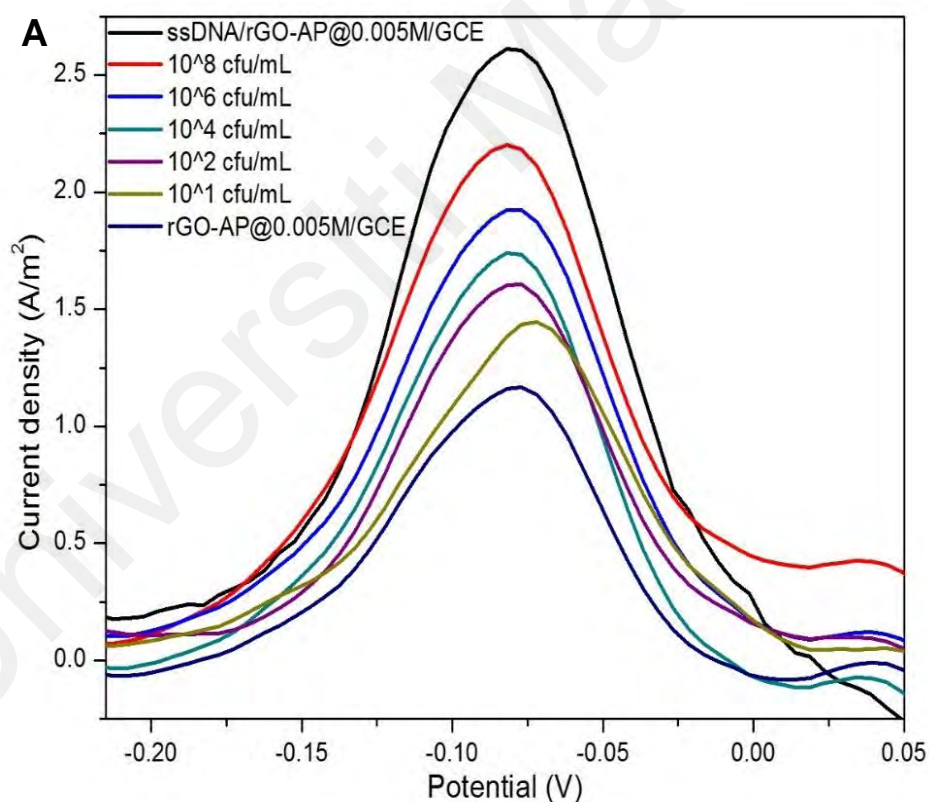


Figure 5.6, continued.

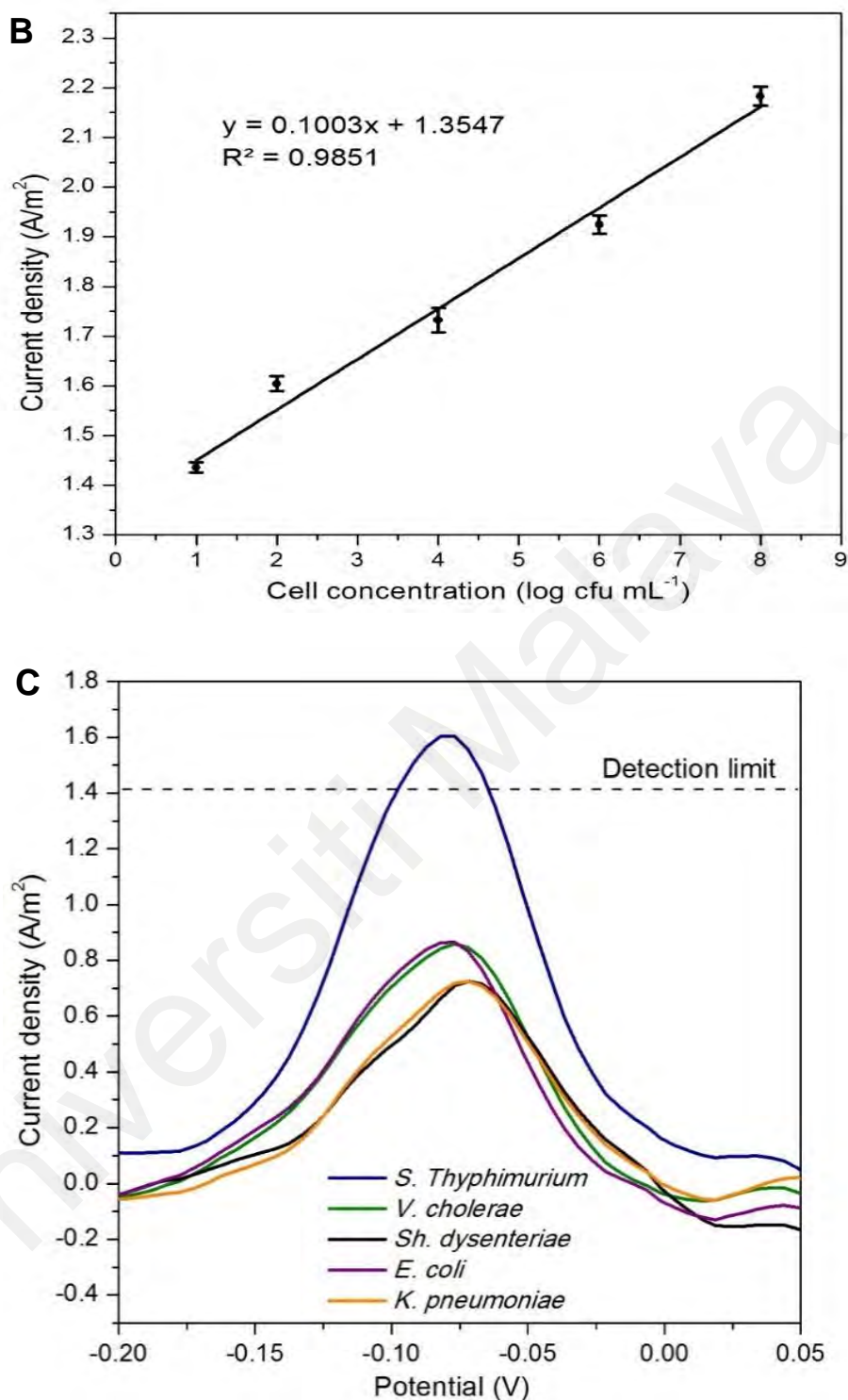


Figure 5.6. (A) DPV of ssDNA/rGO-AP@0.005M/GCE, (b) 10^8 cfu mL^{-1} , (c) 10^6 cfu mL^{-1} (d) 10^4 cfu mL^{-1} , (e) 10^2 cfu mL^{-1} , (f) 10^1 cfu mL^{-1} and (g) rGO-AP@0.005M/GCE in Tris-HCl buffer, pH 7.4. (B) A linear relationship between the current density and cell concentration (logarithm). (C) DPV of *S. Typhimurium*, *E. coli*, *V. cholerae*, *K. pneumoniae* and *Sh. dysenteriae* in Tris-HCl buffer, pH 7.4.

Table 5.1. The comparison of biosensor developed in this study with other detection methods

Method used	Targeted bacteria	Limit of detection	Assay time	Detectable range in food	Ref
Multiplex-PCR	<i>Salmonella</i> spp.	10^3 cfu mL ⁻¹	3 h	10^3 cfu mL ⁻¹	(Wang, Li, & Mustaphai, 2007)
Quantitative PCR	<i>Salmonella enterica</i>	5×10^2 cfu mL ⁻¹	3 h	7×10^2 cfu mL ⁻¹	(Wolffs, Glencross, Thibaudeau, & Griffiths, 2006)
LAMP	<i>Salmonella</i> spp.	10^2 cfu mL ⁻¹	3 h	6.1×10^3 cfu mL ⁻¹	(Chen, Wang, Beaulieu, Stein, & Ge, 2011)
NASBA	<i>S. Enteritidis</i>	10^1 cfu mL ⁻¹	18 h	10^1 cfu/25 g	(D'Souza & Jaykus, 2003)
Immunoassay	<i>S. Typhimurium</i>	10^3 cfu mL ⁻¹	2 h	10^3 cfu mL ⁻¹	(Wu, Li, et al., 2014)
Amperometric aptasensor	<i>S. Typhimurium</i>	10^1 cfu mL ⁻¹	10 min	10^1 cfu mL ⁻¹	This work

5.1.4.4 Evaluation of the ssDNA/rGO-AP@0.005M/GCE in a food sample.

This aptasensor system was tested with chicken meat homogenates (n=6) that contaminated with *S. Typhimurium*. The DPV signals were recorded in Tris-HCl buffer. The measured DPV signal exhibited increased peak currents corresponding to the increase in target cells as shown in **Figure 5.7**. This aptasensor could detect bacterial concentration ranging from 10^1 to 10^4 cfu mL^{-1} present natural food sample. However, 2 out of 6 samples did not show any current response indicating the absence of *S. Typhimurium* in the food sample. As shown in **Table 5.2**, the reading exhibited a similar response with the linear relationship between the current density and cell concentration of ssDNA/rGO-AP@0.005M/GCE sensing platform tested in pure bacterial cultures. There was no significant difference ($P > 0.05$, T-test analysis) between the current density obtained from different concentrations of bacteria from cell culture suspension and from the food homogenates of the spiked sample.

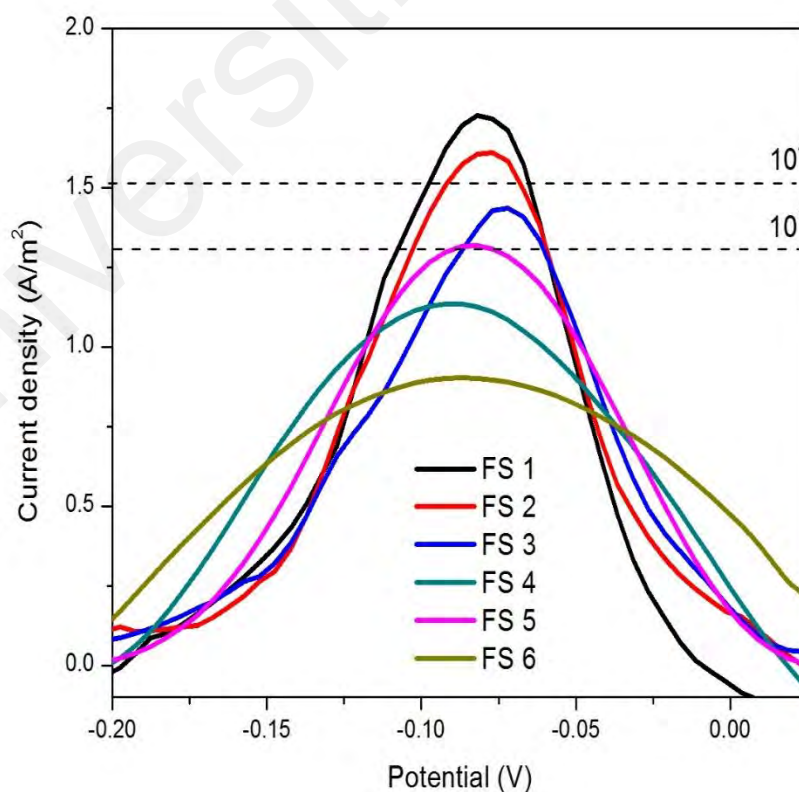


Figure 5.7. DPV of spiked chicken food samples with different concentrations of bacteria recorded in Tris-HCl buffer, pH 7.4.

Table 5.2. Detection response (Mean \pm S.D) (n=3) obtained with bacterial suspensions and spiked food sample

Cell concentration, log c (cfu mL ⁻¹)	Current Density (A m ⁻²)	
	Pure Cultures	Food Sample
10 ¹	1.44 \pm 0.06 ^a	1.43 \pm 0.05 ^a
10 ²	1.60 \pm 0.10 ^a	1.60 \pm 0.08 ^a
10 ⁴	1.73 \pm 0.12 ^a	1.72 \pm 0.06 ^a

a: Differences between alphabets indicate a significant difference between different test condition (ANOVA, Turkey HSD test, p<0.05)

5.1.4.5 Reproducibility and stability of the rGO-AP@0.005M/GCE.

The reproducibility of the aptasensor was investigated by parallel measurements of the conductivity 10X PBS buffer. The results obtained were presented in **Figure 5.8**. The relative standard deviation (RSD) was 1.28% (n=3), revealing acceptable reproducibility for the detection of bacteria. This aptasensor also showed good stability up to 28 days with an decreased in current response by 3.1% when stored in ultrapure water at 4 °C.

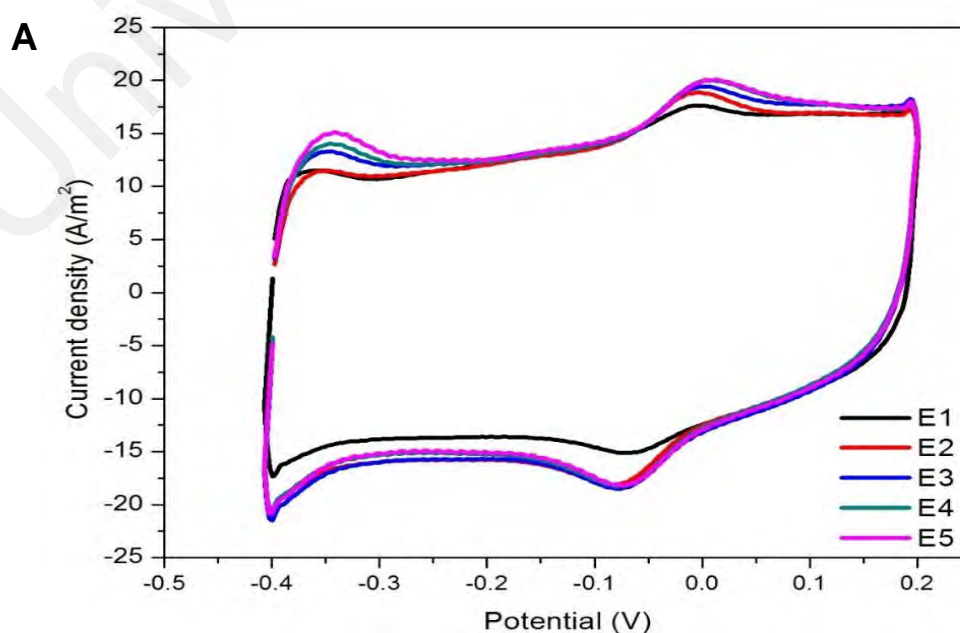


Figure 5.8, continued.

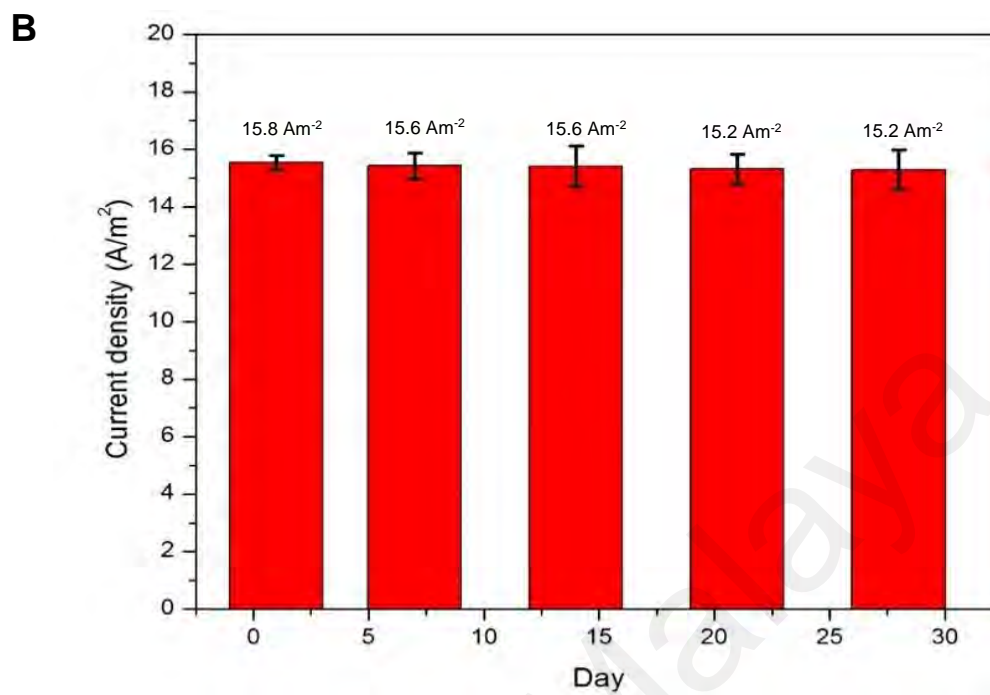


Figure 5.8. (A) CV curves of five different rGO-AP@0.005M/GCE modified electrodes and (B) histogram of shelf life of rGO-AP@0.005M/GCE electrode up to 28 days recorded in 10X PBS at a scan rate of 100 mV/s.

5.2 Reduced Graphene Oxide-Titanium dioxide nanocomposite electrochemical aptasensor for *Salmonella enterica* detection.

5.2.1 Overview

In the past, various types of nanoparticles such as metals and metal oxides were employed to improve the overall analytical performance of biosensors (Justino, Rocha-Santos, Cardoso, & Duarte, 2013). Recently, graphene-based nanomaterials have progressed into becoming a potential material in the electrochemical biosensing field. It is noteworthy that the research on the incorporation of rGO with metal oxides nanoparticles has been intensified to enhance the electronic property, catalytic activity and to increase overall surface area (Bai & Shen, 2012; Guo & Dong, 2011; Wang, Zhai, Wang, & Dong, 2011). Anatase TiO₂ is one such metal oxide that possesses desirable characteristics such as excellent electrochemical properties, good biocompatibility, low toxicity, high stability and strong oxidizing power (Zhang, Li, Cui, & Lin, 2010). Moreover, TiO₂ has the capability to adhere to biomolecules and facilitates electron transfer between biomolecules and transducer (Solanki, Kaushik, Agrawal, & Malhotra, 2011). In the biosensing field, the rGO-TiO₂ composites have been adapted for the detection of foodborne pathogens through electrochemical immunosensing. For instance, Solanki *et al.* (Solanki et al., 2014) have developed rGO-TiO₂ nanocomposite electrochemical immunosensor for the detection of *Vibrio cholerae* using horse-radish peroxidase-conjugated antibodies with a detection limit of 0.12 nmol L⁻¹. Although electrochemical properties of this nanocomposite are widely studied, there is limited research on the application of this material as an electrochemical aptasensing device for foodborne pathogens (Wang, Ao, Wang, Hou, & Qian, 2012; Zhang et al., 2017).

In this research, the one-pot chemical synthesis of rGO-TiO₂ nanocomposite using graphene oxide (GO) and Titanium isopropoxide (TTIP) is proposed. The rGO

concentration was fixed but the TiO₂ concentration functionalized on the graphene surface was optimized to obtain best sensing performance. To the best of our knowledge, rGO-TiO₂ nanocomposite has not been implemented as an electrochemical aptasensor to detect whole-cell *Salmonella enterica*. Hence, this study introduced the electrochemical detection system using label-free single-stranded deoxyribonucleic acid (ssDNA) aptamer specific to *Salmonella enterica*. Coupling rGO functionalized with TiO₂ nanoparticles and aptamer has led to the successful and novel detection of the whole-cell foodborne pathogen. Due to the excellent electrochemical properties of TiO₂, it is widely used for the construction of biosensors. Nevertheless, its high bandgap (~3.2 eV) results in low conductivity of this material (Lee, You, & Park, 2012; Liu et al., 2008; Solanki et al., 2014). Thus, TiO₂ was incorporated with rGO in this study to improve the overall electrical conductivity. The chemical reduction of GO to rGO restores sp²-hybridized carbon networks and its synergetic effect with TiO₂ improves the electronic properties and biocompatibility (Pei & Cheng, 2012; Tang, Li, & Zeng, 2015; Wu, Zhou, et al., 2012). The metal oxides anchored on rGO also prevent the agglomeration and re-stacking of rGO sheets owing to the van der Waals forces thereby, increasing the total surface area leading to high electrochemical activity (Fan et al., 2011; Pandikumar, Soon How, et al., 2014).

The GO-TiO₂ was formed using covalent bonds and reduced to rGO-TiO₂ chemically using hydrazine for better electronic, electrochemical and biochemical properties (Chang et al., 2012; Solanki et al., 2014; Wang, Zhai, Wang, & Dong, 2011). This nanocomposite was deposited by drop-casting onto a GCE electrode to form the rGO-TiO₂/GCE platform. GO interacts with TTIP with the aid of nucleation sites of the functional groups such as -COOH and -OH (Chang et al., 2012). These negatively charged functional groups attract the positively charged Ti⁴⁺ through esterification to form O=C-O-Ti bonds, resulting in the growth of TiO₂ nanoparticles on the rGO sheets

during the reduction process (Xiang, Yu, & Jaroniec, 2011, 2012). In the presence of the DNA aptamer (ssDNA/rGO-TiO₂/GCE), its phosphate group (P=O) interacts with Ti-O to form P-O-Ti-O (Zhang, Wang, et al., 2014; Zhu, Wang, Zhang, Sun, & Yao, 2007). Non-covalent interactions between DNA bases and graphitic domains of rGO further enhance the adsorption of DNA onto the nanocomposite (Lu, Huang, Liu, Ying, & Liu, 2016). When a target bacterium is introduced into the system, this aptamer binds specifically to the outer membrane protein of *Salmonella* cells and formed aptamer-bacteria complex (STM/ssDNA/rGO-TiO₂/GCE) that inhibits the electron kinetics at the electrode interface.

5.2.2 Structural and morphological characterization of rGO-TiO₂ nanocomposite.

The chemical properties of the rGO-TiO₂ nanocomposite were studied using FTIR as shown in **Figure 5.9 (A)**. The FTIR spectrum of rGO showed an intense peak at 1630 cm⁻¹ due to the sp² hybridization of carbon atoms resulting from the reduction of GO by hydrazine. The FTIR spectrum for TiO₂ showed an essential characteristic peak at 3408 cm⁻¹ (stretching vibrations of O-H bond). The peaks at 846 cm⁻¹ and 653cm⁻¹ also indicated Ti-O vibrations in TiO₂ lattice (Alam & Cameron, 2002). The three rGO-TiO₂ nanocomposites with different concentration of TiO₂ had both essential characteristic peaks of rGO and TiO₂. The oxygen-containing functional groups were decreased dramatically and the skeletal vibration peak of the rGO sheets was present at 1630 cm⁻¹. In addition, a broad peak of Ti-O-C also appeared around 638 cm⁻¹ which further indicated the formation of rGO and TiO₂ nanocomposite (Raja et al., 2017). However, the intensity of the peak varies between the rGO-TiO₂@0.2M, rGO-TiO₂@0.4M and rGO-TiO₂@0.6M due to the different concentration of TiO₂ decorated on the graphene surface.

Raman spectroscopy is a non-destructive technique that elucidates the vibration bands and particle size of the rGO-TiO₂ nanocomposites. **Figure 5.9 (B)** shows Raman scattering spectra of the rGO, TiO₂, rGO-TiO₂@0.2M, rGO-TiO₂@0.4M and rGO-TiO₂@0.6M. The spectrum of rGO exhibited two significant in-phase vibrations at 1349 cm⁻¹ (D band) and 1593 cm⁻¹ (G band) representing the presence of structural defects in the sp²-hybridized carbon system and first-order scattering of E_{2g} phonons of sp² carbon atoms. In addition, the TiO₂ spectrum showed anatase-vibration peaks centered at 196, 394, 536 and 637 cm⁻¹ which belong to E_g, B_{1g}, A_{1g} and E_g modes, respectively. The E_g peaks are attributed to the symmetric stretching vibration of O–Ti–O bonds. Furthermore, B_{1g} and A_{1g} peaks are ascribed to the symmetric and asymmetric bending vibrations of O-TiO. Whereas, the rGO-TiO₂ nanocomposites showed both important characteristic peaks of rGO and TiO₂. The presence of D and G bands at 1313 and 1601 cm⁻¹, respectively and four main peaks of TiO₂ indicate successful incorporation of these two materials. Moreover, the formation rGO-TiO₂@0.2M, rGO-TiO₂@0.4M and rGO-TiO₂@0.6M increased the I_D/I_G peak intensity ratio from 0.96 (rGO) to 1.01, 1.41 and 2.06, respectively due to the decreased in-plane sp² domain sizes resulting from the introduction of oxygen-containing groups and increased defects in its graphitic domains (Tan, Ong, Chai, & Mohamed, 2013). This phenomenon demonstrated that the chemical interaction between the surface of the hydroxy group of TiO₂ and the functional group of GO was successfully materialized *via* a simple chemical reduction method. The difference in I_D/I_G peak intensity ratio explains the degree of defects created on the surface of graphene. The rGO-TiO₂@0.4M showed an optimum level of surface defects as compared to others.

The XRD analysis was used to determine the crystallographic structure of the synthesized rGO and rGO-TiO₂. The high-angle powder XRD patterns of rGO and rGO-TiO₂ nanocomposite is shown in **Figure 5.9 (C)**. The XRD peak of rGO-TiO₂ showed the

reflection at 25.5° (101), 37.9° (004), 48.5° (200), 54.4° (105) and 63.2° (204). All the peaks were corresponding to the anatase phase of Titania. The diffraction peaks of rGO were not distinguishable in XRD patterns of the rGO-TiO₂ nanocomposite. This is due to the lower crystallinity degree of rGO as compared to TiO₂ results in the shielding of the rGO peaks (Liu, Duan, et al., 2014; Sakulpaisan et al., 2016). The strong 101 plane reflections of TiO₂ also masked the weak and broad characteristic peak of rGO at $2\theta \sim 25^\circ$ (Kumar, Kumar, & Reddy, 2015).

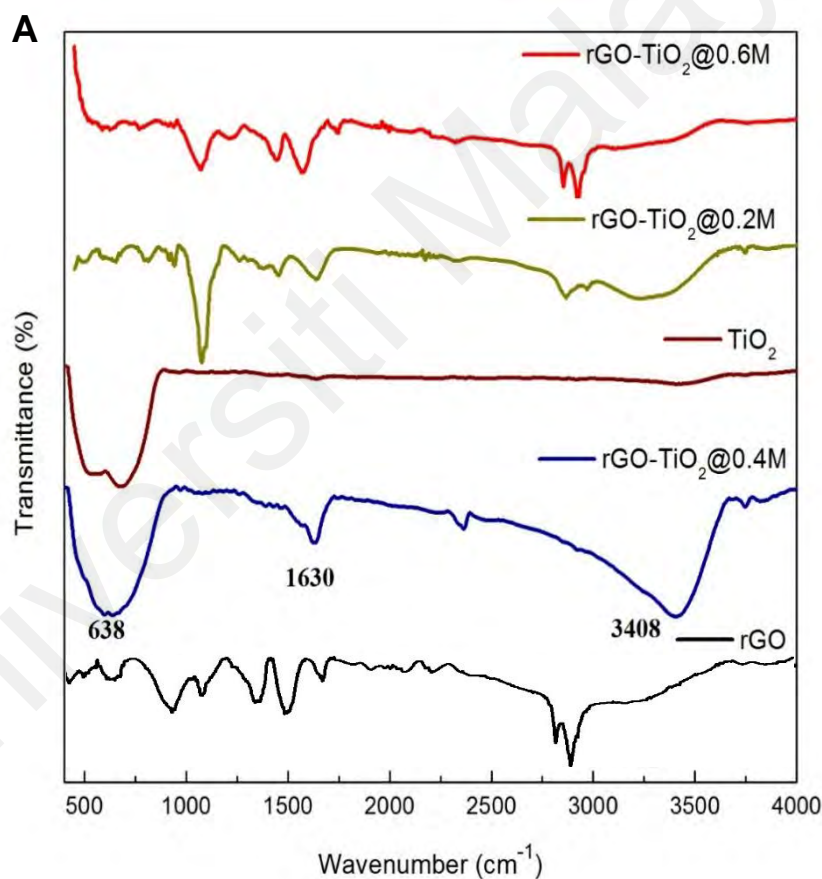


Figure 5.9, continued.

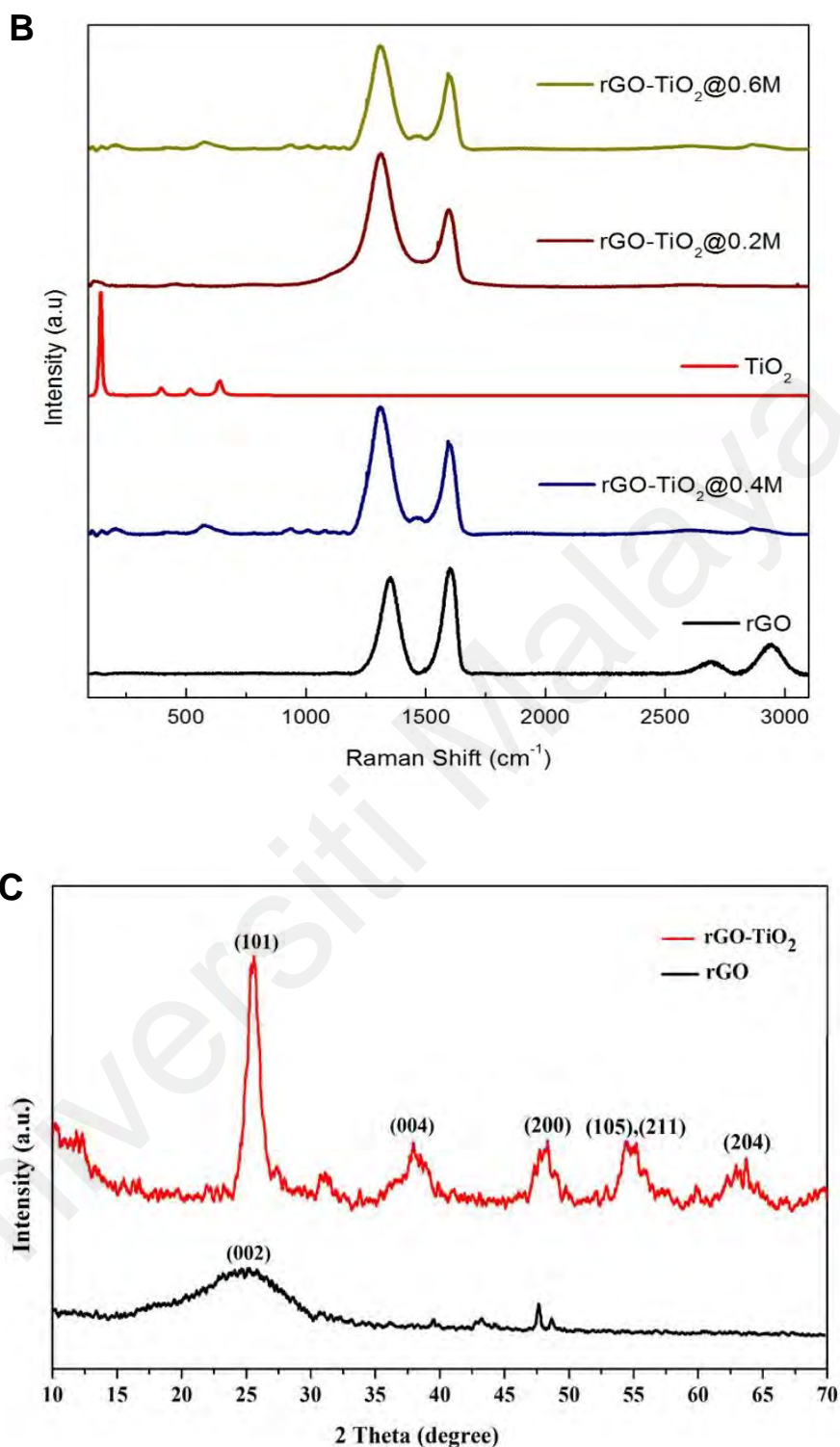


Figure 5.9 (A) The FTIR spectra of rGO, TiO₂, rGO-TiO₂@0.2M, rGO-TiO₂@0.4M and rGO-TiO₂@0.6M. **(B)** The Raman spectra of rGO, TiO₂, rGO-TiO₂@0.2M, rGO-TiO₂@0.4M and rGO-TiO₂@0.6M. **(C)** The XRD spectra of rGO and rGO-TiO₂.

The morphological characteristic of the rGO-TiO₂ nanocomposite was studied using SEM and TEM imaging. **Figure 5.10 (A)** shows the SEM image of (a) rGO, (b) rGO-TiO₂@0.2M, (c) rGO-TiO₂@0.4M and (d) rGO-TiO₂@0.6M. From SEM imaging, the folded and wrinkled rGO nanosheets can be seen. The well-formed TiO₂ nanoparticles covering the surface of rGO can be observed in three nanocomposites indicating the deposition of TiO₂ nanoparticles on rGO nanosheet.

Figure 5.10 (B) shows TEM micrographs of the rGO and three rGO-TiO₂ nanocomposites. The morphology of rGO-TiO₂ remains the same despite the increase in TiO₂ concentration. The presence of dark color spherical-like structures on a semi-transparent rGO nanosheet could be observed in rGO-TiO₂@0.4M and rGO-TiO₂@0.6M but not in rGO-TiO₂@0.2M may be due to the low concentration of TiO₂ nanoparticles. This image clearly showed that the TiO₂ nanoparticles are uniformly and closely embedded in the spherical shape on the rGO nanosheets.

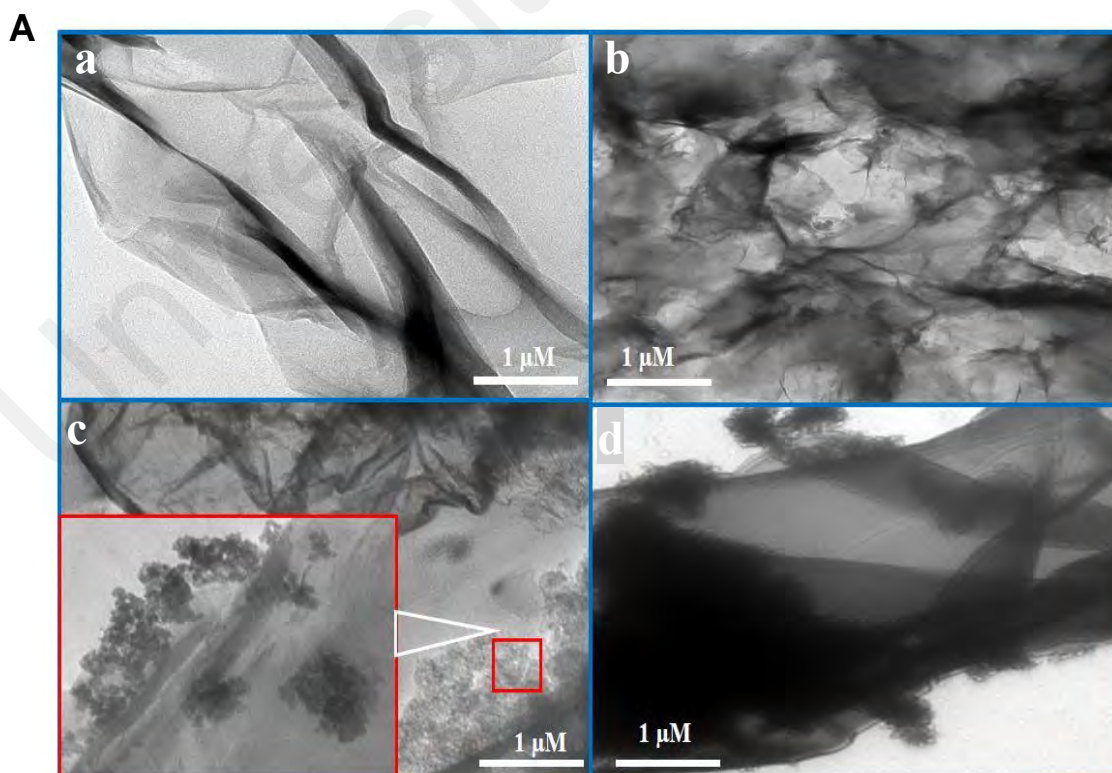


Figure 5.10, continued.

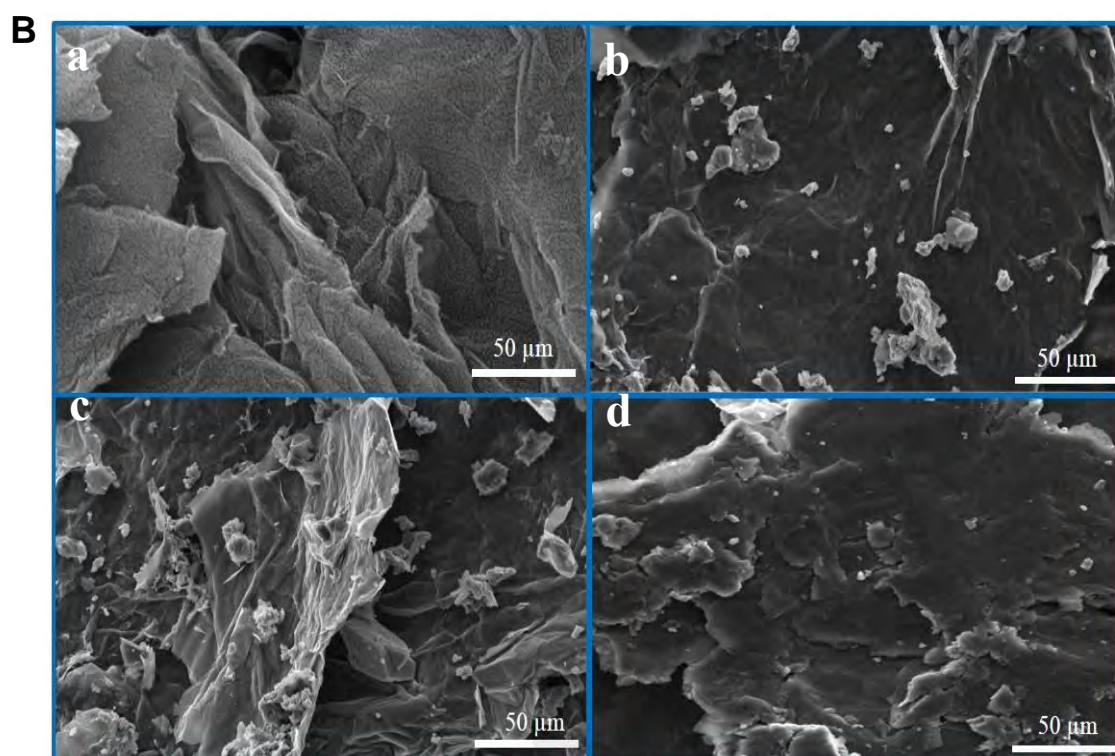


Figure 5.10 (A). SEM images of (a) rGO, (b) rGO-TiO₂@0.2M, (c) rGO-TiO₂@0.4M and (d) rGO-TiO₂@0.6M. **(B)** TEM image of (a) rGO, (b) rGO-TiO₂@0.2M, (c) rGO-TiO₂@0.4M and (d) rGO-TiO₂@0.6M

5.2.3 Electrochemical characterization of rGO-TiO₂ modified GCE electrode

The electrochemical behavior of the rGO-TiO₂ nanocomposite modified GCE electrodes was investigated and compared using CV (**Appendix C1**) and DPV as shown in **Figure 5.11**. Both CV and DPV reveals the differences in electrochemical behavior of the rGO/GCE, rGO-TiO₂@0.2M/GCE, rGO-TiO₂@0.4M/GCE and rGO-TiO₂@0.6M/GCE in Zobel's solution at scan rate 100 mV/s. All the CV plots exhibited a well-defined reversible redox peak. The rGO/GCE recorded the lowest current response. The rGO-TiO₂@0.4M/GCE exhibited the highest current response which indicates rapid electron transfer at the electrode-electrolyte interface due to the good electrical

communication between electrode and electrolyte. The highest redox current response indicates the electrochemical reversibility of the oxidation and reduction of $[\text{Fe}(\text{CN})_6]^{3-/4-}$ ions was greatly improved because of the effective surface area provided by rGO-TiO₂@0.4M/GCE.

The DPV plot for blank GCE, rGO/GCE, rGO-TiO₂@0.2M/GCE, rGO-TiO₂@0.4M/GCE and rGO-TiO₂@0.6M/GCE in Zobel's solution as shown in **Figure 5.11**. This plot shows a drastic increase in the charge transfer rate upon employing the rGO-TiO₂/GCE modified electrode. This is due to the presence of TiO₂ induced better electrical conductivity between the electrode and electrolyte interface (How, Pandikumar, Ming, & Ngee, 2014). The lowest peak current was exhibited by bare GCE and followed by rGO/GCE. The current density value was drastically increased upon decorating rGO sheets with TiO₂ nanoparticles. Among the three nanocomposites, rGO-TiO₂@0.4M/GCE electrode possesses the highest peak current and proves to have better electrochemical behavior. The current density at the electrode/electrolyte interface decreased in following the order of: bare GCE < rGO/GCE < rGO-TiO₂@0.2M/GCE < rGO-TiO₂@0.6M/GCE < rGO-TiO₂@0.4M/GCE.

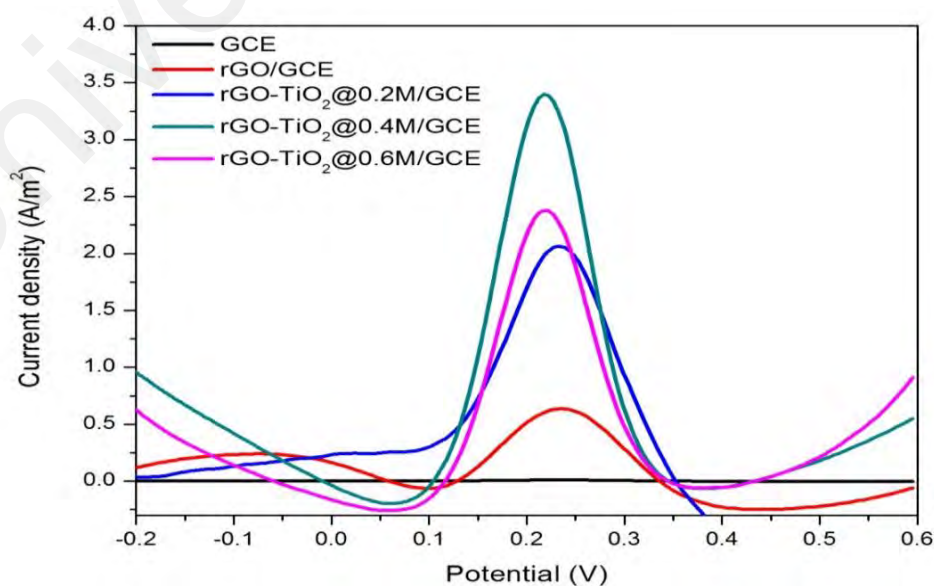


Figure 5.11. The DPV plot of blank GCE, rGO/GCE, rGO-TiO₂@0.2M/GCE, rGO-TiO₂@0.4M/GCE and rGO-TiO₂@0.6M/GCE in Zobel's solution at scan rate 100 mV/s.

5.2.4 Electrochemical detection of *Salmonella* using rGO-TiO₂ nanocomposite-modified electrode

5.2.4.1 Optimization of rGO-TiO₂@0.4M/GCE

To optimize the electrochemical performance of the fabricated electrodes, the effect of rGO-TiO₂@0.4M loading (mg mL⁻¹), aptamer concentrations (μmol L⁻¹) and scan rates (mVs⁻¹) on the sensing performance were studied. Firstly, the effect of rGO-TiO₂@0.4M concentrations was studied by loading the electrodes with different concentrations of a rGO-TiO₂@0.4M solution. As shown in **Appendix C2 (A)**, a maximum current density of 22 Am⁻² was recorded with the loading of 3 mg mL⁻¹ rGO-TiO₂@0.4M solution. At concentrations higher than 3 mg mL⁻¹, the measured current density was reduced to below 13 Am⁻². The current density decreased with increasing rGO-TiO₂@0.4M loading could be attributed to the formation of a thicker film of nanocomposite which blocked the accessibility of the redox probe to the electrode surface and led to the limited electron transfer process (Guo, Guo, et al., 2013).

Secondly, the effect of aptamer concentrations on current density was studied by incubating electrodes in different concentrations of aptamer solution. Based on the results in **Appendix C2 (B)**, the highest current density was observed using an aptamer concentration of 5 μmol L⁻¹. At concentrations of aptamer > 5 μmol L⁻¹, the current density decreased gradually due to saturation of negatively-charged aptamer which forms an electrostatic barrier on the surface of the electrode (Liu, Tuleouva, Ramanculov, & Revzin, 2010).

Lastly, the effect of scan rates on the sensor performance was also studied by measuring the peak current at different scan rates ranging from 10 to 100 mVs⁻¹ using CV. **Appendix C2 (C)** shows that the peak current increased with increasing scan rates

which indicates enhanced electron transfer. A linear relationship ($I = 0.213V + 1.591$, $R_2=0.983$) could be depicted from the peak currents obtained at various scan rates (**Appendix C2 (D)**), showing the redox process is surface-confined (Jia et al., 2016).

5.2.4.2 Electrochemical analysis of rGO-TiO₂@0.4M/GCE

The electrochemical behavior of rGO-TiO₂@0.4M/GCE nanocomposite was investigated with CV performed in Zobel's solution. **Appendix C3** shows the CV that illustrates the changes in electrical conductivity in accordance with each stage of the electrode fabrication process and the detection of bacterial targets. The typical redox peak of the bare GCE electrode was depicted in line d. A prominent increase in current density could be observed after the coating rGO-TiO₂@0.4M on the electrode (line a) as compared to rGO (line c). A well-defined redox peak at +0.3 V was observed for rGO-TiO₂@0.4M/GCE. The increase in peak current for rGO-TiO₂@0.4M/GCE is attributed to the incorporation of TiO₂ with rGO that provides a high surface area, enhanced electron mobility and excellent electrical conductivity. However, the immobilization of aptamer onto the electrode (line b) caused the peak current to decrease as electron transfer to the bioactive material was reduced. In detail, the attachment of aptamer on the rGO-TiO₂@0.4M/GCE leads to electrostatic repulsion or steric hindrance between the negatively charged aptamer and the redox probe $[\text{Fe}(\text{CN})_6]^{3-/4-}$ leading to inhibition of electron transfer process (Jia et al., 2016; Park & Park, 2009).

Similar results were observed in the electrochemical impedance Nyquist plot. The semicircle diameter observed in the Nyquist plot reflects the electron transfer resistance. In **Figure 5.12**, bare GCE exhibited a larger charge transfer resistance (R_{ct}) as shown by the semicircle with large diameter (line a). After the coating of rGO-TiO₂@0.4M nanocomposite onto bare GCE (line e), the R_{ct} decreased drastically due to the effective electron transfer between the coated material and electrode interface. After the attachment

of aptamer (line d), the R_{ct} increases with decreasing electron transfer rate due to the hindrance created by the electron exchange of redox probes at the electrolyte-electrode interface. In the presence of *Salmonella* cells (line c), the diameter of the EIS semicircle increased as compared to ssDNA/rGO-TiO₂@0.4M/GCE. This is because the electron transfer was blocked by the formation of aptamer-bacteria complexes. This reduces the accessibility of the redox probe to the electrode and increases the charge transfer resistance leading to low conductivity (Park & Park, 2009). The EIS result was consistent with CV and the measurement of R_{ct} showed more sensitive results than the conductivity test.

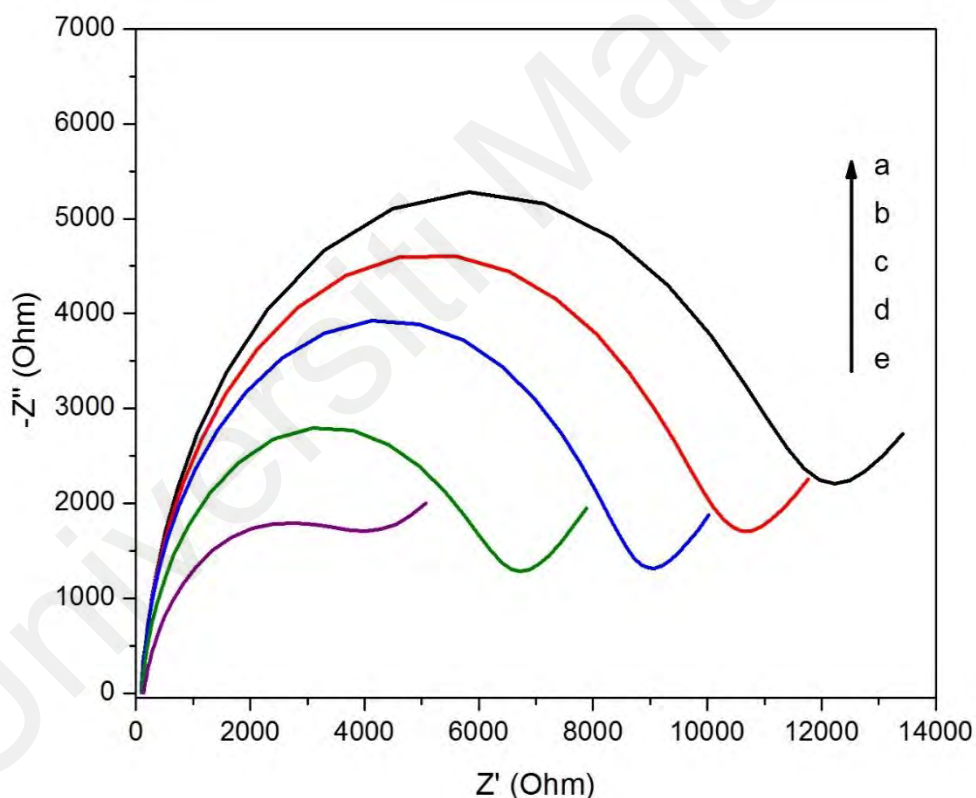


Figure 5.12. The Nyquist plots of (a) bare GCE, (b) rGO/GCE, (c) STM/ssDNA/rGO-TiO₂@0.4M/GCE, (d) ssDNA/rGO-TiO₂@0.4M/GCE and (e) rGO-TiO₂@0.4M/GCE electrodes in Zobell's solution (pH 7.0).

5.2.4.3 Electrochemical detection of bacterial cells using ssDNA/rGO-TiO₂@0.4M/GCE

The sensitivity of the aptasensor (**Figure 5.13 (A)**) for bacterial detection was also investigated using DPV in Zobell's solution. The ssDNA/rGO-TiO₂@0.4M/GCE was incubated with different concentrations of *S. Typhimurium* suspension and the DPV was measured at pulse amplitude: 0.025 V, pulse width: 0.05 s and pulse period: 0.05 s. The peak currents were observed to reduce with decreasing bacterial concentrations. The aptamer adsorbed on the rGO-TiO₂@0.4M/GCE surface complexes with targeted bacterial cells, causing a barrier for electron mobility and inhibiting electron transfer. This phenomenon subsequently results in a decrease of DPV signals (Reich, Stoltenburg, Strehlitz, Frense, & Beckmann, 2017). The overall changes in charge transfer are linear with respect to the concentration of bacterial targets. The logarithm relationship between the bacterial concentration and peak current is plotted as shown in **Figure 5.13 (B)**. The linear relationship is described as follows:

$$I = 0.19 (\pm 0.02) \log c + 0.59 (\pm 0.04)$$

with the correlation coefficient of $R_2 = 0.98$, where I is the current density ($A\ m^{-2}$) and $\log c$ is the logarithm of the bacterial cell concentration. As the bacterial concentration increases, the charge transfer resistance decreases. When a bacterial cell is in contact with rGO, the negatively charged lipopolysaccharides of Gram-negative *Salmonella* cell wall induces hole density on the surface of rGO (Huang, Lim, et al., 2011; Mohanty & Berry, 2008), causing a decrease in charge transfer resistance. The interference of negative charges of the bacterial cell wall with p-type rGO creates holes and causes electrostatic gating effect leading to negative potential gating which increased the hole density on rGO surface (Mohanty & Berry, 2008). The overall conductivity of rGO increased due to its higher levels of hole density. As the number of bacteria increases, more holes are being

created due to the large negative charge interfacing on the surface of rGO resulting in an increase of the current proportional to the bacterial concentration (Huang, Lim, et al., 2011; Mohanty & Berry, 2008).

The selectivity of the aptasensor was further investigated and the results are shown in **Figure 5.13 (C)**. For the selectivity test, the peak currents of non-*Salmonella* bacteria were measured. The results showed differences in conductance between *Salmonella* as compared with other bacteria. Although DPV oxidation signals are recorded for all non-*Salmonella* bacteria, the individual peak current was still lower than the detection limit of our rGO-TiO₂@0.4M/GCE aptasensor. This indicates that the developed aptasensor is highly selective for *Salmonella* with strong discrimination against other non-*Salmonella* bacteria.

The performance of the developed rGO-TiO₂ aptasensor was compared with established DNA-based methods and electrochemical biosensors for pathogen detection, as summarized in **Table 5.3**. This comparison shows the developed rGO-TiO₂ aptasensor exhibited high sensitivity with improved detection limit and allows the rapid detection of *Salmonella*.

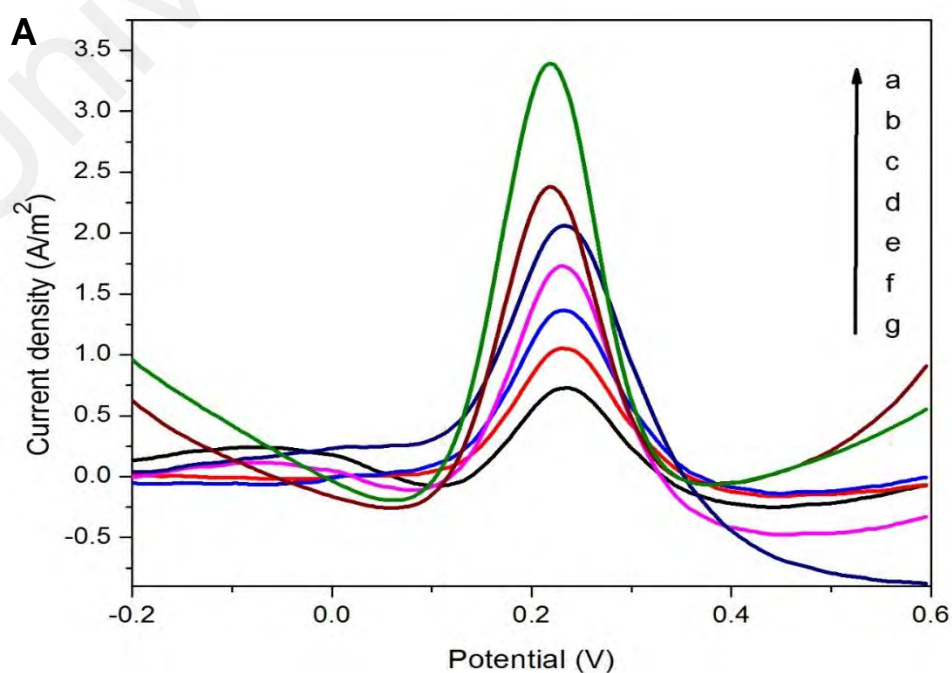


Figure 5.13, continued.

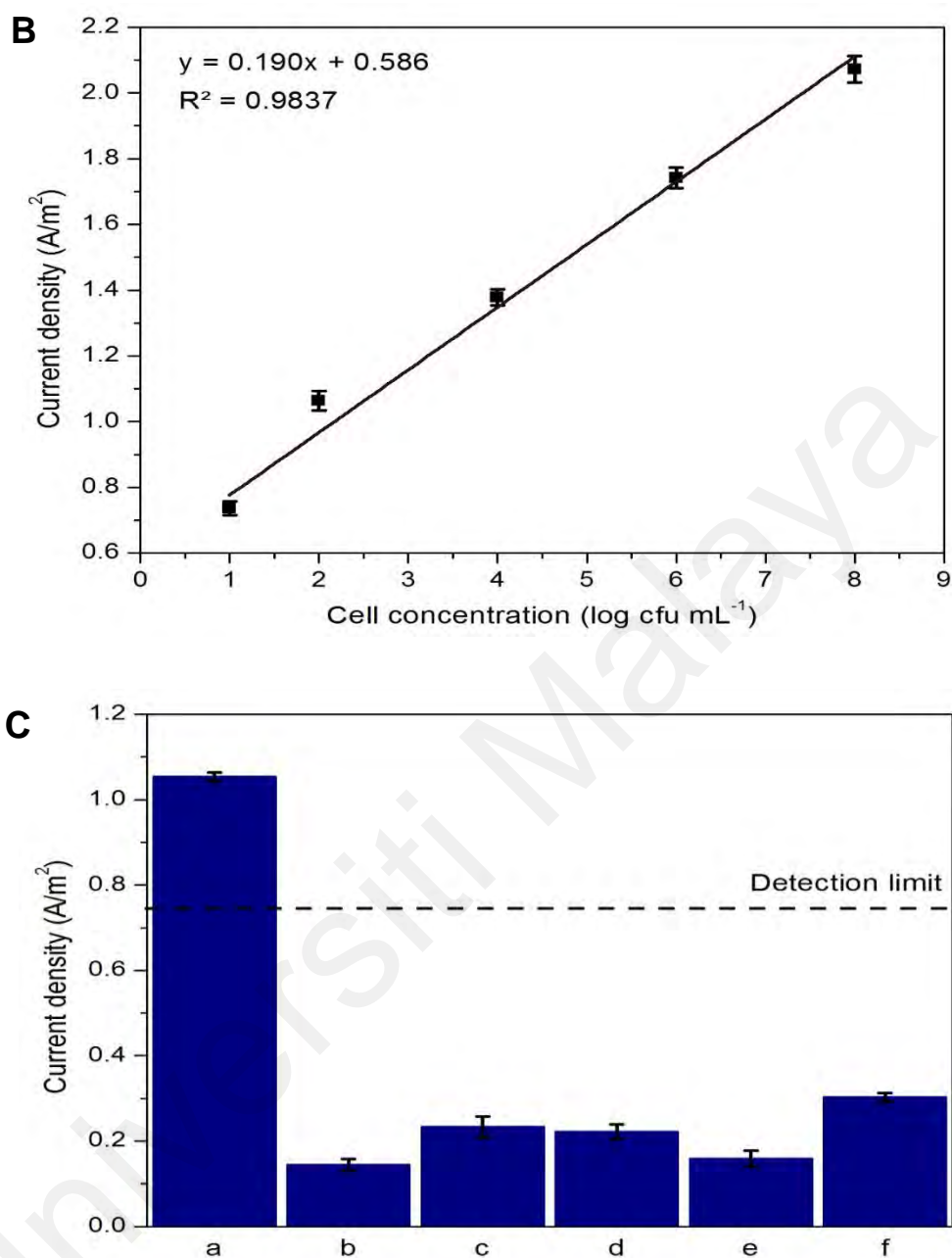


Figure 5.13. Electrochemical detection of bacterial cells using the fabricated electrodes. (A) DPV of (a) rGO-TiO₂@0.4M/GCE, (b) ssDNA/rGO- TiO₂@0.4M/GCE, (c) 10⁸ cfu mL⁻¹, (d) 10⁶ cfu mL⁻¹ (e) 10⁴ cfu mL⁻¹, (f) 10² cfu mL⁻¹ and (g) 10¹ cfu mL⁻¹ in Zobell solution (pH 7.0). (B) Linear relationship between the current density and cell concentration (logarithm). (C). Graph of peak currents obtained for (a) *S. Typhimurium*, (b) *E. coli*, (c) *V. cholerae*, (d) *K. pneumoniae*, (e) *Sh. Dysenteriae* and (f) *Staph. aureus* in Zobell's solution (pH 7.0). Data are expressed as mean ± standard deviation (n = 3).

Table 5.3. Comparison of various bacterial detection techniques with the current study

Detection methods	Sensing Platform	Targeted bacteria	Limit of detection	Assay time	Ref
Multiplex-PCR	-	<i>Salmonella</i> spp.	10^3 cfu ml ⁻¹	3h	(Wang et al., 2007)
Immunological assay	-	<i>S. Typhimurium</i>	10^3 cfu ml ⁻¹	2h	(Wu, Li, et al., 2014)
Electrochemical genosensor	GO-iron oxide-chitosan nanocomposite	<i>E. coli</i>	1×10^{-14} M (DNA target)	1h	(Tiwari, Singh, Pandey, & Sumana, 2015)
Electrochemical immunosensor	Graphene-copper (II) oxide-cysteine	<i>E. coli</i> O157:H7	10^1 cfu ml ⁻¹ *	-	(Pandey et al., 2017)
Electrochemical immunosensor	rGO-TiO ₂	<i>V. cholerae</i>	0.12 nmol L ⁻¹ (target antigen)	-	(Solanki et al., 2014)
Amperometric aptasensor	rGO-TiO ₂	<i>S. Typhimurium</i>	10^1 cfu ml ⁻¹	10 min	This work

*The detection limit was higher for food sample.

5.2.4.4 Evaluation of the ssDNA/rGO-TiO₂@0.4M/GCE in food sample

Out of seven chicken meat samples tested (FS 1 to FS 7), six samples showed a positive electrochemical response with increasing peak current proportional to *Salmonella* concentration (Figure 5.14). One meat sample produced a negligible current, indicating the absence of *Salmonella*. The CV results were validated by the culture method. All the six chicken meat samples had a positive *Salmonella* growth on the selective medium Brilliance *Salmonella* agar™ while one meat sample had no growth on the selective medium. This aptasensor could detect *Salmonella* concentration ranging from 10¹ to 10³ cfu mL⁻¹ in the chicken meat samples. Furthermore, as depicted in Table 5.4, the bacterial concentration of food samples obtained from the electrochemical detection was comparable to the *Salmonella* count on the selective agar plates.

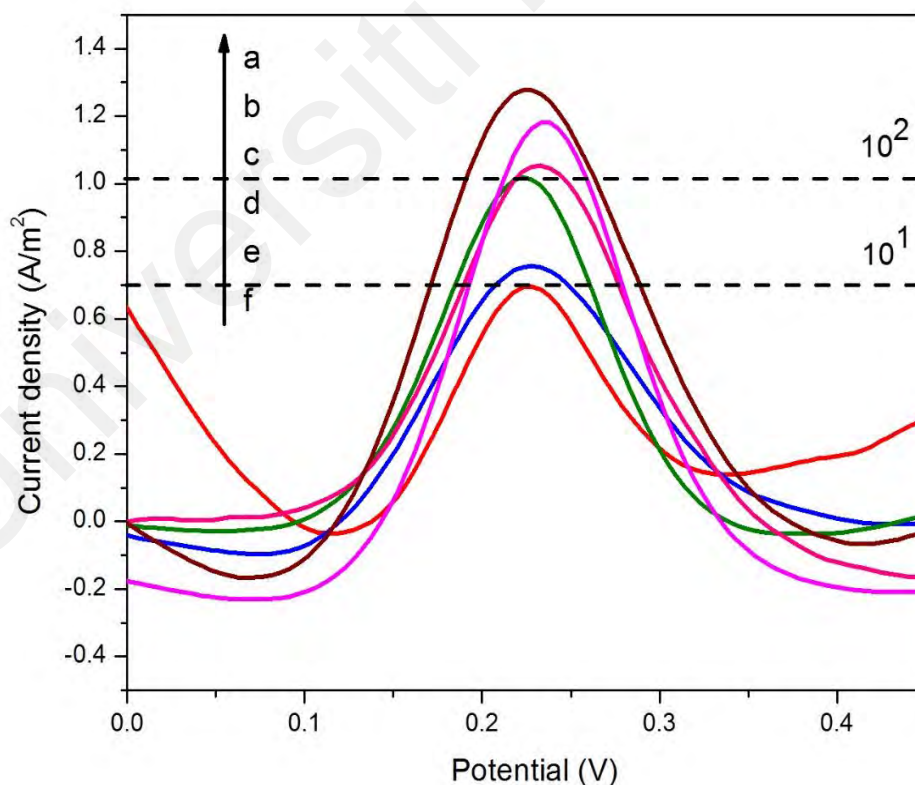


Figure 5.14. DPV signal obtained for food samples tested with the fabricated electrodes.

(a) FS 1, (b) FS 2, (c) FS 3, (d) FS 4, (e) FS 5, (f) FS 6 and (g) FS 7.

Table 5.4. The comparison between measured concentration and enumeration of *S. Typhimurium* from the food samples. Data are expressed as mean \pm standard deviation.

Chicken meat sample	Measured concentration using aptasensor (cfu mL ⁻¹)	<i>S. Typhimurium</i> concentration from plate count (cfu mL ⁻¹)
FS 1	10 ³	(9.1 \pm 1.45) X 10 ³
FS 2	10 ³	(1.5 \pm 0.53) X 10 ³
FS 3	10 ²	(8.4 \pm 1.32) X 10 ²
FS 4	10 ²	(7.7 \pm 0.95) X 10 ²
FS 5	10 ¹	(9.1 \pm 0.11) X 10 ¹
FS 6	10 ¹	(7.0 \pm 0.28) X 10 ¹
FS 7	Not detected	-

5.2.4.5 Reproducibility and stability of ssDNA/rGO-TiO₂@0.4M/GCE

The reproducibility of the aptasensor was also investigated by measuring the current response of rGO-TiO₂/GCE for five different electrodes. Under optimal conditions, the RSD obtained for the oxidation peak was 3.5% (n = 5) which indicated the modified aptasensor has acceptable reproducibility. This aptasensor also showed good stability up to 20 days with a 10% decrease in signal observed after 30 days, when stored in ultrapure water at 4 °C. All the data were presented in **Figure 5.15**.

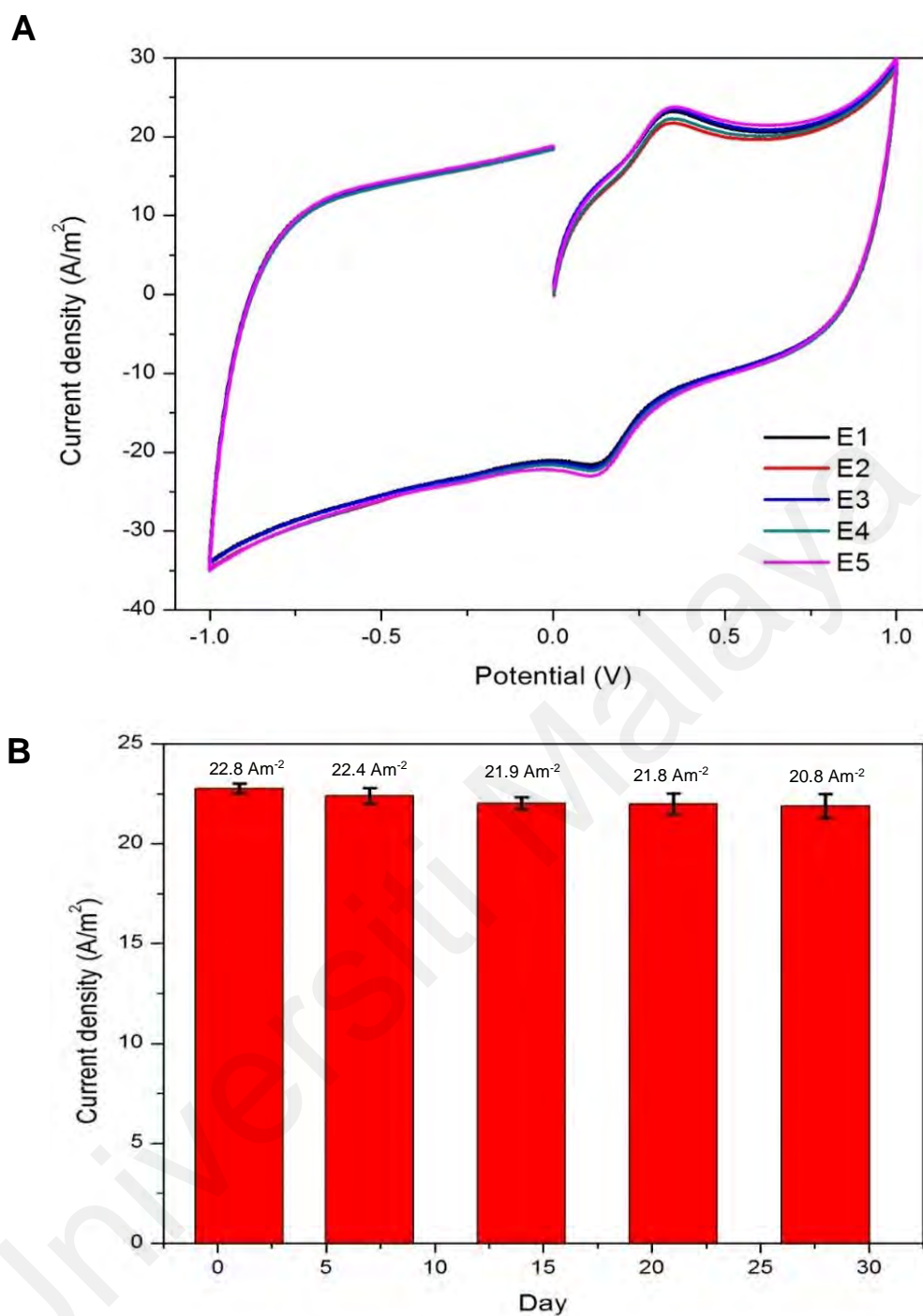


Figure 5.15. (A) Histogram of shelf life of rGO-TiO₂@0.4M/GCE electrode up to 28 days recorded in Zobell's solution at a scan rate of 100 mV/s and (B) CV curves of five different rGO-TiO₂@0.4M/GCE modified electrodes.

5.3 Reduced Graphene Oxide-Nafion (rGO-Nf) nanocomposite electrochemical aptasensor for *Salmonella enterica* detection.

5.3.1 Overview

Conducting polymer (intrinsically conducting polymers (ICPs)) is a part of electroactive biomaterials that poses high electron affinity, electronic conductivity, thermal stability and good mechanical strength. The conductivity (about 10^5 S/cm) of polymers owing to the π -electron along the polymer backbone renders them a semiconducting property (Balint, Cassidy, & Cartmell, 2014). This unique characteristic of the ICP favors their adaptation in electrochemical biosensor application. ICPs such as poly(3,4-ethylene dioxythiophene), polythiophene, poly(p-phenylenevinylene), polyaniline, polyacetylene and polypyrrole (Srinivas, Peng, Barker, & Travas-Sejdic, 2012) are frequently used in sensors applications. Nafion (Nf) (Figure 5.16) is the most widely used cation exchange conducting polymer for electrochemical applications due to its remarkable proton conductivity and stability (Yusoff, 2019). Nafion consists of a polytetrafluoroethylene (PTFE) backbone with perfluoroalkyl ether chains terminating in sulfonic acid groups.

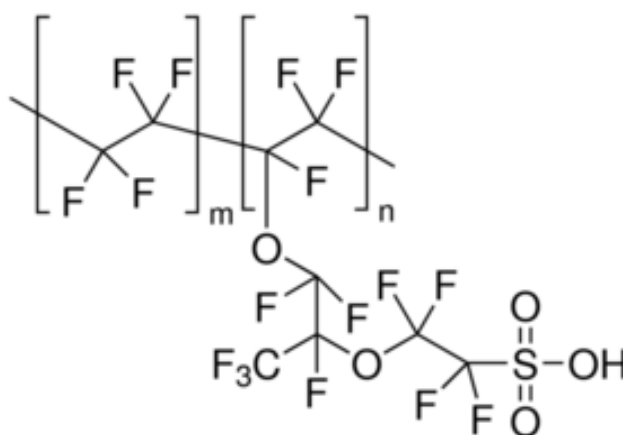


Figure 5.16. The chemical structure of Nafion

Proton conducting polymers including Nafion can be easily synthesized using chemical and electrochemical methods which offer stable and reproducible dispersion in solvents. The main advantage of ICPs which makes them a promising candidate in biomedical applications is the high affinity towards biomolecules (Nigovic, Sadikovic, & Sertic, 2014). Polymers bind to the biological molecules through adsorption and entrapment. The adsorption of biomolecules by polymers occurs through static interactions between the polymer matrix and the surface charge whereas, entrapment of biomolecules happens through trapping the biomolecule inside the polymer (Ahuja, Mir, Kumar, & Rajesh, 2007). The cationic properties of Nafion bind to the negatively-charged DNA aptamer (Branch et al., 2017) via electrostatic interaction to form a polyplex. The binding of the polymers at a high affinity with biomolecule give rise to excellent signal transduction during molecular detection, allowing highly sensitive detection (Tuncel, 2011). The conductivity and electrochemical activity of the polymer towards molecular interaction with biomolecules render them opportunities for sensor application (Zhou, Fang, & Ramasamy, 2019).

Besides enabling immobilization of biomolecules on its surface, conducting polymers also act as an excellent electron promoter in aqueous solutions (Singh, 2012). Researchers have shown that combining carbon nanostructures such as graphene with Nafion results in a significant improvement of the graphene's electrochemical performance and conductivity (Rasouli, Naji, & Hosseini, 2017). This is because the low capacitance of graphene can be improved by compositing with other conducting polymers (Gao, 2017). Electrically conductive graphene-polymer nanocomposites can be prepared by solution-phase mixing of the exfoliated graphite oxide with the polymer solution, followed by chemical reduction (Potts, Dreyer, Bielawski, & Ruoff, 2011). All the functional atoms of graphene can be found on the surface of its sheet-like structure and their molecular interaction via π - π stacking. Therefore, electron transport through

graphene is rapid and highly sensitive to adsorbed molecules (Chen, Tang, Wang, Liu, & Luo, 2011). The synergistic effect between graphene and Nafion also offers great mechanical strength and enhanced biocompatibility. Moreover, the presence of perfluoroalkyl backbones in Nafion provides a high hydrophobicity property serving as an effective matrix to disperse graphene in an aqueous solution (Yin et al., 2010). This will solve the graphene's restacking and agglomeration problem and enable uniform coating of the nanocomposite on the electrode's surface.

In the field of electrochemical biosensing of bacteria, the adaptation of polymers coated working electrode has been widely explored. For instance, Sheikhzadeh, Chamsaz, Turner, Jager, and Beni (2016) reported a gold- polypyrrole-based polymer-modified impedimetric immunosensor for the detection of *S. Typhimurium* using strain-specific aptamer. This system offers a promising detection limit in both pure culture and real food sample (apple juice) with a detection limit of 3×10^0 cfu/mL and 10^2 – 10^6 cfu/mL, respectively. The intrinsic variation of the electrical properties of the polymeric surface of polypyrrole used in this system offers a label-free detection of bacteria without the need for redox probes. The usage of natural biopolymers such as chitosan for the electrochemical detection of bacteria is more prominent as compared to conducting polymers because its thickness, surface charge and chemical groups can be flexibly tuned for enhanced electrochemical performance (Ahmed et al., 2014). To the extent of our knowledge, there is little research focused on the rGO-Nf nanocomposite materials for the electrochemical detection of bacteria. Thus, this study is focused on the development of selective and sensitive electrochemical sensing rGO-Nf nanocomposite platform. The experimental parameters such as the effects of nafion concentration, scan rate, loading volume of material and aptamer concentration on electrocatalytic performance were investigated. The sensitivity and selectivity of this rGO-Nf nanocomposite based aptasensor were also studied. This highly conductive, sensitivity and selectivity of the

rGO-Nf nanocomposite modified aptasensor could be a promising candidate for the electrochemical detection of bacteria cells responsible for foodborne illness.

5.3.2 Structural and morphological characterization of rGO-Nf nanocomposite.

The FTIR technique was used to study the interfacial interactions between rGO and Nafion polymer as shown in **Figure 5.17 (A)**. The FTIR spectra of rGO and rGO-Nafion nanocomposites were elucidated. The removal of various oxygen-containing functional groups in rGO can be seen prominently which causes a drastic decrease in its intensities. The broad O–H peak (3400 cm), C=O (1720cm) and O–H(1400cm) disappeared after the chemical reduction. The C=C at the 1580cm band was completely restored in rGO. The spectra of three rGO–Nf nanocomposites showed all the characteristic bands of both rGO and Nafion. The nanocomposites showed a COC–symmetric stretching bands at 965 and 980 cm⁻¹. Moreover, the presence of S–O stretching of SO₃H at 1056 cm was also prominent in the nanocomposites with increasing intensity proportional to the Nafion concentration. The presence of S–O stretching is attributed to the hydrogen bonding between the sulfonate moieties of the Nafion polymer and the dispersed rGO which enhances electron conductivity (Jung, Jeon, Sridhar, & Oh, 2011).

Figure 5.17 (B) shows Raman scattering spectra of the rGO and rGO-Nf nanocomposites. The representative peaks of graphene which is D and G band were observed in the nanocomposites. The ID/IG band ratio for rGO-Nf nanocomposites differs as evidence for the occurrence of chemical doping (p-type doping) on carbon materials (Aragaw, su, Rick, & Hwang, 2013). The I_D/I_G band ratio increases from 0.96 (rGO) to 0.98, 1.24 and 1.56, respectively. The CF₂ and sulfonic acid groups of Nafion introduce holes on carbon surface which shifts the Fermi level rGO to the valence band which inevitably increases the conductivity of the rGO-Nf nanocomposites(Liu, Gao,

Sun, Wang, & Zhang, 2009; Poh et al., 2012). As the concentration of Nafion increases, the holes created on the rGO surface increases and causes an increase in conductivity.

Figure 5.17 (C) shows the XRD of the rGO and rGO-Nf nanocomposites. The results reveal that both the characteristic peak of rGO and Nafion were present in the composite material. The composite appears with 2 distinctive peaks at 15° and 26° which corresponds to the AP and rGO, respectively. The sharp peak at 15° was related to the crystalline scattering of the polyfluorocarbon chains belongs to Nafion and broad peak at 26° corresponds to (002) planes of graphite-like structure on rGO (Ozden, Ercelik, Ozdemir, Devrim, & Colpan, 2017).

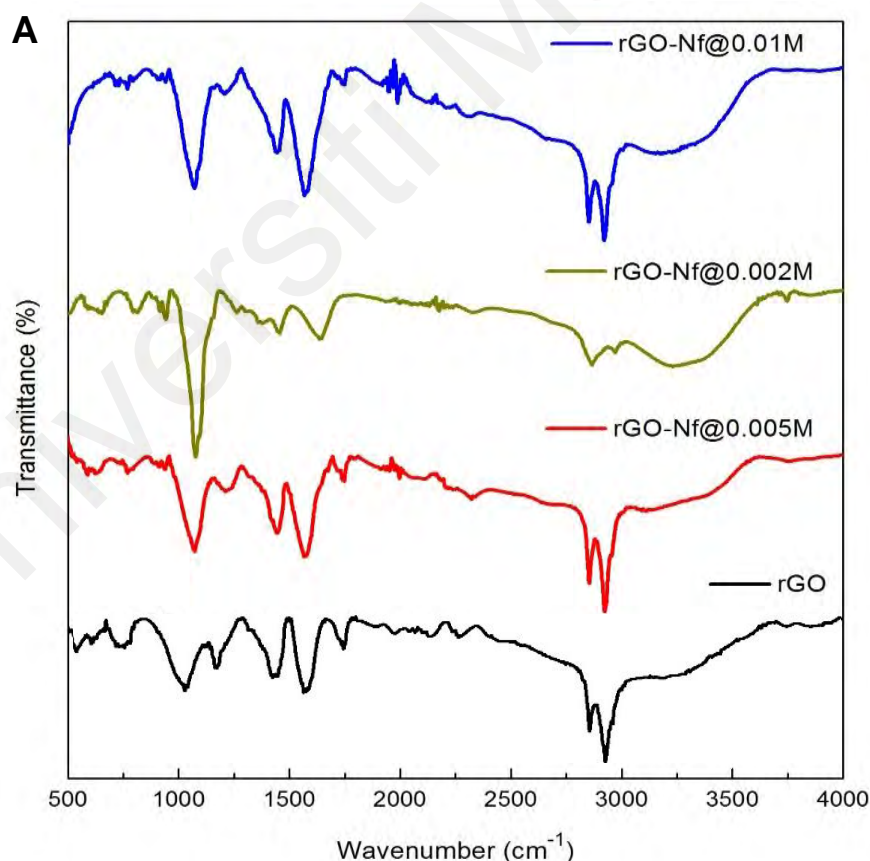


Figure 5.17, continued.

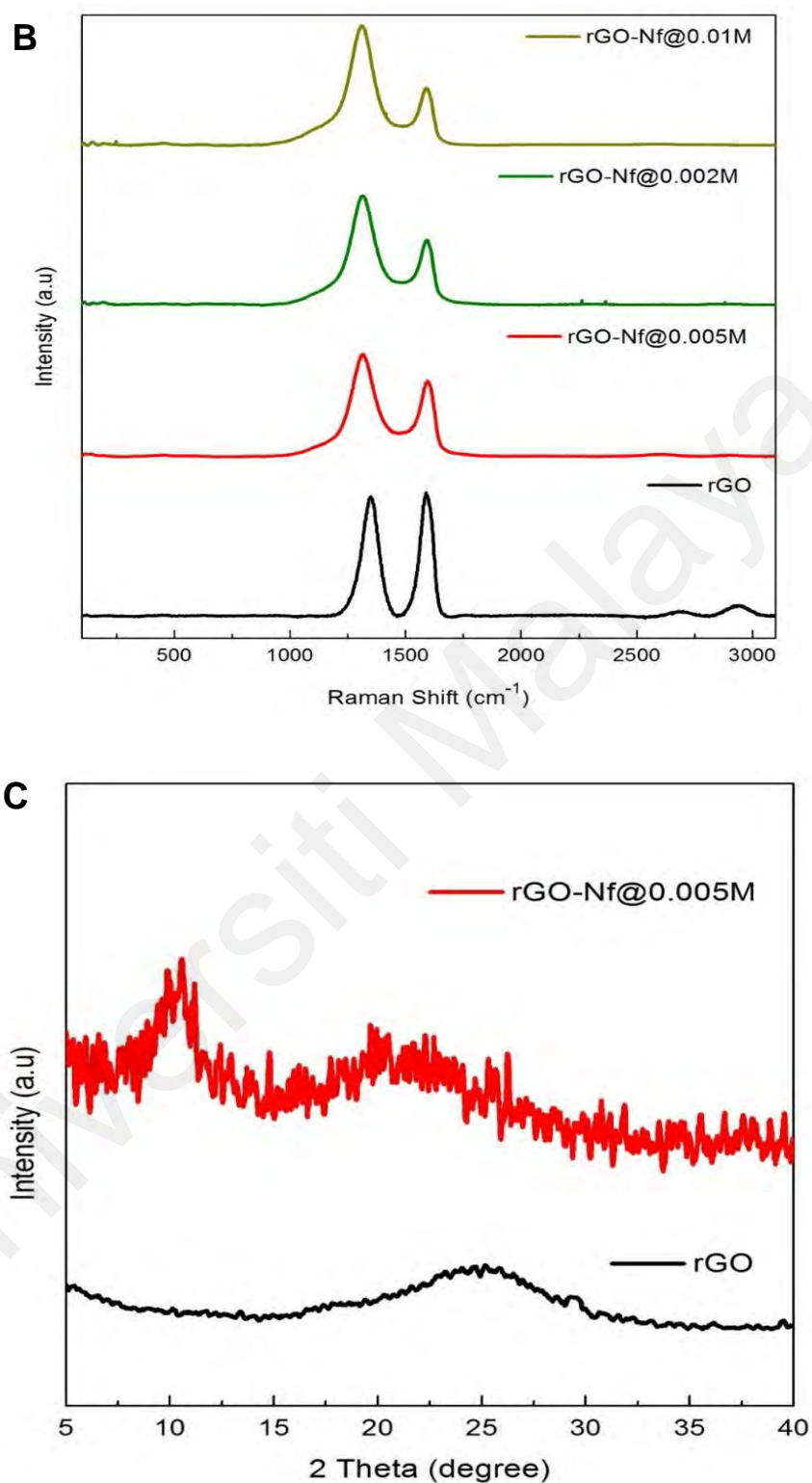


Figure 5.17. (A) FTIR spectra of rGO, rGO-Nf@0.002M, rGO-Nf@0.005M and rGO-Nf@0.01M. (B) Raman spectra of rGO, rGO-Nf@0.002M, rGO-Nf@0.005M and rGO-Nf@0.01M. (C) The XRD spectra of rGO and rGO-Nf.

The morphological characteristic of the rGO-Nf nanocomposites were studied using TEM and SEM. **Figure 5.18 (A)** shows the SEM of the materials. Wavy wrinkles and sheet-like structure of rGO can be observed through SEM. In the presence of Nafion, the polymer introduces more crumples and make the rGO surface rougher which is visible in the SEM image. This proves the successful formation of the rGO-Nafion nanocomposite. However, there is no obvious difference in the morphology of three rGO-Nafion nanocomposites.

Figure 5.18 (B) shows the TEM images of the rGO and rGO-Nf nanocomposites. The rGO exhibits wrinkled transparent flakes of the ultra-thin film along with a few thin ripples within the sheets. Whereas, the rGO-Nf nanocomposites exhibit a rough surface with an increase in the thickness of the layer due to the deposition of Nafion polymer. The coverage of polymers on the surface of rGO increases with the increasing concentration of Nafion.

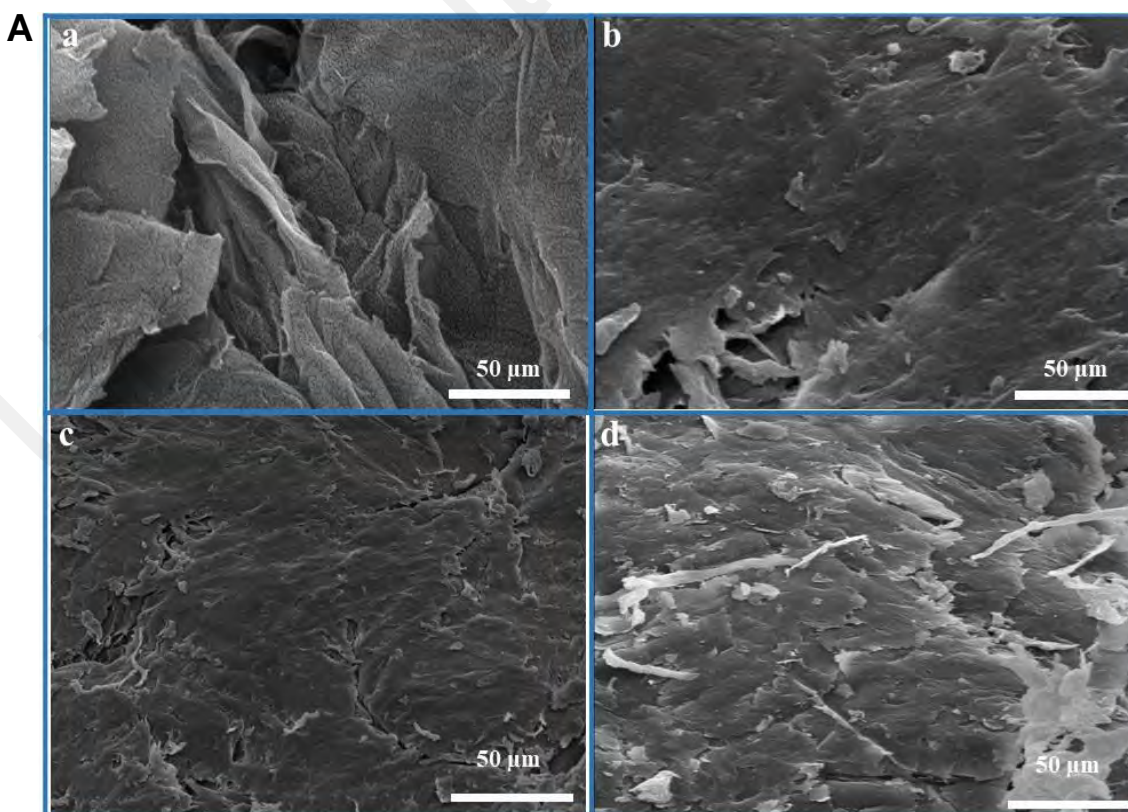


Figure 5.18, continued.

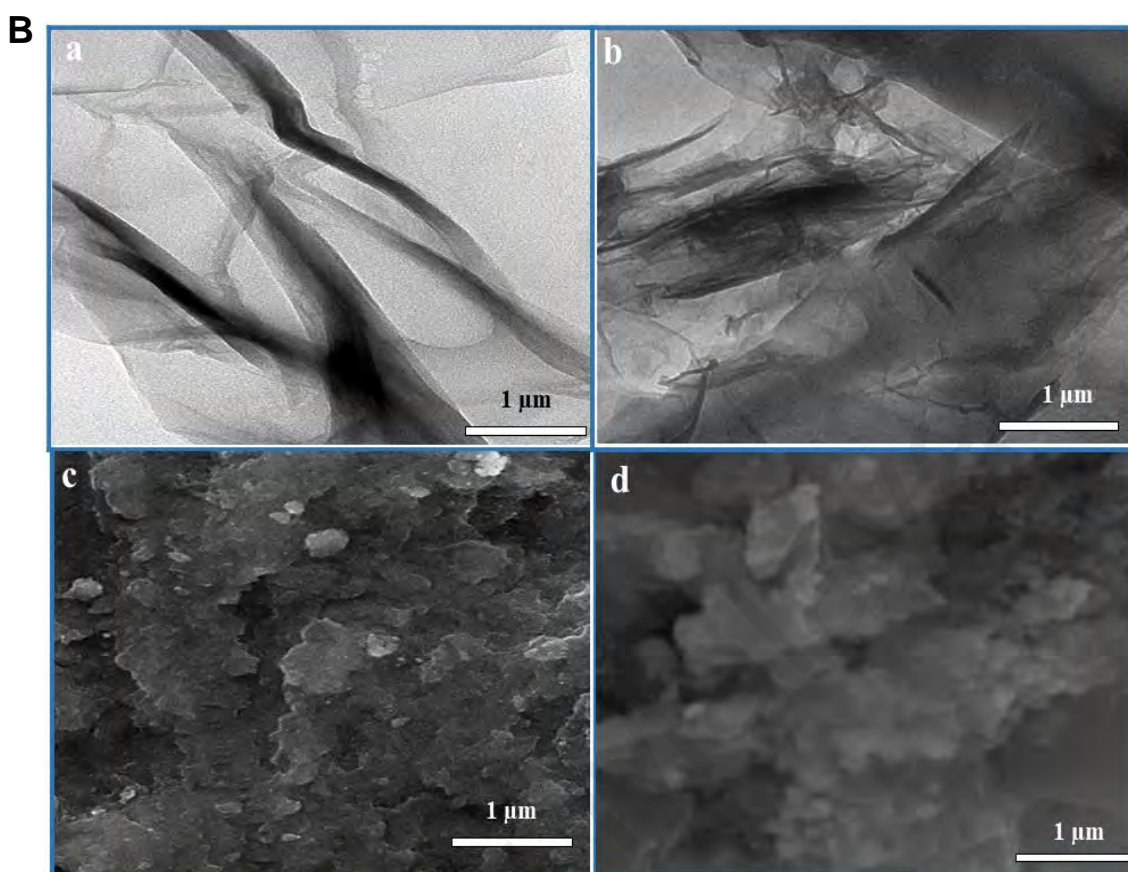


Figure 5.18 (A). SEM of (a) rGO, (b) rGO-Nf@0.002M, (c) rGO-Nf@0.005M and (d) rGO-Nf@0.01M. **(B).** TEM of (a) rGO, (b) rGO-Nf@0.002M, (c) rGO-Nf@0.005M and (d) rGO-Nf@0.01M.

5.3.3 Electrochemical characterization of rGO-Nf/GCE

The electrochemical performance of the rGO-Nf modified electrodes was characterized by using CV and electrochemical impedance spectroscopy (EIS) as shown in **Appendix D1 and Figure 5.19**, respectively. Both the CV and EIS plots were obtained for rGO-Nf nanocomposites synthesized with different concentrations of Nafion in Zobell's solution.

The CV plot for bare GCE, rGO/GCE and all three electrodes (rGO-Nf@0.002M/GCE, rGO-Nf@0.005M/GCE and rGO-Nf@0.01M/GCE) exhibits a quasi-

reversible redox reaction peak (**Appendix D1**). Bare GCE exhibited the lowest peak current but after the coating with rGO, the peak current increases due to the conductive nature of rGO due to the removal of electron insulating groups during the chemical reduction process. The highest redox peak current was obtained for rGO-Nf@0.005M/GCE followed by rGO-Nf@0.01M/GCE and rGO-Nf@0.002M/GCE with peak-to-peak separations of 99 mV, 150 mV and 170 mV, respectively. The peak current increases with increasing concentration of Nafion because the higher amount of Nafion gives rise to a conductive platform by offering a large surface area that promotes rapid electron transfer rate (Lee et al., 2013). However, the peak current decreased at higher concentration of Nafion due to the high resistance created on the surface of electrode resulting from the increased membrane thickness.

Figure 5.19 shows the Nyquist plot for rGO-Nf modified electrodes. For all plots, the existence of one semicircle in the high-frequency range can be seen. The diameter of the semicircle reflects the charge transfer resistance (R_{ct}) and the inclined straight line represents the impedance of the diffusion of the ions on the graphene's surface (Jiang et al., 2014). The bare GCE shows the largest diameter of the semicircle and followed by rGO/GCE. However, the coating of rGO-Nf nanocomposite on the electrode's surface decreases the diameter of the semicircle. The rGO-Nf@0.005M/GCE exhibits the lowest charge transfer resistance as compared to other electrodes. This proves the cationic Nafion coating on the graphene sheets effectively facilitates the electron transfer between the negatively charged electrochemical probe $[\text{Fe}(\text{CN})_6]^{3-/4-}$ and graphene (Xi & Ming, 2012). The synergistic effects exerted by the functional groups of rGO and the electron-withdrawing groups of Nafion causes a significant improvement in both protonation and electron conductivity (Li, Gittleson, Carmo, Sekol, & Taylor, 2012). The electron-withdrawing groups of Nafion, $-\text{CF}_2$ and $-\text{SO}_3$ change the electron density of the graphene plane through p-type doping which shifts the Fermi level to the valence band

(Aragaw, Su, Rick, & Hwang, 2013). This transition will inevitably increase the conductivity of the rGO in the nanocomposite. The equivalent electrical circuit used for fitting the impedance spectra was shown in the inset of **Figure 5.19**.

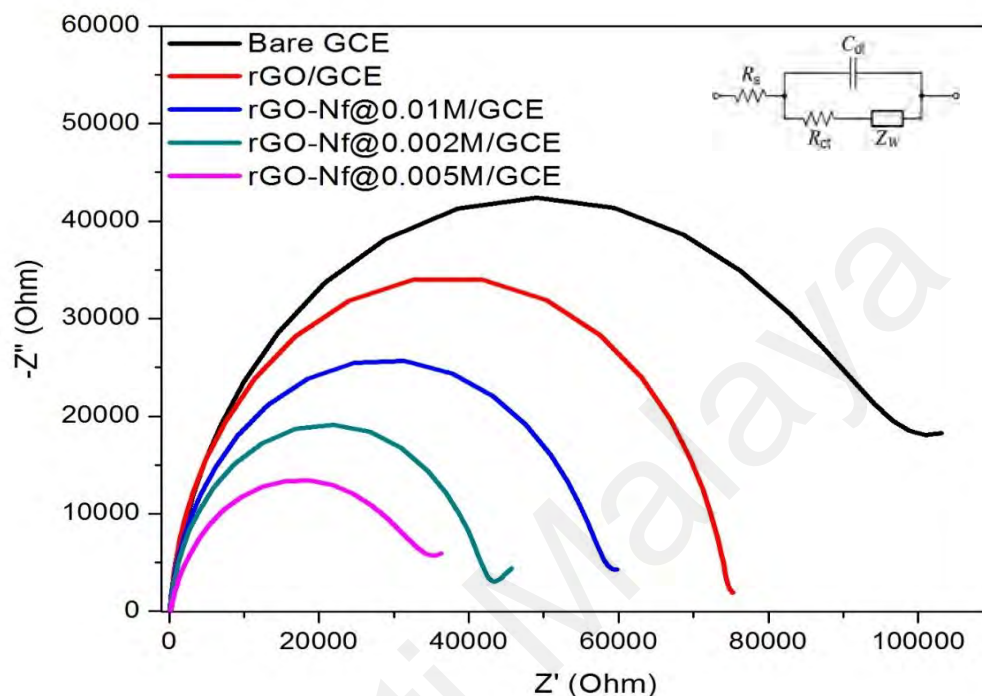


Figure 5.19. The Nyquist plots for bare GCE, rGO-Nf@0.002M, rGO-Nf@0.005M and rGO-Nf@0.01M.

5.3.4 Electrochemical detection of *Salmonella* using rGO-Nf nanocomposite-modified electrode.

5.3.3.1 Optimization of rGO-Nf@0.005M/GCE

The optimization of parameters such as the effect of rGO-Nf loading and aptamer concentration was investigated to achieve optimal sensing performance. The CV measurement of the fabricated electrode was carried out using Zobell solution at a scan rate of 100 mVs^{-1} . Firstly, the effect of rGO-Nf@0.005M loading on the GCE electrode was optimized by loading different amounts of rGO-Nf@0.005M ranging from 1 mg mL^{-1} to 13 mg mL^{-1} (**Appendix D2 (A)**). The current density of rGO-Nf@0.005M/GCE

electrode increased with an increasing amount of rGO-Nf@0.005M/GCE and achieved maximum current density at the amount of 7 mg mL⁻¹. The current density started to decrease as the amount of rGO-Nf@0.005M/GCE more than 7 mg mL⁻¹ due to the formation of thick layer on electrode surface that reduces the electron transfer from the electrolyte to the electrode (Guo, Guo, et al., 2013).

Then, the effect of aptamer concentration on the sensing performance of the electrodes was also optimized (**Appendix D2 (B)**). The fabricated electrodes were exposed to different concentration of the aptamer ranging from 1 μmol L⁻¹ to 15 μmol L⁻¹. The optimum current density was obtained for aptamer concentration of 5 μmol L⁻¹. When the aptamer concentration more than 5 μmol L⁻¹ loaded on the electrode, the current density decreased dramatically. This is attributed to the steric hindrance and strong electrostatic repulsion between the aptamers created by the presence of a high quantity of negatively charged ssDNA on the electrode surface (Urmann, Modrejewski, Scheper, & Walter Johanna, 2017).

The effect of increasing scan rate (10 to 100 mVs⁻¹) on the electrochemical performance of the rGO-Nf@0.005M/GCE was investigated (**Appendix D2 (C)**). Increasing scan rate means an increase in the charging current and reduction in the response time but the actual capacitance is constant for a material. The anodic peak was positively shifted with an increase in the scan rate and exhibited good linearity.

5.3.3.2 Electrochemical analysis of rGO-Nf@0.005M/GCE

The CV and EIS were recorded as shown in **Appendix D3** and **Figure 5.20** to study the electrochemical behavior of rGO-Nf@0.005M/GCE after the immobilization of biorecognition element (aptamer). In both CV and EIS plots, rGO-Nf@0.005M/GCE showed the highest peak current and lowest electron transfer resistance. This is due to the increased in electron transfer rate at the electrode's interface promoted by the coating of

cationic Nafion polymer as described previously. However, after the immobilization of the aptamer on the electrode's surface, a drastic decrease in both conductivity and charge transfer resistance can be observed. The electrostatic attraction between positively charged cationic polymers and negatively charged DNA enables strong anchoring of the aptamer on the surface of the electrode (Mady, Awad, El-Guendy, & A. Elsayed, 2011). The presence of rGO-Nf/aptamer complex (polyplex) will create a barrier for the diffusion of the electrochemical probe $[\text{Fe}(\text{CN})_6]^{3-/4-}$ at the electrode interface which caused a decrease in the conductivity of the ssDNA/rGO-Nf@0.005M/GCE. When the ssDNA/rGO-Nf@0.005M/GCE electrode is exposed to the bacterial cells, the peak current further decreased. The negatively charged cell membrane repels the negatively charged redox probe $[\text{Fe}(\text{CN})_6]^{3-/4-}$, which inhibits the diffusion on the redox molecules on the graphene's surface and this phenomenon further decreases the peak current and increases the charge transfer resistance.

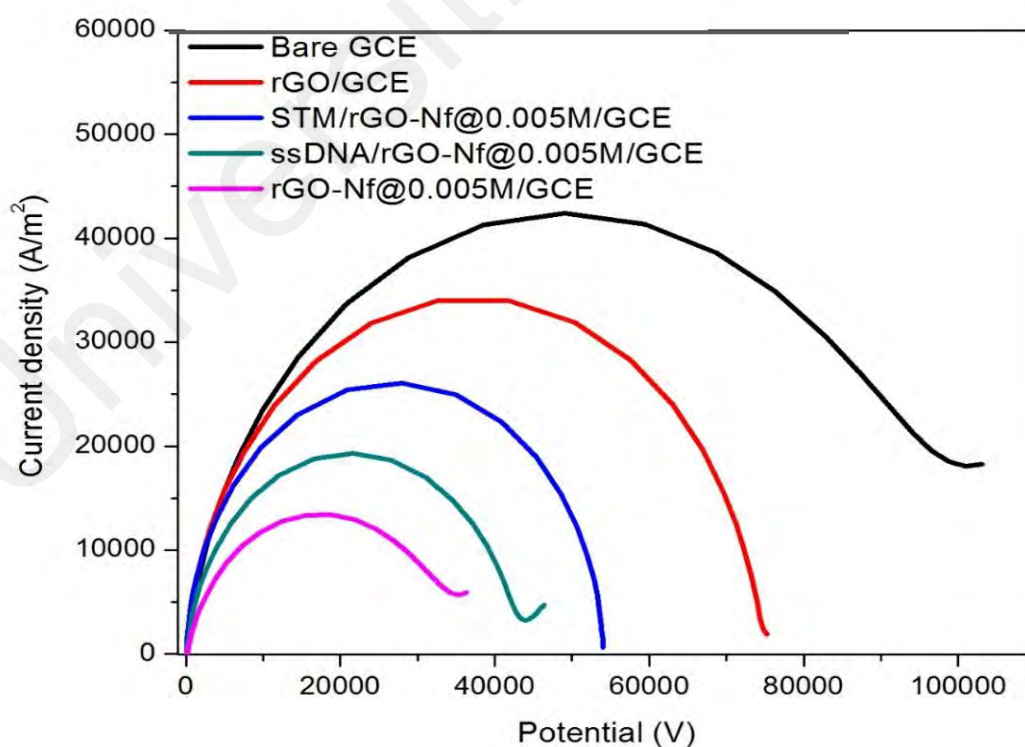


Figure 5.20. The Nyquist plot of bare GCE, rGO-Nf@0.005M/GCE, STM/ssDNA/rGO-Nf@0.005M/GCE and ssDNA/rGO-Nf@0.005M/GCE electrodes in Tris-HCl buffer.

5.3.3.3 Electrochemical detection of bacterial cells using ssDNA/rGO-Nf@0.005M/GCE

The selectivity test was conducted in 0.1 M PBS solution to study the efficiency of the fabricated electrode in detecting the bacterial cells and the limit was identified too. The redox behavior of ssDNA/rGO-Nf@0.005M/GCE at different concentrations of bacteria ranging from 10^8 to 10^1 cfu/mL was investigated by using DPV in 0.1 M PBS (pH 6.5) as shown in **Figure 5.21 (A)**. The results obtained through DPV agreed with the CV and EIS data. Similarly, the ssDNA/rGO-Nf@0.005M/GCE peak current decreased due to the blockage of the electron-transfer of redox probe. The electron-withdrawing groups in Nafion make the rGO-Nf more electrophilic and positively charged. This will promote the electrostatic interaction with a negatively charged DNA aptamer. When the bacterial cells introduced to the system, the peak currents were observed to increase linearly with the increasing bacterial concentrations as shown. This is attributed to the formation of a stem-loop structure by aptamer upon the binding to its targeted cell. The conformational changes between the aptamer-bacterial complex decrease the coverage of aptamer on the electrode surface which enhances the rate of electron transfer rate. The conformational changes between the aptamer and bacterial cell bring the negatively charged *Salmonella* cells closer to the rGO-Nf surface and induce holes in the graphene, causing an increase in conductivity (Mohanty & Berry, 2008). The increase in peak current upon the binding of bacterial cells is proportional to the concentration of bacterial targets. The peak current was plotted with the logarithm of the target bacterial concentration as shown in **Figure 5.21 (B)** and the relationship can be described as:

$$I = 0.15 (\pm 0.03) \log c + 0.94 (\pm 0.05)$$

with the correlation coefficient of $R_2 = 0.98$, where I is the current density ($A m^{-2}$) and $\log c$ is the logarithm of the cell concentration. The binding of the bacterial targets affects

the interfacial electron-transfer kinetics and increases the conductivity of the surface-bound aptamer–bacteria constructs. When the number of bacteria increases, the negatively charged lipopolysaccharides on its cell wall contributes to more negative charges. These strong negative charges induce more holes on the surface of graphene and increase the current proportional to the concentration of the bacterial targets bound on the electrode surface (Thiha et al., 2018).

The selectivity of the aptasensor was also studied by exposing the fabricated electrodes to different types of non-*Salmonella* bacteria (*Escherichia coli*, *Shigella dysenteriae*, *V. cholerae*, *Staph. aureus* and *Klebsiella pneumoniae*). **Figure 5.21 (C)** shows, the no drastic changes in the conductivity of the electrode exposed to non-*Salmonella* bacteria as compared to the *Salmonella* bacteria. This result indicates, the fabricated aptasensor exhibits high selectivity towards *Salmonella* bacterial detection.

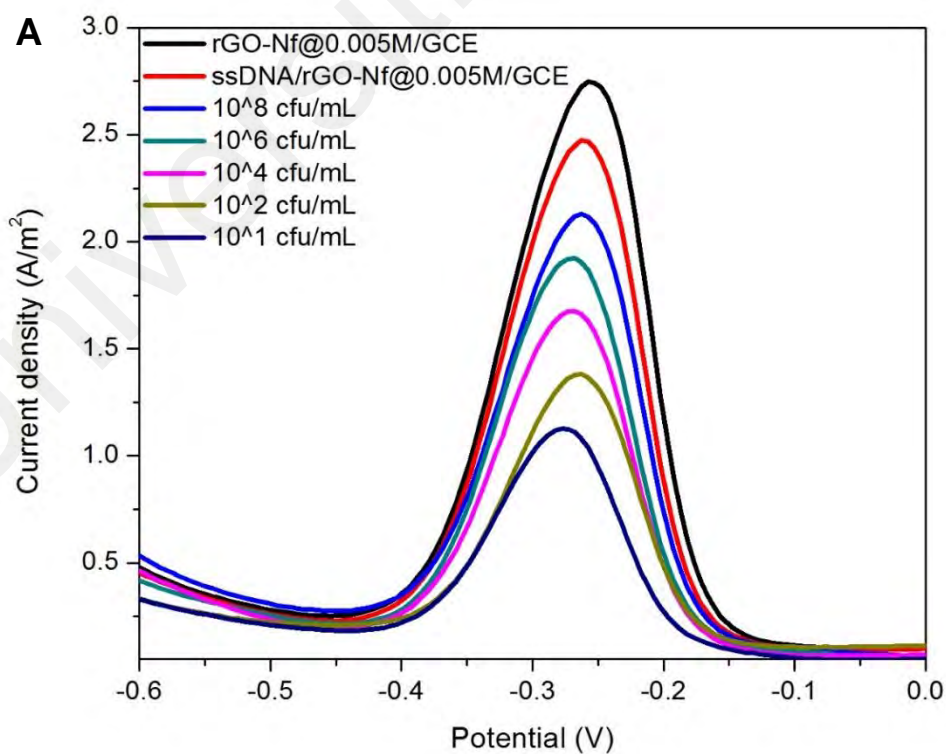


Figure 5.21, continued.

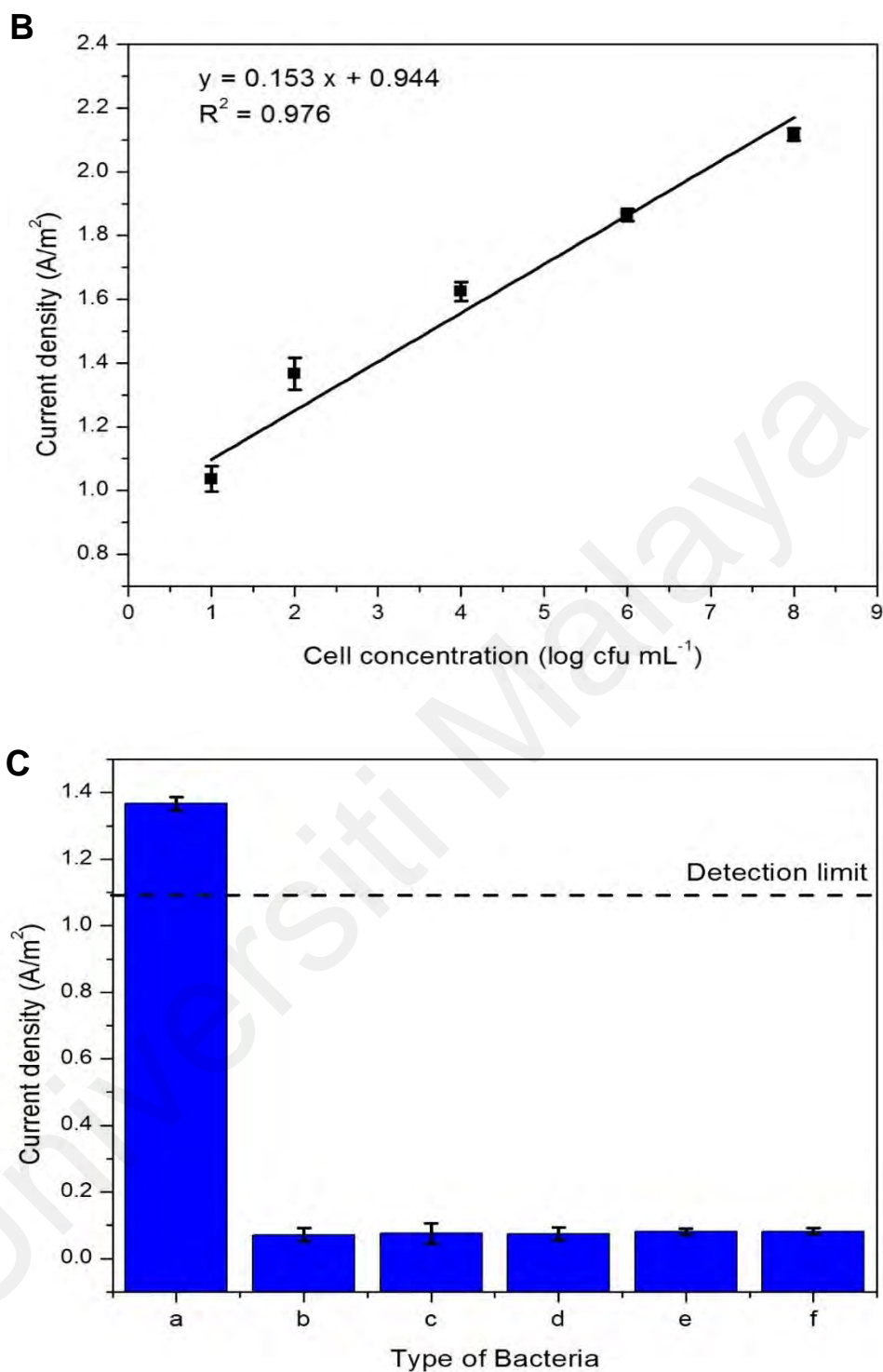


Figure 5.21 (A) DPV of ssDNA/rGO-Nf@0.005M/GCE, (b) 10^8 cfu mL^{-1} , (c) 10^6 cfu mL^{-1} (d) 10^4 cfu mL^{-1} , (e) 10^2 cfu mL^{-1} , (f) 10^1 cfu mL^{-1} and (g) rGO-Nf@0.005M/GCE in Tris-HCl buffer, pH 7.4. (B) A linear relationship between the current density and cell concentration (logarithm). (C). DPV of (a) *S. Typhimurium*, (b) *E. coli*, (c) *V. cholerae*, (d) *K. pneumoniae*, (e) *Sh. dysenteriae* and (f) *Staph. aureus* in Tris-HCl buffer, pH 7.4.

5.3.3.4 Evaluation of the ssDNA/rGO-Nf@0.005M/GCE

The performance of the aptasensor for the detection of *Salmonella* bacteria that were naturally found in contaminated food samples was also studied. The sensor was tested on chicken meat samples obtained from the markets (n=5). **Figure 5.22** shows that the detection of *Salmonella* present in food samples was possible because the current density obtained for all food samples tested was correlated to the linear regression obtained for the sensitivity test.

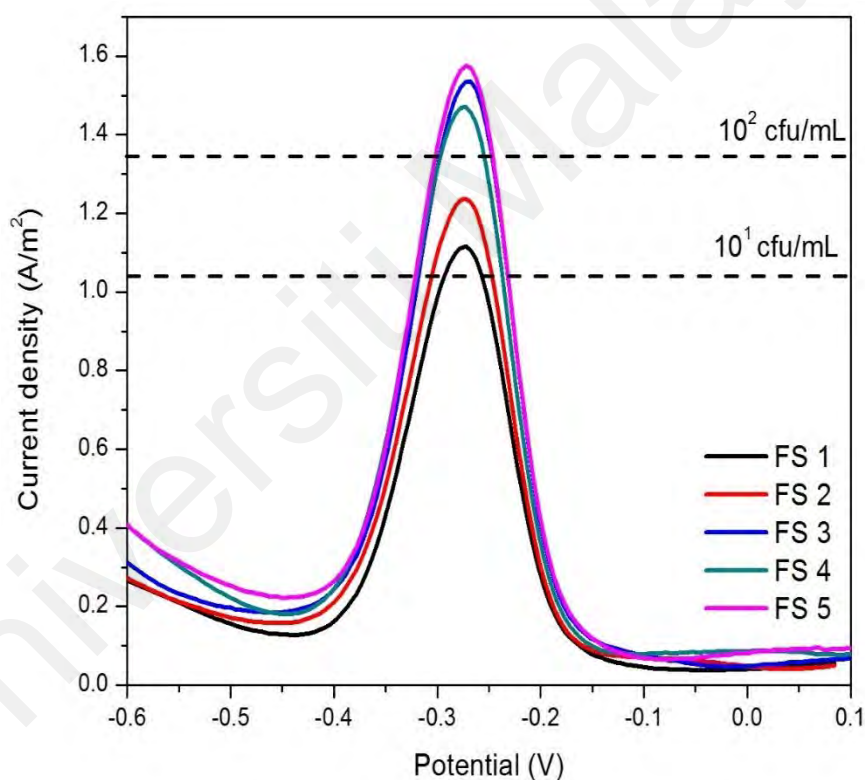


Figure 5.22 DPV of spiked chicken food samples with different concentrations of bacteria recorded in Tris-HCl buffer, pH 7.4.

5.3.3.5 Reproducibility and stability of the rGO-Nf@0.005M/GCE

The reproducibility of the fabricated electrode was studied using a successive CV measurement of five different electrodes in 0.1 M PBS at 100 mVs^{-1} . **Figure 5.23** shows there is no evident changes between the electrodes with good reproducibility with a RSD of 0.71 %. The shelf life of the electrodes was experimented by measuring the CV of an electrode for 28 days. The peak current of the electrode was observed to decrease slightly with an RSD value of 1.15 %. The low RSD values obtained for rGO-Nf@0.005M/GCE showed excellent reproducibility and stability of the electrode.

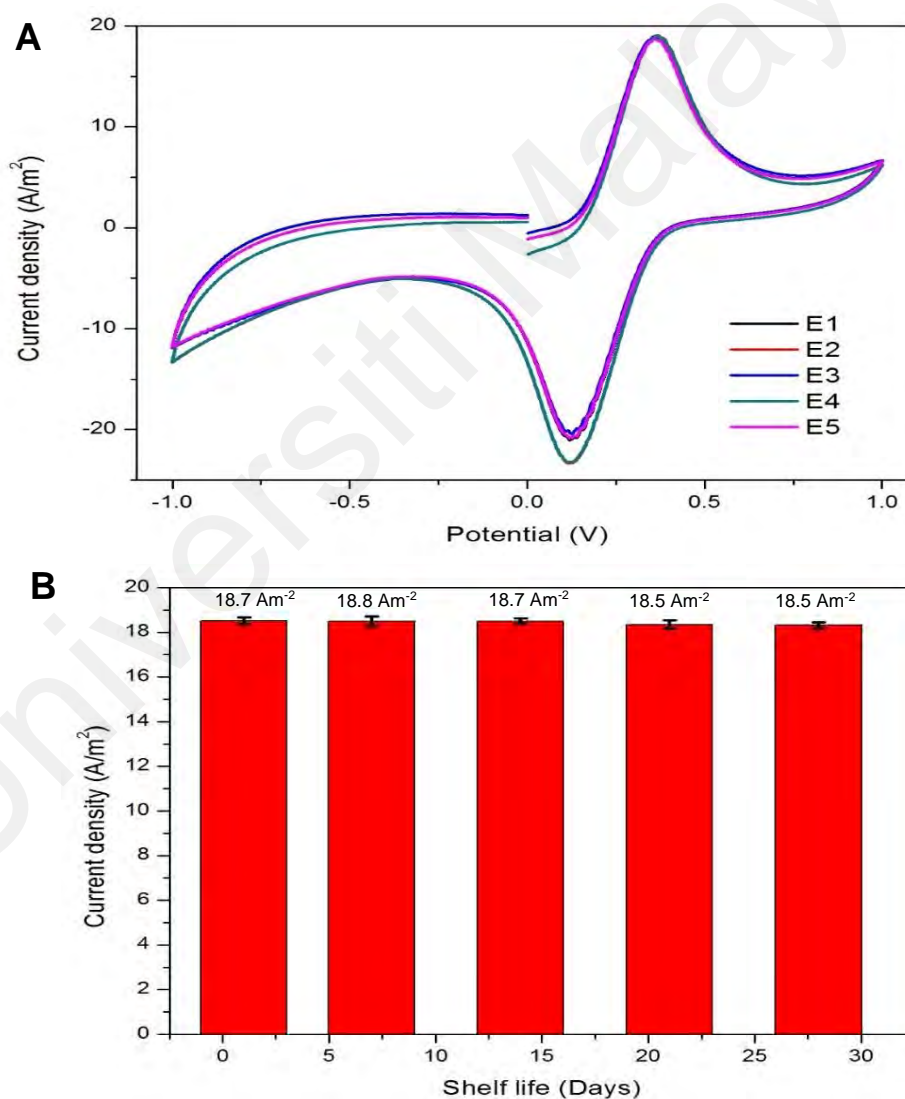


Figure 5.23. (A) CV curves of five different rGO-Nf@0.005M/GCE modified electrodes and (B) histogram of shelf life of rGO-Nf@0.005M/GCE electrode up to 28 days recorded in 10X PBS at a scan rate of 100 mV s^{-1} .

5.4 Validation of experimental results with PCR method

The results obtained by aptasensor for sensitivity test was validated with PCR assay as shown in **Figure 5.24 (A)**. DNA extracted from the different concentrations of *Salmonella* cultures (10^8 - 10^1 cfu mL⁻¹) were tested with PCR. The amplification of the ompC of *S. Typhimurium* gave a DNA fragment of 204 bp. The results obtained also showed the detection limit of PCR was only up to 10^2 cfu mL⁻¹ as compared to the detection limit of aptasensor which was 10^1 cfu mL⁻¹. This shows aptasensing is more sensitive than PCR. Moreover, the selectivity and specificity of the aptamer to other types of *Salmonella* and non-*Salmonella* bacteria were also investigated. For both the selectivity and specificity test, the DNA of *Salmonella* and non-*Salmonella* bacteria were captured using aptamer-conjugated magnetic beads. All the DNA were extracted and subjected to PCR reaction using species-specific primers.

Figure 5.24 (B) shows the selectivity test of the aptamer against other types of *Salmonella* bacteria namely, *S. Paratyphi A*, *S. Enteritidis*, *S. Typhimurium*, *S. Typhi*, *S. Albany*, *S. Corvallis* and *S. Pullorum*. The PCR image showed the presence for a positive band for all other types of *Salmonella* bacteria which indicates the aptamer used in this study is selective for all other *Salmonella* bacteria other than *S. Typhimurium*. Moreover, **Figure 5.24 (C)** shows the PCR obtained for different types of bacteria. The PCR amplification for non-*Salmonella* bacteria showed the absence of a positive band for all the five samples tested indicating the aptamers used in this study were only specific to *Salmonella* bacteria.

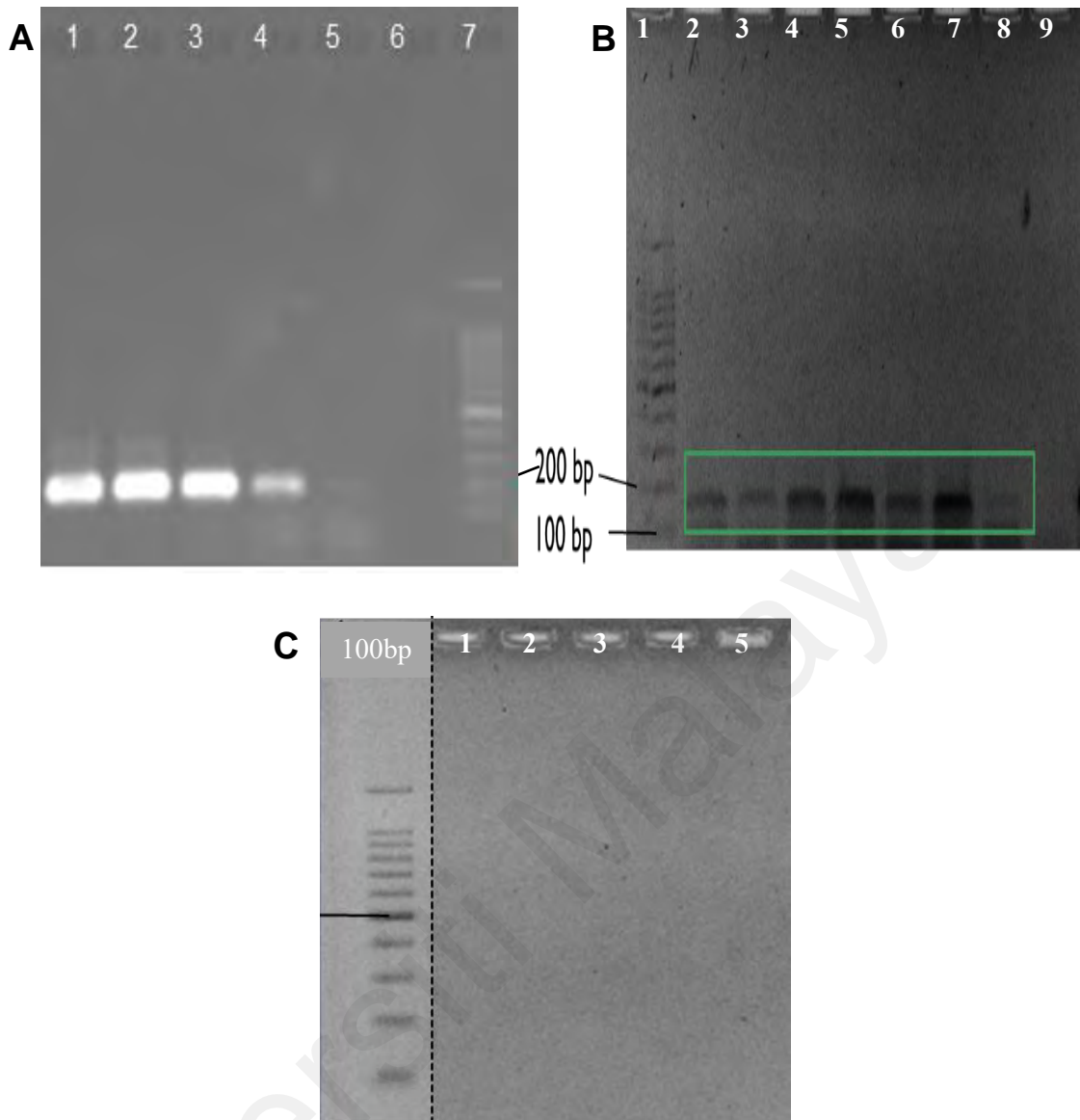


Figure 5.24. (A) The sensitivity of detection by PCR for *S. Typhimurium*. Gel electrophoresis patterns of PCR products obtained at different concentration of DNA: Lane 1, 10^8 cfu mL⁻¹; Lane 2, 10^6 cfu mL⁻¹; Lane 3, 10^4 cfu mL⁻¹; Lane 4, 10^2 cfu mL⁻¹; Lane 5, 10^1 cfu mL⁻¹; Lane 6, negative control; and Lane 7, 100 bp ladder. (B) The specificity test for different types of *Salmonella* bacteria: Lane 1, 100 bp ladder; Lane 2, *S. Typhimurium*; Lane 3, *S. Enteritidis*; Lane 4, *S. Paratyphi A*; Lane 5, *S. Typhi*; Lane 6, *S. Albany*; Lane 7, *S. Corvallis*; Lane 8, *S. Pullorum*; and Lane 9, negative control. (C) The selectivity test for non-*Salmonella* bacteria: Lane 1, *V. cholerae*; Lane 2, *Sh. dysenteriae*; Lane 3, *E. coli*; Lane 4, *K. pneumoniae*; and Lane 5, *Staph. aureus* with 100 bp ladder.

5.5 Summary

The rGO-nanocomposites (AP, TiO₂, Nf dopants) was successfully synthesized using a simple and facile chemical reduction method which has been used to modify GCE electrodes. The effect of the dopant concentration on the electrochemical sensing performance was performed and the results showed that rGO-AP@0.005M/GCE, rGO-TiO₂@0.4M/GCE and rGO-Nf@0.005M/GCE demonstrates the highest cathodic current response.

Under the optimized experimental condition, these electrodes showed sensitive and selective electrochemical sensing of *S. Typhimurium*. The rGO-AP@0.005M/GCE, rGO-TiO₂@0.4M/GCE and rGO-Nf@0.005M/GCE achieved lowest detection limit of 1.0 cfu mL⁻¹, 2.0 cfu mL⁻¹ and 1.0 cfu mL⁻¹, respectively. It is noteworthy that these modified electrodes were highly selective and resistant toward common interfering bacterial species such as *V. cholerae*, *Sh. dysenteriae*, *E. coli*, *K. pneumoniae* and *Staph. aureus*. Further investigations on the reproducibility and shelf life of the electrodes were also studied. The results show that the rGO-nanocomposites electrodes exhibited good reproducibility and shelf life up to 28 days. Furthermore, these electrodes also showed good accuracy and high precision for detecting the presence of *Salmonella* in food samples.

The strong synergistic effect between rGO and AP, TiO₂, Nf dopants enhances the sensing performance due to the increased active surface area, effective electron transfer, hence improved the sensitivity of the sensor electrode. The results obtained prove a great potential of organic dye, metal oxide and polymer-modified rGO for the development of novel electrochemical sensing devices for the detection of foodborne pathogens.

CHAPTER 6

THE MECHANISM OF APTAMER-BACTERIAL INTERACTION ON THE SURFACE OF RGO-NANOCOMPOSITE

6.1 Overview

The presence of bacterial pathogens at an infectious level in the food supply is often correlated to the occurrence of foodborne illness worldwide. The highly conductive nature of graphene-based nanomaterials has driven exploration of their applications in the field of biosensors (nanoelectronics devices) for the detection of foodborne pathogens. For the optimal performance of the graphene-based biosensor, aqueous solution or electrolyte is necessary to provide the liquid condition for the operation (Wu, Meyyappan, & Lai, 2018). Moreover, the surface functionalization of graphene with a sensing probe such as the aptamer is crucial for specific and sensitive detection of the whole-cell bacteria (Zhao, Wang, Jia, & Li, 2018). This concept has been established in this work in the previous sections.

Graphene is a zero-gap semiconductor which consists of conduction and valence bands meets at Dirac points that result in the conductive nature of graphene (Giubileo & Di Bartolomeo, 2017). The Brillouin zone of graphene is the unit cell of the reciprocal lattice which is formed by the π -band electron dispersion and also known as honeycomb lattice. This zone consists of Γ center and two equivalent corners (k and k') as shown in **Figure 6.1** (Huang, Nurbawono, Zeng, Gupta, & Liang, 2016).

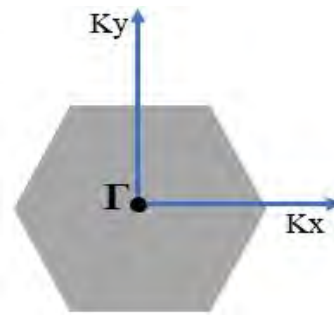


Figure 6.1. The Brillouin zone of graphene

Six points in the two-dimensional Brillouin zone where the bands meet is Dirac points. Each carbon atom has three bonds in the plane and one orbital perpendicular to the plane. During the chemisorption on the surface of graphene, the π bond breaks and produces an additional σ bond that transit graphene structure from sp^2 to sp^3 hybridization. Electrons from the perpendicular orbitals form bands closest to the Fermi level are denoted as π and π^* bands which contribute to the electronic properties of graphene. In the band structure of monolayer graphene, the π band corresponds to the valence band and the π^* band is the conduction band. As shown in **Figure 6.2**, the linear bands cross exactly at the Fermi energy (circled), thus there is only one state which can be treated as a hole or as an electron. Since there are no conducting states at the Fermi level, graphene behaves like a gapless semiconductor (also called semi-metal) (Lu, Yu, Wen, & Chen, 2013).

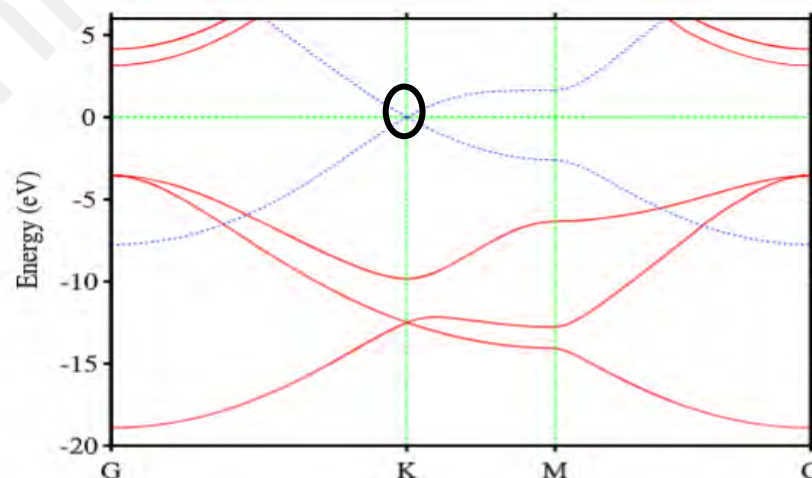


Figure 6.2. The electronic band structure of graphene. Red lines indicate σ bands and the blue line indicates π band. Adapted from (Boukhvalov & Katsnelson, 2009).

However, the electronic applications are handicapped by the absence of a semiconducting gap in graphene. Thus, the physical and electronic properties of graphene can be improved through surface functionalization with chemical dopants such as organic dyes, metal oxides and polymers (Loh, Bao, Eda, & Chhowalla, 2010). These modifications create a doping effect on graphene that will shift the Fermi level of graphene from valence to the conduction band which increases the overall conductivity of the composite material (Rani & Jindal, 2013). Another fascinating property of graphene is the shifting of Fermi level to conduction band from the valence band is very tunable by applying a gate voltage (Craciun, Russo, Yamamoto, & Tarucha, 2011). The gate voltage gives graphene an ambipolar electric field effect. The perpendicular electric field applied to multilayers of graphene modifies the electronic structure near the K point and may induce an energy gap in the electronic spectrum (Avetisyan, Partoens, & Peeters, 2009).

Doping controls many of the electronic properties of graphene, such as the carrier concentration and conductivity (Pinto & Markevich, 2014). Doping helps to keep the defect density of graphene minimal because defects may degrade the electrical properties such as mobility and conductivity (Beams, Gustavo Cancado, & Novotny, 2015). In fact, graphene is far more sensitive to changes in carrier concentration than semiconductors such as silicon. Zero-bandgap graphene has limited photoluminescent property but the presence of oxygen in rGO improves the PL properties of graphene (Rajoba, Sartale, & Jadhav, 2018). The chemical doping further increases the PL property of graphene which gives the material a definite bandgap (Xu et al., 2017). The shifts of the Fermi level in graphene can be characterized by using PL that helps to study the bandgap introduced on the electronic configuration of graphene (D. Lounis et al., 2010). Since the conduction and valence band intersect at the Dirac point, intuitively the Fermi level must be extremely sensitive to the carrier concentration (Garg, Dutta, & Roy Choudhury, 2014).

Dirac cone with no doping, hole doping and electron doping are shown in **Figure 6.3**. The Fermi level for each type of doping differs. For p-type doping which is also a hole doping, the Fermi level shifts downwards and vice versa for n-type doping (electron doping). During p-type doping, more holes are created resultant of the flowing of electrons from graphene to adsorbent. The holes created easily jump to the valence band and this phenomenon is represented by a shift of Fermi level near the valence band. However, during n-doping, the proportion of electrons is more than holes in which it is easier for the free electrons to gain very low energy and jump into the conduction band. This is because the electrons are sitting at the Fermi level (which is very close to the conduction band) and they can shift to the conduction band by gaining a few eV of energy.

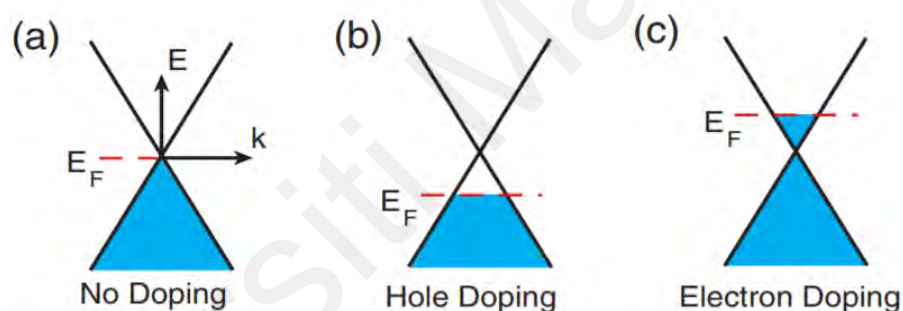


Figure 6.3. The Fermi level in graphene for (a) absence of doping, (b) p-doped and (c) n-doped. Adapted from (Beams et al., 2015).

Although the excellent electrochemical performance of graphene has been achieved experimentally using electrochemical approaches, understanding the changes happened on the surface of graphene upon the interactions with bacterial targets is crucial for further development and optimization of aptasensors for various applications. Thus, in this section multi-analytical approaches (Raman, FTIR, PL) were undertaken to understand the detailed mechanism involving bacterial detection and to prove the existing theoretical explanation. Theoretically, some studies reported that the changes in the current response resulting from the binding of bacteria on the surface of probe-modified

graphene were due to the modification in the graphene's charge carrier density (Wu et al., 2017; Wu et al., 2018). The aptamer immobilized on the surface of graphene binds to the whole-cell bacteria with high affinity and undergo conformational changes which bring the negatively charged bacterial cells closer to the surface of graphene. This binding will induce holes in graphene and increases the hole carrier density which results in electrical detection. This proposed mechanism in this study could serve as a guidance for the design, optimization and operation of graphene-based biosensors for future applications.

6.2 Chemical characterization of aptamer-bacteria interaction on graphene-nanocomposite.

6.2.1 Raman spectroscopy

Raman spectroscopy is highly sensitive to detect changes in the electronic structure of materials and widely used to study the doping effect on the graphene (Beams et al., 2015). The shift of the G band and its intensity ratio (I_D/I_G) in the Raman spectrum are the indicators of doping effect on graphene. **Figure 6.4** shows the Raman spectra of the nanocomposites and rGO. The G bands of composite materials were observed to the left side as compared to rGO. The iLO and iTO phonons are responsible for the main Raman bands observed in graphene. It is important to note that the iTO and iLO phonon energies are highly dispersive at the K points. The phonon energy softening at these points is known as the Kohn anomaly (Piscanec, Lazzeri, Mauri, Ferrari, & Robertson, 2004) which is caused by phonon energy renormalization due to electron-phonon coupling.

In this process, the phonon creates a virtual electron-hole pair that re-combines and creates another phonon. The doping of graphene decreased the probability of excited charge carrier recombination (Beams et al., 2015). The decreased probability afforded non-adiabatic photon perturbations removed the Kohn anomaly and increased the energy of the phonons at the Γ point and K point. The increased phonon energy resulted in the

Raman G and D peaks with higher frequency and larger wavelength. This can be observed in Raman peaks illustrated in **Figure 6.4**. The Raman peaks of rGO-nanocomposites slightly shifted to a larger wavelength after the chemical doping proves as compared to rGO. Chemical doping can change the Fermi level and potentially open a bandgap in graphene.

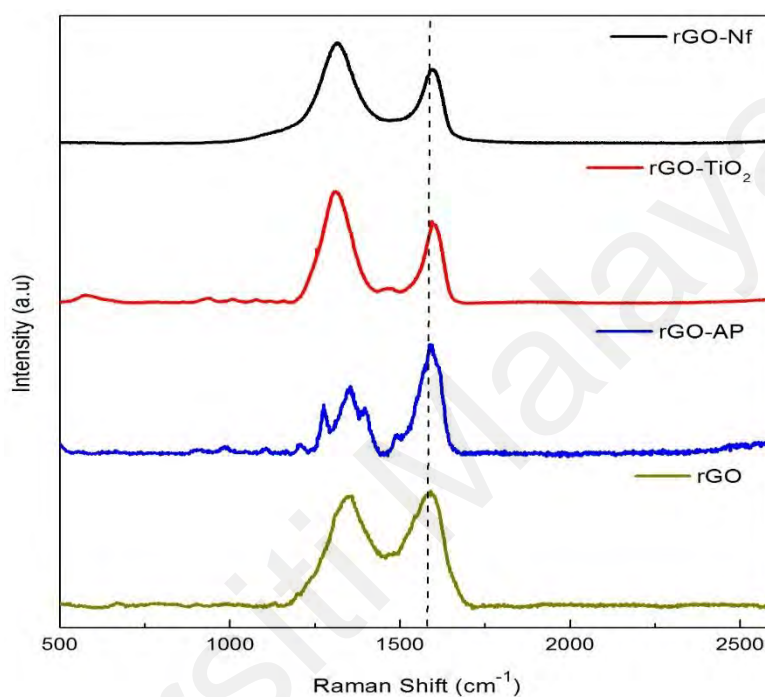


Figure 6.4. The Raman spectra of rGO-nanocomposites in the presence of aptamer and bacteria.

6.2.2 Photoluminescence spectroscopy

The chemically doped graphene behaves more like an extrinsic semiconductor. This is because any impurities or dopants added to a pure material will give semiconductors an extrinsic property as compared to pure graphene which is an intrinsic semiconductor (Hofmann, Hsieh, Chang, Tsai, & Chen, 2015). In extrinsic semiconductors, the Fermi level is not situated in between the gaps and the position is dependent on the type of dopant and carrier concentration (Roy, 1977). When the impurities are added to a material, the overall carrier concentration (the number of

electrons in the conduction band or the number of holes in valence band) increases. However, the increasing concentration of carriers can decrease the mobility of the electrons at a constant temperature. Thus, the relationship between the bandgap and conductivity in an extrinsic semiconductor is dependent on the concentration of carriers. To further understand the relationship between the bandgap and conductivity without neglecting the type of dopants, the photoluminescence analytical tool was employed in this study.

Through PL, the bandgap energy of the graphene in the presence of dopants, aptamer and bacterial cells can be calculated. The changes in the bandgap energy can be used to study the change in the electronic configuration of graphene. Based on the results obtained for PL of rGO-nanocomposites as shown in **Figure 6.5**, the changes in the bandgap energy for nanocomposites upon the interaction with dopants, aptamer and bacterial cells were summarized in **Table 6.1**.

Table 6.1: Summary of the changes in the bandgap in rGO-nanocomposites

rGO-nanocomposite	Bandgap Energy (eV)		
	Dopants	Aptamer	Bacterial cells
rGO-AP	2.15	1.81	1.97
rGO-TiO ₂	1.72	1.91	2.00
rGO-Nf	1.98	2.05	2.12

In general, the bandgap for nanocomposites decreases upon the introduction of chemical dopants as compared to rGO (2.25 eV). There is some correlation exists between the bandgap energy and the conductivity of the rGO-nanocomposite. All the dopants bind to graphene through covalent interactions when the GO was mixed with AP, TiO₂ and Nf separately to make a nanocomposite molecule. These chemical dopants induce either n-type or p-type doping on the graphene sheets which increase the electron density or rate

of electron transfer of the sensing material and leading to a drastic increase in conductivity of the composite compared to rGO (Muhammad Farooq, Muhammad Zahir, Muhammad Waqas, & Jonghwa, 2014; Wu, Jiang, et al., 2012). Besides carrier concentration, the changes in the bandgap can be directly correlated to the conductivity of the extrinsic semiconductors at room temperature with an applied electrical field or gate voltage due to the shifting of the fermi-level based on the type of dopants (Said, Okba, & Hachemi Ben, 2014).

Surface transfer doping is non-destructive and occurs due to the charge transfer between graphene and surface adsorbates through electronic doping in this case (Pinto & Markevich, 2014). The PL peak of rGO forms at the blue region of the spectrum due to the recovery of the sp^2 carbon network during the reduction process which widens the bandgap energy (2.25 eV) and the intensity is lowest due to surface defects created due to the removal of oxygens. The n-type doping happens on the graphene surface in the presence of Titania due to its electropositivity that easily loses an electron to graphene and makes graphene n-type doped which will shrink the bandgap by expanding the conduction band (Sivek, Leenaerts, Partoens, & Peeters, 2013). The PL peak of rGO-TiO₂ exhibited a red shift (longer wavelength) and the intensity of the peak increased (fewer surface defects as the holes in graphene are recovered by the electrons of Titania) as compared to rGO due to the increase in electron-rich density distribution near the Fermi levels. The bandgap energy is calculated to be 1.72 eV as compared to rGO which is 2.25 eV and the decrease in bandgap energy reflects the increase in conductivity of the nanocomposite.

On the other hand, sulfonated AP dye and perfluorinated Nf give graphene p-type doping due to the electron-withdrawing properties of sulfonic acid groups which withdraw electrons from the graphene surface and create a hole (Kwon et al., 2018). However, in both cases the conductivity of graphene increases due to the hole density of

graphene created through p-type doping and presence of a small number of holes through p-type doping can finely tune the conductivity of graphene (Jafri et al., 2009; Jo et al., 2015). In p-type doping, keeping the hole density smaller is crucial because high-density defects will reduce the conductivity of graphene drastically (Chen et al., 2018). Due to this phenomenon, a drastic increase in the conductivity of rGO nanocomposites (discussed in the previous chapter) can be observed as compared to the rGO only. The bandgap for rGO-AP and rGO-Nf were 2.15 eV and 2.08 respectively. The PL peak for both nanocomposites showed a red shift which narrows the bandgap as compared to rGO. Both PL peaks exhibited the highest intensities indicating fewer defects created during the functionalization process. The covalent binding effectively introduces a bandgap through chemical doping and makes the functionalized graphene potentially useful as semiconducting nanomaterials and nanoelectronic devices. Moreover, the concentration of dopants should be precisely controlled to preserve the electrical properties of graphene that could be potentially tailored in nanoelectronics (Yadav & Dixit, 2017).

As discussed earlier, the binding of the aptamer on the surface of rGO-nanocomposite induces immediate changes in the rate of electron transfer on the surface of the nanocomposite material which affects the overall conductivity of the sensing material. The short synthetic DNA aptamer that folds to its unique 3D structure will securely anchor on the nanocomposite material and form an ultrathin layer. Aptamer immobilized on the rGO-nanocomposite through π - π stacking or non-covalent bonding between aromatic bases of aptamer with rGO nanosheets or electrostatic interaction among charged groups of the rGO-nanocomposite and functional groups (-P or -OH) of aptamer (Kim, Ha, Jung, Kim, & Yoon; Sharma, Kanchi, Sabela, & Bisetty, 2016). The binding of the aptamer will cause the electrode's voltage to change which can be characterized using CV or EIS as explained in previous sections. The changes in conductivity resulting from the aptamer immobilization on the sensing platform can also

be studied using the changes occur in the bandgap energy upon the aptamer hybridization on the rGO-nanocomposite. Based on the results shown in **Figure 6.5**, after the aptamer immobilization, the PL peaks of ssDNA/rGO-TiO₂ and ssDNA/rGO-Nf shifted to the blue region which widens the bandgap to 1.91 eV and 2.05, respectively as compared to rGO-TiO₂ and rGO-Nf which is associated to the p-type doping that creates holes on the graphene. The peak intensity remains the same for rGO-TiO₂ because the non-covalent bonding of aptamer on the graphene prevents the creation of surface defects. However, the aptamer binding shifts the ssDNA/rGO-AP (1.81 eV) to the red region as well as to longer wavelength which further narrows the bandgap as compared to rGO-AP. These results are comparable to the CV results obtained for aptamer immobilization on rGO-nanocomposites which exhibited an increase in current for ssDNA/rGO-AP/GCE and a decrease in current for ssDNA/rGO-TiO₂/GCE and ssDNA/rGO-Nf/GCE. The difference in conductivity of different types of rGO-nanocomposite is solely dependent on the charge carrier concentration induced by chemical dopants on the graphene nanosheet. Besides, the binding of aptamer itself causes the doping effect of the rGO-nanocomposite which is responsible for the changes in the overall electrical conductivity of the sensing material. The possible mechanism that can be elucidated based on the results obtained is the negative charge of the aptamer acts as an electron-withdrawing group that introduces p-type doping on the rGO-nanocomposite material which creates a significant number of holes on graphene sheet (Yue et al., 2017). These holes can either decrease or increase the conductivity of the material. A considerable number of holes were proved to increase the conductivity of the graphene in many cases as the small vacancy defect gives graphene a metallic property. However, higher defect density can widen the bandgap of graphene and defects also may act as scattering centers which decrease the conductivity of graphene (Yu, Liao, Chae, Lee, & Duan, 2011; Zhang et al., 2011). Many studies have proved the Dirac points or Fermi level of graphene are sensitive to the immobilization of DNA

aptamer due to the doping effect (Xu, Meshik, et al., 2014). The weak π - π stacking or van der Waals interaction between aptamer and graphene can preserve the superb physical properties of graphene.

The aptamer binds to the *Salmonella* cells with high affinity. This aptamer specifically binds to the OMP of *Salmonella* which is the unique identification sequence of the protein of *Salmonella* bacteria (Joshi et al., 2009). The aptamer, in this case, folds into its G-quadruplexes structure consisting of stem-loops that carry complementary DNA sequence for a distinct non-covalent interaction of shape complementary with the epitope of protein at each binding interface. The interactions between the amino acid side chain of protein and chemical groups in the bases of DNA (Setny, Bahadur, & Zacharias, 2012). The binding of the aptamer to the bacterial cells undergoes conformational changes to fold into a distinctive structure that led to the formation of the aptamer-protein complex (Stoltenburg, Schubert, & Strehlitz, 2015). The bases in hairpin stem-loops are rich in electron densities which helps to form salt bridges between the aptamer and binding sites of protein epitopes (Cheung et al., 2013). The presence of the bacteria in the electrochemical system induces p-type doping on the rGO-nanocomposite. This is because the negative charge on the cell wall of the bacteria further increases the hole carrier density of the graphene (Wu et al., 2017). In the presence of bacteria, the conductivity of the sensing material is observed to decrease with increasing bandgap for STM/ssDNA/rGO-TiO₂ (2.00 eV) and STM/ssDNA/rGO-Nf (2.12 eV). The PL peak in the presence of negatively charged bacteria shifts to the blue-region and the intensity of the PL decreases drastically due to the surface defects created. However, in STM/ssDNA/rGO-AP, the PL peak intensity decreases and remains in the red region (longer wavelength). The bandgap for STM/ssDNA/rGO-AP (1.97 eV) decreases as

compared rGO-AP but increases as compared to the ssDNA/rGO-AP which in turn decreases the conductivity.

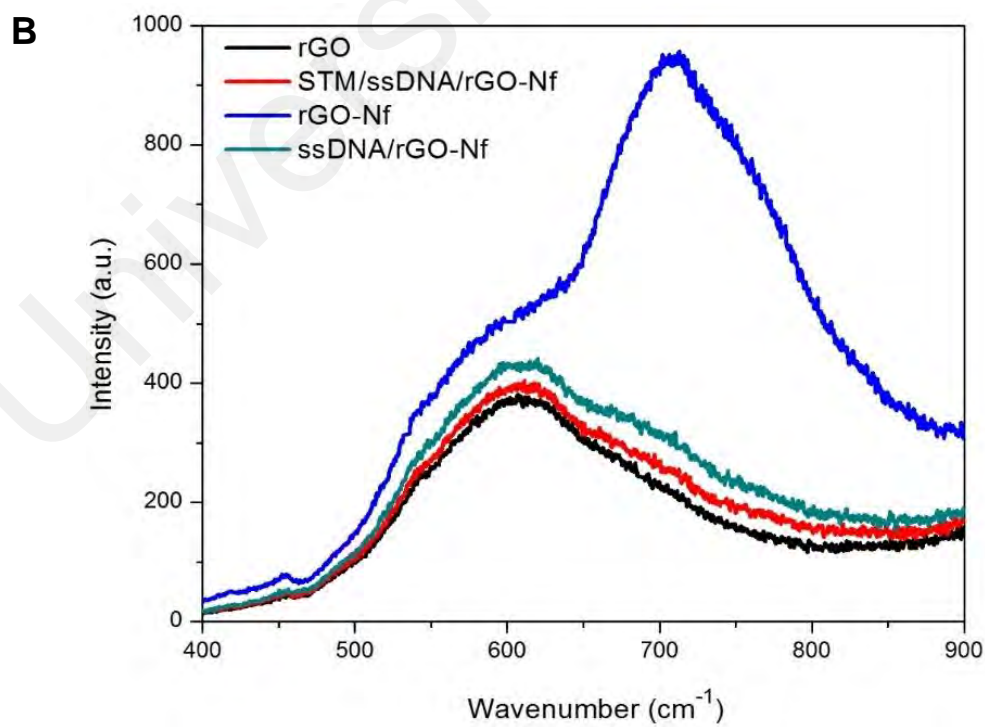
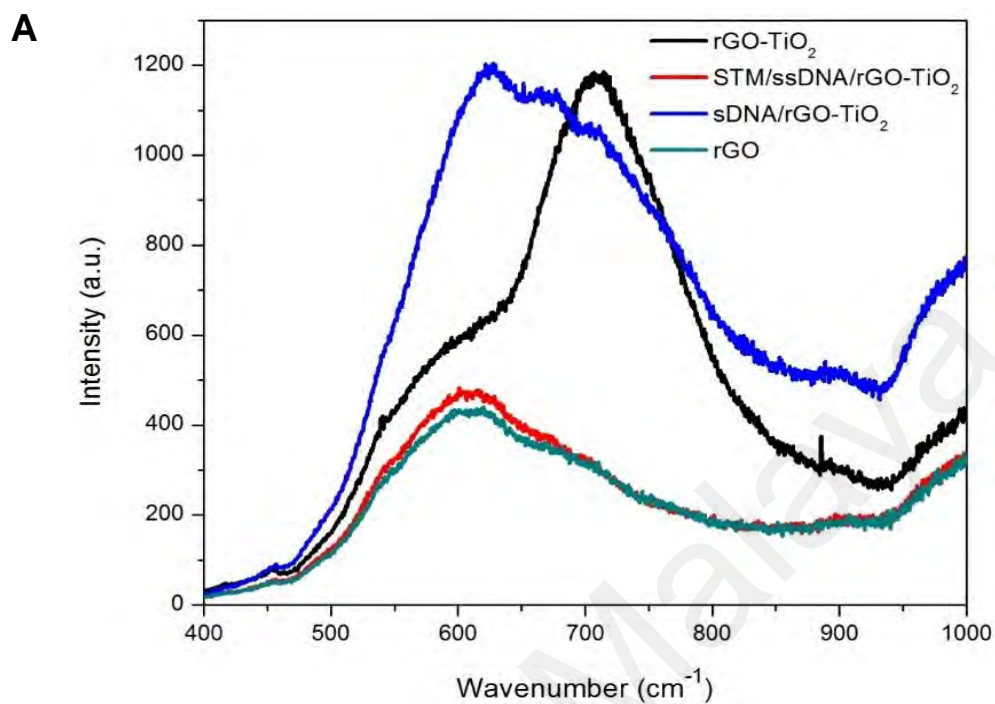


Figure 6.5, continued.

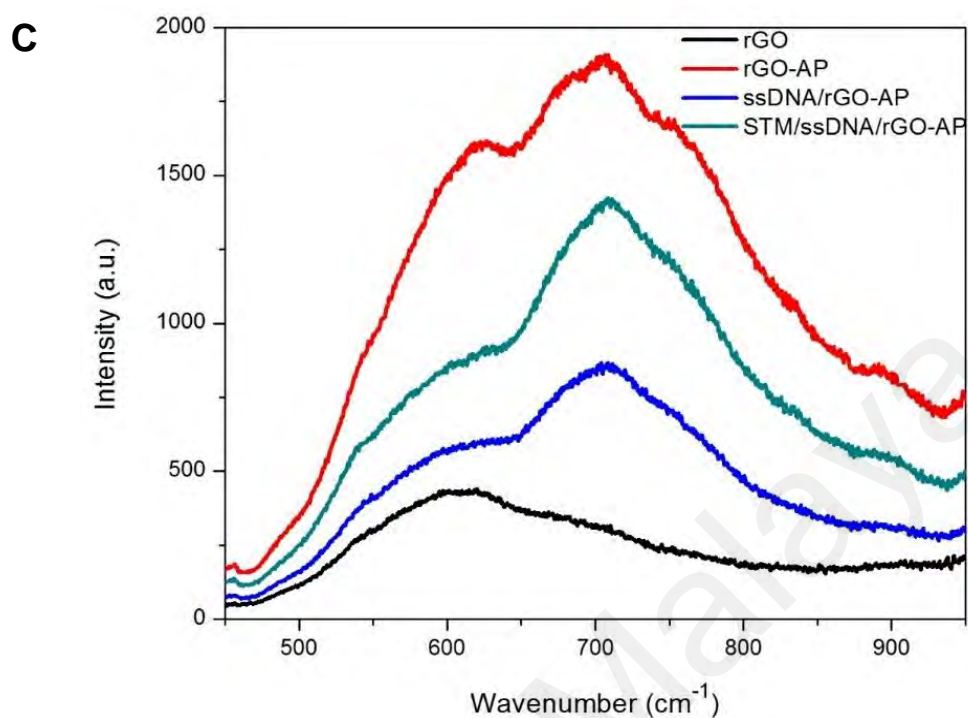


Figure 6.5. The photoluminescence spectra of rGO-nanocomposites in the presence of aptamer and bacteria.

6.2.3 FTIR spectroscopy

FTIR which is a non-destructive technique that allows the rapid and simultaneous characterization of complex materials like aptamer and bacteria immobilized on the surface of rGO-nanocomposite was adopted in this study to prove their respective presence (Helm, Labischinski, Schallehn, & Naumann, 1991). The FTIR spectra were recorded for the rGO-nanocomposites in the presence of aptamer and bacteria. The results are presented in **Figure 6.6**. The main characteristic peak of aptamer which is phosphate, -NH and aromatic ring peaks can be observed at around 1250 cm⁻¹ (phosphate anti-symmetric stretching), 750 cm⁻¹ (sugar-phosphate vibration or -NH), 950 cm⁻¹ (O-P-O bending) and about 1750 cm⁻¹ (aromatic rings of DNA bases) (Mello & Vidal, 2012) in

the rGO-nanocomposites. Besides that, some important peaks of bacteria also can be observed the FTIR of rGO-nanocomposites (Schuster, Mertens, & Gapes, 1999). The peaks are -CH_2 and CH_3 at $2850\text{-}2950\text{ cm}^{-1}$ indicate the lipid and protein contents of the cells. Moreover, PO_2^- antisymmetric stretching vibration of the bacteria can be observed at 1240 cm^{-1} which indicates the presence of nucleic acids and phospholipids. The peak at 3300 cm^{-1} also proves the presence of N-H and O-H stretching vibration of polysaccharides and proteins. Although there are peaks of aptamer and bacteria that can be prominently recorded using FTIR spectra, the important characteristic peak of rGO (1630 cm^{-1}), TiO_2 (800 cm^{-1} , 1400 cm^{-1}), AP ($500\text{-}700\text{ cm}^{-1}$) and Nf ($965\text{-}980\text{ cm}^{-1}$) still can be observed. This indicates that the presence of bacteria and aptamer does not cause any significant changes through covalent bonding to the rGO-nanocomposites thus, the conductivity of the composite material is well preserved throughout this study.

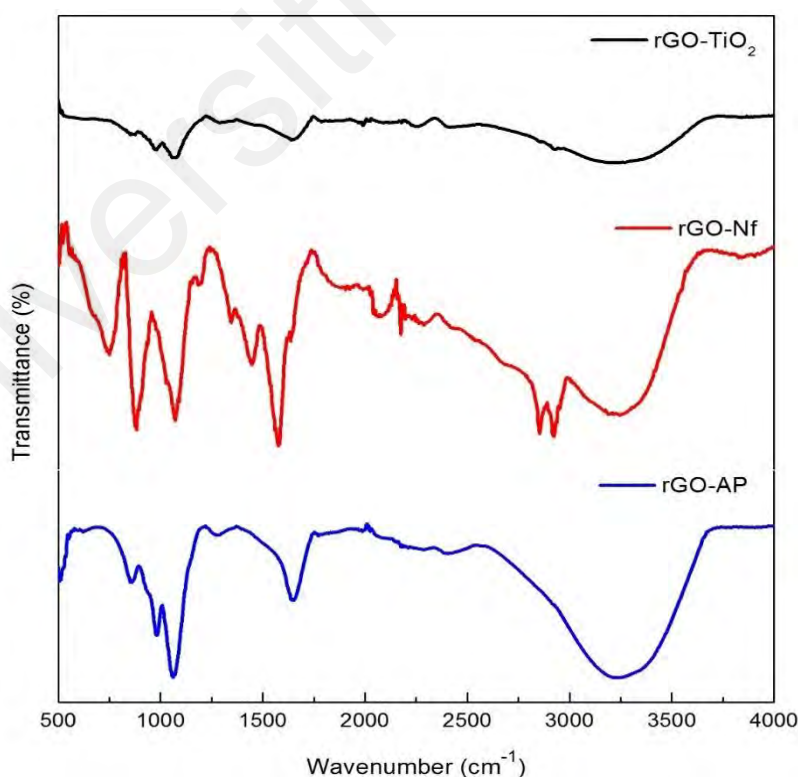


Figure 6.6. The FTIR spectra of rGO-nanocomposites in the presence of aptamer and bacteria.

6.3 Summary

Three main analytical tools such as Raman, PL and FTIR were used to study the bacterial interaction with the biorecognition element and graphene-based nanomaterials. The covalent interaction of AP dye, TiO₂ metal nanoparticles, and Nf polymer with rGO greatly modifies its Fermi level and introduces band gap. The covalent bonding between them introduced a doping effect on the rGO nanomaterial that induce changes in energy levels and contribute to the non-resonance effect resulting in an effective or enhanced charge transfer mechanism. The interaction of aptamer and bacterial cells further enhances the doping effect on the rGO-nanocomposites and changes the intensity of the bandgap in graphene. The presence of bandgap in rGO is important to tune the conductivity of rGO and transform them into functional nanoelectronic devices.

Through Raman technique, the charge transfer interaction due to the altered electron density of rGO-nanocomposites resulting from the interaction of aptamer and bacterial cells could be studied. The charge transfer event is dependent on the electronic structure of the rGO-nanocomposite itself. Based on the Raman spectra, the interaction of the aptamer and bacterial cells together with the nanoparticles changes the position of the G-band and the intensity ratio (I_D/I_G) drastically. This proves the occurrence of the doping effect and changes in the Fermi levels upon the successful functionalization of the nanoparticles and the interactions of bacterial cells on the surface. Moreover, the PL spectra also supports the findings as it helps to study the magnitude of the bandgap changes that happened at nanomaterial levels. In general, the results showed an overall decrease in the bandgap energy due to the surface functionalization of the rGO which in turn tunes the overall conductivity of the nanomaterials. Upon the interaction of the aptamer and bacteria, the increase and decrease in bandgap energy happened depending on the type p-doping effect created by them. The creation hole and electron doping tune

the overall carrier density which results in electrical detection. Moreover, FTIR technique was also employed to confirm the successful surface functionalization and attachment of aptamer-bacterial cells on the rGO-nanocomposite. All the essential peaks belong to the aptamer and bacterial cell were present along the rGO, AP, TiO₂ and Nf characteristic peaks.

Overall, this study has improved the understanding on the mechanism of the aptamer-bacterial cells interactions with rGO-nanocomposite and the changes in the nanomaterial level that causes the changes in the conductivity also could be identified. The understanding gained from this study will serve as guidance for the better design, optimization and easy or rapid operation of graphene-based biosensors for future applications.

CHAPTER 7

CONCLUSION

7.1 Conclusion and future perspectives

Carbonaceous materials, such as rGO is advantageous due to its extraordinary electronic, physical, chemical, mechanical, thermal, and optical properties that enable them to detect small changes occurring at the electrolyte-electrode interface. However, the large surface area of graphene and strong van der Waals force cause severe aggregation in solutions. Thus, this study was designed to address this issue through developing novel rGO-nanocomposites sensing materials consisting of different types of nanoparticles such as the Azophloxine, Titanium dioxide and Nafion to improve conductivity, electrocatalytic properties, biocompatibility, signal-to-noise and overall sensing performance of graphene-based sensing device to achieve high sensitivity and selectivity towards the detection of the foodborne pathogens.

The optimization and preliminary electrochemical studies were conducted to produce cost-effective good quality rGO. The rGO synthesis method especially the reduction time was carefully optimized to produce highly conductive sensing material because the heating duration determines the degree of the structural defects created on rGO. Based on the structural, morphological, and electrochemical characterization results, the optimum chemical reduction time for rGO was identified as 12h. The rGO produced at 6h and 24h reduction time were tended to agglomerate which reduces the overall quality of the product. The rGO nanomaterial produced at this duration formed an uniform suspension in aqueous solution which help the material to form a stable and uniform coating on the GCE. The electrochemical properties and conductivity of the

sensing material were evaluated by exposing the working electrode to different concentrations of AA and the results showed that under optimized condition, the rGO@12h achieved an excellent electrochemical limit of detection which is at 1.64 μM . This proves that, the 12h reduction time produces an optimal amount of surface defects that increase the overall conductivity and the sensitivity of the sensing material.

Furthermore, the electrochemical properties of rGO and rGO-nanocomposites as an active material platform for biosensors for sensitive and selective detection of foodborne pathogens were also studied. Different types of novel rGO-nanocomposites were investigated. Firstly, rGO-AP nanocomposite aptasensor was developed for a sensitive, rapid, and robust detection of foodborne pathogens. Besides providing an excellent conductive and soluble rGO nanocomposite, AP dye also acts as an electroactive indicator for redox reactions. Under optimum conditions, this aptasensor exhibited a linear range of detection from 10^8 cfu mL⁻¹ to 10^1 cfu mL⁻¹ with good linearity ($R^2 = 0.98$) and a detection limit of 10^1 cfu mL⁻¹. Secondly, rGO-TiO₂ nanocomposite aptasensor was developed through chemical synthesis followed by, immobilization of label-free aptamer through simple π - π stacking and electrostatic interaction. The changes in electrical conductivity on the surface of electrode were evaluated using CV, DPV and EIS techniques. In the presence of *S. Typhimurium*, the optimized aptasensor exhibits high sensitivity with wide detection range (10^8 to 10^1 cfu mL⁻¹), low detection limit (10^1 cfu mL⁻¹) and good selectivity. Then, another novel combination of nanomaterial which is rGO-Nf was synthesized to explore the capability of polymers in electrochemical detection of bacteria. This sensing material also exhibited similar results in which it achieved a lower detection limit of 1.0 cfu mL⁻¹ with good selectivity against non-*Salmonella* bacterial cells. The shelf-life of these electrodes were up to 28 days. The results demonstrated that the rGO-nanocomposites proposed in this study possess high

potential to be adapted for effective and rapid detection of a specific foodborne pathogen by an electrochemical approach.

The interaction of aptamer with bacterial cells on the surface of rGO-nanocomposites was also investigated in this study. Through Raman, PL and FTIR, the changes happened at the material level resulting in the covalent binding of nanocomposites which changes the Fermi levels in graphene can be clearly seen. Moreover, in the presence of the aptamer-bacterial cells, the conductivity of the rGO-nanocomposites changed significantly due to the doping effect created on the surface. Besides electrochemical characterizations, these techniques give more solid proof-of-concept and elucidate the mechanism of the interaction and detection better.

This research has explored the unique chemical and physical properties of the rGO-nanocomposites make it potentially useful for designing new and improved electrochemical aptasensing devices for the detection of the foodborne pathogen. Besides that, the proof of concept of the sensing capabilities and interaction of the hybrid nanomaterial rGO/aptamers-bacterial cells was demonstrated by the real-time detection of *Salmonella* bacteria in buffer solutions. The major limitation of this study is the fabricated electrochemical biosensors are bulky and unable to provide a point-of-care detection using the electrochemical approach. Thus, as for future perspectives a portable and handheld electrochemical aptasensor device using affordable and scalable manufacturing technology in the form of chips needs to be developed. Moreover, multiple bacteria detections on a single chip could be explored by developing multiplex biosensors using aptamers as a biorecognition element. These miniaturized and multiplex aptasensing chips or devices will have a high potential to become the next generation of food industry standards.

REFERENCES

- Abbaspour, A., Norouz-Sarvestani, F., Noori, A., & Soltani, N. (2015). Aptamer-conjugated silver nanoparticles for electrochemical dual-aptamer-based sandwich detection of staphylococcus aureus. *Biosens Bioelectron*, 68, 149-155. doi: 10.1016/j.bios.2014.12.040
- Abbaspour, A., Norouz-Sarvestani, F., Noori, A., & Soltani, N. (2015). Aptamer-conjugated silver nanoparticles for electrochemical dual-aptamer-based sandwich detection of *Staphylococcus aureus*. *Biosens. Bioelectron*, 68, 149-155. doi: 10.1016/j.bios.2014.12.040
- Abdalahi, M. H., Fernandes, A. M., Xia, X., Musa, A., Ji, J., & Sun, X. (2015). Electrochemical Genosensor To Detect Pathogenic Bacteria (*Escherichia coli* O157:H7) As Applied in Real Food Samples (Fresh Beef) To Improve Food Safety and Quality Control. *J Agric Food Chem*, 63(20), 5017-5025. doi: 10.1021/acs.jafc.5b00675
- Abe, K., & Ikebukuro, K. (2011). *Aptamer Sensors Combined with Enzymes for Highly Sensitive Detection*.
- Abu-Salah, K. M., Alrokyan, S. A., Khan, M. N., & Ansari, A. A. (2010). Nanomaterials as Analytical Tools for Genosensors. *Sensors (Basel, Switzerland)*, 10(1), 963-993. doi: 10.3390/s100100963
- Adhikari, B. R., Govindhan, M., & Chen, A. (2015). Carbon Nanomaterials Based Electrochemical Sensors/Biosensors for the Sensitive Detection of Pharmaceutical and Biological Compounds. *Sensors*, 15(9), 22490-22508. doi: 10.3390/s150922490
- Ahmed, A., Rushworth, J. V., Hirst, N. A., & Millner, P. A. (2014). Biosensors for Whole-Cell Bacterial Detection. *Clinical Microbiology Reviews*, 27(3), 631-646. doi: 10.1128/CMR.00120-13
- Ahuja, T., Mir, I. A., Kumar, D., & Rajesh. (2007). Biomolecular immobilization on conducting polymers for biosensing applications. *Biomaterials*, 28(5), 791-805. doi: https://doi.org/10.1016/j.biomaterials.2006.09.046
- Akbari, E., Buntat, Z., Afroozeh, A., Zeinalinezhad, A., & Nikoukar, A. (2015). *Escherichia coli* bacteria detection by using graphene-based biosensor (Vol. 9).
- Akbari, E., Buntat, Z., Afroozeh, A., Zeinalinezhad, A., & Nikoukar, A. (2015). *Escherichia coli* bacteria detection by using graphene-based biosensor. *IET nanobiotechnology*, 9(5), 273-279. doi: 10.1049/iet-nbt.2015.0010
- Akhavan, O., Ghaderi, E., & Rahighi, R. (2012). Toward Single-DNA Electrochemical Biosensing by Graphene Nanowalls. *ACS Nano*, 6(4), 2904-2916. doi: 10.1021/nn300261t
- Alahi, M. E. E., & Mukhopadhyay, S. C. (2017). Detection Methodologies for Pathogen and Toxins: A Review. *Sensors (Basel)*, 17(8). doi: 10.3390/s17081885

- Alam, M. J., & Cameron, D. C. (2002). Preparation and Characterization of TiO₂ Thin Films by Sol-Gel Method. *Journal of Sol-Gel Science and Technology*, 25(2), 137-145. doi: 10.1023/A:1019912312654
- Allen, M. J., Tung, V. C., & Kaner, R. B. (2010). Honeycomb carbon: a review of graphene. *Chem Rev*, 110(1), 132-145. doi: 10.1021/cr900070d
- Alvarez, J., Sota, M., Vivanco, A. B., Perales, I., Cisterna, R., Rementeria, A., & Garaizar, J. (2004). Development of a Multiplex PCR Technique for Detection and Epidemiological Typing of Salmonella in Human Clinical Samples. *Journal of Clinical Microbiology*, 42(4), 1734-1738. doi: 10.1128/JCM.42.4.1734-1738.2004
- Ambrosi, A., Chua, C. K., Latiff, N. M., Loo, A. H., Wong, C. H. A., Eng, A. Y. S., . . . Pumera, M. (2016). Graphene and its electrochemistry - an update. *Chemical Society Reviews*, 45(9), 2458-2493. doi: 10.1039/C6CS00136J
- Angione, M. D., Pilolli, R., Cotrone, S., Magliulo, M., Mallardi, A., Palazzo, G., . . . Torsi, L. (2011). Carbon based materials for electronic bio-sensing. *Materials Today*, 14(9), 424-433. doi: https://doi.org/10.1016/S1369-7021(11)70187-0
- Appaturi, J. N., Pulingam, T., Thong, K. L., Muniandy, S., Ahmad, N., & Leo, B. F. (2020). Rapid and sensitive detection of Salmonella with reduced graphene oxide-carbon nanotube based electrochemical aptasensor. *Analytical Biochemistry*, 589, 113489. doi: https://doi.org/10.1016/j.ab.2019.113489
- Aragaw, B., su, w.-n., Rick, J., & Hwang, B. J. (2013). *Highly efficient synthesis of reduced graphene oxide–Nafion nanocomposites with strong coupling for enhanced proton and electron conduction* (Vol. 3).
- Aragaw, B. A., Su, W.-N., Rick, J., & Hwang, B.-J. (2013). Highly efficient synthesis of reduced graphene oxide–Nafion nanocomposites with strong coupling for enhanced proton and electron conduction. *RSC Advances*, 3(45), 23212-23221. doi: 10.1039/C3RA44207A
- Artiles, M. S., Rout, C. S., & Fisher, T. S. (2011). Graphene-based hybrid materials and devices for biosensing. *Advanced Drug Delivery Reviews*, 63(14), 1352-1360. doi: https://doi.org/10.1016/j.addr.2011.07.005
- Avetisyan, A. A., Partoens, B., & Peeters, F. M. (2009). Electric field tuning of the band gap in graphene multilayers. *Physical Review B*, 79(3), 035421. doi: 10.1103/PhysRevB.79.035421
- Bahadır, E., & Sezgintürk, M. (2014). A review on impedimetric biosensors. *Artificial cells, nanomedicine, and biotechnology*, 44, 1-15. doi: 10.3109/21691401.2014.942456
- Bahadır, E. B., & Sezginturk, M. K. (2016). A review on impedimetric biosensors. *Artif Cells Nanomed Biotechnol*, 44(1), 248-262. doi: 10.3109/21691401.2014.942456
- Bai, S., & Shen, X. (2012). Graphene-inorganic nanocomposites. *RSC Advances*, 2(1), 64-98. doi: 10.1039/C1RA00260K

- Bai, S., & Shen, X. (2012). Graphene–inorganic nanocomposites. *RSC Advances*, 2(1), 64-98. doi: 10.1039/C1RA00260K
- Bai, X., Chen, G., & Shiu, K.-K. (2013). Electrochemical biosensor based on reduced graphene oxide modified electrode with Prussian blue and poly(toluidine blue O) coating. *Electrochimica Acta*, 89, 454-460. doi: https://doi.org/10.1016/j.electacta.2012.11.086
- Balint, R., Cassidy, N. J., & Cartmell, S. H. (2014). Conductive polymers: Towards a smart biomaterial for tissue engineering. *Acta Biomaterialia*, 10(6), 2341-2353. doi: https://doi.org/10.1016/j.actbio.2014.02.015
- Bănică, F.-G. (2012). Amperometric Enzyme Sensors *Chemical Sensors and Biosensors* (pp. 314-331): John Wiley & Sons, Ltd.
- Bauman, D., Fan, Z.-X., & Haase, W. (1989). An X-ray diffraction study of a mixture of azo dyes with 4-n-pentyl-4'-cyano-p-terphenyl. *Liquid Crystals*, 6(2), 239-246. doi: 10.1080/02678298908033218
- Beams, R., Gustavo Cancado, L., & Novotny, L. (2015). Raman characterization of defects and dopants in graphene. *J Phys Condens Matter*, 27(8), 083002. doi: 10.1088/0953-8984/27/8/083002
- Becerro, S., Paredes, J., & Arana, S. (2015). Multiparametric Biosensor for Detection and Monitoring of Bacterial Biofilm Adhesion and Growth. In I. Lacković & D. Vasic (Eds.), *6th European Conference of the International Federation for Medical and Biological Engineering: MBEC 2014, 7-11 September 2014, Dubrovnik, Croatia* (Vol. 45, pp. 333-336). Cham: Springer International Publishing.
- Bekyarova, E., Itkis, M. E., Ramesh, P., Berger, C., Sprinkle, M., de Heer, W. A., & Haddon, R. C. (2009). Chemical Modification of Epitaxial Graphene: Spontaneous Grafting of Aryl Groups. *Journal of the American Chemical Society*, 131(4), 1336-1337. doi: 10.1021/ja8057327
- Bhalla, N., Jolly, P., Formisano, N., & Estrela, P. (2016). Introduction to biosensors. *Essays in biochemistry*, 60(1), 1-8. doi: 10.1042/EBC20150001
- Bhattacharya, M. (2016). Polymer Nanocomposites—A Comparison between Carbon Nanotubes, Graphene, and Clay as Nanofillers. *Materials*, 9(4), 262. doi: 10.3390/ma9040262
- Bich Ha, N., & Van Hieu, N. (2016). Promising applications of graphene and graphene-based nanostructures. *Advances in Natural Sciences: Nanoscience and Nanotechnology*, 7(2), 023002.
- Billington, C., Hudson, J. A., & D'Sa, E. (2014). Prevention of bacterial foodborne disease using nanobiotechnology. *Nanotechnology, science and applications*, 7, 73-83. doi: 10.2147/NSA.S51101
- Bintsis, T. (2017). Foodborne pathogens. *AIMS microbiology*, 3(3), 529-563. doi: 10.3934/microbiol.2017.3.529
- Boukhvalov, D., & Katsnelson, M. (2009). *Chemical functionalization of graphene* (Vol. 21).

- Branch, W. D., Vreeland, C. E., McClain, L. J., Murton, K. J., James, D. C., & Achyuthan, E. K. (2017). Rapid Nucleic Acid Extraction and Purification Using a Miniature Ultrasonic Technique. *Micromachines*, 8(7). doi: 10.3390/mi8070228
- Carrasco, E., Morales-Rueda, A., & García-Gimeno, R. M. (2012). Cross-contamination and recontamination by Salmonella in foods: A review. *Food Research International*, 45(2), 545-556. doi: <https://doi.org/10.1016/j.foodres.2011.11.004>
- Cesaratto, A., Centeno, S. A., Lombardi, J. R., Shibayama, N., & Leona, M. (2017). A complete Raman study of common acid red dyes: application to the identification of artistic materials in polychrome prints. *J. Raman Spectrosc.* doi: 10.1002/jrs.5082
- Chaivisuthangkura, P., Pengsuk, C., Longyant, S., & Sithigorngul, P. (2013). Evaluation of monoclonal antibody based immunochromatographic strip test for direct detection of Vibrio cholerae O1 contamination in seafood samples. *J Microbiol Methods*, 95(2), 304-311. doi: 10.1016/j.mimet.2013.09.013
- Chang, B. Y., Huang, N. M., An'amt, M. N., Marlinda, A. R., Norazriena, Y., Muhamad, M. R., . . . Chia, C. H. (2012). Facile hydrothermal preparation of titanium dioxide decorated reduced graphene oxide nanocomposite. *Int J Nanomedicine*, 7, 3379-3387. doi: 10.2147/ijn.s28189
- Chang, D. W., & Baek, J.-B. (2016). Covalently functionalized graphene with organic semiconductors for energy and optoelectronic applications. *Materials Research Express*, 3(4), 044001. doi: 10.1088/2053-1591/3/4/044001
- Chang, J., Zhou, G., Christensen, E. R., Heideman, R., & Chen, J. (2014). Graphene-based sensors for detection of heavy metals in water: a review. *Analytical and bioanalytical chemistry*, 406(16), 3957-3975. doi: 10.1007/s00216-014-7804-x
- Chang, Y.-C., Yang, C.-Y., Sun, R.-L., Cheng, Y.-F., Kao, W.-C., & Yang, P.-C. (2013). Rapid single cell detection of Staphylococcus aureus by aptamer-conjugated gold nanoparticles. *Scientific Reports*, 3, 1863. doi: 10.1038/srep01863
- <https://www.nature.com/articles/srep01863#supplementary-information>
- Chatterjee, S., & Chen, A. (2012). Functionalization of carbon buckypaper for the sensitive determination of hydrogen peroxide in human urine. *Biosensors and Bioelectronics*, 35(1), 302-307. doi: <https://doi.org/10.1016/j.bios.2012.03.005>
- Chen, L., Han, J., Ito, Y., Fujita, T., Huang, G., Hu, K., . . . Chen, M. (2018). Heavily Doped and Highly Conductive Hierarchical Nanoporous Graphene for Electrochemical Hydrogen Production. *Angewandte Chemie International Edition*, 57(40), 13302-13307. doi: doi:10.1002/anie.201809315
- Chen, L., Tang, Y., Wang, K., Liu, C., & Luo, S. (2011). Direct electrodeposition of reduced graphene oxide on glassy carbon electrode and its electrochemical application. *Electrochemistry Communications*, 13(2), 133-137. doi: <https://doi.org/10.1016/j.elecom.2010.11.033>
- Chen, S., Wang, F., Beaulieu, J. C., Stein, R. E., & Ge, B. (2011). Rapid Detection of Viable Salmonellae in Produce by Coupling Propidium Monoazide with Loop-

Mediated Isothermal Amplification. *Applied and Environmental Microbiology*, 77(12), 4008-4016. doi: 10.1128/aem.00354-11

- Chen, X. (2014). Development of a rapid and sensitive quantum dot-based immunochromatographic strip by double labeling PCR products for detection of *Staphylococcus aureus* in food. *Food control*, v. 46, pp. 225-232-2014 v.2046. doi: 10.1016/j.foodcont.2014.04.044
- Chen, Y., Fu, K., Zhu, S., Luo, W., Wang, Y., Li, Y., . . . Wan, J. (2016). Reduced Graphene Oxide Films with Ultrahigh Conductivity as Li-Ion Battery Current Collectors. *Nano Lett*, 16(6), 3616-3623. doi: 10.1021/acs.nanolett.6b00743
- Chen, Y., Zhang, X., Zhang, D., Yu, P., & Ma, Y. (2011). High performance supercapacitors based on reduced graphene oxide in aqueous and ionic liquid electrolytes. *Carbon*, 49(2), 573-580. doi: https://doi.org/10.1016/j.carbon.2010.09.060
- Cheng, C., Peng, Y., Bai, J., Zhang, X., Liu, Y., Fan, X., . . . Gao, Z. (2014). Rapid detection of *Listeria monocytogenes* in milk by self-assembled electrochemical immunosensor. *Sensors and Actuators B: Chemical*, 190, 900-906. doi: https://doi.org/10.1016/j.snb.2013.09.041
- Cheung, Y.-W., Kwok, J., Law, A. W. L., Watt, R. M., Kotaka, M., & Tanner, J. A. (2013). Structural basis for discriminatory recognition of *Plasmodium lactate* dehydrogenase by a DNA aptamer. *Proceedings of the National Academy of Sciences of the United States of America*, 110(40), 15967-15972. doi: 10.1073/pnas.1309538110
- Choi, Y. J., Kim, E., Han, J., Kim, J. H., & Gurunathan, S. (2016). A Novel Biomolecule-Mediated Reduction of Graphene Oxide: A Multifunctional Anti-Cancer Agent. *Molecules*, 21(3), 375. doi: 10.3390/molecules21030375
- Chua, C. K., & Pumera, M. (2014). Chemical reduction of graphene oxide: a synthetic chemistry viewpoint. *Chem Soc Rev*, 43(1), 291-312. doi: 10.1039/c3cs60303b
- Cinti, S., Volpe, G., Piermarini, S., Delibato, E., & Palleschi, G. (2017). Electrochemical Biosensors for Rapid Detection of Foodborne Salmonella: A Critical Overview. *Sensors (Basel)*, 17(8). doi: 10.3390/s17081910
- Craciun, M., Russo, S., Yamamoto, M., & Tarucha, S. (2011). *Tunable electronic properties in graphene* (Vol. 6).
- Curtin, A. E., Fuhrer, M. S., Tedesco, J. L., Myers-Ward, R. L., Jr., C. R. E., & Gaskill, D. K. (2011). Kelvin probe microscopy and electronic transport in graphene on SiC(0001) in the minimum conductivity regime. *Applied Physics Letters*, 98(24), 243111. doi: 10.1063/1.3595360
- D'Souza, D. H., & Jaykus, L. A. (2003). Nucleic acid sequence based amplification for the rapid and sensitive detection of *Salmonella enterica* from foods. *J Appl Microbiol*, 95(6), 1343-1350. doi: 10.1046/j.1365-2672.2003.02106.x
- D. Lounis, S., Siegel, D., Broesler, R., Hwang, C., E. Haller, E., & Lanzara, A. (2010). *Resonant photoluminescent charging of epitaxial graphene* (Vol. 96).

- Dai, G., Li, Z., Luo, F., Ai, S., Chen, B., & Wang, Q. (2019). Electrochemical determination of *Salmonella typhimurium* by using aptamer-loaded gold nanoparticles and a composite prepared from a metal-organic framework (type UiO-67) and graphene. *Microchimica Acta*, 186(9), 620. doi: 10.1007/s00604-019-3724-y
- Davydova, A., Vorobjeva, M., Pyshnyi, D., Altman, S., Vlassov, V., & Venyaminova, A. (2016). Aptamers against pathogenic microorganisms. *Critical Reviews in Microbiology*, 42(6), 847-865. doi: 10.3109/1040841X.2015.1070115
- Dhand, V., Rhee, K. Y., Ju Kim, H., & Ho Jung, D. (2013). A Comprehensive Review of Graphene Nanocomposites: Research Status and Trends. *Journal of Nanomaterials*, 2013, 14. doi: 10.1155/2013/763953
- Dinshaw, I. J., Muniandy, S., Teh, S. J., Ibrahim, F., Leo, B. F., & Thong, K. L. (2017). Development of an aptasensor using reduced graphene oxide chitosan complex to detect *Salmonella*. *Journal of Electroanalytical Chemistry*, 806(Supplement C), 88-96. doi: 10.1016/j.jelechem.2017.10.054
- Dinshaw, I. J., Muniandy, S., Teh, S. J., Ibrahim, F., Leo, B. F., & Thong, K. L. (2017). Development of an aptasensor using reduced graphene oxide chitosan complex to detect *Salmonella*. *Journal of Electroanalytical Chemistry*, 806, 88-96. doi: <https://doi.org/10.1016/j.jelechem.2017.10.054>
- Dong-Fang, H., Chang-Sheng, S., Guo, L.-P., Li, N., & Dong-Xue, H. (2010). *Electro-oxidation of Ascorbic Acid on PVP-stabilized Graphene Electrode* (Vol. 26).
- Dong, H. S., & Qi, S. J. (2015). Realising the potential of graphene-based materials for biosurfaces – A future perspective. *Biosurface and Biotribology*, 1(4), 229-248. doi: <https://doi.org/10.1016/j.bsbt.2015.10.004>
- Dong, Y., Xu, Y., Yong, W., Chu, X., & Wang, D. (2014). *Aptamer and Its Potential Applications for Food Safety* (Vol. 54).
- Dwivedi, H. P., Smiley, R. D., & Jaykus, L. A. (2013). Selection of DNA aptamers for capture and detection of *Salmonella Typhimurium* using a whole-cell SELEX approach in conjunction with cell sorting. *Appl Microbiol Biotechnol*, 97(8), 3677-3686. doi: 10.1007/s00253-013-4766-4
- Eng, S.-K., Pusparajah, P., Ab Mutalib, N.-S., Ser, H.-L., Chan, K.-G., & Lee, L.-H. (2015). *Salmonella*: A review on pathogenesis, epidemiology and antibiotic resistance. *Frontiers in Life Science*, 8(3), 284-293. doi: 10.1080/21553769.2015.1051243
- Fan, Y., Lu, H.-T., Liu, J.-H., Yang, C.-P., Jing, Q.-S., Zhang, Y.-X., . . . Huang, K.-J. (2011). Hydrothermal preparation and electrochemical sensing properties of TiO₂-graphene nanocomposite. *Colloids and Surfaces B: Biointerfaces*, 83(1), 78-82. doi: <https://doi.org/10.1016/j.colsurfb.2010.10.048>
- Fang, Z., Wu, W., Lu, X., & Zeng, L. (2014). *Lateral flow biosensor for DNA extraction-free detection of Salmonella based on aptamer mediated strand displacement amplification* (Vol. 56).

- Fernández-Merino, M. J., Guardia, L., Paredes, J. I., Villar-Rodil, S., Solís-Fernández, P., Martínez-Alonso, A., & Tascón, J. M. D. (2010). Vitamin C Is an Ideal Substitute for Hydrazine in the Reduction of Graphene Oxide Suspensions. *The Journal of Physical Chemistry C*, *114*(14), 6426-6432. doi: 10.1021/jp100603h
- Finn, S., Condell, O., McClure, P., Amézquita, A., & Fanning, S. (2013). Mechanisms of survival, responses and sources of Salmonella in low-moisture environments. *Frontiers in Microbiology*, *4*, 331-331. doi: 10.3389/fmicb.2013.00331
- Galkina, S. I., Romanova, J. M., Bragina, E. E., Tiganova, I. G., Stadnichuk, V. I., Alekseeva, N. V., . . . Klein, T. (2011). Membrane tubules attach Salmonella Typhimurium to eukaryotic cells and bacteria. *FEMS Immunology & Medical Microbiology*, *61*(1), 114-124. doi: 10.1111/j.1574-695X.2010.00754.x
- Gao, Y. (2017). Graphene and Polymer Composites for Supercapacitor Applications: a Review. *Nanoscale Research Letters*, *12*, 387. doi: 10.1186/s11671-017-2150-5
- Garg, R., Dutta, N., & Roy Choudhury, N. (2014). *Work Function Engineering of Graphene* (Vol. 4).
- Gedi, V., & Kim, Y.-P. (2014). Detection and characterization of cancer cells and pathogenic bacteria using aptamer-based nano-conjugates. *Sensors*, *14*(10), 18302-18327. doi: 10.3390/s141018302
- Georgakilas, V., Otyepka, M., Bourlinos, A. B., Chandra, V., Kim, N., Kemp, K. C., . . . Kim, K. S. (2012). Functionalization of Graphene: Covalent and Non-Covalent Approaches, Derivatives and Applications. *Chemical Reviews*, *112*(11), 6156-6214. doi: 10.1021/cr3000412
- Georgakilas, V., Perman, J. A., Tucek, J., & Zboril, R. (2015). Broad Family of Carbon Nanoallotropes: Classification, Chemistry, and Applications of Fullerenes, Carbon Dots, Nanotubes, Graphene, Nanodiamonds, and Combined Superstructures. *Chem Rev*, *115*(11), 4744-4822. doi: 10.1021/cr500304f
- Ghanbari, K., & Bonyadi, S. (2018). An electrochemical sensor based on reduced graphene oxide decorated with polypyrrole nanofibers and zinc oxide-copper oxide p-n junction heterostructures for the simultaneous voltammetric determination of ascorbic acid, dopamine, paracetamol, and tryptophan. *New Journal of Chemistry*, *42*(11), 8512-8523. doi: 10.1039/C8NJ00857D
- Giubileo, F., & Di Bartolomeo, A. (2017). The role of contact resistance in graphene field-effect devices. *Progress in Surface Science*, *92*(3), 143-175. doi: https://doi.org/10.1016/j.progsurf.2017.05.002
- Grieshaber, D., MacKenzie, R., Voeroes, J., & Reimhult, E. (2008). Electrochemical biosensors-sensor principles and architectures. *Sensors*, *8*(3), 1400-1458. doi: 10.3390/s8031400
- Grumezescu, A. (2016). *Surface Chemistry of Nanobiomaterials: Applications of Nanobiomaterials*: William Andrew.
- Guo, S., & Dong, S. (2011). Graphene nanosheet: synthesis, molecular engineering, thin film, hybrids, and energy and analytical applications. *Chem Soc Rev*, *40*(5), 2644-2672. doi: 10.1039/C0CS00079E

- Guo, Y., Guo, Y., & Dong, C. (2013). Ultrasensitive and label-free electrochemical DNA biosensor based on water-soluble electroactive dye azophloxine-functionalized graphene nanosheets. *Electrochim. Acta*, *113*, 69-76. doi: 10.1016/j.electacta.2013.09.039
- Guo, Y., Guo, Y., & Dong, C. (2013). Ultrasensitive and label-free electrochemical DNA biosensor based on water-soluble electroactive dye azophloxine-functionalized graphene nanosheets. *Electrochimica Acta*, *113*, 69-76. doi: https://doi.org/10.1016/j.electacta.2013.09.039
- Guo, Y., Han, Y., Guo, Y., & Dong, C. (2013). Graphene-Orange II composite nanosheets with electroactive functions as label-free aptasensing platform for “signal-on” detection of protein. *Biosensors and Bioelectronics*, *45*, 95-101. doi: https://doi.org/10.1016/j.bios.2013.01.054
- Gupta, S., & Irihamye, A. (2015). Probing the nature of electron transfer in metalloproteins on graphene-family materials as nanobiocatalytic scaffold using electrochemistry. *AIP Advances*, *5*(3), 037106. doi: 10.1063/1.4914186
- Gurunathan, S., & Kim, J.-H. (2016). Synthesis, toxicity, biocompatibility, and biomedical applications of graphene and graphene-related materials. *Int J Nanomedicine*, *11*, 1927-1945. doi: 10.2147/IJN.S105264
- Han, F., Wang, F., & Ge, B. (2011). Detecting Potentially Virulent *Vibrio vulnificus* Strains in Raw Oysters by Quantitative Loop-Mediated Isothermal Amplification. *Applied and Environmental Microbiology*, *77*(8), 2589-2595. doi: 10.1128/aem.02992-10
- Hatamie, S., Ahadian, M. M., Ghiass, M. A., Iraj Zad, A., Saber, R., Parseh, B., . . . Shانهsazzadeh, S. (2016). Graphene/cobalt nanocarrier for hyperthermia therapy and MRI diagnosis. *Colloids Surf B Biointerfaces*, *146*, 271-279. doi: 10.1016/j.colsurfb.2016.06.018
- Havelaar, A. H., Kirk, M. D., Torgerson, P. R., Gibb, H. J., Hald, T., Lake, R. J., . . . on behalf of World Health Organization Foodborne Disease Burden Epidemiology Reference, G. (2015). World Health Organization Global Estimates and Regional Comparisons of the Burden of Foodborne Disease in 2010. *PLOS Medicine*, *12*(12), e1001923. doi: 10.1371/journal.pmed.1001923
- Helm, D., Labischinski, H., Schallehn, G., & Naumann, D. (1991). Classification and identification of bacteria by Fourier-transform infrared spectroscopy. *J Gen Microbiol*, *137*(1), 69-79. doi: 10.1099/00221287-137-1-69
- Hernandez, F. J., & Ozalp, V. C. (2012). Graphene and Other Nanomaterial-Based Electrochemical Aptasensors. *Biosensors*, *2*(1). doi: 10.3390/bios2010001
- Hernández, R., Vallés, C., Benito, A. M., Maser, W. K., Xavier Rius, F., & Riu, J. (2014). Graphene-based potentiometric biosensor for the immediate detection of living bacteria. *Biosensors and Bioelectronics*, *54*, 553-557. doi: https://doi.org/10.1016/j.bios.2013.11.053
- Heymans, R., Vila, A., van Heerwaarden, C. A. M., Jansen, C. C. C., Castelijin, G. A. A., van der Voort, M., & Biesta-Peters, E. G. (2018). Rapid detection and

- differentiation of Salmonella species, Salmonella Typhimurium and Salmonella Enteritidis by multiplex quantitative PCR. *PLoS ONE*, 13(10), e0206316. doi: 10.1371/journal.pone.0206316
- Hidong, K., Otgonbayar, D., Altaibaatar, L., & Jae, M. S. (2016). Charge neutrality of quasi-free-standing monolayer graphene induced by the intercalated Sn layer. *Journal of Physics D: Applied Physics*, 49(13), 135307.
- Hirata, M., Gotou, T., Horiuchi, S., Fujiwara, M., & Ohba, M. (2004). Thin-film particles of graphite oxide 1:: High-yield synthesis and flexibility of the particles. *Carbon*, 42(14), 2929-2937. doi: <https://doi.org/10.1016/j.carbon.2004.07.003>
- Hoffmann, S., & Scallan, E. (2017). Chapter 2 - Epidemiology, Cost, and Risk Analysis of Foodborne Disease *Foodborne Diseases (Third edition)* (pp. 31-63): Academic Press.
- Hofmann, M., Hsieh, Y.-P., Chang, K.-W., Tsai, H.-G., & Chen, T.-T. (2015). Dopant morphology as the factor limiting graphene conductivity. *Scientific Reports*, 5, 17393. doi: 10.1038/srep17393
- Hong, B. J., An, Z., Compton, O. C., & Nguyen, S. T. (2012). Tunable Biomolecular Interaction and Fluorescence Quenching Ability of Graphene Oxide: Application to “Turn-on” DNA Sensing in Biological Media. *Small (Weinheim an der Bergstrasse, Germany)*, 8(16), 2469-2476. doi: 10.1002/smll.201200264
- How, G. T. S., Pandikumar, A., Ming, H. N., & Ngee, L. H. (2014). Highly exposed {001} facets of titanium dioxide modified with reduced graphene oxide for dopamine sensing. *Scientific Reports*, 4, 5044. doi: 10.1038/srep05044
- <https://www.nature.com/articles/srep05044#supplementary-information>
- Huang, D., Chen, C., Wu, Y.-M., Zhang, H., Sheng, L., Xu, H.-J., & Liu, Z.-D. (2011). *The Determination of Dopamine Using Glassy Carbon Electrode Pretreated by a Simple Electrochemical Method* (Vol. 7).
- Huang, H., Su, S., Wu, N., Wan, H., Wan, S., Bi, H., & Sun, L. (2019). Graphene-Based Sensors for Human Health Monitoring. *Frontiers in Chemistry*, 7(399). doi: 10.3389/fchem.2019.00399
- Huang, N. M., Lim, H. N., Chia, C. H., Yarmo, M. A., & Muhamad, M. R. (2011). Simple room-temperature preparation of high-yield large-area graphene oxide. *Int J Nanomedicine*, 6, 3443-3448. doi: 10.2147/ijn.s26812
- Huang Po-Jung, J., Liu, M., & Liu, J. (2013). Functional nucleic acids for detecting bacteria *Reviews in Analytical Chemistry* (Vol. 32, pp. 77).
- Huang, W., Nurbawono, A., Zeng, M., Gupta, G., & Liang, G. (2016). *Electronic structure of graphene based materials and their carrier transport properties*.
- Hughes, Z. E., & Walsh, T. R. (2017). Structural Disruption of an Adenosine-Binding DNA Aptamer on Graphene: Implications for Aptasensor Design. *ACS Sensors*, 2(11), 1602-1611. doi: 10.1021/acssensors.7b00435

- Hummers, W. S., & Offeman, R. E. (1958). Preparation of Graphitic Oxide. *Journal of the American Chemical Society*, 80(6), 1339-1339. doi: 10.1021/ja01539a017
- Humphries, R. M., & Linscott, A. J. (2015). Laboratory Diagnosis of Bacterial Gastroenteritis. *Clinical Microbiology Reviews*, 28(1), 3-31. doi: 10.1128/cmr.00073-14
- Ikhsan, N. I., Rameshkumar, P., Pandikumar, A., Mehmood Shahid, M., Huang, N. M., Vijay Kumar, S., & Lim, H. N. (2015). Facile synthesis of graphene oxide-silver nanocomposite and its modified electrode for enhanced electrochemical detection of nitrite ions. *Talanta*, 144, 908-914. doi: 10.1016/j.talanta.2015.07.050
- Jafri, S. H. M., Carva, K., Widenkvist, E., Blom, T., Sanyal, B., Fransson, J., . . . Leifer, K. (2009). *Conductivity engineering of graphene by defect formation* (Vol. 43).
- Jafri, S. H. M., Carva, K., Widenkvist, E., Blom, T., Sanyal, B., Fransson, J., . . . Leifer, K. (2010). Conductivity engineering of graphene by defect formation. *Journal of Physics D: Applied Physics*, 43(4), 045404.
- Jajere, S. M. (2019). A review of Salmonella enterica with particular focus on the pathogenicity and virulence factors, host specificity and antimicrobial resistance including multidrug resistance. *Veterinary world*, 12(4), 504-521. doi: 10.14202/vetworld.2019.504-521
- Jia, F., Duan, N., Wu, S., Dai, R., Wang, Z., & Li, X. (2016). Impedimetric Salmonella aptasensor using a glassy carbon electrode modified with an electrodeposited composite consisting of reduced graphene oxide and carbon nanotubes. *Microchimica Acta*, 183(1), 337-344. doi: 10.1007/s00604-015-1649-7
- Jia, F., Duan, N., Wu, S., Ma, X., Xia, Y., Wang, Z., & Wei, X. (2014). Impedimetric aptasensor for Staphylococcus aureus based on nanocomposite prepared from reduced graphene oxide and gold nanoparticles. *Microchimica Acta*, 181(9), 967-974. doi: 10.1007/s00604-014-1195-8
- Jiang, B.-B., Wei, X.-W., Wu, F.-H., Wu, K.-L., Chen, L., Yuan, G.-Z., . . . Ye, Y. (2014). A non-enzymatic hydrogen peroxide sensor based on a glassy carbon electrode modified with cuprous oxide and nitrogen-doped graphene in a nafion matrix. *Microchimica Acta*, 181(11), 1463-1470. doi: 10.1007/s00604-014-1232-7
- Jiang, Y., Chen, D., Song, J., Jiao, Z., Ma, Q., Zhang, H., . . . Chu, Y. (2013). A facile hydrothermal synthesis of graphene porous NiO nanocomposite and its application in electrochemical capacitors. *Electrochimica Acta*, 91, 173-178. doi: https://doi.org/10.1016/j.electacta.2012.12.032
- Jin, Z., Nackashi, D., Lu, W., Kittrell, C., & Tour, J. M. (2010). Decoration, Migration, and Aggregation of Palladium Nanoparticles on Graphene Sheets. *Chemistry of Materials*, 22(20), 5695-5699. doi: 10.1021/cm102187a
- Jo, I., Kim, Y. I., Moon, J., Park, S., San Moon, J., Bae Park, W., . . . Hee Hong, B. (2015). *Stable n-type doping of graphene by high-molecular-weight ethylene amines* (Vol. 17).

- Johnson, R. R., Johnson, A. C., & Klein, M. L. (2008). Probing the structure of DNA–carbon nanotube hybrids with molecular dynamics. *Nano Lett*, 8(1), 69-75. doi: 10.1021/nl071909j
- Joshi, R., Janagama, H., Dwivedi, H. P., Senthil Kumar, T. M., Jaykus, L. A., Scheffers, J., & Sreevatsan, S. (2009). Selection, characterization, and application of DNA aptamers for the capture and detection of *Salmonella enterica* serovars. *Mol Cell Probes*, 23(1), 20-28. doi: 10.1016/j.mcp.2008.10.006
- Joung, C.-K., Kim, H.-N., Lim, M.-C., Jeon, T.-J., Kim, H.-Y., & Kim, Y.-R. (2013). A nanoporous membrane-based impedimetric immunosensor for label-free detection of pathogenic bacteria in whole milk. *Biosensors and Bioelectronics*, 44, 210-215. doi: <https://doi.org/10.1016/j.bios.2013.01.024>
- Jung, J.-H., Jeon, J.-H., Sridhar, V., & Oh, I.-K. (2011). Electro-active graphene–Nafion actuators. *Carbon*, 49(4), 1279-1289. doi: <https://doi.org/10.1016/j.carbon.2010.11.047>
- Justino, C. I. L., Rocha-Santos, T. A. P., Cardoso, S., & Duarte, A. C. (2013). Strategies for enhancing the analytical performance of nanomaterial-based sensors. *TrAC Trends in Analytical Chemistry*, 47, 27-36. doi: <https://doi.org/10.1016/j.trac.2013.02.004>
- Kawasaki, S., Fratamico, P. M., Horikoshi, N., Okada, Y., Takeshita, K., Sameshima, T., & Kawamoto, S. (2010). Multiplex real-time polymerase chain reaction assay for simultaneous detection and quantification of *Salmonella* species, *Listeria monocytogenes*, and *Escherichia coli* O157:H7 in ground pork samples. *Foodborne Pathog Dis*, 7(5), 549-554. doi: 10.1089/fpd.2009.0465
- Ke, Q., & Wang, J. (2016). Graphene-based materials for supercapacitor electrodes – A review. *Journal of Materiomics*, 2(1), 37-54. doi: <https://doi.org/10.1016/j.jmat.2016.01.001>
- Khan, M., Tahir, M. N., Adil, S. F., Khan, H. U., Siddiqui, M. R. H., Al-warthan, A. A., & Tremel, W. (2015). Graphene based metal and metal oxide nanocomposites: synthesis, properties and their applications. *Journal of Materials Chemistry A*, 3(37), 18753-18808. doi: 10.1039/C5TA02240A
- Kibret, M., & Abera, B. (2012). The Sanitary Conditions of Food Service Establishments and Food Safety Knowledge and Practices of Food Handlers in Bahir Dar Town. *Ethiopian Journal of Health Sciences*, 22(1), 27-35.
- Kim, A.-R., Ha, N.-R., Jung, I.-P., Kim, S.-H., & Yoon, M.-Y. Development of a ssDNA aptamer system with reduced graphene oxide (rGO) to detect nonylphenol ethoxylate in domestic detergent. *Journal of Molecular Recognition*, 0(0), e2764. doi: doi:10.1002/jmr.2764
- Kim, J. S., Taitt, C. R., Ligler, F. S., & Anderson, G. P. (2010). Multiplexed magnetic microsphere immunoassays for detection of pathogens in foods. *Sensing and instrumentation for food quality and safety*, 4(2), 73-81. doi: 10.1007/s11694-010-9097-x

- Kim, Y.-R., Bong, S., Kang, Y.-J., Yang, Y., Mahajan, R. K., Kim, J. S., & Kim, H. (2010). Electrochemical detection of dopamine in the presence of ascorbic acid using graphene modified electrodes. *Biosensors and Bioelectronics*, 25(10), 2366-2369. doi: <https://doi.org/10.1016/j.bios.2010.02.031>
- Kralik, P., & Ricchi, M. (2017). A Basic Guide to Real Time PCR in Microbial Diagnostics: Definitions, Parameters, and Everything. *Frontiers in Microbiology*, 8, 108-108. doi: [10.3389/fmicb.2017.00108](https://doi.org/10.3389/fmicb.2017.00108)
- Krishnan, S. K., Singh, E., Singh, P., Meyyappan, M., & Nalwa, H. S. (2019). A review on graphene-based nanocomposites for electrochemical and fluorescent biosensors. *RSC Advances*, 9(16), 8778-8881. doi: [10.1039/C8RA09577A](https://doi.org/10.1039/C8RA09577A)
- Kristkova, Z. S., Grace, D. and Kuiper, M. (2017). *The economics of food safety in India – a rapid assessment*. Wageningen University & Research, Amsterdam, Netherlands.
- Kumar, B. K., Raghunath, P., Devegowda, D., Deekshit, V. K., Venugopal, M. N., Karunasagar, I., & Karunasagar, I. (2011). Development of monoclonal antibody based sandwich ELISA for the rapid detection of pathogenic *Vibrio parahaemolyticus* in seafood. *Int J Food Microbiol*, 145(1), 244-249. doi: [10.1016/j.ijfoodmicro.2010.12.030](https://doi.org/10.1016/j.ijfoodmicro.2010.12.030)
- Kumar, K. D., Kumar, G. P., & Reddy, K. S. (2015). Rapid Microwave Synthesis of Reduced Graphene Oxide-supported TiO₂ Nanostructures as High Performance Photocatalyst. *Materials Today: Proceedings*, 2(4), 3736-3742. doi: <https://doi.org/10.1016/j.matpr.2015.07.204>
- Kumar, S., Singh, R., Mahajan, A., Bedi, R. K., Saxena, V., & Aswal, D. K. (2018). Optimized reduction of graphite oxide for highly exfoliated silver nanoparticles anchored graphene sheets for dye sensitized solar cell applications. *Electrochimica Acta*, 265, 131-139. doi: <https://doi.org/10.1016/j.electacta.2018.01.154>
- Kurt, B. Z., Durmus, Z., & Durmus, A. (2016). Preparation and characterization of platinum (Pt) and palladium (Pd) nanoparticle decorated graphene sheets and their utilization for the elimination of basic fuchsin and indigo carmine dyes. *Solid State Sciences*, 51, 51-58. doi: <https://doi.org/10.1016/j.solidstatesciences.2015.11.012>
- Kusunoki, M., Norimatsu, W., Bao, J., Morita, K., & Starke, U. (2015). Growth and Features of Epitaxial Graphene on SiC. *Journal of the Physical Society of Japan*, 84(12), 121014. doi: [10.7566/JPSJ.84.121014](https://doi.org/10.7566/JPSJ.84.121014)
- Kwon, S.-J., Han, T.-H., Ko, T. Y., Li, N., Kim, Y., Kim, D. J., . . . Lee, T.-W. (2018). Extremely stable graphene electrodes doped with macromolecular acid. *Nature Communications*, 9(1), 2037. doi: [10.1038/s41467-018-04385-4](https://doi.org/10.1038/s41467-018-04385-4)
- Labib, M., Zamay, A. S., Kolovskaya, O. S., Reshetneva, I. T., Zamay, G. S., Kibbee, R. J., . . . Berezovski, M. V. (2012). Aptamer-based impedimetric sensor for bacterial typing. *Anal. Chem*, 84(19), 8114-8117. doi: [10.1021/ac302217u](https://doi.org/10.1021/ac302217u)

- Lake, R. J., Cressey, P. J., Campbell, D. M., & Oakley, E. (2010). Risk ranking for foodborne microbial hazards in New Zealand: burden of disease estimates. *Risk Anal*, 30(5), 743-752. doi: 10.1111/j.1539-6924.2009.01269.x
- Laube, T., Cortes, P., Llagostera, M., Alegret, S., & Pividori, M. I. (2014). Phagomagnetic immunoassay for the rapid detection of Salmonella. *Appl Microbiol Biotechnol*, 98(4), 1795-1805. doi: 10.1007/s00253-013-5434-4
- Law, J. W.-F., Ab Mutalib, N.-S., Chan, K.-G., & Lee, L.-H. (2014). Rapid methods for the detection of foodborne bacterial pathogens: principles, applications, advantages and limitations. *Frontiers in Microbiology*, 5, 770. doi: 10.3389/fmicb.2014.00770
- Law, J. W.-F., Ab Mutalib, N.-S., Chan, K.-G., & Lee, L.-H. (2015). Rapid methods for the detection of foodborne bacterial pathogens: principles, applications, advantages and limitations. *Frontiers in microbiology*, 5, 770. doi: 10.3389/fmicb.2014.00770
- Law, J. W.-F., Ab Mutalib, N.-S., Chan, K.-G., & Lee, L.-H. (2015). Rapid methods for the detection of foodborne bacterial pathogens: principles, applications, advantages and limitations. *Frontiers in Microbiology*, 5(770). doi: 10.3389/fmicb.2014.00770
- Layek, R. K., & Nandi, A. K. (2013). A review on synthesis and properties of polymer functionalized graphene. *Polymer*, 54(19), 5087-5103. doi: https://doi.org/10.1016/j.polymer.2013.06.027
- Lee, B. (2017). Foodborne Disease and the Need for Greater Foodborne Disease Surveillance in the Caribbean. *Veterinary Sciences*, 4(3). doi: 10.3390/vetsci4030040
- Lee, J. S., You, K. H., & Park, C. B. (2012). Highly Photoactive, Low Bandgap TiO₂ Nanoparticles Wrapped by Graphene. *Advanced Materials*, 24(8), 1084-1088. doi: 10.1002/adma.201104110
- Lee, S.-M., Kim, J.-H., & Ahn, J.-H. (2015). Graphene as a flexible electronic material: mechanical limitations by defect formation and efforts to overcome. *Materials Today*, 18(6), 336-344. doi: https://doi.org/10.1016/j.mattod.2015.01.017
- Lee, S. U., Choi, B. G., & Hong, W. H. (2013, 2013//). *Simple Fabrication of Exfoliated Graphene/Nafion Hybrid as Glucose Bio-sensor Electrodes*. Paper presented at the 4th International Conference on Biomedical Engineering in Vietnam, Berlin, Heidelberg.
- Li, D., Zhang, W., Yu, X., Wang, Z., Su, Z., & Wei, G. (2016). When biomolecules meet graphene: from molecular level interactions to material design and applications. *Nanoscale*, 8(47), 19491-19509. doi: 10.1039/C6NR07249F
- Li, X., Gittleson, F., Carmo, M., Sekol, R. C., & Taylor, A. D. (2012). Scalable fabrication of multifunctional freestanding carbon nanotube/polymer composite thin films for energy conversion. *ACS Nano*, 6(2), 1347-1356. doi: 10.1021/nn2041544

- Li, X., Zhu, Y., Cai, W., Borysiak, M., Han, B., Chen, D., . . . Ruoff, R. S. (2009). Transfer of Large-Area Graphene Films for High-Performance Transparent Conductive Electrodes. *Nano Letters*, 9(12), 4359-4363. doi: 10.1021/nl902623y
- Liu, G., Chai, C., & Yao, B. (2013). Rapid evaluation of *Salmonella pullorum* contamination in chicken based on a portable amperometric sensor. *J. Biosens. Bioelectron*, 4(137), 2.
- Liu, G., Zhao, Y., Sun, C., Li, F., Lu, G. Q., & Cheng, H.-M. (2008). Synergistic Effects of B/N Doping on the Visible-Light Photocatalytic Activity of Mesoporous TiO₂. *Angewandte Chemie International Edition*, 47(29), 5277-5277. doi: 10.1002/anie.200890140
- Liu, H., Duan, C., Su, X., Dong, X., Shen, W., & Zhu, Z. (2014). Titania nanoparticles modified reduced graphene oxide nanocomposite with a double-layered structure encapsulating hemoglobin for a mediator-free biosensor. *Ceramics International*, 40(7, Part A), 9867-9874. doi: https://doi.org/10.1016/j.ceramint.2014.02.080
- Liu, J., Morris, M. D., Macazo, F. C., Schoukroun-Barnes, L. R., & White, R. J. (2014). The current and future role of aptamers in electroanalysis. *J. Electrochem. Soc.*, 161(5), H301-H313. doi: 10.1149/2.026405jes
- Liu, Y., Gao, L., Sun, J., Wang, Y., & Zhang, J. (2009). Stable Nafion-functionalized graphene dispersions for transparent conducting films. *Nanotechnology*, 20(46), 465605. doi: 10.1088/0957-4484/20/46/465605
- Liu, Y., Hao, W., Yao, H., Li, S., Wu, Y., Zhu, J., & Jiang, L. (2018). Solution Adsorption Formation of a π -Conjugated Polymer/Graphene Composite for High-Performance Field-Effect Transistors. *Advanced Materials*, 30(3), 1705377. doi: 10.1002/adma.201705377
- Liu, Y., Tuleouva, N., Ramanculov, E., & Revzin, A. (2010). Aptamer-Based Electrochemical Biosensor for Interferon Gamma Detection. *Anal. Chem*, 82(19), 8131-8136. doi: 10.1021/ac101409t
- Liu, Y., Tuleouva, N., Ramanculov, E., & Revzin, A. (2010). Aptamer-Based Electrochemical Biosensor for Interferon Gamma Detection. *Analytical Chemistry*, 82(19), 8131-8136. doi: 10.1021/ac101409t
- Loh, K. P., Bao, Q., Eda, G., & Chhowalla, M. (2010). Graphene oxide as a chemically tunable platform for optical applications. *Nat Chem*, 2(12), 1015-1024. doi: 10.1038/nchem.907
- Lopes, A. T. S., Albuquerque, G. R., & Maciel, B. M. (2018). Multiplex Real-Time Polymerase Chain Reaction for Simultaneous Quantification of *Salmonella* spp., *Escherichia coli*, and *Staphylococcus aureus* in Different Food Matrices: Advantages and Disadvantages. *BioMed Research International*, 2018, 12. doi: 10.1155/2018/6104015
- López-Campos, G., Martínez-Suárez, J. V., Aguado-Urda, M., & López-Alonso, V. (2012). Detection, identification, and analysis of foodborne pathogens *Microarray Detection and Characterization of Bacterial Foodborne Pathogens* (pp. 13-32): Springer.

- López-Campos, G., Martínez-Suárez, J. V., Aguado-Urda, M., & López-Alonso, V. (2012). Detection, Identification, and Analysis of Foodborne Pathogens: *Microarray Detection and Characterization of Bacterial Foodborne Pathogens* (pp. 13-32). Boston, MA: Springer US.
- Losurdo, M., Giangregorio, M. M., Capezzuto, P., & Bruno, G. (2011). Graphene CVD growth on copper and nickel: role of hydrogen in kinetics and structure. *Physical Chemistry Chemical Physics*, 13(46), 20836-20843. doi: 10.1039/C1CP22347J
- Lu, C., Huang, P.-J. J., Liu, B., Ying, Y., & Liu, J. (2016). Comparison of Graphene Oxide and Reduced Graphene Oxide for DNA Adsorption and Sensing. *Langmuir*, 32(41), 10776-10783. doi: 10.1021/acs.langmuir.6b03032
- Lu, G., Yu, K., Wen, Z., & Chen, J. (2013). *Semiconducting graphene: Converting graphene from semimetal to semiconductor* (Vol. 5).
- Lu, T., Zhang, Y., Li, H., Pan, L., Li, Y., & Sun, Z. (2010). Electrochemical behaviors of graphene-ZnO and graphene-SnO₂ composite films for supercapacitors. *Electrochimica Acta*, 55(13), 4170-4173. doi: https://doi.org/10.1016/j.electacta.2010.02.095
- Luz, R. A. S., Iost, R. M., & Crespilho, F. N. (2013). Nanomaterials for Biosensors and Implantable Biodevices. In F. N. Crespilho (Ed.), *Nanobioelectrochemistry: From Implantable Biosensors to Green Power Generation* (pp. 27-48). Berlin, Heidelberg: Springer Berlin Heidelberg.
- Lvovich, V. F. (2015). *Impedance Spectroscopy: Applications to Electrochemical and Dielectric Phenomena*: Wiley.
- Ma, X., Jiang, Y., Jia, F., Yu, Y., Chen, J., & Wang, Z. (2014). An aptamer-based electrochemical biosensor for the detection of Salmonella. *Journal of Microbiological Methods*, 98, 94-98. doi: https://doi.org/10.1016/j.mimet.2014.01.003
- Ma, X., Jiang, Y., Jia, F., Yu, Y., Chen, J., & Wang, Z. (2014). An aptamer-based electrochemical biosensor for the detection of Salmonella. *J Microbiol Methods*, 98, 94-98. doi: 10.1016/j.mimet.2014.01.003
- Mady, M., Awad, W., El-Guendy, N., & A. Elsayed, A. (2011). *Interaction of DNA and Polyethylenimine: FTIR and DSC Studies* (Vol. 6).
- Mahe, L. S. A. (2015). *Development of a graphene-based electrochemical immunobiosensor for the sepsis biomarker procalcitonin*. (PhD in Physics), University of Exeter. Retrieved from <http://hdl.handle.net/10871/18792>
- Majowicz, S. E., Musto, J., Scallan, E., Angulo, F. J., Kirk, M., O'Brien, S. J., . . . Hoekstra, R. M. (2010). The global burden of nontyphoidal Salmonella gastroenteritis. *Clin Infect Dis*, 50(6), 882-889. doi: 10.1086/650733
- Mandal, P., Biswas, A., Choi, K., & Pal, U. (2011). Methods for rapid detection of foodborne pathogens: an overview. *American Journal Of Food Technology*, 6(2), 87-102.

- Mao, L., Zhang, K., On Chan, H. S., & Wu, J. (2012). Surfactant-stabilized graphene/polyaniline nanofiber composites for high performance supercapacitor electrode. *Journal of Materials Chemistry*, 22(1), 80-85. doi: 10.1039/C1JM12869H
- Marlinda, A. R., Huang, N. M., Muhamad, M. R., An'amt, M. N., Chang, B. Y. S., Yusoff, N., . . . Kumar, S. V. (2012). Highly efficient preparation of ZnO nanorods decorated reduced graphene oxide nanocomposites. *Materials Letters*, 80, 9-12. doi: <https://doi.org/10.1016/j.matlet.2012.04.061>
- Marton, S., Cleto, F., Krieger, M. A., & Cardoso, J. (2016). Isolation of an Aptamer that Binds Specifically to E. coli. *PLoS ONE*, 11(4), e0153637. doi: 10.1371/journal.pone.0153637
- Marzel, A., Desai, P. T., Goren, A., Schorr, Y. I., Nissan, I., Porwollik, S., . . . Gal-Mor, O. (2016). Persistent Infections by Nontyphoidal Salmonella in Humans: Epidemiology and Genetics. *Clin Infect Dis*, 62(7), 879-886. doi: 10.1093/cid/civ1221
- Mattevi, C., Kim, H., & Chhowalla, M. (2011). A review of chemical vapour deposition of graphene on copper. *Journal of Materials Chemistry*, 21(10), 3324-3334. doi: 10.1039/C0JM02126A
- Mazánek, V., Luxa, J., Matějková, S., Kučera, J., Sedmidubský, D., Pumera, M., & Sofer, Z. (2019). Ultrapure Graphene Is a Poor Electrocatalyst: Definitive Proof of the Key Role of Metallic Impurities in Graphene-Based Electrocatalysis. *ACS Nano*, 13(2), 1574-1582. doi: 10.1021/acsnano.8b07534
- McCallion, C., Burthem, J., Rees-Unwin, K., Golovanov, A., & Pluen, A. (2016). Graphene in therapeutics delivery: Problems, solutions and future opportunities. *European Journal of Pharmaceutics and Biopharmaceutics*, 104, 235-250. doi: <https://doi.org/10.1016/j.ejpb.2016.04.015>
- McLinden, T., Sargeant, J. M., Thomas, M. K., Papadopoulos, A., & Fazil, A. (2014). Component costs of foodborne illness: a scoping review. *BMC Public Health*, 14, 509-509. doi: 10.1186/1471-2458-14-509
- McPherson, M., Kirk, M. D., Raupach, J., Combs, B., & Butler, J. R. (2011). Economic costs of Shiga toxin-producing Escherichia coli infection in Australia. *Foodborne Pathog Dis*, 8(1), 55-62. doi: 10.1089/fpd.2010.0608
- Medley, C. D., Bamrungsap, S., Tan, W., & Smith, J. E. (2011). Aptamer-conjugated nanoparticles for cancer cell detection. *Anal Chem*, 83(3), 727-734. doi: 10.1021/ac102263v
- Mei, X., Zhai, X., Lei, C., Ye, X., Kang, Z., Wu, X., . . . Wang, H. (2019). Development and application of a visual loop-mediated isothermal amplification combined with lateral flow dipstick (LAMP-LFD) method for rapid detection of Salmonella strains in food samples. *Food Control*, 104, 9-19. doi: <https://doi.org/10.1016/j.foodcont.2019.04.014>

- Meirinho, S. G., Dias, L. G., Peres, A. M., & Rodrigues, L. R. (2015). Development of an electrochemical RNA-aptasensor to detect human osteopontin. *Biosens Bioelectron*, *71*, 332-341. doi: 10.1016/j.bios.2015.04.050
- Mello, M., & Vidal, B. (2012). *Changes in the Infrared Microspectroscopic Characteristics of DNA Caused by Cationic Elements, Different Base Richness and Single-Stranded Form* (Vol. 7).
- Mohanty, N., & Berry, V. (2008). Graphene-Based Single-Bacterium Resolution Biodevice and DNA Transistor: Interfacing Graphene Derivatives with Nanoscale and Microscale Biocomponents. *Nano Letters*, *8*(12), 4469-4476. doi: 10.1021/nl802412n
- Monteserín, C., Blanco, M., Aranzabe, E., Aranzabe, A., & Vilas, J. L. (2017). Effects of graphene oxide and chemically reduced graphene oxide on the curing kinetics of epoxy amine composites. *Journal of Applied Polymer Science*, *134*(19). doi: 10.1002/app.44803
- Moon, J., Kim, G., Park, S. B., Lim, J., & Mo, C. (2015). Comparison of whole-cell SELEX methods for the identification of *Staphylococcus aureus*-specific DNA aptamers. *Sensors (Basel, Switzerland)*, *15*(4), 8884-8897. doi: 10.3390/s150408884
- Morales-Torres, S., Pastrana-Martínez, L. M., Figueiredo, J. L., Faria, J. L., & Silva, A. M. T. (2012). Design of graphene-based TiO₂ photocatalysts—a review. *Environmental Science and Pollution Research*, *19*(9), 3676-3687. doi: 10.1007/s11356-012-0939-4
- Muhammad Farooq, K., Muhammad Zahir, I., Muhammad Waqas, I., & Jonghwa, E. (2014). Improving the electrical properties of graphene layers by chemical doping. *Science and Technology of Advanced Materials*, *15*(5), 055004.
- Mulchandani, A., & Wang, C. L. (1996). Bienzyme sensors based on poly(anilinomethylferrocene)-modified electrodes. *Electroanalysis*, *8*(5), 414-419. doi: 10.1002/elan.1140080503
- Muthoosamy, K., Bai, R. G., Abubakar, I. B., Sudheer, S. M., Lim, H. N., Loh, H. S., . . . Manickam, S. (2015). Exceedingly biocompatible and thin-layered reduced graphene oxide nanosheets using an eco-friendly mushroom extract strategy. *Int J Nanomedicine*, *10*, 1505-1519. doi: 10.2147/ijn.s75213
- Ng, S. P., Qiu, G., Ding, N., Lu, X., & Wu, C. L. (2017). Label-free detection of 3-nitro-l-tyrosine with nickel-doped graphene localized surface plasmon resonance biosensor. *Biosens Bioelectron*, *89*(Pt 1), 468-476. doi: 10.1016/j.bios.2016.04.017
- Ngoi, S. T., Teh, C. S. J., Chai, L. C., & Thong, K. L. (2015). Overview of Molecular Typing Tools for The Characterization of *Salmonella enterica* in Malaysia. *Biomed. Environ. Sci*, *28*(10), 751-764. doi: 10.3967/bes2015.105
- Nigovic, B., Sadikovic, M., & Sertic, M. (2014). Multi-walled carbon nanotubes/Nafion composite film modified electrode as a sensor for simultaneous determination of

ondansetron and morphine. *Talanta*, 122, 187-194. doi: 10.1016/j.talanta.2014.01.026

- Nimse, S. B., Song, K., Sonawane, M. D., Sayyed, D. R., & Kim, T. (2014). Immobilization techniques for microarray: challenges and applications. *Sensors (Basel)*, 14(12), 22208-22229. doi: 10.3390/s141222208
- Norimatsu, W., & Kusunoki, M. (2014). Epitaxial graphene on SiC{0001}: advances and perspectives. *Physical Chemistry Chemical Physics*, 16(8), 3501-3511. doi: 10.1039/C3CP54523G
- Notley, S. M., Crawford, R. J., & Ivanova, E. P. (2013). Bacterial Interaction with Graphene Particles and Surfaces. In M. Aliofkhazraei (Ed.), *Advances in Graphene Science* (pp. Ch. 05). Rijeka: InTech.
- Novoselov, K. S., Geim, A. K., Morozov, S. V., Jiang, D., Zhang, Y., Dubonos, S. V., . . . Firsov, A. A. (2004). Electric Field Effect in Atomically Thin Carbon Films. *Science*, 306(5696), 666.
- Nurjayadi, M., Pertiwi, Y. P., Islami, N., Azizah, N., Efrianti, U. R., Saamia, V., . . . El-Enshasye, H. A. (2019). Detection of the Salmonella typhi bacteria in contaminated egg using real-time PCR to develop rapid detection of food poisoning bacteria. *Biocatalysis and Agricultural Biotechnology*, 20, 101214. doi: <https://doi.org/10.1016/j.bcab.2019.101214>
- Nurzulaikha, R., Lim, H. N., Harrison, I., Lim, S. S., Pandikumar, A., Huang, N. M., . . . Ibrahim, I. (2015). Graphene/SnO₂ nanocomposite-modified electrode for electrochemical detection of dopamine. *Sensing and Bio-Sensing Research*, 5, 42-49. doi: <https://doi.org/10.1016/j.sbsr.2015.06.002>
- Nyachuba, D. G. (2010). Foodborne illness: is it on the rise? *Nutr Rev*, 68(5), 257-269. doi: 10.1111/j.1753-4887.2010.00286.x
- Organization, W. H. (2015). WHO estimates of the global burden of foodborne diseases: foodborne disease burden epidemiology reference group 2007-2015: World Health Organization.
- Othman, M., Ritikos, R., Muhammad Hafiz, S., Khanis, N. H., Abdul Rashid, N. M., & Abdul Rahman, S. (2015). Low-temperature plasma-enhanced chemical vapour deposition of transfer-free graphene thin films. *Materials Letters*, 158, 436-438. doi: <https://doi.org/10.1016/j.matlet.2015.06.039>
- Ozden, A., Ercelik, M., Ozdemir, Y., Devrim, Y., & Colpan, C. O. (2017). Enhancement of direct methanol fuel cell performance through the inclusion of zirconium phosphate. *International Journal of Hydrogen Energy*, 42(33), 21501-21517. doi: <https://doi.org/10.1016/j.ijhydene.2017.01.188>
- Pandey, C. M., Tiwari, I., Singh, V. N., Sood, K. N., Sumana, G., & Malhotra, B. D. (2017). Highly sensitive electrochemical immunosensor based on graphene-wrapped copper oxide-cysteine hierarchical structure for detection of pathogenic bacteria. *Sensors and Actuators B: Chemical*, 238, 1060-1069. doi: <https://doi.org/10.1016/j.snb.2016.07.121>

- Pandikumar, A., Soon How, G. T., See, T. P., Omar, F. S., Jayabal, S., Kamali, K. Z., . . . Huang, N. M. (2014). Graphene and its nanocomposite material based electrochemical sensor platform for dopamine. *RSC Advances*, 4(108), 63296-63323. doi: 10.1039/C4RA13777A
- Pandikumar, A., Thien, G., Peik See, T., Saiha Omar, F., Jayabal, S., Zangeneh Kamali, K., . . . Ming, H. (2014). *Graphene and its nanocomposite material based electrochemical sensor platform for dopamine* (Vol. 4).
- Park, J. Y., & Park, S. M. (2009). DNA hybridization sensors based on electrochemical impedance spectroscopy as a detection tool. *Sensors (Basel)*, 9(12), 9513-9532. doi: 10.3390/s91209513
- Pei, S., & Cheng, H.-M. (2012). The reduction of graphene oxide. *Carbon*, 50(9), 3210-3228. doi: <https://doi.org/10.1016/j.carbon.2011.11.010>
- Peng, H., Hui, Y., Ren, R., Wang, B., Song, S., He, Y., & Zhang, F. (2019). A sensitive electrochemical aptasensor based on MB-anchored GO for the rapid detection of *Cronobacter sakazakii*. *Journal of Solid State Electrochemistry*, 23(12), 3391-3398. doi: 10.1007/s10008-019-04426-y
- Peng, J., & Weng, J. (2017). Enhanced peroxidase-like activity of MoS₂/graphene oxide hybrid with light irradiation for glucose detection. *Biosens Bioelectron*, 89(Pt 1), 652-658. doi: 10.1016/j.bios.2015.12.034
- Perreault, F., Fonseca de Faria, A., & Elimelech, M. (2015). Environmental applications of graphene-based nanomaterials. *Chemical Society Reviews*, 44(16), 5861-5896. doi: 10.1039/C5CS00021A
- Pethig, R. (1985). Dielectric and Electrical Properties of Biological Materials. *J. Bioelectr*, 4(2), vii-ix. doi: 10.3109/15368378509033258
- Pethig, R., & Markx, G. H. (1997). Applications of dielectrophoresis in biotechnology. *Trends Biotechnol*, 15(10), 426-432. doi: 10.1016/S0167-7799(97)01096-2
- Piccinini, E., Bliem, C., Reiner-Rozman, C., Battaglini, F., Azzaroni, O., & Knoll, W. (2017). Enzyme-polyelectrolyte multilayer assemblies on reduced graphene oxide field-effect transistors for biosensing applications. *Biosensors and Bioelectronics*, 92, 661-667. doi: <https://doi.org/10.1016/j.bios.2016.10.035>
- Pinto, H., & Markevich, A. (2014). Electronic and electrochemical doping of graphene by surface adsorbates. *Beilstein Journal of Nanotechnology*, 5, 1842-1848. doi: 10.3762/bjnano.5.195
- Pinto, S. D. S., Thayse, C., Marciane, M., Juliane, A., Yoko, H. E., & Moreira, d. O. T. C. R. (2011). Multiplex PCR for the simultaneous detection of *Salmonella* spp. and *Salmonella* Enteritidis in food. *International Journal of Food Science & Technology*, 46(7), 1502-1507. doi: doi:10.1111/j.1365-2621.2011.02646.x
- Piscanec, S., Lazzeri, M., Mauri, F., Ferrari, A. C., & Robertson, J. (2004). Kohn Anomalies and Electron-Phonon Interactions in Graphite. *Physical Review Letters*, 93(18), 185503. doi: 10.1103/PhysRevLett.93.185503

- Poh, H. L., Šaněk, F., Ambrosi, A., Zhao, G., Sofer, Z., & Pumera, M. (2012). Graphenes prepared by Staudenmaier, Hofmann and Hummers methods with consequent thermal exfoliation exhibit very different electrochemical properties. *Nanoscale*, 4(11), 3515-3522. doi: 10.1039/C2NR30490B
- Potts, J. R., Dreyer, D. R., Bielawski, C. W., & Ruoff, R. S. (2011). Graphene-based polymer nanocomposites. *Polymer*, 52(1), 5-25. doi: https://doi.org/10.1016/j.polymer.2010.11.042
- Poulsen, F., & Hansen, T. (2017). Band Gap Energy of Gradient Core–Shell Quantum Dots. *The Journal of Physical Chemistry C*, 121(25), 13655-13659. doi: 10.1021/acs.jpcc.7b01792
- Priyanka, B., Patil, R. K., & Dwarakanath, S. (2016). A review on detection methods used for foodborne pathogens. *The Indian journal of medical research*, 144(3), 327-338. doi: 10.4103/0971-5916.198677
- Pumera, M. (2011). Graphene in biosensing. *Materials Today*, 14(7), 308-315. doi: https://doi.org/10.1016/S1369-7021(11)70160-2
- Punckt, C., Muckel, F., Wepfer, S., A. Aksay, I., Chavarin, C., Bacher, G., & Mertin, W. (2013). *The effect of degree of reduction on the electrical properties of functionalized graphene sheets* (Vol. 102).
- Punckt, C., Pope Michael, A., Liu, J., Lin, Y., & Aksay Ilhan, A. (2010). Electrochemical Performance of Graphene as Effected by Electrode Porosity and Graphene Functionalization. *Electroanalysis*, 22(23), 2834-2841. doi: 10.1002/elan.201000367
- Qiao, S.-J., Xu, X.-N., Qiu, Y., Xiao, H.-C., & Zhu, Y.-F. (2016). Simultaneous Reduction and Functionalization of Graphene Oxide by 4-Hydrazinobenzenesulfonic Acid for Polymer Nanocomposites. *Nanomaterials*, 6(2), 29. doi: 10.3390/nano6020029
- Qin, H., Shi, X., Yu, L., Li, K., Wang, J., Chen, J., . . . Xu, H. (2020). Multiplex real-time PCR coupled with sodium dodecyl sulphate and propidium monoazide for the simultaneous detection of viable *Listeria monocytogenes*, *Cronobacter sakazakii*, *Staphylococcus aureus* and *Salmonella* spp. in milk. *International Dairy Journal*, 108, 104739. doi: https://doi.org/10.1016/j.idairyj.2020.104739
- Qing, Z., Hao, W., Nan, W., Rui, Y., Yuehui, M., Weijun, G., . . . Kejian, D. (2014). Graphene-based Biosensors for Biomolecules Detection. *Current Nanoscience*, 10(5), 627-637. doi: http://dx.doi.org/10.2174/1573413710666140422231701
- R. New, C. Y., Ubong, A., Premarathne, J.M.K.J.K., Thung, T.Y., Lee, E., Chang, W.S., Loo, Y.Y., Kwan, S.Y., Tan, C.W., Kuan, C.H. and Son. (2017). Microbiological food safety in Malaysia from the academician's perspective. *Food Research*, 1(6), 183 - 202. doi: http://doi.org/10.26656/fr.2017.6.013
- Radhakrishnan, S., Krishnamoorthy, K., Sekar, C., Wilson, J., & Kim, S. J. (2014). A highly sensitive electrochemical sensor for nitrite detection based on Fe₂O₃ nanoparticles decorated reduced graphene oxide nanosheets. *Applied Catalysis B*:

- Radi, A.-E. (2011). Electrochemical Aptamer-Based Biosensors: Recent Advances and Perspectives. *International Journal of Electrochemistry*, 2011, 17. doi: 10.4061/2011/863196
- Radzi Hanifah, M. F., Jaafar, J., Aziz, M., Ismail, A. F., Othman, M. H. D., & Rahman, M. A. (2015). Effects of reduction time on the structural, electrical and thermal properties of synthesized reduced graphene oxide nanosheets. *Bulletin of Materials Science*, 38(6), 1569-1576. doi: 10.1007/s12034-015-0970-4
- Rahayu, W. P., Fardiaz, D., Kartika, G. D., Nababan, H., Fanaike, R., & Puspitasari, R. (2016). Estimation of economic loss due to food poisoning outbreaks. *Food Science and Biotechnology*, 25(1), 157-161. doi: 10.1007/s10068-016-0113-8
- Raja, R., Krishnan, K., Maggie Dayana, A., Maheswari, G., V, E., Nagaraj, D.-P., . . . Victor Williams, R. (2017). Reduced graphene oxide embedded titanium dioxide nanocomposite as novel photoanode material in natural dye-sensitized solar cells. *Journal of Materials Science: Materials in Electronics*, 28(18), 13678–13689. doi: <https://doi.org/10.1007/s10854-017-7211-0>
- Rajagopalan, B., & Chung, J. S. (2014). Reduced chemically modified graphene oxide for supercapacitor electrode. *Nanoscale Research Letters*, 9(1), 535-535. doi: 10.1186/1556-276X-9-535
- Rajoba, S. J., Sartale, S. D., & Jadhav, L. D. (2018). Investigating functional groups in GO and r-GO through spectroscopic tools and effect on optical properties. *Optik*, 175, 312-318. doi: <https://doi.org/10.1016/j.ijleo.2018.09.018>
- Ramli, M., Abdullah, M. M. A. B., Che Halin, D. S., Mat Isa, S. S., Talip, L., Danial, N., & Zainol Murad, S. A. (2017). *Interdigitated electrodes as impedance and capacitance biosensors: A review* (Vol. 1885).
- Ramli, M. M., Hanim, K. N., Muda, M. R., Mat Isa, S. S., & Jamlos, M. F. (2015). The Effect of Different Reduction Methods on Conductivity of Reduced-Graphene Oxide (r-GO). *Applied Mechanics and Materials*, 815, 216-220. doi: 10.4028/www.scientific.net/AMM.815.216
- Ramnani, P., Saucedo, N. M., & Mulchandani, A. (2016). Carbon nanomaterial-based electrochemical biosensors for label-free sensing of environmental pollutants. *Chemosphere*, 143(Supplement C), 85-98. doi: <https://doi.org/10.1016/j.chemosphere.2015.04.063>
- Ramos Ferrer, P., Mace, A., Thomas, S. N., & Jeon, J.-W. (2017). Nanostructured porous graphene and its composites for energy storage applications. *Nano Convergence*, 4(1), 29. doi: 10.1186/s40580-017-0123-0
- Rani, P., & Jindal, V. K. (2013). Designing band gap of graphene by B and N dopant atoms. *RSC Advances*, 3(3), 802-812. doi: 10.1039/C2RA22664B
- Rasouli, H., Naji, L., & Hosseini, M. G. (2017). Electrochemical and electromechanical behavior of Nafion-based soft actuators with PPy/CB/MWCNT nanocomposite electrodes. *RSC Advances*, 7(6), 3190-3203. doi: 10.1039/C6RA25771B

- Raza, H. (2012). *Graphene nanoelectronics: metrology, synthesis, properties and applications*: Springer Science & Business Media.
- Reich, P., Stoltenburg, R., Strehlitz, B., Frense, D., & Beckmann, D. (2017). Development of An Impedimetric Aptasensor for the Detection of *Staphylococcus aureus*. *International Journal of Molecular Sciences*, *18*(11), 2484. doi: 10.3390/ijms18112484
- Reina, A., Jia, X., Ho, J., Nezich, D., Son, H., Bulovic, V., . . . Kong, J. (2009). Large Area, Few-Layer Graphene Films on Arbitrary Substrates by Chemical Vapor Deposition. *Nano Letters*, *9*(1), 30-35. doi: 10.1021/nl801827v
- Reinemann, C., & Strehlitz, B. (2014). Aptamer-modified nanoparticles and their use in cancer diagnostics and treatment. *Swiss Med Wkly*, *144*, w13908. doi: 10.4414/smw.2014.13908
- Reiner-Rozman, C., Larisika, M., Nowak, C., & Knoll, W. (2015). Graphene-Based Liquid-Gated Field Effect Transistor for Biosensing: Theory and Experiments. *Biosens Bioelectron*, *70*, 21-27. doi: 10.1016/j.bios.2015.03.013
- Revin, S. B., & John, S. A. (2012). Electrochemical sensor for neurotransmitters at physiological pH using a heterocyclic conducting polymer modified electrode. *Analyst*, *137*(1), 209-215. doi: 10.1039/C1AN15746A
- Rhouati, A., Catanante, G., Nunes, G., Hayat, A., & Marty, J.-L. (2016). Label-Free Aptasensors for the Detection of Mycotoxins. *Sensors (Basel, Switzerland)*, *16*(12), 2178. doi: 10.3390/s16122178
- Rohde, A., Hammerl, J. A., Appel, B., Dieckmann, R., & Al Dahouk, S. (2015). Sampling and Homogenization Strategies Significantly Influence the Detection of Foodborne Pathogens in Meat. *BioMed Research International*, *2015*, 8. doi: 10.1155/2015/145437
- Ronkainen, N. J., Halsall, H. B., & Heineman, W. R. (2010). Electrochemical biosensors. *Chem Soc Rev*, *39*(5), 1747-1763. doi: 10.1039/b714449k
- Roushani, M., & Shahdost-Fard, F. (2016). Covalent attachment of aptamer onto nanocomposite as a high performance electrochemical sensing platform: Fabrication of an ultra-sensitive ibuprofen electrochemical aptasensor. *Mater Sci Eng C Mater Biol Appl*, *68*, 128-135. doi: 10.1016/j.msec.2016.05.099
- Roy, C. L. (1977). Carrier concentrations and Fermi-levels in extrinsic semiconductors. *Czechoslovak Journal of Physics B*, *27*(7), 769-776. doi: 10.1007/bf01589318
- Said, B., Okba, B., & Hachemi Ben, T. (2014). Effect of band gap energy on the electrical conductivity in doped ZnO thin film. *Journal of Semiconductors*, *35*(7), 073001.
- Sakulpaisan, S., Vongsetskul, T., Reamouppaturm, S., Luangkachao, J., Tantirungrotechai, J., & Tangboriboonrat, P. (2016). Titania-functionalized graphene oxide for an efficient adsorptive removal of phosphate ions. *Journal of Environmental Management*, *167*, 99-104. doi: https://doi.org/10.1016/j.jenvman.2015.11.028

- Salavagione, H. J., Diez-Pascual, A. M., Lazaro, E., Vera, S., & Gomez-Fatou, M. A. (2014). Chemical sensors based on polymer composites with carbon nanotubes and graphene: the role of the polymer. *Journal of Materials Chemistry A*, 2(35), 14289-14328. doi: 10.1039/C4TA02159B
- Salleh, W., Lani, M. N., Abdullah, W. Z. W., Chilek, T. Z. T., & Hassan, Z. (2017). A review on incidences of foodborne diseases and interventions for a better national food safety system in Malaysia. *Malaysian Applied Biology*, 46(3), 1-7.
- Sang, M., Shin, J., Kim, K., & Yu, K. J. (2019). Electronic and Thermal Properties of Graphene and Recent Advances in Graphene Based Electronics Applications. *Nanomaterials (Basel, Switzerland)*, 9(3), 374. doi: 10.3390/nano9030374
- Scharff, R. L. (2012). Economic burden from health losses due to foodborne illness in the United States. *J Food Prot*, 75(1), 123-131. doi: 10.4315/0362-028x.jfp-11-058
- Schlierf, A., Yang, H., Gebremedhn, E., Treossi, E., Ortolani, L., Chen, L., . . . Casiraghi, C. (2013). Nanoscale insight into the exfoliation mechanism of graphene with organic dyes: effect of charge, dipole and molecular structure. *Nanoscale*, 5(10), 4205-4216. doi: 10.1039/C3NR00258F
- Schrader, C., Schielke, A., Ellerbroek, L., & Johne, R. (2012). PCR inhibitors – occurrence, properties and removal. *Journal of Applied Microbiology*, 113(5), 1014-1026. doi: 10.1111/j.1365-2672.2012.05384.x
- Schuster, K. C., Mertens, F., & Gapes, J. R. (1999). FTIR spectroscopy applied to bacterial cells as a novel method for monitoring complex biotechnological processes. Based on a poster presented at AIRS III, Vienna, July 1998.1. *Vibrational Spectroscopy*, 19(2), 467-477. doi: https://doi.org/10.1016/S0924-2031(98)00058-7
- Sekharappa, S., Kishore, B., Penki, T., & Munichandraiah, N. (2014). *Symmetric supercapacitor based on partially exfoliated and reduced graphite oxide in neutral aqueous electrolyte* (Vol. 199).
- Setny, P., Bahadur, R. P., & Zacharias, M. (2012). Protein-DNA docking with a coarse-grained force field. *BMC Bioinformatics*, 13, 228. doi: 10.1186/1471-2105-13-228
- Settingington, E. B., & Alocilja, E. C. (2012). Electrochemical Biosensor for Rapid and Sensitive Detection of Magnetically Extracted Bacterial Pathogens. *Biosensors*, 2(1), 15. doi: 10.3390/bios2010015
- Sevim, M., Francia, C., Amici, J., Vankova, S., Şener, T., & Metin, Ö. (2016). Bimetallic MPt (M: Co, Cu, Ni) alloy nanoparticles assembled on reduced graphene oxide as high performance cathode catalysts for rechargeable lithium-oxygen batteries. *Journal of Alloys and Compounds*, 683, 231-240. doi: https://doi.org/10.1016/j.jallcom.2016.05.094
- Shahid, M. M., Rameshkumar, P., Pandikumar, A., Lim, H. N., Ng, Y. H., & Huang, N. M. (2015). An electrochemical sensing platform based on a reduced graphene oxide-cobalt oxide nanocube@platinum nanocomposite for nitric oxide detection.

Journal of Materials Chemistry A, 3(27), 14458-14468. doi: 10.1039/C5TA02608C

- Shan, C., Yang, H., Han, D., Zhang, Q., Ivaska, A., & Niu, L. (2010). Graphene/AuNPs/chitosan nanocomposites film for glucose biosensing. *Biosens Bioelectron*, 25(5), 1070-1074. doi: 10.1016/j.bios.2009.09.024
- Shao, Y., Wang, J., Wu, H., Liu, J., Aksay, I. A., & Lin, Y. (2010). Graphene Based Electrochemical Sensors and Biosensors: A Review. *Electroanalysis*, 22(10), 1027-1036. doi: 10.1002/elan.200900571
- Shao, Y., Zhu, S., Jin, C., & Chen, F. (2011). Development of multiplex loop-mediated isothermal amplification-RFLP (mLAMP-RFLP) to detect *Salmonella* spp. and *Shigella* spp. in milk. *Int J Food Microbiol*, 148(2), 75-79. doi: 10.1016/j.ijfoodmicro.2011.05.004
- Sharma, D., Kanchi, S., Sabela, M. I., & Bisetty, K. (2016). Insight into the biosensing of graphene oxide: Present and future prospects. *Arabian Journal of Chemistry*, 9(2), 238-261. doi: <https://doi.org/10.1016/j.arabjc.2015.07.015>
- Sheikhzadeh, E., Chamsaz, M., Turner, A., Jager, E., & Beni, V. (2016). *Label-free impedimetric biosensor for Salmonella Typhimurium detection based on poly [pyrrole-co-3-carboxyl-pyrrole] copolymer supported aptamer* (Vol. 80).
- Shen, Z., Hou, N., Jin, M., Qiu, Z., Wang, J., Zhang, B., . . . Li, J. (2014). A novel enzyme-linked immunosorbent assay for detection of *Escherichia coli* O157:H7 using immunomagnetic and beacon gold nanoparticles. *Gut Pathog*, 6, 14. doi: 10.1186/1757-4749-6-14
- Singh, A., Poshtiban, S., & Evoy, S. (2013). Recent advances in bacteriophage based biosensors for food-borne pathogen detection. *Sensors (Basel)*, 13(2), 1763-1786. doi: 10.3390/s130201763
- Singh, R. P. (2012). Prospects of Organic Conducting Polymer Modified Electrodes: Enzymosensors. *International Journal of Electrochemistry*, 2012, 14. doi: 10.1155/2012/502707
- Sinwat, N., Angkittitrakul, S., Coulson, K. F., Pilapil, F. M. I. R., Meunsene, D., & Chuanchuen, R. (2016). High prevalence and molecular characteristics of multidrug-resistant *Salmonella* in pigs, pork and humans in Thailand and Laos provinces. *J. Med. Microbiol*, 65(10), 1182-1193. doi: doi:10.1099/jmm.0.000339
- Sivek, J., Leenaerts, O., Partoens, B., & Peeters, F. (2013). *Adsorption of titanium and titanium dioxide on graphene: n and p-type doping*.
- Solanki, P. R., Kaushik, A., Agrawal, V. V., & Malhotra, B. D. (2011). Nanostructured metal oxide-based biosensors. *Npg Asia Materials*, 3, 17. doi: 10.1038/asiamat.2010.137
- Solanki, P. R., Srivastava, S., Ali, M. A., Srivastava, R. K., Srivastava, A., & Malhotra, B. D. (2014). Reduced graphene oxide-titania based platform for label-free biosensor. *RSC Advances*, 4(104), 60386-60396. doi: 10.1039/C4RA09265A

- Sousa, A. M., & Pereira, M. O. (2013). A prospect of current microbial diagnosis methods. *Microbial pathogens and strategies for combating them: science, technology and education*, 3, 1429-1438.
- Srinivas, A. R., Peng, H., Barker, D., & Travas-Sejdic, J. (2012). Switch on or switch off: an optical DNA sensor based on poly(p-phenylenevinylene) grafted magnetic beads. *Biosens Bioelectron*, 35(1), 498-502. doi: 10.1016/j.bios.2012.03.022
- Stojanović, D., Woehrl, N., & Buck, V. (2012). Synthesis and characterization of graphene films by hot filament chemical vapor deposition. *Physica Scripta*, 2012(T149), 014068.
- Stoltenburg, R., Schubert, T., & Strehlitz, B. (2015). In vitro Selection and Interaction Studies of a DNA Aptamer Targeting Protein A. *PLoS ONE*, 10(7), e0134403. doi: 10.1371/journal.pone.0134403
- Sun, C.-L., Lee, H.-H., Yang, J.-M., & Wu, C.-C. (2011). The simultaneous electrochemical detection of ascorbic acid, dopamine, and uric acid using graphene/size-selected Pt nanocomposites. *Biosensors and Bioelectronics*, 26(8), 3450-3455. doi: https://doi.org/10.1016/j.bios.2011.01.023
- Sun, H., Zhu, X., Lu, P. Y., Rosato, R. R., Tan, W., & Zu, Y. (2014). Oligonucleotide Aptamers: New Tools for Targeted Cancer Therapy. *Molecular Therapy. Nucleic Acids*, 3(8), e182. doi: 10.1038/mtna.2014.32
- Surajit, S., Prasenjit, B., EunHee, H., Keunsik, L., Yeoheung, Y., Sohyeon, S., & Hyoyoung, L. (2012). Can Commonly Used Hydrazine Produce n-Type Graphene? *Chemistry – A European Journal*, 18(25), 7665-7670. doi: doi:10.1002/chem.201200104
- Suvarnaphaet, P., & Pechprasarn, S. (2017). Graphene-Based Materials for Biosensors: A Review. *Sensors (Basel)*, 17(10). doi: 10.3390/s17102161
- Tan, L.-L., Ong, W.-J., Chai, S.-P., & Mohamed, A. R. (2013). Reduced graphene oxide-TiO₂ nanocomposite as a promising visible-light-active photocatalyst for the conversion of carbon dioxide. *Nanoscale Research Letters*, 8(1), 465-465. doi: 10.1186/1556-276X-8-465
- Tang, W., Li, L., & Zeng, X. (2015). A glucose biosensor based on the synergistic action of nanometer-sized TiO₂ and polyaniline. *Talanta*, 131, 417-423. doi: 10.1016/j.talanta.2014.08.019
- Tennant, S. M., MacLennan, C. A., Simon, R., Martin, L. B., & Khan, M. I. (2016). Nontyphoidal salmonella disease: Current status of vaccine research and development. *Vaccine*, 34(26), 2907-2910. doi: https://doi.org/10.1016/j.vaccine.2016.03.072
- Teodorescu, M., & Bercea, M. (2015). Poly(vinylpyrrolidone) – A Versatile Polymer for Biomedical and Beyond Medical Applications. *Polymer-Plastics Technology and Engineering*, 54(9), 923-943. doi: 10.1080/03602559.2014.979506
- Thavanathan, J., Huang, N. M., & Thong, K. L. (2014). Colorimetric detection of DNA hybridization based on a dual platform of gold nanoparticles and graphene oxide. *Biosens Bioelectron*, 55, 91-98. doi: 10.1016/j.bios.2013.11.072

- Thévenot, D. R., Toth, K., Durst, R. A., & Wilson, G. S. (2001). Electrochemical biosensors: recommended definitions and classification. *International Union of Pure and Applied Chemistry: Physical Chemistry Division, Commission I.7 (Biophysical Chemistry); Analytical Chemistry Division, Commission V.5 (Electroanalytical Chemistry)*.1. *Biosensors and Bioelectronics*, *16*(1), 121-131. doi: [https://doi.org/10.1016/S0956-5663\(01\)00115-4](https://doi.org/10.1016/S0956-5663(01)00115-4)
- Thiha, A., Ibrahim, F., Muniandy, S., Dinshaw, I. J., Teh, S. J., Thong, K. L., . . . Madou, M. (2018). All-carbon suspended nanowire sensors as a rapid highly-sensitive label-free chemiresistive biosensing platform. *Biosensors and Bioelectronics*, *107*, 145-152. doi: <https://doi.org/10.1016/j.bios.2018.02.024>
- Thung, T. Y., Mahyudin, N. A., Basri, D. F., Wan Mohamed Radzi, C. W., Nakaguchi, Y., Nishibuchi, M., & Radu, S. (2016). Prevalence and antibiotic resistance of *Salmonella* Enteritidis and *Salmonella* Typhimurium in raw chicken meat at retail markets in Malaysia. *Poult Sci*, *95*(8), 1888-1893. doi: 10.3382/ps/pew144
- Tien, H.-W., Huang, Y.-L., Yang, S.-Y., Wang, J.-Y., & Ma, C.-C. M. (2011). The production of graphene nanosheets decorated with silver nanoparticles for use in transparent, conductive films. *Carbon*, *49*(5), 1550-1560. doi: <https://doi.org/10.1016/j.carbon.2010.12.022>
- Tiwari, I., Singh, M., Pandey, C. M., & Sumana, G. (2015). Electrochemical genosensor based on graphene oxide modified iron oxide–chitosan hybrid nanocomposite for pathogen detection. *Sensors and Actuators B: Chemical*, *206*, 276-283. doi: <https://doi.org/10.1016/j.snb.2014.09.056>
- Torres-Mendieta, R., Ventura-Espinosa, D., Sabater, S., Lancis, J., Mínguez-Vega, G., & Mata, J. A. (2016). In situ decoration of graphene sheets with gold nanoparticles synthesized by pulsed laser ablation in liquids. *Scientific Reports*, *6*, 30478. doi: 10.1038/srep30478
- <https://www.nature.com/articles/srep30478#supplementary-information>
- Tothill, I. (2011). Biosensors and nanomaterials and their application for mycotoxin determination. *World Mycotoxin Journal*, *4*(4), 361-374. doi: 10.3920/WMJ2011.1318
- Tour, J. M. (2014). Top-Down versus Bottom-Up Fabrication of Graphene-Based Electronics. *Chemistry of Materials*, *26*(1), 163-171. doi: 10.1021/cm402179h
- Troeger, C., Blacker, B. F., Khalil, I. A., Rao, P. C., Cao, S., Zimsen, S. R. M., . . . Reiner, R. C., Jr. (2018). Estimates of the global, regional, and national morbidity, mortality, and aetiologies of diarrhoea in 195 countries: a systematic analysis for the Global Burden of Disease Study 2016. *The Lancet Infectious Diseases*, *18*(11), 1211-1228. doi: 10.1016/S1473-3099(18)30362-1
- Tuncel, D. (2011). Non-covalent interactions between carbon nanotubes and conjugated polymers. *Nanoscale*, *3*(9), 3545-3554. doi: 10.1039/C1NR10338E
- Turner, A. P. (2013). Biosensors: sense and sensibility. *Chem Soc Rev*, *42*(8), 3184-3196. doi: 10.1039/c3cs35528d

- Urmann, K., Arshavsky-Graham, S., Walter, J. G., Scheper, T., & Segal, E. (2016). Whole-cell detection of live lactobacillus acidophilus on aptamer-decorated porous silicon biosensors. *Analyst*, *141*(18), 5432-5440. doi: 10.1039/C6AN00810K
- Urmann, K., Modrejewski, J., Scheper, T., & Walter Johanna, G. (2017). Aptamer-modified nanomaterials: principles and applications *BioNanoMaterials* (Vol. 18).
- Van Noorden, R. (2012). Production: Beyond sticky tape. *Nature*, *483*, S32. doi: 10.1038/483S32a
- Vandenabeele, P., Moens, L., Edwards, H. G., & Dams, R. (2000). Raman spectroscopic database of azo pigments and application to modern art studies. *J. Raman Spectrosc*, *31*(6), 509-517. doi: 10.1002/1097-4555(200006)31:6<509::AID-JRS566>3.0.CO;2-0
- Vikas, M. (2014). Functional Polymer Nanocomposites with Graphene: A Review. *Macromolecular Materials and Engineering*, *299*(8), 906-931. doi: doi:10.1002/mame.201300394
- Wang, L., Dimitrijević, S., Fissel, A., Walker, G., Chai, J., Hold, L., . . . Iacopi, A. (2016). Growth mechanism for alternating supply epitaxy: the unique pathway to achieve uniform silicon carbide films on multiple large-diameter silicon substrates. *RSC Advances*, *6*(20), 16662-16667. doi: 10.1039/C5RA24797G
- Wang, L., Li, Y., & Mustaphai, A. (2007). Rapid and simultaneous quantitation of Escherichia coli 0157:H7, Salmonella, and Shigella in ground beef by multiplex real-time PCR and immunomagnetic separation. *J Food Prot*, *70*(6), 1366-1372. doi: 10.4315/0362-028X-70.6.1366
- Wang, L., Shi, L., Su, J., Ye, Y., & Zhong, Q. (2013). Detection of Vibrio parahaemolyticus in food samples using in situ loop-mediated isothermal amplification method. *Gene*, *515*(2), 421-425. doi: 10.1016/j.gene.2012.12.039
- Wang, L., Xu, M., Han, L., Zhou, M., Zhu, C., & Dong, S. (2012). Graphene enhanced electron transfer at aptamer modified electrode and its application in biosensing. *Anal. Chem*, *84*(17), 7301-7307. doi: 10.1021/ac300521d
- Wang, P., Ao, Y., Wang, C., Hou, J., & Qian, J. (2012). Enhanced photoelectrocatalytic activity for dye degradation by graphene–titania composite film electrodes. *Journal of Hazardous Materials*, *223-224*, 79-83. doi: https://doi.org/10.1016/j.jhazmat.2012.04.050
- Wang, P., Zhai, Y., Wang, D., & Dong, S. (2011). Synthesis of reduced graphene oxide- anatase TiO₂ nanocomposite and its improved photo-induced charge transfer properties. *Nanoscale*, *3*(4), 1640-1645. doi: 10.1039/c0nr00714e
- Wang, P., Zhai, Y., Wang, D., & Dong, S. (2011). Synthesis of reduced graphene oxide- anatase TiO₂ nanocomposite and its improved photo-induced charge transfer properties. *Nanoscale*, *3*(4), 1640-1645. doi: 10.1039/C0NR00714E
- Wang, Y., Li, Z., Wang, J., Li, J., & Lin, Y. (2011). Graphene and graphene oxide: biofunctionalization and applications in biotechnology. *Trends in Biotechnology*, *29*(5), 205-212. doi: https://doi.org/10.1016/j.tibtech.2011.01.008

- Wang, Y., & Salazar, J. K. (2016). Culture-Independent Rapid Detection Methods for Bacterial Pathogens and Toxins in Food Matrices. *Comprehensive Reviews in Food Science and Food Safety*, 15(1), 183-205. doi: 10.1111/1541-4337.12175
- Wang, Y., Wan, Y., & Zhang, D. (2010). Reduced graphene sheets modified glassy carbon electrode for electrocatalytic oxidation of hydrazine in alkaline media. *Electrochemistry Communications*, 12(2), 187-190. doi: https://doi.org/10.1016/j.elecom.2009.11.019
- Wang, Y., Ye, Z., & Ying, Y. (2012). New trends in impedimetric biosensors for the detection of foodborne pathogenic bacteria. *Sensors*, 12(3), 3449-3471. doi: 10.3390/s120303449
- Winter, S. E., Thiennimitr, P., Winter, M. G., Butler, B. P., Huseby, D. L., Crawford, R. W., . . . Baumler, A. J. (2010). Gut inflammation provides a respiratory electron acceptor for Salmonella. *Nature*, 467(7314), 426-429. doi: 10.1038/nature09415
- Wolffs, P. F. G., Glencross, K., Thibaudeau, R., & Griffiths, M. W. (2006). Direct Quantitation and Detection of Salmonellae in Biological Samples without Enrichment, Using Two-Step Filtration and Real-Time PCR. *Applied and Environmental Microbiology*, 72(6), 3896-3900. doi: 10.1128/aem.02112-05
- Wu, G., Dai, Z., Tang, X., Lin, Z., Lo, P., Meyyappan, M., & Lai, K. (2017). *Biosensing: Graphene Field-Effect Transistors for the Sensitive and Selective Detection of Escherichia coli Using Pyrene-Tagged DNA Aptamer (Adv. Healthcare Mater. 19/2017)* (Vol. 6).
- Wu, G., Dai, Z., Tang, X., Lin, Z., Lo, P. K., Meyyappan, M., & Lai, K. W. C. (2017). Graphene Field-Effect Transistors for the Sensitive and Selective Detection of Escherichia coli Using Pyrene-Tagged DNA Aptamer. *Advanced Healthcare Materials*, 6(19), 1700736. doi: doi:10.1002/adhm.201700736
- Wu, G., Meyyappan, M., & Lai, W. K. (2018). Simulation of Graphene Field-Effect Transistor Biosensors for Bacterial Detection. *Sensors*, 18(6). doi: 10.3390/s18061715
- Wu, S., Yang, R., Cheng, M., Yang, W., Xie, G., Chen, P., . . . Zhang, G. (2014). Defect-enhanced coupling between graphene and SiO₂ substrate. *Applied Physics Letters*, 105(6), 063113. doi: 10.1063/1.4892959
- Wu, W., Li, J., Pan, D., Li, J., Song, S., Rong, M., . . . Lu, J. (2014). Gold nanoparticle-based enzyme-linked antibody-aptamer sandwich assay for detection of Salmonella Typhimurium. *ACS Appl Mater Interfaces*, 6(19), 16974-16981. doi: 10.1021/am5045828
- Wu, W., Li, J., Pan, D., Li, J., Song, S., Rong, M., . . . Lu, J. (2014). Gold Nanoparticle-Based Enzyme-Linked Antibody-Aptamer Sandwich Assay for Detection of Salmonella Typhimurium. *ACS Applied Materials & Interfaces*, 6(19), 16974-16981. doi: 10.1021/am5045828
- Wu, Y., Jiang, W., Ren, Y., Cai, W., Lee, W. H., Li, H., . . . Ruoff, R. S. (2012). Tuning the doping type and level of graphene with different gold configurations. *Small*, 8(20), 3129-3136. doi: 10.1002/smll.201200520

- Wu, Z.-S., Zhou, G., Yin, L.-C., Ren, W., Li, F., & Cheng, H.-M. (2012). Graphene/metal oxide composite electrode materials for energy storage. *Nano Energy*, *1*(1), 107-131. doi: <https://doi.org/10.1016/j.nanoen.2011.11.001>
- Xi, X., & Ming, L. (2012). A voltammetric sensor based on electrochemically reduced graphene modified electrode for sensitive determination of midecamycin. *Analytical Methods*, *4*(9), 3013-3018. doi: 10.1039/C2AY25537E
- Xia, H., Zhang, X., Shi, Z., Zhao, C., Li, Y., Wang, J., & Qiao, G. (2015). Mechanical and thermal properties of reduced graphene oxide reinforced aluminum nitride ceramic composites. *Mater. Sci. Eng. A*, *639*, 29-36. doi: 10.1016/j.msea.2015.04.091
- Xiang, Q., Yu, J., & Jaroniec, M. (2011). Enhanced photocatalytic H₂-production activity of graphene-modified titania nanosheets. *Nanoscale*, *3*(9), 3670-3678. doi: 10.1039/C1NR10610D
- Xiang, Q., Yu, J., & Jaroniec, M. (2012). Graphene-based semiconductor photocatalysts. *Chem Soc Rev*, *41*(2), 782-796. doi: 10.1039/C1CS15172J
- Xu, C., Yuan, R.-s., & Wang, X. (2014). Selective reduction of graphene oxide. *New Carbon Materials*, *29*(1), 61-66. doi: [https://doi.org/10.1016/S1872-5805\(14\)60126-8](https://doi.org/10.1016/S1872-5805(14)60126-8)
- Xu, J., Zhang, P., Zhuang, L., Zhang, D., Qi, K., Dou, X., . . . Gong, J. (2019). Multiplex polymerase chain reaction to detect Salmonella serovars Indiana, Enteritidis, and Typhimurium in raw meat. *Journal of Food Safety*, *39*(5), e12674. doi: 10.1111/jfs.12674
- Xu, K., Meshik, X., Nichols, B. M., Zakar, E., Dutta, M., & Stroschio, M. A. (2014). Graphene- and aptamer-based electrochemical biosensor. *Nanotechnology*, *25*(20), 205501. doi: 10.1088/0957-4484/25/20/205501
- Xu, X., Gao, F., Bai, X., Liu, F., Kong, W., & Li, M. (2017). Tuning the Photoluminescence of Graphene Quantum Dots by Photochemical Doping with Nitrogen. *Materials*, *10*(11), 1328. doi: 10.3390/ma10111328
- Yadav, R., & Dixit, C. (2017). *Review on: Synthesis, Characterization and Potential application of Nitrogen-doped Graphene* (Vol. 2).
- Yan, H., Liu, C.-C., Bai, K.-K., Wang, X., Liu, M., Yan, W., . . . He, L. (2013). Electronic structures of graphene layers on a metal foil: The effect of atomic-scale defects. *Applied Physics Letters*, *103*(14), 143120. doi: 10.1063/1.4824206
- Yang, W., Ratinac, K. R., Ringer, S. P., Thordarson, P., Gooding, J. J., & Braet, F. (2010). Carbon Nanomaterials in Biosensors: Should You Use Nanotubes or Graphene? *Angewandte Chemie International Edition*, *49*(12), 2114-2138. doi: 10.1002/anie.200903463
- Yang, X., Kirsch, J., & Simonian, A. (2013). Campylobacter spp. detection in the 21st century: A review of the recent achievements in biosensor development. *J Microbiol Methods*, *95*(1), 48-56. doi: <https://doi.org/10.1016/j.mimet.2013.06.023>

- Yang, X., Tu, Y., Li, L., Shang, S., & Tao, X.-m. (2010). Well-Dispersed Chitosan/Graphene Oxide Nanocomposites. *ACS Applied Materials & Interfaces*, 2(6), 1707-1713. doi: 10.1021/am100222m
- Yang, Y., Asiri, A. M., Tang, Z., Du, D., & Lin, Y. (2013). Graphene based materials for biomedical applications. *Materials Today*, 16(10), 365-373. doi: https://doi.org/10.1016/j.mattod.2013.09.004
- Ye, M., Hu, J., Peng, M., Liu, J., Liu, J., Liu, H., . . . Tan, W. (2012). Generating Aptamers by Cell-SELEX for Applications in Molecular Medicine. *International Journal of Molecular Sciences*, 13(3). doi: 10.3390/ijms13033341
- Ye, Y., Yan, W., Liu, Y., He, S., Cao, X., Xu, X., . . . Gunasekaran, S. (2019). Electrochemical detection of Salmonella using an invA genosensor on polypyrrole-reduced graphene oxide modified glassy carbon electrode and AuNPs-horseradish peroxidase-streptavidin as nanotag. *Analytica Chimica Acta*, 1074, 80-88. doi: https://doi.org/10.1016/j.aca.2019.05.012
- Yeh, M.-H., Sun, C.-L., Su, J.-S., Lin, L.-Y., Lee, C.-P., Chen, C.-Y., . . . Ho, K.-C. (2012). A low-cost counter electrode of ITO glass coated with a graphene/Nafion® composite film for use in dye-sensitized solar cells. *Carbon*, 50(11), 4192-4202. doi: https://doi.org/10.1016/j.carbon.2012.05.001
- Yeo, J.-S., Yun, J.-M., Jung, Y.-S., Kim, D.-Y., Noh, Y.-J., Kim, S.-S., & Na, S.-I. (2014). Sulfonic acid-functionalized, reduced graphene oxide as an advanced interfacial material leading to donor polymer-independent high-performance polymer solar cells. *J. Mater. Chem. A*, 2(2), 292-298. doi: 10.1039/C3TA13647G
- Yi, M., & Shen, Z. (2015). A review on mechanical exfoliation for the scalable production of graphene. *Journal of Materials Chemistry A*, 3(22), 11700-11715. doi: 10.1039/C5TA00252D
- Yin, H., Zhou, Y., Ma, Q., Ai, S., Ju, P., Zhu, L., & Lu, L. (2010). Electrochemical oxidation behavior of guanine and adenine on graphene–Nafion composite film modified glassy carbon electrode and the simultaneous determination. *Process Biochemistry*, 45(10), 1707-1712. doi: https://doi.org/10.1016/j.procbio.2010.07.004
- Yin, J., Qi, X., Yang, L., Hao, G., Li, J., & Zhong, J. (2011). A hydrogen peroxide electrochemical sensor based on silver nanoparticles decorated silicon nanowire arrays. *Electrochimica Acta*, 56(11), 3884-3889. doi: https://doi.org/10.1016/j.electacta.2011.02.033
- Yin, P. T., Kim, T.-H., Choi, J.-W., & Lee, K.-B. (2013). Prospects for graphene–nanoparticle-based hybrid sensors. *Physical chemistry chemical physics : PCCP*, 15(31), 12785-12799. doi: 10.1039/c3cp51901e
- Yin, P. T., Shah, S., Chhowalla, M., & Lee, K.-B. (2015). Design, Synthesis, and Characterization of Graphene–Nanoparticle Hybrid Materials for Bioapplications. *Chemical Reviews*, 115(7), 2483-2531. doi: 10.1021/cr500537t
- Yu, G., Hu, L., Vosgueritchian, M., Wang, H., Xie, X., McDonough, J. R., . . . Bao, Z. (2011). Solution-Processed Graphene/MnO₂ Nanostructured Textiles for High-

- Performance Electrochemical Capacitors. *Nano Letters*, 11(7), 2905-2911. doi: 10.1021/nl2013828
- Yu, W. J., Liao, L., Chae, S. H., Lee, Y. H., & Duan, X. (2011). Toward Tunable Band Gap and Tunable Dirac Point in Bilayer Graphene with Molecular Doping. *Nano Letters*, 11(11), 4759-4763. doi: 10.1021/nl2025739
- Yue, W., Tang, C., Wang, C., Bai, C., Liu, S., Xie, X., . . . Li, D. (2017). An electricity-fluorescence double-checking biosensor based on graphene for detection of binding kinetics of DNA hybridization. *RSC Advances*, 7(70), 44559-44567. doi: 10.1039/C7RA08246K
- Yun, W., & K., S. J. (2016). Culture-Independent Rapid Detection Methods for Bacterial Pathogens and Toxins in Food Matrices. *Comprehensive Reviews in Food Science and Food Safety*, 15(1), 183-205. doi: doi:10.1111/1541-4337.12175
- Yusoff, N. (2019). Chapter 7 - Graphene–Polymer Modified Electrochemical Sensors. In A. Pandikumar & P. Rameshkumar (Eds.), *Graphene-Based Electrochemical Sensors for Biomolecules* (pp. 155-186): Elsevier.
- Zavyalova, E., & Kopylov, A. (2018). Chapter 7 - DNA aptamer-based molecular nanoconstructions and nanodevices for diagnostics and therapy A2 - Grumezescu, Alexandru Mihai *Nanostructures for the Engineering of Cells, Tissues and Organs* (pp. 249-290): William Andrew Publishing.
- Zelada-Guillen, G. A., Sebastian-Avila, J. L., Blondeau, P., Riu, J., & Rius, F. X. (2012). Label-free detection of *Staphylococcus aureus* in skin using real-time potentiometric biosensors based on carbon nanotubes and aptamers. *Biosens Bioelectron*, 31(1), 226-232. doi: 10.1016/j.bios.2011.10.021
- Zhang, C., Lv, X., Han, X., Man, Y., Saeed, Y., Qing, H., & Deng, Y. (2015). Whole-cell based aptamer selection for selective capture of microorganisms using microfluidic devices. *Analytical Methods*, 7(15), 6339-6345. doi: 10.1039/C5AY01016K
- Zhang, D., Hu, B., Guan, D., & Luo, Z. (2016). Essential roles of defects in pure graphene/Cu₂O photocatalyst. *Catalysis Communications*, 76, 7-12. doi: <https://doi.org/10.1016/j.catcom.2015.12.013>
- Zhang, H., Sun, J.-T., Yang, H., Li, L., Fu, H., Meng, S., & Gu, C. (2016). Tunable magnetic moment and potential half-metal behavior of Fe-nanostructure-embedded graphene perforation. *Carbon*, 107, 268-272. doi: <https://doi.org/10.1016/j.carbon.2016.06.001>
- Zhang, Q., Zhang, Y., Meng, Z., Tong, W., Yu, X., & An, Q. (2017). Constructing the magnetic bifunctional graphene/titania nanosheet-based composite photocatalysts for enhanced visible-light photodegradation of MB and electrochemical ORR from polluted water. *Scientific Reports*, 7(1), 12296. doi: 10.1038/s41598-017-12504-2
- Zhang, W., Lin, C.-T., Liu, K.-K., Tite, T., Su, C.-Y., Chang, C.-H., . . . Li, L.-J. (2011). Opening an Electrical Band Gap of Bilayer Graphene with Molecular Doping. *ACS Nano*, 5(9), 7517-7524. doi: 10.1021/nn202463g

- Zhang, X.-Y., Li, H.-P., Cui, X.-L., & Lin, Y. (2010). Graphene/TiO₂ nanocomposites: synthesis, characterization and application in hydrogen evolution from water photocatalytic splitting. *Journal of Materials Chemistry*, 20(14), 2801-2806. doi: 10.1039/B917240H
- Zhang, X., Rajaraman, B. R. S., Liu, H., & Ramakrishna, S. (2014). Graphene's potential in materials science and engineering. *RSC Advances*, 4(55), 28987-29011. doi: 10.1039/C4RA02817A
- Zhang, X., Wang, F., Liu, B., Kelly, E. Y., Servos, M. R., & Liu, J. (2014). Adsorption of DNA Oligonucleotides by Titanium Dioxide Nanoparticles. *Langmuir*, 30(3), 839-845. doi: 10.1021/la404633p
- Zhao, X., Lin, C. W., Wang, J., & Oh, D. H. (2014). Advances in rapid detection methods for foodborne pathogens. *J Microbiol Biotechnol*, 24(3), 297-312.
- Zhao, Y.-W., Wang, H.-X., Jia, G.-C., & Li, Z. (2018). Application of Aptamer-Based Biosensor for Rapid Detection of Pathogenic Escherichia coli. *Sensors*, 18(8). doi: 10.3390/s18082518
- Zheng, L., Cheng, X., Cao, D., Wang, G., Wang, Z., Xu, D., . . . Shen, D. (2014). Improvement of Al₂O₃ Films on Graphene Grown by Atomic Layer Deposition with Pre-H₂O Treatment. *ACS Applied Materials & Interfaces*, 6(10), 7014-7019. doi: 10.1021/am501690g
- Zhou, Y., Fang, Y., & Ramasamy, R. P. (2019). Non-Covalent Functionalization of Carbon Nanotubes for Electrochemical Biosensor Development. *Sensors (Basel)*, 19(2). doi: 10.3390/s19020392
- Zhu, C., Guo, S., Fang, Y., & Dong, S. (2010). Reducing Sugar: New Functional Molecules for the Green Synthesis of Graphene Nanosheets. *ACS Nano*, 4(4), 2429-2437. doi: 10.1021/nn1002387
- Zhu, L., Luo, L., & Wang, Z. (2012). DNA electrochemical biosensor based on thionine-graphene nanocomposite. *Biosensors and Bioelectronics*, 35(1), 507-511. doi: https://doi.org/10.1016/j.bios.2012.03.026
- Zhu, R.-R., Wang, S.-L., Zhang, R., Sun, X.-Y., & Yao, S.-D. (2007). A Novel Toxicological Evaluation of TiO₂ Nanoparticles on DNA Structure. *Chinese Journal of Chemistry*, 25(7), 958-961. doi: 10.1002/cjoc.200790186
- Zhu, Z. (2017). An Overview of Carbon Nanotubes and Graphene for Biosensing Applications. *Nano-Micro Letters*, 9(3), 25. doi: 10.1007/s40820-017-0128-6
- Zifruddin, A. N., & Thong, K. L. (2018). Potential Use of DNA Aptamer-Magnetic Bead Separation-PCR Assay for Salmonella Detection in Food. *Journal of Food Quality and Hazards Control*, 5(3), 94-101. doi: 10.29252/jfqhc.5.3.94
- Zuo, P., Li, X., Dominguez, D. C., & Ye, B.-C. (2013). A PDMS/paper/glass hybrid microfluidic biochip integrated with aptamer-functionalized graphene oxide nano-biosensors for one-step multiplexed pathogen detection. *Lab on a Chip*, 13(19), 3921-3928. doi: 10.1039/C3LC50654A

LIST OF PUBLICATIONS

1. **Muniandy, S.**, Dinshaw, I. J., Teh, S. J., Lai, C. W., Ibrahim, F., Thong, K. L., & Leo, B. F. (2017). Graphene-based label-free electrochemical aptasensor for rapid and sensitive detection of foodborne pathogen. *Analytical and bioanalytical chemistry*, 409(29), 6893-6905. doi.org/10.1007/s00216-017-0654-6. (ISI-Publication-Q1: 3.28)
2. **Muniandy, S.**, Teh, S. J., Appaturi, J. N., Thong, K. L., Lai, C. W., Ibrahim, F., & Leo, B. F. (2019). A reduced graphene oxide-titanium dioxide nanocomposite based electrochemical aptasensor for rapid and sensitive detection of *Salmonella enterica*. *Bioelectrochemistry*, 127,136-144. doi.org/10.1016/j.bioelechem.2019.02.005. (ISI-Publication-Q1: 4.47)
3. **Muniandy, S.**, Teh, S. J., Thong, K. L., Thiha, A., Dinshaw, I. J., Lai, C. W., & Leo, B. F. (2019). Carbon Nanomaterial-Based Electrochemical Biosensors for Foodborne Bacterial Detection. *Critical reviews in analytical chemistry*, 1-24. doi: 10.1080/10408347.2018.1561243 (ISI-Publication-Q2: 4.32).